Doctoral theses at NTNU, 2021:340

Eirik Helno Herø

Experimental Investigations of Single Oil Droplet Breakage in a Turbulent Water Flow

Doctoral thesis

NTNU
Norwegian University of Science and Technology
Thesis for the Degree of
Philosophiae Doctor
Faculty of Natural Sciences
Department of Chemical Engineering

NTNU
Norwegian University of
Science and Technology

Eirik Helno Herø

Experimental Investigations of Single Oil Droplet Breakage in a Turbulent Water Flow

Thesis for the Degree of Philosophiae Doctor

Trondheim, November 2021

Norwegian University of Science and Technology
Faculty of Natural Sciences
Department of Chemical Engineering

NTNU
Norwegian University of
Science and Technology

NTNU
Norwegian University of Science and Technology

Thesis for the Degree of Philosophiae Doctor

Faculty of Natural Sciences
Department of Chemical Engineering

ISBN 978-82-326-5213-6 (printed ver.)
ISBN 978-82-326-5643-1 (electronic ver.)
ISSN 1503-8181 (printed ver.)
ISSN 2703-8084 (online ver.)

Doctoral theses at NTNU, 2021:340

Printed by NTNU Grafisk senter

Abstract

Multiphase flow and the transient behavior of the dispersed phase is important to numerous industrial applications. Predictive modeling of the dispersed phase would be beneficial in designing, for example, phase separation equipment. A possible framework for modeling of the dispersed phase is the population balance equation. As the dispersed phase may undergo breakage, the breakage phenomena must be sufficiently understood to formulate universally predictive models describing the breakage processes. However, additional data from experimental investigations is required as the current understanding of the breakage phenomena is not at the required level.

In this work, the breakage phenomena are investigated experimentally by high-speed imaging of single octanol droplets in a turbulent water flow. A new experimental facility has been designed and constructed to perform the investigation. To determine the design criteria of the experimental facility the derivation of available turbulent breakage models were examined. In addition, a review of previous experimental setups and a review of isotropic turbulence facilities were performed. Four criteria were identified as critical for experimental investigation of turbulent droplet breakage. One, single droplets should be considered. Two, the entire breakage event must be observed by high-speed imaging and the procedure for extracting data must be transparent and well defined. Three, the experiments must be repeatable and reproducible as several experiments under the same conditions are required. Four, the region of breakage should be defined by known local flow conditions exhibiting low gradients in the turbulence level. To fulfill the determined criteria, a facility utilizing channel flow was constructed.

A LDV investigation was performed to characterize the continuous flow conditions. The resulting instantaneous velocity measurements were used to obtain the turbulent kinetic energy. Taylor's frozen hypothesis was used for estimating two-point correlations, which were used to obtain the turbulent kinetic energy dissipation rate.

A well-defined image analysis procedure was defined, elucidating the procedure of interpreting individual videos of breakage. Two interpretations of the breakage event, the initial breakage event definition and the cascade breakage event definition, were considered in the analysis.

To combine the information obtained from several videos, a clearly defined statistical analysis procedure was provided. In the procedure a quantitative precision of the measured quantities were obtained using 95% confidence intervals. Based on the statistical procedure it was determined that the number of investigations required for statistically

relevant results were ~ 30.

Single octanol droplet experiments were performed and investigated to elucidate the breakage phenomena. The impact of both the mother drop size and the turbulence characteristics could be investigated, as each breakage event was associated with known local flow conditions from the LDV investigation. Known model concepts could be fitted to the data for the breakage time and the breakage probability with reasonable accuracy. However, the model coefficients were different from previous investigations, thus the models can not be considered to be universal. The average number of daughters and the daughter size distribution function exhibits behaviors which are not in agreement with available model concepts.

Acknowledgments

First and foremost, a special thanks to my main supervisor Professor Hugo Jakobsen for giving me this opportunity. Your investment in the project, enthusiasm and skill have been a great source of motivation.

I would like to express my gratitude to the numerous other people involved in this work, both mentioned here or not. Especially Dr. Nicolas La Forgia for the close collaboration and great office environment and Professor Jannike Solsvik for enlightening discussions and insights. For their contributions to the experimental work I would also like to thank Ingeborg Dahl and Dr. Jing Shi.

Thanks to Professor Hanna Knuutila for giving me the opportunity to teach and contributing to a very positive experience.

The workplace does not only consist of work, and thanks to Haakon, Ida, Mathias, Gro, Hanna, Marcin, Joakim, Samuel, Ina, Stine, Ricardo, Sindre and many more for their contributions to a great social environment. Thanks to Hanna, Gro and Ida for listening when I really needed it.

To all my family, thank you for all your support and encouragement. To Elise, this would not have been possible without you and I hope you know that. And finally, to Edmund, of course.

List of Publications and Presentations

Publications in Journals

Paper 1

La Forgia, N., Herø, E. H., Solsvik, J. and Jakobsen, H. A. Dissipation rate estimation in a rectangular shaped test section with periodic structure at the walls. Chem. Eng. Sci. 195, 159–178 (2018).

CRediT: **Nicolas La Forgia** Conceptualization, Methodology, Formal analysis, Investigation, Data Curation, Writing - Original Draft **Eirik H. Herø** Conceptualization, Methodology, Investigation, Writing - Review & Editing **Jannike Solsvik** Conceptualization, Methodology, Writing - Review & Editing **Hugo A. Jakobsen** Conceptualization, Methodology, Writing - Review & Editing, Supervision

Paper 2

Herø, E. H., La Forgia, N., Solsvik, J. and Jakobsen, H. A. Determination of Breakage Parameters in Turbulent Fluid-Fluid Breakage. Chem. Eng. Technol. 42, 903–909 (2019).

CRediT: **Eirik H. Herø** Conceptualization, Methodology, Software, Formal analysis, Investigation, Data Curation, Writing - Original Draft **Nicolas La Forgia** Conceptualization, Methodology, Software, Investigation, Writing - Review & Editing **Jannike Solsvik** Conceptualization, Methodology, Writing - Review & Editing **Hugo A. Jakobsen** Conceptualization, Methodology, Writing - Review & Editing, Supervision

Paper 3

Herø, E. H., La Forgia, N., Solsvik, J. and Jakobsen, H. A. Single Drop Breakage in Turbulent Flow: Statistical Data Analysis. Chem. Eng. Sci. X 100082 (2020).

CRediT: **Eirik H. Herø** Conceptualization, Methodology, Software, Formal analysis, Investigation, Data Curation, Writing - Original Draft **Nicolas La Forgia** Conceptualization, Methodology, Software, Investigation, Writing - Review & Editing **Jannike**

Solsvik Conceptualization, Writing - Review & Editing **Hugo A. Jakobsen** Conceptualization, Writing - Review & Editing, Supervision

Paper 4

Herø, E. H., La Forgia, N., Solsvik, J. and Jakobsen, H. A. Single Oil Drop Breakage in Water: Impact of Turbulence Level in Channel Flow. Chem. Eng. Sci. X 100111 (2021)

CRediT: **Eirik H. Herø** Conceptualization, Methodology, Software, Formal analysis, Investigation, Data Curation, Writing - Original Draft **Nicolas La Forgia** Conceptualization, Methodology, Software, Investigation, Writing - Review & Editing **Jannike Solsvik** Conceptualization, Writing - Review & Editing **Hugo A. Jakobsen** Conceptualization, Writing - Review & Editing, Supervision

Presentations and Posters in Conferences

Presentation 1 Shi, J., Herø*, E. H., Solsvik, J. and Jakobsen, H. A. Experimental and numerical study on single droplet breakage in turbulent flow. 12th International Conference on Computational Fluid Dynamics In the Oil and Gas, Metallurgical and Process Industries. Trondheim, Norway, May 30 - June 1, 2017. *Presentation held by Herø

Presentation 2 Herø, E. H., La Forgia, N., Shi, J., Solsvik, J. and Jakobsen, H. A. On the turbulent dissipation rate in experimental investigation of single droplet breakage in fluid-fluid system. 6th International Conference on Population Balance Modelling, Ghent, Belgium, 7 - 9 May, 2018.

Presentation 3 Herø, E. H., La Forgia, N., Solsvik, J. and Jakobsen, H. A., Investigation of the impact of turbulence on oil droplet breakage. Tekna Separation Technology 2018, Stavanger, Norway, October 16 - 17, 2018.

Poster Herø, E. H., Shi, J., Solsvik, J. and Jakobsen, H. A., Experimental investigation of single fluid particle breakage due to turbulence. 22nd International Congress of Chemical and Process Engineering CHISA 2016, Prague, Czechia, 27 - 31 August, 2016.

Table of Contents

Nomenclature

Latin Letters

$\bar{S}$	Rate of strain [1/s]
$\boldsymbol{r}$	space coordinate vector [m]
$\boldsymbol{u}$	velocity vector [m/s]
ΔN	number of breaking drops
ΔP	pressure drop [Pa]
ΔV_d	daughter size range
Δx	displacement from channel centerline [m]
A	area [m^2]
b	breakage frequency [1/s]
B_B	birth due to breakage [1/(m^3 m s)]
B_D	death due to breakage [1/(m^3 m s)]
c	parameter
C_D	drag force coefficient
C_k	Kolmogorv constant
c_L	model parameter
D	drop diameter [m]
D_d	daughter drop diameter [m]
D_m	mother drop diameter [m]
D_{crit}	Hinze critical diameter [m]
E	energy [J]

E	energy spectrum [m^2/s^3]
F	hypergeometric function
f_L, f_η	Pope's model spectrum functions
F_n	force of type n [N]
f_n	number density function [$1/(m^3\ m)$]
g	gravitational constant [m/s^2]
h	breakage yield reistribution function [1/m]
K	Bessel function
k	turbulent kinetic energy [m^2/s^2]
L	integral length scale [m]
N	total number of drops
$p0$	Pope's model spectrum constant
P_B	breakage probability
P_{DSD}	daughter size distribution function [1/m]
P^*_{DSD}	dimensionless daughter size distribution function
r_d	model distance [m]
s	function
t	time [s]
t_B	breakage time [s]
t_e	eddy turnover time [s]
T_n	function, n = 1, 2, 3, 4, 5
u	velocity [m/s]
V_d	daughter drop volume [m^3]
V_m	mother drop volume [m^3]
AB	distance [m]
Re_P	particle scale Reynolds number
Re_λ	Taylor scale Reynolds number

U	velocity during experiments [m/s]

Greek Letters

β	Komogorov constant
β_E	Pope's model spectrum constant
ϵ	turbulent energy dissipation rate [m^2/s^3]
η	Kolmogorov micro scale [m]
Γ	gamma function
γ	interfacial tension [N/m]
κ	wave number [1/m]
λ	model parameter [1/s]
μ_c	continuous phase dynamic viscosity [kg/(m s)]
μ_d	dispersed phase dynamic viscosity [kg/(m s)]
ν	average number of daughters
ν_c	continuous phase kinematic viscosity [m^2/s]
ν_d	dispersed phase kinematic viscosity [m^2/s]
$\overline{\delta u^2}$	second order longitudinal velocity structure function [m^2/s^2]
ρ_c	continuous phase density [kg/m^3]
ρ_d	dispersed phase density [kg/m^3]
σ_s	surface restoring stress [Pa]
σ_t	turbulent stress [Pa]
$\sigma_{s,v}$	stabilizing viscous stress [Pa]
$\sigma_{t,S}$	turbulent shear stress [Pa]

Chapter 1

Background

1.1 Introduction

Phase separation of oil, gas and water is critical for oil and gas production, where the treatment of produced water is among the most important aspects. The amount of water produced is increased as fields mature and may surpass the produced amount of oil [1]. The produced water must either be discharged or re-injected into the reservoir. For discharging, there is an upper limit to the amount of oil-in-water which is allowed for pollution concerns [1]. The amount of oil-in-water is also important for re-injection to avoid formation plugging or reduced injectivity [2]. Hence, the equipment for phase separation is pivotal for efficient production of oil and gas.

1.1.1 Phase Separation

The separation of oil and water can be achieved in a horizontal three-phase gravity separator. These separators consist of large cylindrical vessels with low fluid flow velocity and long residence times. The working principle is that the difference in density between the oil and water phases results in a buoyancy force on the dispersed phase. In turn, the oil settles in a layer on top of the water when given sufficient time.

The important forces acting on a dispersed droplet in either phase is the buoyancy, drag and gravity. The buoyancy can be given as

$$F_B = g\rho_c \pi D^3/6 \tag{1.1}$$

where ρ_c is the density of the continuous phase, D is the diameter of the drop and g is the gravitational constant. Similarly, the force of gravity can be given as

$$F_G = g\rho_d \pi D^3/6 \tag{1.2}$$

where ρ_d is the density of the dispersed phase. For a rigid sphere in laminar flow and very low Reynolds numbers ($\mathrm{Re}_P \ll 1$), Stokes showed that the drag force can be found by theoretical analysis [3]

$$F_D = 3\pi\mu_c D u_{rel} \tag{1.3}$$

where μ_c is the viscosity of the continuous phase and u_{rel} is the velocity of the particle relative to the continuous phase. Re_P is given as

$$\mathrm{Re}_P = \frac{u_t D}{\nu} \tag{1.4}$$

where ν is the kinematic viscosity of the continuous phase and u_t is a terminal velocity which is achieved when the buoyancy, drag and gravity forces are in equilibrium. Summing the forces as $F_B - F_G - F_D = 0$ the expression for the terminal velocity can be given as

$$u_t = \frac{(\rho_c - \rho_d)\, D^2\, g}{18\mu_c} \tag{1.5}$$

This classic expression is valid in the narrow range of $\mathrm{Re}_P \ll 1$. Larger droplet sizes fall outside this range and a general drag force for these droplets can be given as

$$F'_D = \frac{1}{2} C_D \rho_c A u_{rel}^2 \tag{1.6}$$

where $A = \pi D^2/4$ is the projected area normal to the relative velocity and C_D is a drag coefficient. The expression for the terminal velocity based on the general drag force (1.6) becomes

$$u_t = \sqrt{\frac{4}{3} \frac{(\rho_c - \rho_d)\, D\, g}{\rho_c\, C_D}} \tag{1.7}$$

From this expression, it can be seen that the terminal velocity is sensitive to the droplet diameter and drag coefficient. However, the correct drag force on a droplet outside of the Stokes law regime is complex. For example, a droplet may deform and exhibit internal flow which affects the drag force [4, 5]. The following discussion of C_D is limited to the better understood drag coefficient of a rigid sphere in a steady uniform flow field. Under these conditions, C_D can be shown to be a function of Re_P only [5] and can be given by the standard drag curve, shown in Figure 1.1. As can be seen from the figure, C_D is at its maximum value for low Re_P and decreases significantly as Re_P increases until $\mathrm{Re}_P \lesssim 10^3$. For larger Re_P the drag coefficient increases slightly until $\mathrm{Re}_P \sim 10^5$ where the flow around the particle becomes turbulent [4], causing a sharp drop in the value of C_D.

Assuming that the drag coefficient of a rigid sphere can describe the drag coefficient of a drop, it follows that larger drops have both a larger diameter and a lower drag coefficient than smaller drops. The corresponding terminal velocity (1.7) of larger drops is bigger than for smaller drops, thus larger drops require shorter residence times in the separator for phase separation to be achieved. The design of phase separation equipment should account for this effect of larger drops, and attempt to mitigate the amount of breaking drops.

The specific design and internal components of individual gravity separators may vary depending on design constraints, inlet conditions, etc. For example, offshore installations have stricter size constraints than onshore installations [6]. Nevertheless, the general design of a gravity separator remains the same, for which a simplified sketch is shown in

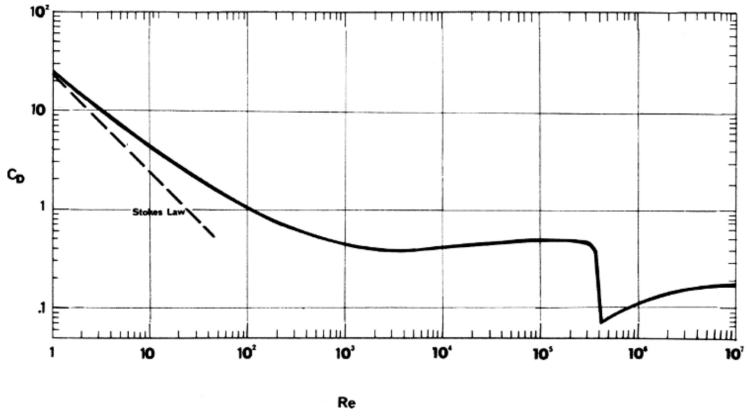

Figure 1.1: The standard drag curve; the drag coefficient of a rigid sphere in a steady uniform flow as a function of Re_P [4]

Figure 1.2. The critical parts are the inlet, separate outlets for each phase and a weir. The three phases to be separated enters at the inlet. The gas phase outlet is placed at the top of the separator, while the denser oil and water phases have their outlets at the bottom of the separator. To separate the oil outlet from the water phase, the weir is placed after the water outlet. The weir stops the flow of water, but as the top of the oil layer reaches higher than the weir, the oil overflows into the section containing the oil outlet.

Gravity separators are often equipped with an internal device designed to lower the horizontal velocity, which increases the residence time. Traditionally, this device was a plate facing normal to the inlet flow, called a momentum breaker. The momentum breaker facilitates breakage of the dispersed phases due to the large forces required for the abrupt negative acceleration of the flow. An improvement is the schoepentoeter device which dampens the horizontal velocity more smoothly [6], reducing the amount of breakage induced.

Phase separation could be improved by moving the separation equipment subsea. When separation occurs closer to the well there is less agitation and mixing of the phases as they are transported through fewer valves, chokes and other equipment. Additional advantages are de-bottlenecking of topside separation facilities and increased production [7]. On the other hand, subsea separation comes with a significant disadvantage; the cost associated with installation, reparation and replacement is very high at remote locations and great depths. Larger equipment such as phase separators further increases the costs. The designed equipment must be robust as well as cost and size efficient for subsea separation to be a viable concept.

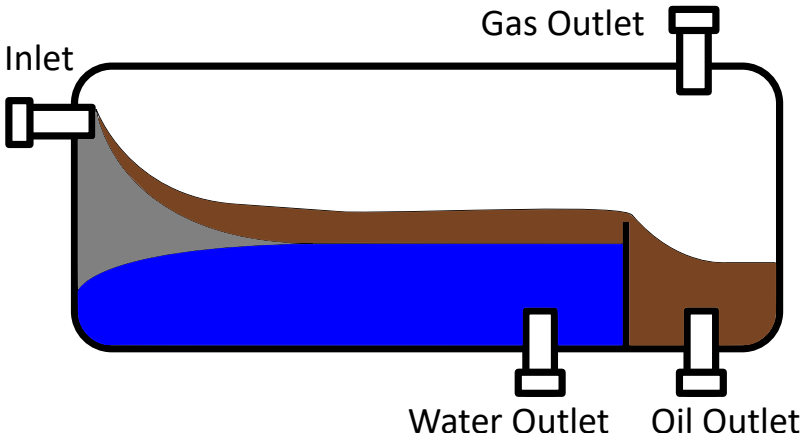

Figure 1.2: Schematic drawing of a horizontal gravity separator.

1.1.2 PBE and Breakage Modeling

Improved modeling of the multiphase flow is a promising approach for enhancing the equipment design process. A model framework for phase separators must account for the size distribution of the dispersed phase due to the importance of droplet size in phase separation. One such framework is the population balance equation, PBE [8]. The PBE dynamically describes the dispersed phase particles as they are transported, coalescing and breaking. In closing the PBE, the source terms representing coalescence and breakage must be modeled. These source terms consists of underlying kernel functions, shortened to kernel functions.

Several models have been developed for the source terms representing fluid particle breakage, which have been reviewed by e.g. Lasheras et al. [9], Liao and Lucas [10] and Solsvik et al. [11]. The current models for breakage in liquid-liquid dispersions are not predictive as the complex breakage phenomena are not sufficiently elucidated [12, 13]. The breakage models, e.g. Coulaloglou and Tavlarides [14], have traditionally been validated with experimental data from dense dispersion studies. In these investigations [14, 15, 16, 17] the dispersed phase is observed at separate time instances and locations. The model parameters are subsequently adapted or fitted to the experimental data, assuming that the model will predict the observed change in the dispersed phase. The assumptions made in the model development are neither verified nor disproved in this procedure as individual breakages are not observed. To elucidate the breakage phenomena and verify model assumptions single droplet studies are required. Here, the entire single droplet breakage events can be observed, allowing for insight into the mechanisms of breakage. For example, almost all models assume that breakup always results in two daughters, but this assumption is contrary to what has been observed in several

experimental single droplet breakage studies [18, 19, 13, 20].

1.1.3 Single Droplet Breakage Studies

Several single droplet breakage studies are reported in the literature [18, 19, 21, 13, 20]. One issue is that these studies investigate only selected kernel functions and not a complete set. Model validation based on these studies must rely on the results from several studies to obtain all the experimental data required to investigate the breakage phenomena. This approach based on several studies does not ensure consistency in the set of experimental data as the different studies may utilize different equipment, system properties or flow characteristics. Moreover, the interpretation of the observed breakage events to describe the kernel functions is not trivial, but the interpretation procedure employed is often vaguely described or not given. The flow field of the equipment utilized may be an additional confounding factor. The equipment is often relevant for the industry, such as a stirred tank reactor or an orifice flow. However, the region of droplet breakage often exhibit large turbulence level and high viscous shear. This complicates the interpretation of the results as both the turbulence level and the viscous shear are hypothesized to give rise to important forces leading to breakage [11]. In addition, the breakages may occur in close proximity to a wall, impeller, obstruction, etc., where wall effects on the continuous phase flow or direct interaction with the solid surface may impact the breakups. Hence, there is a need for single droplet studies that consider breakage due to turbulence in low viscous shear regions without wall interference. These single droplet studies should report a complete set of kernel functions from a well defined procedure.

1.2 Research Goals and Objectives

The goal of this PhD work is to elucidate the phenomena of oil particle breakage in water due to turbulent interactions. The breakage phenomena and the underlying mechanisms should be elucidated by well planned experimental investigations. The experimental data should help to investigate the kernel functions needed to close the breakage source terms of the population balance equation. The following objectives have been identified as required to achieve the outlined goal:

1. Design and construct an experimental facility for the investigation of single particle breakage in turbulent flow.
2. Characterize the turbulence level of the continuous flow in the experimental facility.
3. Determine and outline a procedure for extracting information on the kernel functions from the observed breakage events.
4. Perform experiments under different flow conditions, system conditions and dispersed phase properties.
5. Investigate the experimental data to elucidate the breakage phenomena.

1.3 Dissertation Structure

The structure of the dissertation chronologically covers the research objectives outlined in the previous section.

The current chapter provides a short background for the research and outlines the aim of the PhD work. The population balance equation is presented in detail in Chapter 2, including an outline of breakage model concepts and the turbulence theory employed for conventional model development. Previous experimental investigations of fluid particle breakage are found in Chapter 3 and previous experimental investigations of isotropic turbulence are found in Chapter 4. The Chapters 2, 3 and 4 provides the basis for Chapter 5 where the design of the experimental facility is presented.

Paper 1 is presented in Chapter 6 and covers the determination of turbulent characteristics in the continuous phase by LDV. This work provides the information required for associating turbulent characteristics with the observed droplets breakages during the subsequent single droplet experiments.

Paper 2 is presented in Chapter 7, describing the methodology of extracting data on the kernel functions from individual videos obtained experimentally. The procedure provides data associated with single experimental observations, which must be combined and averaged to describe the kernel functions. The statistical framework employed in the averaging procedure is shown in Paper 3, constituting Chapter 8. The statistical analysis is extended to include considerations on the number of repetitions required for adequate statistical precision.

Paper 3 also investigates the breakage phenomena by analyzing the experimental data. The analysis is accompanied by a comparison with conventional model concepts. This analysis is expanded with additional data in Paper 4, constituting Chapter 9, with additional experiments and model concepts.

Finally, the overall conclusions of this work is presented in Chapter 10 and suggestions to further work is given in Chapter 11.

Chapter 2

Theoretical Background

2.1 Population Balance Equation

In the continuum mechanical approach the population balance equation can be formulated in two ways [5], the macroscopic [14, 22] and microscopic [8] descriptions. This work focuses on the microscopic approach as it is a fundamental approach and thus considered to be more general [5].

General derivations of the microscopic formulation is readily available elsewhere [8, 5]. Hence, the PBE is presented here in a simplified form relevant to the current work on single droplet breakage. Liquid-liquid dispersions may undergo coalescence, but this is not relevant for single droplet experiments and outside the scope of the current work. The simplified form of the PBE is limited to accumulation, convection in physical space and breakup, and may be given as

$$\frac{\partial f_n}{\partial t} + \nabla \cdot [\boldsymbol{u} f_n] = B_B - B_D \tag{2.1}$$

Here, the number density function f_n denotes the number of drops of size D ($1/\mathrm{m}^3$[D]) and is a function of the drop size D, the space coordinate vector $\boldsymbol{r}$ and time t. Furthermore, $\boldsymbol{u}$ denotes the velocity vector and B_B and B_D denotes the source and sink terms of breakage birth and breakage death, respectively. The breakage death term describes the number of drops of size D which are removed due to breakage. It may be given as

$$B_D = b\, f_n \tag{2.2}$$

where b is the breakage frequency, which represents the number fraction of drops breaking per unit time. The breakage birth term describes the number of drops of size D which are generated due to the breakup of larger drops. This term requires an integration over all drops with sizes larger than D and may be given as

$$B_B = \int_D^{D_{max}} \nu(D')\, P_{DSD}(D', D)\, b(D')\, f_n(D')\, dD' \tag{2.3}$$

Here, D' denotes the drop sizes of the larger drops. ν is the average number of daughter drops generated upon breakage and P_{DSD} is the daughter size distribution function, which describes the probability of obtaining a drop of size D when a drop of size D' breaks. The daughter size distribution function must be number conserving, which can be formulated as

$$\int_0^{D'} P_{DSD}(D', D)\, dD = 1 \tag{2.4}$$

In addition, ν and P_{DSD} are not really independent and may be combined to give the breakage yield redistribution function as $h(D', D) = \nu P_{DSD}(D', D)$. h must be volume conserving which may be expressed as

$$\int_0^{D'} D^3\, h(D', D)\, dD = D'^3 \tag{2.5}$$

The breakage frequency b, the average number of daughter drops generated ν and the daughter size distribution function P_{DSD} are expected to be functions of D, the flow conditions, fluid and system properties. To close the PBE, these kernel functions must be modeled, which requires an fundamental understanding of the breakage phenomena.

2.2 Drop Breakage

The possible mechanisms of drop breakage can be classified into four categories: turbulent motions and stresses, viscous shear stress, shearing-off processes and interfacial instabilities [11]. The flow near a momentum breaker, and many other industrial applications, is highly turbulent. The breakage mechanism that dominate under these conditions are the turbulent motions and stresses [23].

The investigations on fluid particle breakage in turbulent flow can be traced back to the pioneering works of Kolmogorov [24] and Hinze [23]. They used the second order structure function, $\overline{\delta u^2}$, to formulate an expression for the turbulent stresses. The second order structure function is defined as the covariance of the difference in velocity between two points in physical space [5]. Letting D denote this distance the second order structure function can be written as

$$\overline{\delta u^2}(\boldsymbol{r}, D) = \overline{[u(\boldsymbol{r} + D) - u(\boldsymbol{r})]^2} \tag{2.6}$$

where $\boldsymbol{r}$ denotes the space coordinate vector. A formulation of the second order structure function by the turbulent quantities may be found through isotropic turbulence theory.

2.3 Turbulence

The concept of eddies in turbulent flow is not rigorously defined [5]. Eddies are considered to be coherent structures within the mean flow. These structures have different length scales and exhibit vorticity and pressure fluctuations [25]. The turbulent kinetic energy is passed continuously from larger to smaller scales, until it is dissipated to heat due to

viscous effects at the smallest scales [26]. This energy distribution over the various eddy scales can be described by the turbulent energy cascade which consists of the energy containing subrange, the inertial subrange and the dissipating subrange of turbulence.

The largest scales of eddies are formed from velocity gradients in the mean flow [27] and are in the energy containing subrange of turbulence. The turbulence in this subrange is anisotropic and dependent on the production of turbulence occurring in the mean flow. For scales smaller than the energy containing subrange of turbulence, Kolmogrov stated that the turbulence is universal and isotropic [28]. In the dissipation subrange the very smallest scales of turbulence are uniquely defined by the kinematic viscosity ν_c and the turbulent energy dissipation rate ϵ. Based on these two parameters the Kolmogorov length microscale $\eta = (\nu_c^3/\epsilon)^{1/4}$ [5] can be expressed, describing the size of the smallest eddies. Kolmogorov [28] also stated that a second universal subrange called the inertial subrange of turbulence may exists between the energy containing and dissipation subranges. The prerequisite is sufficiently high Reynolds numbers. As the energy is expected to be dissipated by viscous effects in the dissipation range only, Kolmogorov stated that the viscosity does not describe the inertial subrange of turbulence. Hence, the inertial subrange of turbulence is described by ϵ only [28].

Pope [29] suggested approximate boundaries for the different subranges of turbulence. The dissipating subrange contains the scales $\eta < D < 60\eta$, the inertial subrange occupies the range $60\eta < D < L/6$ and the energy containing subrange occupies the range $L/6 < D < 6L$. Here D denotes the length scale of the eddy and $L = k^{3/2}/\epsilon$ [29] is the integral length scale where k is the turbulent kinetic energy.

Kolmogorov formulated an energy spectrum describing the kinetic energy of the eddies in the inertial subrange of turbulence [28, 24]

$$E(\kappa) = C_k \epsilon^{2/3} \kappa^{-5/3} \tag{2.7}$$

Here, κ is the wave number of the eddy, which is related to the eddy size D as $\kappa = 2\pi/D$. C_k is a constant set to 1.5 [30]. There is an exact relationship between the energy spectrum and the second order structure function [31]

$$\overline{\delta u^2}(D) = \frac{4}{3} \int_0^\infty E(\kappa) \left[1 - 3 \left\{ \frac{\sin(\kappa D)}{[\kappa D]^3} + \frac{\cos(\kappa D)}{[\kappa D]^2} \right\} \right] d\kappa \tag{2.8}$$

Hence, the Kolmogorov structure function valid in the inertial subrange is given as [28, 24]

$$\overline{\delta u^2}(D) = \beta(\epsilon D)^{2/3} \tag{2.9}$$

in which the Kolmogorov constant β can be set to 2 [32]. In addition to only being valid for values of D in the intertial subrange, this formulation is also limitied to very large Reynolds numbers. Pope [29] later formulated a model energy spectrum valid in the entire range of turbulence

$$E(\kappa) = C_k \epsilon^{2/3} \kappa^{-5/3} f_L(\kappa L) f_\eta(\kappa \eta) \tag{2.10}$$

where f_L and f_η are functions. The function $f_L(\kappa L)$ is given as

$$f_L(\kappa L) = \left[\frac{\kappa L}{[(\kappa L)^2 + C_L]^{1/2}}\right]^{5/3+p0} \tag{2.11}$$

and the function $f_\eta(\kappa\eta)$ is given as

$$f_\eta(\kappa\eta) = \exp\left[-\beta_E[(\kappa\eta)^4 + C_\eta^4]^{1/4} - C_\eta\right] \tag{2.12}$$

Here, $p0 = 2$ and $\beta_E = 5.2$. The parameters C_L and C_η depend on Re_λ and C_k. For Re_λ in the range 10^2 to 10^5 the parameters can be estimated from [25]

$$C_L(\mathrm{Re}_\lambda, C_k) = \exp\left[-\frac{4.478 + 18.362C_k}{\mathrm{Re}_\lambda^{1.075-0.070C_k}}\right] - 1.913 + 2.169C_k \tag{2.13}$$

$$C_\eta(\mathrm{Re}_\lambda, C_k) = \exp\left[-\frac{14.043 - 4.222C_k}{\mathrm{Re}_\lambda^{1.986-0.363C_k}}\right] - [0.089 + 0.339C_k] \tag{2.14}$$

Re_λ is the Taylor scale Reynolds number given as

$$\mathrm{Re}_\lambda = \sqrt{\frac{20}{3}\frac{k^2}{\epsilon\nu_c}} \tag{2.15}$$

Based on the model spectrum by Pope [29] (2.10) and the transformation (2.8) Solsvik and Jakobsen [27] proposed a semi-empirical formulation for the second order structure function. This formulation is valid in the entire range of turbulence and for any turbulent Re_λ value. The expression can be given as [27]

$$\overline{\delta u^2}(D) = \frac{4}{3}k\left(\frac{D^2}{r_d^2 + D^2}\right)^{2/3} \cdot (1 - [T_1(D) + T_2(T_3(D)T_4(D) - T_5(D))]) \tag{2.16}$$

where r_d is a crossover length scale, which is related to the transition between the dissipation subrange and the inertial subrange of turbulence. The expression for r_d is given by

$$r_d = (15\beta)^{3/4}\eta \tag{2.17}$$

The different T_n expressions are given as

$$T_1(D) = \frac{2}{[s(D)]^2}F\left(\left(-\frac{1}{3}\right)^{\frac{1}{2}}, \left(\frac{3}{2}\right)\middle|\, \frac{[s(D)]^2}{4}\right) \tag{2.18}$$

$$T_2 = 3^{3/2}\Gamma\left(\frac{2}{3}\right) \tag{2.19}$$

$$T_3(D) = 27 \cdot 2^{1/3}[s(D)]^{2/3}\Gamma\left(\frac{2}{3}\right) \tag{2.20}$$

$$T_4(D) = \frac{1}{352\pi} F\left(\left(\frac{7}{3}\right)^{\frac{11}{6}}, \left(\frac{17}{6}\right) \middle| \frac{[s(D)]^2}{4}\right) \tag{2.21}$$

$$T_5(D) = \frac{2^{2/3}}{2\pi[s(D)]^{2/3}} K_{\frac{4}{3}}(s(D)) \tag{2.22}$$

in which F is the hypergeometric function, K is the Bessel function and Γ is the gamma function. Finally, $s(D)$ is found from

$$s(D) = D/(c_L^{-1/2} L) \tag{2.23}$$

2.4 Modeling of Breakage due to Turbulence

Modeling the breakage kernel functions in the population balance equation framework has been of interest to the chemical engineering community for a long time. An ideal model should be predictive and universal, i.e. valid for all fluid flow characteristics, fluid properties and system conditions. Several different models and model concepts have been suggested for the breakage frequency b, average number of daughter drops ν and daughter size distribution function P_{DSD}. These models have been the subject of several reviews [9, 10, 11]. A selected number of models and their derivation are considered in the current study. The models for the breakage frequency is considered and compared first. Models for the average number of daughter drops and the daughter size distribution are discussed in the subsequent section.

2.4.1 Breakage Frequency

2.4.1.1 Coulaloglou and Tavlarides

Coulaloglou and Tavlarides [14] formulated a pioneering model for drop breakage. They postulated that the breakage frequency b can be determined as the reciprocal of a breakage time t_B multiplied by the fraction of drops breaking $\frac{\Delta N}{N}$. This fraction of drops breaking is interpreted as the the probability that a drop will break P_B, often referred to as breakage probability. Formulated mathematically, the breakage frequency can be given as

$$b(D) = \frac{1}{t_B(D)} \frac{\Delta N(D)}{N(D)} = \frac{1}{t_B(D)} P_B(D) \tag{2.24}$$

In developing their model Coulaloglou and Tavlarides [14] assumed the drop size to be within the inertial subrange of turbulence and the turbulence was assumed to be locally isotropic. Local pressure fluctuations arising from the turbulence were assumed to deform the drop and *an oscillating deformed drop will break if the turbulent kinetic energy transmitted to the droplet by turbulent eddies exceeds the drop surface energy* [14]. The expression for the breakage probability is determined from the latter postulation. The breakage probability was assumed proportional to the fraction of the turbulent eddies that collides with the drop where the energy of the turbulent eddy is larger than

the drop surface energy. Assuming random motion, this fraction of turbulent eddies was described by the Maxwell-Boltzmann 2D energy distribution [11]. Furthermore, it was assumed that the kinetic energy distribution of the drops is the same as the kinetic energy distribution of the eddies. Hence, the energy distribution describes the fraction of drops with kinetic energy larger than surface energy, which is also the breakage probability P_B

$$\int_{E_c(D)}^{\infty} P(E(D))dE = \exp\left(-\frac{E_c(D)}{E(D)}\right) = P_B(D) \tag{2.25}$$

in which $E(D)$ is the turbulent energy associated with eddies of size D and $E_c(D)$ is the critical value that the turbulent energy $E(D)$ must overcome. The critical energy was assumed to be proportional to the surface energy

$$E_c(D) \propto \gamma D^2 \tag{2.26}$$

in which γ is the interfacial tension. The energy of the turbulent eddies was expressed using the second order structure function of size D

$$E(D) \propto \rho_d D^3 \overline{\delta u^2}(D) \tag{2.27}$$

where ρ_d is the density of the dispersed phase. Here, it is assumed that eddies larger than the drop only contributes transportation of the drop and does not contribute to breakup, while eddies of the same size or smaller provide the required local strain. The concept that large eddies transport drops and small eddies generate local strain may be traced back to Taylors investigations into the spectrum of single phase turbulence [33], and this concept is of importance for many model derivations. In the original formulation the second order structure function was determined from Kolmogorov theory (2.9), yielding the final expression of the breakage probability as

$$P_B(D) = \exp\left(-\frac{c_1\gamma}{\rho_d \epsilon^{2/3} D^{5/3}}\right) \tag{2.28}$$

in which c_1 is a parameter.

Coulaloglou and Tavlarides [14] assumed that the motion of the eventual centers of mass of the daughter drops could be described by the motion of two turbulent eddies, which had previously been described by Batchelor [34]. A separation distance AB of two eddies in the inertial subrange at time t is given as

$$[AB(t)]^2 \propto (AB_0\ \epsilon)^{2/3} t^2 \tag{2.29}$$

Here AB_0 is some initial separation distance, not further specified. Assuming both AB_0 and the distance at breakage to be proportional to the mother drop diameter, the equation can be solved for t_B as

$$t_B(D) = c_2 D^{2/3} \epsilon^{-1/3} \tag{2.30}$$

in which c_2 is a parameter. This expression is proportional to the eddy turnover time ($t_e(D) = D^{2/3}\epsilon^{-1/3}$) for eddies of size D [9, 11].

The final expression for the breakage frequency can be found by inserting (2.30) and (2.28) into (2.24)

$$b(D) = c_2^{-1} D^{-2/3} \epsilon^{1/3} \exp\left(-\frac{c_1 \gamma}{\rho_d \epsilon^{2/3} D^{5/3}}\right) \tag{2.31}$$

2.4.1.2 Modifications to the Model by Coulaloglou and Tavlarides by Solsvik and Jakobsen

Solsvik and Jakobsen [35] showed that the model of Coulaloglou and Tavlarides [14] can be expanded to consider the full range of turbulence. In the derivation of the breakage probability, the second order structure function valid in the entire range of turbulence (2.16) can be used instead of the inertial subrange formulation (2.9). The expression for the breakage probability becomes

$$P_B(D) = \exp\left(-\frac{c_3 \gamma}{\rho_d D \overline{\delta u^2}(D)}\right) \tag{2.32}$$

Solsvik and Jakobsen [35] also recognized that the eddy turnover time could be approximated as $t_e(D) \approx D/\sqrt{\overline{\delta u^2}(D_m)}$. Hence, the breakage time can be given as

$$t_B(D) = c_4 \frac{D}{\sqrt{\overline{\delta u^2}(D)}} \tag{2.33}$$

If the expression for $\overline{\delta u^2}$ is valid for the entire range of turbulence, the model of Coulaloglou and Tavlarides [14] may be assumed valid in the entire range of turbulence.

2.4.1.3 Modifications to the Model by Coulaloglou and Tavlarides According to Chen et al.

Coulaloglou and Tavlarides [14] considered only the surface tension energy as a restoring effect. However, the viscosity of the drop may also counteract breakage, as suggested by Hinze [23]. Several authors, such as Chen et al. [36] and Vankova et al. [37] have added a viscous stabilizing energy term to the critical energy (2.26) as $E_c = E_s + E_v$, where E_s is the surface energy and E_v is the viscous energy. E_v can be given as

$$E_v = \mu_d D^2 \sqrt{\overline{\delta u^2}(D)} \tag{2.34}$$

where μ_d is the dynamic viscosity of the dispersed phase. Following the same procedure as Coulaloglou and Tavlarides [14], but accounting for the viscous stabilizing energy and the formulation valid in the entire range of turbulence, the breakage frequency can be given as

$$b(D) = c_5 \frac{\sqrt{\overline{\delta u^2}(D)}}{D} \exp\left(-\frac{c_6 \gamma}{\rho_d D \overline{\delta u^2}(D)} - \frac{c_7 \mu_d}{\rho_d D \sqrt{\overline{\delta u^2}(D)}}\right) \tag{2.35}$$

2.4.1.4 Martinez-Bazan et al.

Although originally designed for gas-liquid systems, the model by Martinez-Bazan et al. [38, 39, 40] and model adaptions [41, 11] have been found to provide good agreement with data from liquid-liquid experiments. Some examples can be seen in the appendix of Solsvik et al. [11]. An important novelty of the Martinez-Bazan et al. [38, 39, 40] model is that it avoids the eddy concept. Instead, the fluid particle-turbulence interaction is expressed in terms of the second order structure function directly.

In their model derivation Martinez-Bazan et al. [38, 39] adopted the common assumptions of locally isotropic turbulence and a bubble diameter within the inertial subrange of turbulence. The main assumption is that a bubble deforms and breaks if the turbulent stresses of the surrounding fluid flow is sufficiently large. The surface restoring stress was given as

$$\sigma_s = \frac{6E_s(D)}{\pi D^3} = 6\frac{\gamma}{D} \tag{2.36}$$

where $E_s(D)$ is the surface energy due to interfacial tension, defined as $E_c(D) = \pi\gamma D^2$. The turbulent stress was estimated from the second order structure function directly

$$\sigma_t = 1/2\rho_c\overline{\delta u^2}(D) = 1/2\rho_c\beta(\epsilon D)^{2/3} \tag{2.37}$$

where ρ_c is the density of the continuous phase. Martinez-Bazan et al. [38, 39] argued that when $\sigma_t > \sigma_s$ breakup will eventually occur and conversely that breakup never occurs for $\sigma_t < \sigma_s$. Further, they postulated that the rate of breakup is inversely proportional to the difference $\sigma_t - \sigma_s$. Defining a characteristic breakup velocity as

$$v_B = \sqrt{\sigma_t - \sigma_s} \tag{2.38}$$

Then, the breakup time could be estimated as $t_B \propto D/v_B$ and the breakage frequency as

$$b(D) = c_6\frac{\sqrt{\overline{\delta u^2}(D) - 12\gamma/(\rho_c D)}}{D} \tag{2.39}$$

Or valid in the intertial subrange only

$$b(D) = K_g\frac{\sqrt{\beta(\epsilon D)^{2/3} - 12\gamma/(\rho_c D)}}{D} \tag{2.40}$$

Where Martinez-Bazan et al. [38, 39] experimentally determined the value of K_g as 0.25 and used the value of 8.2 for β.

2.4.1.5 Narsimhan et al. and Alopaeus et al.

Narsimhan et al. [42] proposed a breakage frequency model based on a stochastic modeling concept. They assumed that breakage occur due to oscillations in the drop surface and that these oscillations are the result of the relative velocity fluctuations in the turbulent flow around the drop. Breakup occurs if the turbulent motions provides at least the

minimum increase in the surface energy of the drop which is required for breakup. Furthermore, Narsimhan et al. [42] adopted the common assumptions of drop sizes within the inertial subrange and locally isotropic turbulence.

Narsimhan et al. [42] recognized that a droplet in turbulent flow may be bombarded by eddies of different scales. Each eddy-drop collision causes the surface to oscillate. Hence, there are two critical timescales; the time between bombarding eddies and the time required for a single oscillation of the drop to dampen. Based on the classic assumption that only eddies of the same size of the drop or lower can contribute to breakage and the fact that the smallest eddies have the largest frequencies, Narsimhan et al. [42] assumed that the timescale for dampening was the smallest. It follows that breakage occurs when a single eddy of sufficient energy collides with the drop. Furthermore, this is independent of previous eddy-drop collisions.

The eddy-drop collisions were assumed to form a Poisson process, where events happen continuously, independently and at a constant average rate. A parameter λ describes the average number of eddies arriving on the drop surface per unit time. λ was expected to depend on both D and ϵ, but assumed to be a constant during the model development. Two events were formulated considering a small time interval Δt:

- A: An eddy arrives on the surface of the drop.
- B: The arriving eddy has energy greater than or equal to the minimum increase in the surface energy required to break the drop.

The expression for the probability of breakage occurring in the time interval Δt is $P(A) \times P(B|A)$. It follows from the definition of λ that $P(A) = \lambda \Delta t$. Narsimhan et al. [42] then defined the breakage frequency b as

$$b(V) = \frac{P(A) \times P(B|A)}{\Delta t} = \lambda P(B|A) \tag{2.41}$$

here V denotes the volume of the drop. To approximate $P(B|A)$, Narsimhan et al. [42] first stated that the increase in the surface energy is at its minimum for binary equal sized breakage. Alopaeus et al. [43] realized that this is erroneous, as binary equal sized breakage corresponds to the largest possible increase in surface energy. Nevertheless, the expression for the "minimum" increase in surface energy became

$$E_{min}(V) = (2^{1/3} - 1)\gamma \pi^{1/3} 6^{2/3} V^{2/3} \tag{2.42}$$

This energy must be overcome by the kinetic energy transferred to the drop interface, given as $E_k = 1/2 \rho_c V u_e^2$ where u_e is the velocity of the eddy colliding with the drop. Setting $E_k \geq E_{min}$ yields an expression for the minimum velocity required as $u_e^2 \geq u_{min}^2$. The distribution of this velocity was assumed to fit a normal probability density distribution function on the form

$$P_N(u_e) = \frac{1}{\sqrt{2\pi}\sigma} \exp\left[\frac{u_e}{2\sigma^2}\right] \tag{2.43}$$

where the variance was assumed to be $\sigma^2 = \overline{\delta u^2}$ and the second order structure function was determined from (2.9). The required probability $P(B|A)$ is interpreted as $P_N(u_e^2 \geq u_{min}^2)$ which may be determined from (2.43) by statistical definitions [11]. The final expression for the breakage frequency in terms of diameter became [43]

$$b(D) = c_7 \operatorname{erfc}\left(\sqrt{\frac{c_8\,\gamma}{\rho_c \epsilon^{2/3} D^{5/3}}}\right) \tag{2.44}$$

c_7 has been substituted for λ to signify that this is a parameter. It is noted that c_7 has the units [1/s] and must be problem dependent.

Alopaeus et al. [43] later introduced a dependency of $\epsilon^{1/3}$ to c_7. In addition, they added the stabilizing effect of the drop viscosity to the minimum surface energy as $E_{min} = E_s + E_v$ where E_s is the original expression of Narsimhan et al. [42] and $E_v = \sqrt{\frac{\rho_c}{\rho_d}\mu_d \epsilon^{1/3} V^{7/9}}$. The resulting expression for the breakage frequency was

$$b(D) = c_9 \epsilon^{1/3} \operatorname{erfc}\left(\sqrt{\frac{c_{10}\,\gamma}{\rho_c \epsilon^{2/3} D^{5/3}} + \frac{c_{11}\,\mu_d}{\sqrt{\rho_c \rho_d}\epsilon^{1/3} D^{4/3}}}\right) \tag{2.45}$$

Which can be generalized with the second order structure function as

$$b(D_m) = c_{12} \epsilon^{1/3} \operatorname{erfc}\left(\sqrt{\frac{c_{13}\,\gamma}{\rho_c \overline{\delta u^2}(D)} D + \frac{c_{14}\,\mu_d}{\sqrt{\rho_c \rho_d \overline{\delta u^2}(D)} D}}\right) \tag{2.46}$$

As was the case for the model by Narsimhan et al. [42], the parameter c_{12} has dimensions [$m^{3/2}$], and is likely problem dependent. Alopaeus et al. [43] found no dependency of D on c_{12} in their study.

2.4.1.6 Viscous Shear Force

Shinnar [44] recognized that fluid particles smaller than the Kolmogorov micro scale η may break. He showed that in the dissipating subrange of turbulence the viscous shear force of the smallest eddies dominate and inertial forces are negligible. Hence, droplets smaller than η must be subject to a viscous stress exerted by the turbulent eddies of size η. Shinnar [44] formulated a viscous shear stress as

$$\sigma_{t,S} = \mu_c \bar{S} = \mu_c \sqrt{\epsilon/\nu_c} \tag{2.47}$$

where $\bar{S}$ is the local rate of strain due to velocity gradients, expressed as the Kolmogorov local rate of strain. A generalization of this strain rate has been proposed by Håkansson et al. [45] and Karimi and Andersson [46] formulated as $\bar{S} = \sqrt{\overline{\delta u^2}(D)}/D$. The viscous shear stress using this formulation is assumed valid when the expression for the second order structure function is valid and may be applied to all subranges of turbulence, as an addition to the inertial stress. However, there is some ambiguity to the use of

the second order structure function in this way. As seen in the model developments presented in this chapter, the second order structure function is used to approximate the velocity difference, pressure difference or stress across a particle in turbulent flow. It is not obvious that the second order structure function may also describe a turbulent viscous shear force.

The formulations of an additional force arising from the second order structure function appears to be based on the view of Walstra and Smulders [47]. They claimed that, for all scales and ranges of turbulence, eddies of comparable size to the drop act by inertial forces. This is in reasonable agreement with the already mentioned common model assumption that large eddies transport drops and small eddies generate local strain, which may be traced back to Taylor [33]. On the other hand, Walstra and Smulders [47] claimed that eddies larger than the drops exert a shear stress. While this may be true, it is clear that special care should be taken when including the viscous shear force in the entire range of turbulence.

2.4.1.7 Summary of Breakage Frequency Models

The model by Coulaloglou and Tavlarides [14] provides a very useful formulation of the breakage frequency as a function of breakage time and breakage probability. In addition, the final model formulation is relatively simple and computationally cheap. On the other hand, the model development relies on many assumptions of one quantity, fraction or distribution to be proportional to another conceivably unrelated quantity, fraction or distribution. The resulting model parameters are likely to include many physical phenomena related to breakage. A distinct breakage criteria extendable to e.g. a single droplet case is not possible.

The model by Narsimhan et al. [42] (and the adaption by Alopaeus et al. [43]) does assume that a single eddy-drop collision is responsible for breakage. The advantage of this model is that this assumption could be proved or disproved. However, the model framework relies on a parameter with units, which by definition must include phenomena related to the breakage in the given system.

The interpretation of the model framework by Martinez-Bazan et al. [38, 39, 40] is quite clear as it avoids the eddy concept. Two possible challenges still arises. One, no breakage occurs for particles below a system dependent maximum stable drop diameter. In the framework by Martinez-Bazan et al. [38, 39, 40] this maximum stable diameter is larger than proposed in other works [23]. Two, the breakage frequency rises monotonously with both ϵ and D, which is not in agreement with experimental data [21]. Solsvik et al. [48] adapted the model by adding a breakage probability to the breakage frequency. As this was based on the model of Coulaloglou and Tavlarides [14], the physically vague model parameters and the dependency on the eddy concept was introduced.

2.4.2 Average Number of Daughter Drops and the Daughter Size Distribution

As discussed in section 2.1, the daughter size distribution function P_{DSD} and the average number of daughters ν must be number and volume conserving. Hence, the two kernel functions are not independent which presents a challenge for model development. With the exception of the binary breakage model of Dorao and Jakobsen [49], no model frameworks consider the breakage yield redistribution function, $h(D', D) = \nu(D')P_{DSD}(D', D)$. Instead, the model frameworks available in the literature solves the challenge of the two dependent kernel functions by assuming ν to be known a priori. A substantial amount of models assume binary breakage ($\nu = 2$), which significantly simplifies the development of the daughter size distribution function. Moreover, the shape of P_{DSD} is assumed to be universal. Formulated in terms of volume, the shape may generally be classified as one of the following

- Normal distribution (Coulaloglou and Tavlarides [14])
- β distribution (Hsia and Tavlarides [50])
- Uniform distribution (Narsimhan et al. [42])
- U-shaped distribution (Luo and Svendsen [22])
- M-shaped distribution (Lehr et al. [51])

It is noted that the formulation of P_{DSD} may dependent on system properties or the turbulent characteristics, but the shape is universal.

2.4.2.1 Binary Breakage Models

Coulaloglou and Tavlarides [14] assumed the daughter size distribution to fit a normal distribution. The variance was chosen such that $> 99.6\%$ of the daughter drops obtains a size in the range $[0\ V_m]$, where V_m denotes the volume of the mother drop. The expression becomes [14]

$$P_{DSD}(V_m, V_d) = \frac{2.4}{V_m} \exp\left(-\frac{4.5(2V_d - V_m)^2}{V_m^2}\right) \tag{2.48}$$

where V_d denotes the daughter drop volume.

In designing their daughter size distribution function, Martinez-Bazan et al. [38, 39] considered the surplus stress associated with the two new drop diameters $D_{d,1}$ and $D_{d,2}$ formulated as

$$\Delta\sigma(D_{d,n}) = \frac{1}{2}\rho_c\beta(\epsilon D_{d,n})^{2/3} - 6\gamma/D_m \tag{2.49}$$

here, n is either 1 or 2 and D_m is the diameter of the mother drop. Martinez-Bazan et al. [38, 39] then postulated that the probability of forming two drops of diameter $D_{d,1}$ and $D_{d,2}$ is weighted by the product $[\Delta\sigma(D_{d,1})][\Delta\sigma(D_{d,2})]$. If the diameter of one drop is determined, the diameter of the second drop is given from volume conservation.

Thus, the original formulation for the probability of forming a drop of size $D* = D_d/D_m$ became

$$P_d(D^*) \propto \left(\frac{1}{2}\rho_c\beta(\epsilon D_m)^{2/3}\right)^2 \left[D^{*2/3} - \Lambda^{5/3}\right]\left[(1-D^{*3})^{2/9} - \Lambda^{5/3}\right] \tag{2.50}$$

in which $\Lambda = D_c/D_m$ and D_c is the diameter for which the turbulent stress is equal to the surface restoring stress, i.e. D_c satisfies the equation $\sigma_t = \sigma_s$, seen in (2.36) and (2.37). The final step was to determine a dimensionless daughter size distribution as $P^*_{DSD} = P_{DSD}/D_m$ and utilize the number conserving property (2.4)

$$P^*_{DSD}(1, D^*) = \frac{P_d(D^*)}{\int_0^1 P_d(D^*)dD^*} \tag{2.51}$$

This original formulation was not volume conserving. Later, Martinez-Bazan et al. [40] updated (2.50) to be written on volume form. Following the same procedure, a volume conserving P^*_{DSD} could be given as

$$P^*_{DSD}(1, V^*) = \frac{V^{*2}[V^{*2/9} - \Lambda^{5/3}][(1-V^*)^{2/9} - \Lambda^{5/3}]}{\int_{V^*_{min}}^{V^*_{max}} V^{*2}[V^{*2/9} - \Lambda^{5/3}][(1-V^*)^{2/9} - \Lambda^{5/3}]dV^*} \tag{2.52}$$

The minimum volume V_{min} is the smallest volume of a daughter drop which satisfies $\sigma_t = \sigma_s$. The maximum volume V_{max} is the complimentary volume that conserves the mass of the mother drop. The dimensionless volumes are obtained as $V^*_{max} = V_{max}/V_m$ and $V^*_{min} = V_{min}/V_m$. Eq. (2.52) corresponds to normal distribution where equal sized daughters are the most likely outcome of a breakage event.

Narsimhan et al. [42] assumed the daughter size distribution function to be uniform. The simple expression became

$$P_{DSD}(V_m, V_d) = \frac{1}{V_m} \tag{2.53}$$

2.4.2.2 Non-Binary Breakage

An alternative to the binary breakage models is the framework of Han et al. [52, 53, 54] and Solsvik et al. [55]. They proposed a set of kernel functions where the daughter numbers are fixed at 2, 3 or 4. The corresponding shape of the daughter size distribution function is specified by the daughter number only. Equal sized breakage is the most likely outcome of a breakage event.

Another multiple daughter outcome alternative to the binary breakage models was proposed by Diemer and Olson [56], where the average number of daughters can be any positive number. This may be an important advantage as ν is the average of several breakage events and not required to be an integer [8]. On the other hand, the model system requires different shape factors to be adjusted to fulfill the number and volume conservation requirements. Thus, also this model requires the shape of the daughter size distribution function and the average number of daughters to be known a priori. Finally, the model by Diemer and Olson [56] predicts equal sized breakage as the most likely outcome of the breakage event.

Chapter 3

Single Drop Breakage Investigations

3.1 The Breakage Event Definitions

As discussed in Chapter 1, single droplet experiments are required to validate the individual kernel functions. A prerequisite for this statement to be valid is that the entire breakage event is observed by high-speed imaging. Furthermore, the experimental values corresponding to the kernel functions can not be directly measured and must be derived from the obtained images. In this derivation there must be a procedure for the interpretation of the images, requiring a definition of what constitutes a breakage event. Solsvik et al. [57] recognized that formal definitions of the breakage event were not available in the literature and postulated two breakage definitions applicable to breakage experiments; the initial breakage event definition and the cascade breakage event definition. In both definitions the breakage event starts when a spherical stable mother starts to deform. The two definitions interpret the end of the breakage event differently:

- Breakage event end for the initial breakage event definition is when the initial mother drop separates.
- Breakage event end for the cascade breakage event definition is when the final intermediary daughter separates.

The difference between the two definitions is illustrated in Figure 3.1. For a binary breakage the two breakage event definitions coincide. For more complex breakups, the cascade breakage event definition yields a longer breakage time, a larger number of daughter drops and smaller daughters than the initial breakage event definition.

3.2 Experimental Conditions and Kernel Functions Considered

The number of single droplet breakage studies available in the literature are few and utilize varied equipment:

- Galinat et al. [18, 19] performed experiments in an orifice flow.

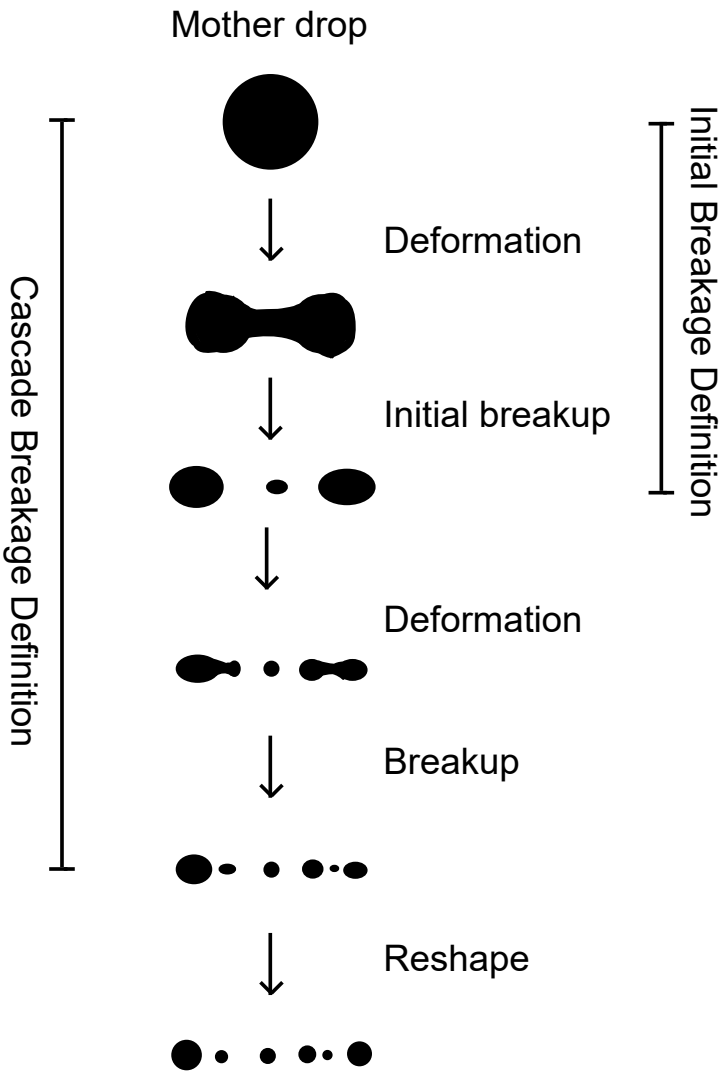

Figure 3.1: Illustration showing a sequential breakage interpreted through the initial and the cascade breakage event definitions. The figure is reproduced from Paper 2 [58]

- Andersson and Andersson [12] observed breakages in a static mixer.
- Maaß et al. [59, 60], Zaccone et al. [61], Maaß and Kraume [21] and Nachtigall et al. [62] investigated breakage in a channel flow designed to mimic a stirred tank.
- Solsvik and Jakobsen [13] utilized a stirred tank.
- Ashar et al. [20] investigated breakage in a rotor-stator mixer.
- Ji et al. [63] performed experiments in a head-on impinging microfluidic facility.

Further details on the experimental facility and experimental procedure are given in Section 3.3. In addition to different experimental facilities, the studies reported in the literature also vary with regard to the continuous and dispersed phase utilized. A summary of the fluids utilized and the resulting fluid and system properties is presented in Table 3.1. As can be seen from the table, the interfacial tension and viscosity can vary with several orders of magnitude between the studies. The investigated drop sizes and turbulent energy dissipation rate also varies, shown in Figure 3.2 and Figure 3.3, respectively. As can be seen from the figures, most of the studies have mother drop sizes in the range 0.5-4 mm and turbulent kinetic energy dissipation rate in the range 0.3-12 m^2/s^3. The relatively recent studies by Ashar et al. [20] and Ji et al. [63] occupy a different range of values. The two studies exhibit smaller drop sizes and significantly larger dissipation rates compared to the older studies.

The comparison of fluid and system properties, drop size and turbulence level may give the impression that experimental data is available for all these conditions. However, each study reported in the literature only investigates some of the kernel functions required to close the PBE and these selected kernel functions are seldom investigated for every considered drop size, turbulence level and dispersed phase considered in the study. Galinat et al. [18, 19] investigated the breakage probability, daughter size distribution and average number of daughters. The results were reported by the Weber number, combining the impact of both drop size and turbulence level. Therefore, the individual impact of mother drop size or turbulence level on the kernel function can not be investigated by the data reported by Galinat et al. [18, 19]. Andersson and Andersson [12] reported the breakage time for different ϵ levels. They also reported the daughter number distribution of dodecane drops for two of the ϵ levels. Maaß et al. [59] and Zaccone et al. [61] investigated the daughter size distribution for different daughter numbers and reported the daughter number distribution. Maaß et al. [60] and Maaß and Kraume [21] investigated the daughter number distribution, breakage time and breakage probability. Nachtigall et al. [62] investigated the breakage time with emphasis on the deformation process. Solsvik and Jakobsen [13] reported the breakage time as a function of the mother drop size and the distribution of daughter drop numbers for different drop sizes. Ashar et al. [20] investigated the breakage probability and the average number of daughters. The results were reported as functions of the Weber number. Finally, Ji et al. [63] reported the breakage probability, breakage time and the average number of daughters.

Reference	Continuous phase	Dispersed phase	γ x10^{-3}	ρ	μ_d x10^{-3}
Galinat et al. [18]	Tap water			996	0.82
		Heptane	47	683.7	0.45
		Colored heptane	23.6		
Galinat et al. [19]	Tap water with glycerin			1100	
		Colored heptane	24.4		
Andersson and	Unspecified water				
Andersson [64, 12]		Dodecane	53	750	1.5
		Octanol	8.5	819	6.5
Maas et al. [59] and		Petroleum		760	1.9
Zaccone et al. [61]	Unspecified water		2		
	Colored water		28		
Maaß et al. [60] and	Unspecified water				
Maaß and Kraume [21]		Toluene	32	870	0.55
		Petroleum	38.5	790	0.65
Nachtigall et al. [62]		Petroleum		760	1.7
	Unspecified water		43.2		
	Water with SDS*		5.9		
		Paraffin oil		861	127
	Unspecified water		53.3		
	Water with SDS*		8.4		
Solsvik and	Distilled water				
Jakobsen [13]		Toluene	33	866.7	0.6
		Petroleum	44.5	754	1.14
		n-Dodecane	41.5	745	1.38
		1-Octanol	8.4	822	7.52
Ashar et al. [20]	Deionized water			988	1
		Rapeseed oil	20	920	70
Ji et al. [63]	Unspecified water			N/A	N/A
	with 1% w.t. Tween20	Rapeseed oil	N/A	N/A	N/A

Table 3.1: Fluid and system properties reported in the previous studies. The units are given as [N/m], [kg/m^3] and [kg/(m s)] for γ, ρ and μ_d, respectively. The table is reproduced from Paper 3 [65]. * SDS denotes sodium dodecyl sulfate.

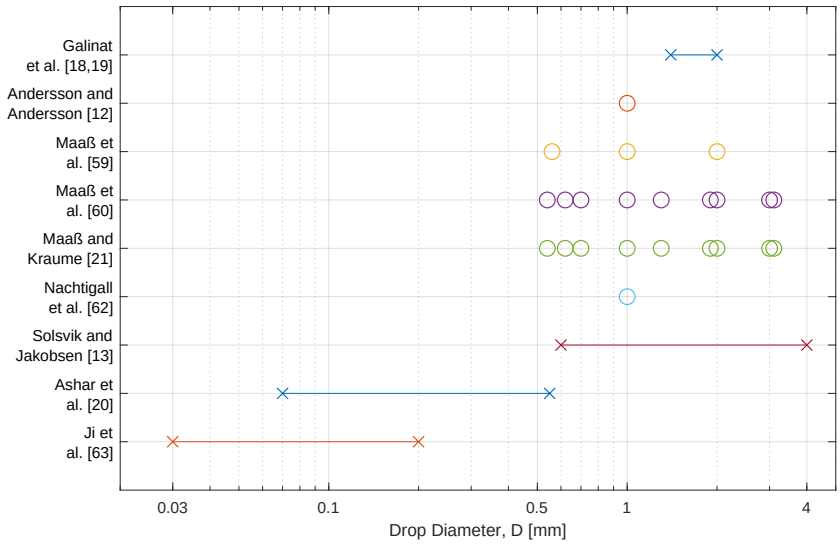

Figure 3.2: Graphical comparison of the drop sizes investigated in the literature. Circles denotes that the drop size is given as point values, while crosses connected by a line denotes that the drop size is given as a range of drops.

In general, the differences in the studies given above makes it challenging to compare the experimental results. Comparison is further complicated by the use of different breakage event definitions. In the studies by Galinat et al. [18, 19], Andersson and Andersson [12], Maaß et al. [59], Zaccone et al. [61] the breakage definition is not given or is unclear. The initial breakage definition is employed in the studies by Maaß et al. [60], Maaß and Kraume [21] and Nachtigall et al. [62]. Solsvik and Jakobsen [13], Ashar et al. [20] and Ji et al. [63] utilized the cascade breakage event definition.

3.3 Experimental Procedures and Facilities

As turbulent breakage occurs under chaotic conditions, the studies on singe drop breakage utilizes many repetitions and determine the experimental values corresponding to the kernel functions as average values. Paper 3 [65] (Chapter 8) investigates the required number of experiments for statistically relevant results. A short summary is provided here to avoid excessive repetition of the introduction of Paper 3 [65]. The needed number of repetitions are previously not well understood and no single droplet breakage investigates this issue using a statistical procedure. To obtain a single data point, i.e. an average experimental value, the single droplet breakage studies rely on a significant num-

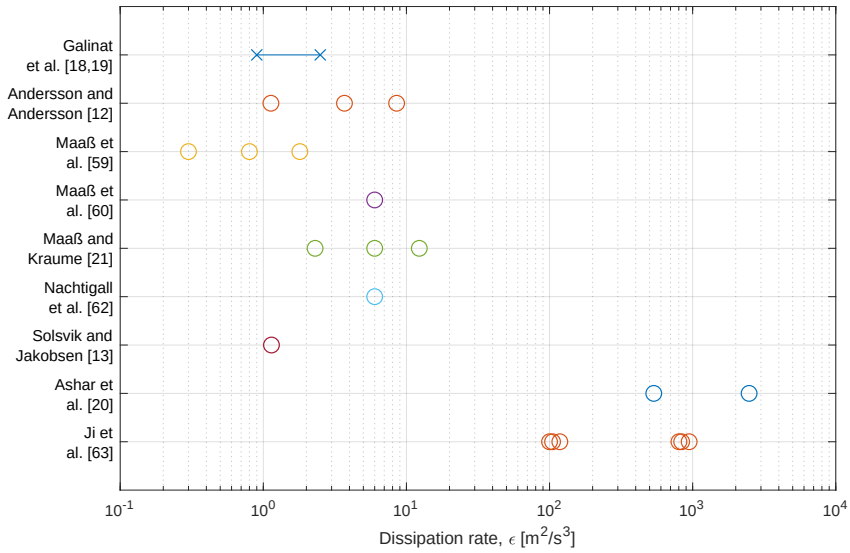

Figure 3.3: Graphical comparison of the turbulent kinetic energy dissipation rates ϵ investigated in the literature. Circles denotes that ϵ is given as point values, while crosses connected by a line denotes that ϵ is given as a range.

ber of individual experiments. From ~ 50 [12] breakage events to as many as ~ 1000 [62] events are reported. The amount of repetitions required are of paramount importance as the interpretation of the high-speed images are manual labor intensive. Investigating more experiments than statistically required may be the reason previous studies only investigate selected kernel functions and not a complete set of them.

3.3.1 Galinat et al.

Galinat et al. [18] investigated single oil droplet breakage in an orifice flow. The dispersed phase was heptane or heptane colored with red sudan and the continuous phase was tap water (Table 3.1). The coloring of the dispersed phase improves the optical contrast between the dispersed and continuous phase. Later, Galinat et al. [19] performed additional experiments with water-glycerin as the continuous phase and colored heptane as the dispersed phase. In both studies, the experimental facility (Figure 3.4) consisted of a 1 m vertical cylindrical pipe 3 cm in diameter, where an orifice was located 0.4 m from the base of the pipe. This orifice caused a pressure drop from which the average turbulent kinetic energy dissipation rate level in the breakup region could be determined. Upstream of the pipe, single dispersed droplets were injected using a capillary tube 1 mm in diameter. The capillary tube was mounted perpendicular to the continuous phase

velocity and connected to an electrical syringe pump. To observe the breakages Galinat et al. [18, 19] used a high-speed camera with 456.2 fps and 1024 x 256 pixels covering a field of size 12 x 3 cm^2. High-speed imaging requires sufficient lighting due to short exposure times, thus the area was backlit by a halogen lamp (1000 W). The resulting black-and-white images were treated in an imageprocessing algorithm designed in visilog 5. First, a reference image was subtracted. Second, a thresholding technique was used to detect the drop contour. Third, the three geometric properties area, perimeter, moment of inertia are obtained.

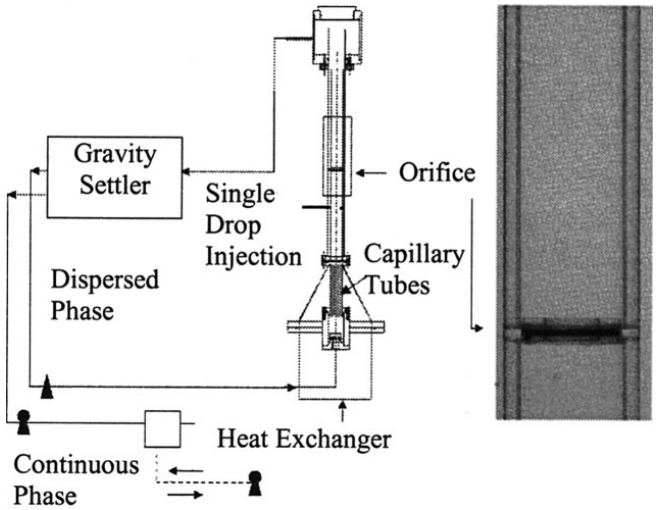

Figure 3.4: Orifice flow facility utilized in the experiments by Galinat et al. [18, 19]

3.3.2 Andersson and Andersson

Andersson and Andersson [12] studied single oil droplet breakage using dodecane or octanol as the dispersed phase and unspecified water as the continuous phase (Table 3.1). The breakages were observed in a static mixer, which may be described as a channel with significant obstructions protruding into the channel in a repeating pattern. The internal design of the mixer is shown in Figure 3.5b. PIV-experiments and LES was used to determine the volume averaged turbulent kinetic energy and turbulent kinetic energy dissipation rate level in the mixer [66] and these investigations showed that the turbulence was very homogeneous within each mixing element [12]. The dispersed phase was inserted by an injection nozzle directly in front of an obstruction, some way downstream of the inlet where the continuous flow had reached steady state. The drops were observed by a high-speed camera at 4000 fps with very short exposure times of 10-100 μs. A hybrid light technique where front-light was reflected back towards the camera was used. The resolution of the video was given as 309,000 pixels/cm^2. However, it is

not clear how large the observed section of the static mixer was nor how the images were investigated (manually, image analysis, etc.).

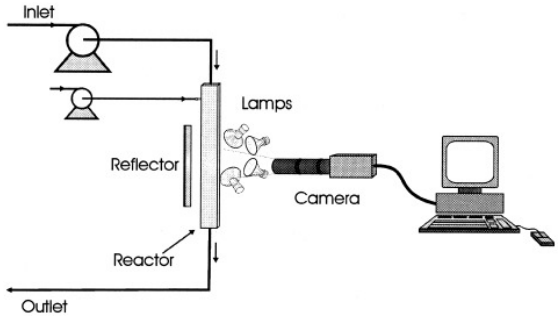

(a) Schematic overview [12]

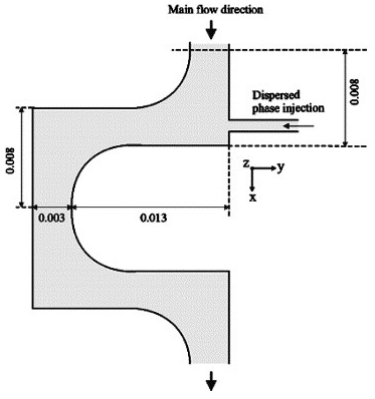

(b) Geometry of breakage region [66]

Figure 3.5: Experimental facility utilized in the study by Andersson and Andersson [12]

3.3.3 Maaß et al., Zaccone et al. and Nachtigall et al.

Maaß et al. [59, 60], Zaccone et al. [61], Maaß and Kraume [21] and Nachtigall et al. [62] investigated single oil drop breakage in the same experimental setup, seen in Figure 3.6. It consisted of a channel flow designed to mimic a stirred tank. A single blade 8 cm in diameter was fixed in a rectangular channel of cross-section of 30 mm x 30 mm x 60 mm [62]. Upstream of the channel a Hamilton dosing pump introduced the dispersed phase droplet [67] by a glass cannula or metal needle [62]. The continuous phase was water (with additives in Nachtigall et al. [62]) and the dispersed phase varied across the different studies (Table 3.1). The dispersed phase was dyed to increase the optical contrast between the dispersed and continuous phase. A volume averaged ϵ was

determined from CFD simulations with a k-ϵ model [67].

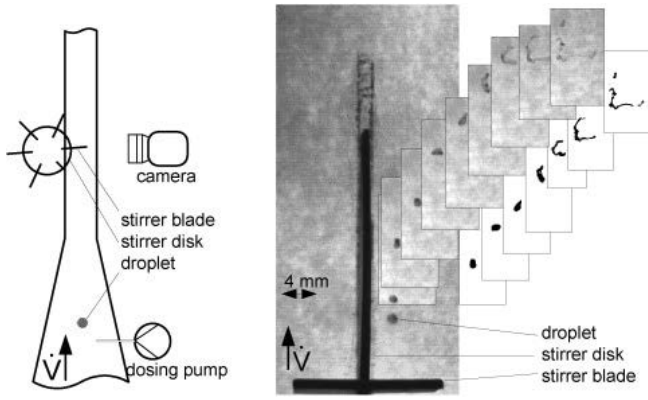

Figure 3.6: Single blade-channel flow facility utilized in the experiments by Maaß et al. [59, 60], Zaccone et al. [61], Maaß and Kraume [21] and Nachtigall et al. [62]. Figure from Maaß et al.[67]

The use of camera and image analysis evolved and varied with the sequential studies. Originally, Maaß et al. [59] and Zaccone et al. [61] used a flash camera downstream of the blade to investigate the daughter size distribution. The area around the impeller blade, where breakage happened, was observed with a high-speed camera utilizing 650 fps. However, the area observed and camera resolution employed are not given. Later, only a high-speed camera was used, observing the whole channel (30 mm x 60 mm) using 286 $\times$ 608 pixels [67] and 822 fps [60, 21]. The initial image analysis used the commercial software ImagePro-Plus which identified number, size and center of mass of all objects in each image [67]. This procedure was similar to that of Galinat et al. [18, 19] where first a reference image was subtracted, then a grayscale threshold is set to obtain fully black particles and a white background. Later, Maaß and Kraume [21] developed a fully automatic image analysis in MATLAB, based on the same principles of subtracting a reference image and grayscale thresholding. Details on the image analysis are given Nachtigall et al. [62]. The illumination employed is not given, but in the schematic of the experimental facility in Nachtigall et al. [62] it appears that some type of illumination is providing back-light.

3.3.4 Solsvik and Jakobsen

Solsvik and Jakobsen [13] investigated single drop breakage in a stirred tank (Figure 3.7). Toluene, petroleum, n-dodecane or 1-octanol was used as the dispersed phase and distilled water was used as the continuous phase. The volume averaged ϵ was determined theoretically by the power number equation. A black and white high-speed video camera was used with a resolution of 1024 x 1024 pixels and 1000 fps. In this configuration,

the diameter of the smallest observable drop was about 0.1 mm. The dispersed phases were dyed with Sudan Black to increase the optical contrast between the dispersed and continuous phase. Halogen lamps with diffuser paper provided sufficient illumination for high speed imaging. A commercial software (KLONK Image Measurments) was used to measure the mother drop size, while the number of daughter drops and the breakage time was determined manually.

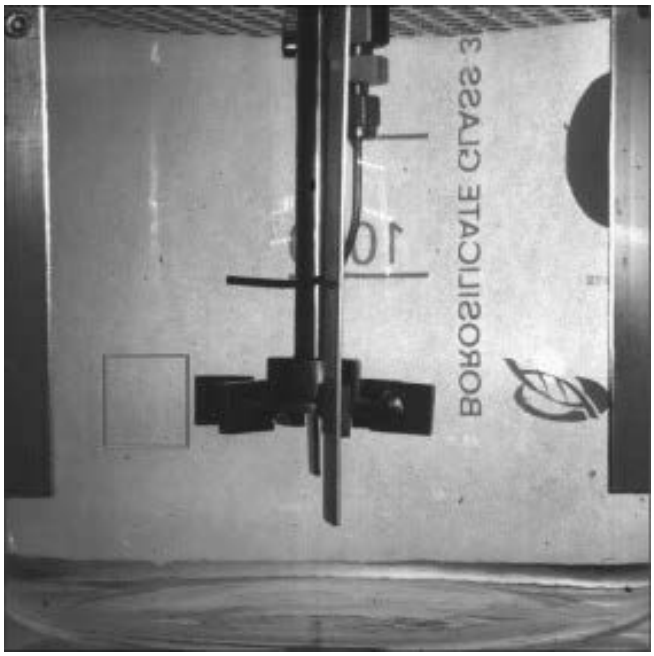

Figure 3.7: Stirred tank employed by Solsvik and Jakobsen [13]

3.3.5 Ashar et al.

Ashar et al. [20] investigated single drop breakage in a rotor-stator mixer, shown in Figure 3.8. The dispersed phase were rapeseed oil and the continuous phase was deionized water. The dispersed phase was injected through the bottom of the tank through a 0.4 mm diameter stainless steel capillary connected to a syringe pump. The rotor diameter was 188 mm, which left a 0.5 mm clearance to the surrounding stator. The stator had thickness of 5 mm and openings of 6 mm x 30 mm. The observed region was one of the stator openings, as seen in Figure 3.8b. To provide illumination, Ashar et al. [20] used five 50W halogen lamps in a front-light configuration, which was sufficient to perform the experiments without a need to color the dispersed phase. They also tested fluorescent tracer and laser illumination, but neither gave increased performance. This illumination

was sufficient for a 5 ms exposure time, which resulted in sharp images. The high-speed camera recorded at 2800-3000 fps and the resolution was given as 25 μm/pixel. The analysis of the videos were done manually, which was noted as time consuming. Finally, the turbulent energy dissipation rate level was determined from a procedure arising from PIV analysis, and given as a local average value of the volume near the impeller.

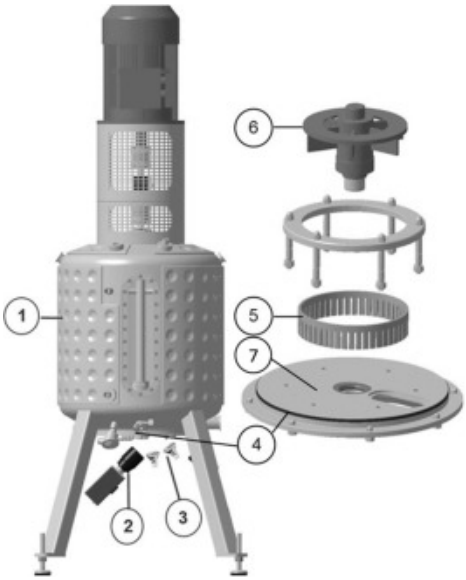

(a) Exploded view [20]

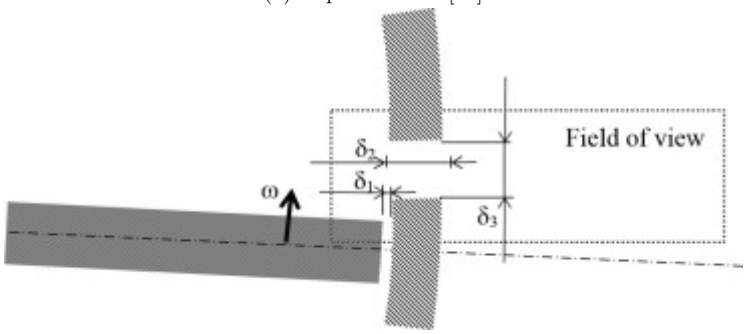

(b) Closeup of the location observed for breakage [20]

Figure 3.8: Experimental facility utilized in the study by Ashar et al. [20]

3.3.6 Ji et al.

Ji et al. [63] performed experiments in a head-on impinging microfluidic facility, shown in Figure 3.9. The facility consists of a four-way intersection where two inlet water channel flows meet head-on, creating a region of sufficient turbulence for breakage. One of the inlet flows transports rapeseed oil dispersion so dilute that only one oil drop enter the intersection at a time, allowing for single drop breakage to be observed. The facility has two configurations, one where all channels have an cross-section of 600 μm x 600 μm, and another where the dispersed phase inlet channel is smaller at 300 μm x 300 μm. The channel intersection and one of the outlet channels are observed by a high speed camera recording at 300 kHz with a resolution of 2.2 μm/pixel. A 50 W Halogen lamp provides back-light and the exposure time is set to the longest available (1/583,784 s). The turbulent energy dissipation rate was estimated as a channel average from a theoretical expression, dependent on the momentum fluxes of the channel flows.

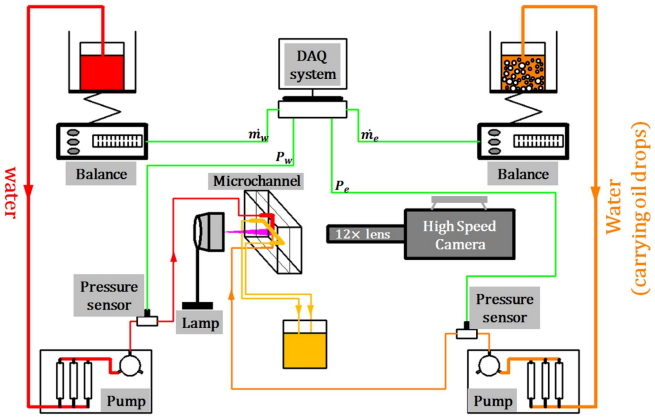

(a) Ji

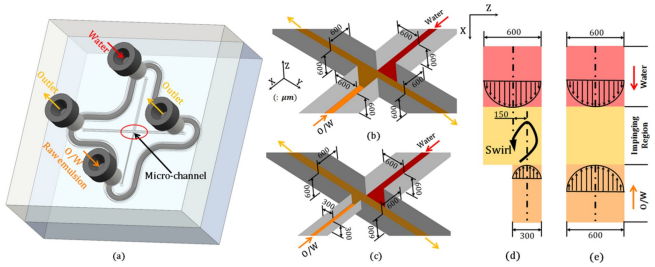

(b) Ji

Figure 3.9: Microfluidic facility utilized in the study by Ji et al. [63]

3.3.7 Overall Remarks

The experimental facilities discussed above share some similarities in the flow conditions in the breakage region. The flow conditions all exhibit large gradients in the turbulence level, which makes the actual conditions for breakage difficult to determine. Furthermore, the breakage region exhibits large mean flow shear stresses and the droplet trajectories are often in close proximity or even touching a wall, blade or other obstacles, which may contribute to breakup.

In the use of high-speed camera, there is a requirement of strong illumination on two accounts. First, short shutter speeds gives sharper images, but leaves less exposure time of each image [20]. Second, illumination is required to provide sufficient optical contrast between the continuous and dispersed phases. The required level of illumination may be reduced by the use of coloring, which is primarily applied to the dispersed phase.

Droplets are commonly generated by cannulas connected to a syringe pump. In such a setup, the flow conditions in the generation region is critical in order to obtain similar drop sizes as well as spherical (and stable) droplets. Solsvik et al.[13] and Ashar et al. [20] found it challenging to control the size of droplets generated in stirred tanks. Spherical droplets are easier to obtain when the generation is performed in less turbulent conditions, as found downstream of the breakage region in channel flow. Galinat et al.[18] reported some variation in the droplet size, while Maaß et al. [67] claimed their similar setup was very precise.

Chapter 4

Experimental Investigations of Isotropic Turbulence

As discussed in Chapter 2 the turbulent breakage models developed to close the PBE are based on isotropic turbulence theory. The studies intended to validate the breakage models should ideally perform experiments in isotropic turbulence. Facilities capable of generating isotropic turbulence have previously been studied in the field of turbulence and fluid dynamics. Two experimental facilities from the field of isotropic turbulence have been considered and is presented in this chapter.

4.1 French washing machine

The "French washing machine" was investigated by PIV measurements in the studies by Lawson and Dawson [68, 69]. The machine consists of a cylinder 2 m high and 2 m in diameter, with 1.6 m diameter impellers at the top and bottom. The impellers counter-rotate slowly creating a very small region of isotropic turbulence in the center of the cylinder. In the studies by Lawson and Dawson [68, 69] the measured volume was $\sim$120 mm x $\sim$ 120 mm x $\sim$ 20 mm and the whole measured volume was not fully isotropic. The volume average value of ϵ in the measured volume was estimated to be in the range 0.89 - 1.41 m^2/s^3, which is sufficient for single droplet studies. However, the Kolmogorov micro length scale η, denoting the scale of the smallest turbulent vortices, was determined to be 0.93 mm, which is on the same scale as the droplets commonly investigated in single droplet studies. In conclusion, the "French washing machine" creates too large turbulent structures in a too small volume to be viable in single droplet studies studying turbulent breakage.

4.2 Oscillating grid

Experimental facilities utilizing a single oscillating grid have been shown to produce regions of nearly isotropic turbulence and no-shear flow [70, 71, 72, 73, 74]. In this

type of facility, a grid is oscillating in one end of a rectangular box typically filled with water. At some distance (dependent on grid geometry and fluid properties) from the oscillating grid the jets and flow structures induced by the grid movement is dissipated. The turbulence at this distance and further from the grid exhibit a 2D isotropy in the plane parallel to the grid. Moreover, the generated turbulent kinetic energy k decreases with the distance from the grid z in the form of a power law, $k \propto z^{-n}$, where n has been found to be in the range 0.8 to 2 [72, 73]. Hence, the sensitivity of the turbulence on z is reduced with increasing z and near isotropic turbulence is obtained for larger values of z.

Shy et al. [72] constructed a facility utilizing two oscillating grids, one grid placed in each end of an rectangular box. The facility can be seen in Figure 4.1. Two boxes were tested, with dimensions $30 \times 15 \times 15$ cm^3 and $60 \times 30 \times 30$ cm^3, which gave similar results. The oscillating grids were designed with bars of diameter d arranged in a square array with a mesh size of M, such that $M/d = 5$. The resulting grid solidity is $\sim$36.9%, which is less than the limit of 40% where secondary motions are possible [73]. Secondary motions were also found by Shy et al. [72] for frequencies f_{Hz} larger than 8 Hz. Hence, there is an upper limit to both grid solidity and frequency in oscillating grid experiments. Shy et al. [72] operated with a fixed stroke length S set to 2 cm.

Shy et al. [72] found a region of near isotropic turbulence around the midpoint between the two oscillating grids. Denoting the distance between the two grids (oscillation midpoint to oscillation midpoint) as H, an empirical relation for the height h of the near isotropic region was found as $h = 0.48H - 1.5$. Here, both h and H is given in cm and the equation is valid for $H > 6$ cm and f_{Hz} in the range 1-8 Hz. In the near isotropic turbulence region the turbulent intensity q was found to be given by [72]

$$q = C^* f_{Hz} S^{1.5} M^{0.5} H^{-n} \tag{4.1}$$

where $C^* = 0.89$ cm$^{1/2}$ and $n = 1.5$. Eq. (4.1) provides a good estimate for the conditions: $4 \leq H/M \leq 6$, $S = 2$cm, $M/d = 5$ and $f_{Hz} = 1 - 8$ Hz [72]. The turbulent intensity q is defined as

$$q = \sqrt{\frac{1}{N} \sum_{i=1}^{N} \frac{(u_i')^2 + (v_i')^2 + (w_i')^2}{3}} \tag{4.2}$$

where u', v' and w' denotes the turbulent fluctuations. The turbulent intensity can describe the turbulent kinetic energy dissipation rate in isotropic turbulence by [75]

$$\epsilon = A \frac{q}{L} \tag{4.3}$$

where $A \sim 1$ at high Reynolds number turbulence [76] and L is the integral length scale. In the near isotropic region the integral length scale in dual oscillating grid experiments can be estimated as $L \approx 0.1H/2$ [70]. Employing the Eqs. (4.1) and (4.3) with the values $L = 0.1H/2$, $M = 10$ cm, $H = 30$ cm, $f_{Hz} = 8$ Hz, $C^* = A = 1$, $n = 1$ and $S = 5$ cm the corresponding turbulent energy dissipation rate is $\epsilon \approx 0.055$ m^2/s^3. This

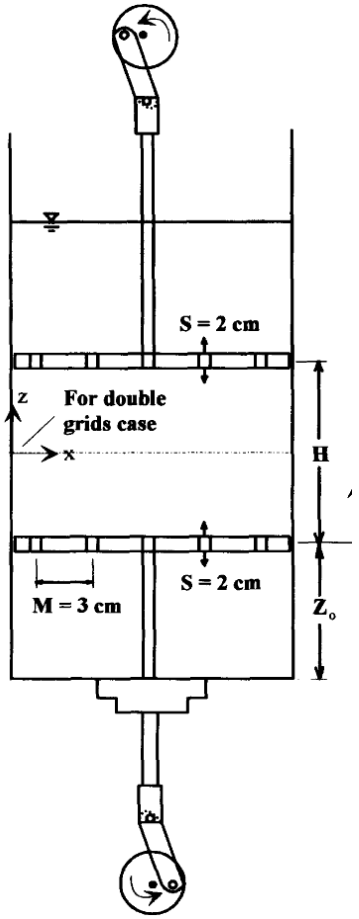

Figure 4.1: Dual oscillating grid facility employed in the study by Shy et al. [72]

turbulence level is quite low for single drop breakage experiments and it is noted that the estimate is questionable, as the values employed are outside of the range for which (4.1) was validated. The low turbulence level and additional reasons for not designing a dual grid facility are discussed in section 5.1.1.

Chapter 5

Experimental Design Procedure

This chapter describes the process of designing the experimental facility based on the information presented in the previous chapters. The experimental facility itself and the operating procedure is well described in the papers. A detailed handbook for operating the facility was provided in the master thesis by Ingeborg Dahl [77], which may be relevant for subsequent operators of the experimental facility.

5.1 Design Parameters

The main objective was to construct an experimental facility for the investigation of the complete set of kernel functions. In order to validate the results against previous investigations, similar experimental conditions to that of the previous investigations are required. Moreover, expanded experimental conditions would be advantageous, including experimental conditions which are representative for separation equipment. The target conditions for the initial design process were defined as droplet sizes of 0.5-2 mm in diameter and a turbulent energy dissipation rate of $\sim 1\ m^2/s^3$. The possibility to expand the range of experimental conditions beyond these values is important. In addition to the experimental conditions, three general points were identified as critical for experimental facilities intended to study single droplet breakage:

1. *High-speed imaging of the entire breakage event*

   The entire event is important to obtain a complete set of the kernel functions, as discussed previously (Chapters 1 and 3).

2. *Repeatable and reproducible experiments*

   Single droplet breakage studies require a significant number of drops to be assessed under the same conditions, but the exact number of drops required for statistically relevant results is unknown. To ensure that enough data can be obtained within a reasonable timeframe, the experimental facility should be able to efficiently repeat the experimental runs. In other words, the need for manual work between the experimental runs should be at a minimum.

The injection of the dispersed phase drops is particularly impacted by the requirement of repeatable and reproducible experiments. For reproducibility, the size of the drops should be consistent. Additionally, the drops entering the region of breakage should not be deformed nor otherwise affected by the droplet generation and the flow conditions upstream of the region of breakage. For an efficient procedure, the generation of drops must reliably occur with minimal manual input. An efficient procedure also requires the removal of the dispersed phase after each single experiment to be automatic, not require manual cleaning.

3. *Known local flow conditions*

   Many previous studies determine the flow conditions by a volume averaged turbulent energy dissipation rate. The regions of breakage exhibit large gradients in the turbulence level, large mean flow shear force and close proximity to an obstacle or wall, which may lead to wall interactions. An ideal setup investigates breakup in isotropic turbulence, but an experimental facility where the local turbulent characteristics are known and associated with the breakage events would also constitute an improvement. The latter is especially true if the region of breakage exhibit low shear force, small gradients in the turbulence level and low probability of wall or obstacle interaction.

5.1.1 Isotropic Turbulence Facilities

A dual oscillating grids facility is unlikely to produce the turbulence level required for droplet breakage experiments. The practical limitations to grid solidity, stroke length and oscillation frequency are too large. The required turbulence level is probably only achievable under conditions that also generates jets or other large flow structures that may significantly impact droplet breakage. At the very least, additional work on the turbulence generated in dual oscillating grid experiments is required to determine the feasibility in single droplet breakage studies.

Droplet generation and removal are other challenges. In a setup where the grids are oscillating in a horizontal direction, the droplets could conceivably be generated in a chamber or channel below the box, to be transported by buoyancy or a channel flow. This chamber or channel can be expected to have an impact on the flow pattern in box. More pertinent, the automatic removal of droplets has no clear solution. If the droplets are interacting with the turbulence, they can be expected to exhibit horizontal movement. Hence, if the droplets are to be transported out of the box by buoyancy, a large channel must be placed in the top of the box, which again can be expected to have an impact on the flow pattern in the box. Instead, manual cleaning or removal of the drop is likely required, which is not a feasible approach to single drop breakage experiments. Droplet generation and removal are also the major challenges with utilizing a french washing machine, if the problem of size of the turbulent structures could be circumvented.

As a final note, an oscillating grids facility is a challenging setup mechanically. The oscillating grids are connected to rods which provide the oscillating motion. These rods

must go through the box walls and the opening must be sealed such that the liquid in the box does not leak, without hindering the motion of the rods.

5.2 Experimental Facility

As discussed above, the method of injection of the dispersed phase drops is critical for the performance of the experimental facility. The facilities utilized by Galinat et al. [18, 19] and Maaß et al. [59, 67, 60, 21] have similar setups for droplet generation and both facilities produced drops of consistent sizes. These drops also entered the region of breakage undeformed. The setup of Maaß et al. [59, 67, 60, 21] generated droplets in volumes of different cross-sectional areas and claimed to have a controllable and very narrow distribution of drop sizes. Hence, it was decided to construct a facility utilizing a channel flow with a cannula placed transverse to the flow direction.

A significant advantage of channel flow is that it can be part of a loop setup. In a loop setup the drops can be transported from the region of breakage by the continuous phase. Downstream of the region of breakage a gravity separator can separate the dispersed phase, allowing the continuous phase to be reused. This means the consumption of continuous phase is relatively low. A more noteworthy advantage is that the cleaning, or other reasons for downtime, between individual experiments is virtually non-existent.

The requirement for known local flow conditions is critical for the design of the breakage region of the facility. Having decided on utilizing a loop design in the experimental facility, some type of channel flow is required to create the wanted breakage conditions. Turbulent pipe flow has a uniform velocity profile in the center of the channel [5], which means there is low mean flow viscous shear in this region. A channel flow, i.e. square cross section, is assumed to exhibit similar conditions. For drops traveling along the channel centerline, there is a significant distance to the wall and no other obstacles. Hence, two of the desired flow characteristics are achieved by utilizing a channel flow. Turbulence is naturally generated at the walls at high enough Reynolds numbers. There will likely be significant gradients in the turbulence level in the transversal direction, but low gradients in the streamwise direction.

A schematic of the final facility can be seen in Figure 5.1. It consists of a loop utilizing a large tank for dispersed phase separation, a positive displacement pump, a droplet generation section and a breakage section. As aforementioned, additional details are given in the articles in the following chapters. The droplet generation section was constructed with three regions of different cross-sectional area. Hence, for each mean flow condition in the breakage channel, three different flow conditions are available for droplet generation. Each droplet generation region was equipped with two opposing walls of glass, allowing high-speed imaging of the droplet generation with illumination by backlight. The high-speed cameras and the lamps providing the illumination can be moved to observe either the generation of droplets or the breakage channel. The breakage section of 30 mm x 30 mm x 1 m was constructed with two opposing walls of metal and two opposing walls of glass. In the same way as for the droplet generation section, the glass walls allow the droplet breakage to be observed by the high-speed cam-

eras with backlight illumination. The two metal walls were constructed with significant protrusions to induce more turbulence than a smooth wall. A symmetrical 2D pattern of the protrusions ensures a symmetrical flow profile. The estimation of the protrusion length is discussed in the following section.

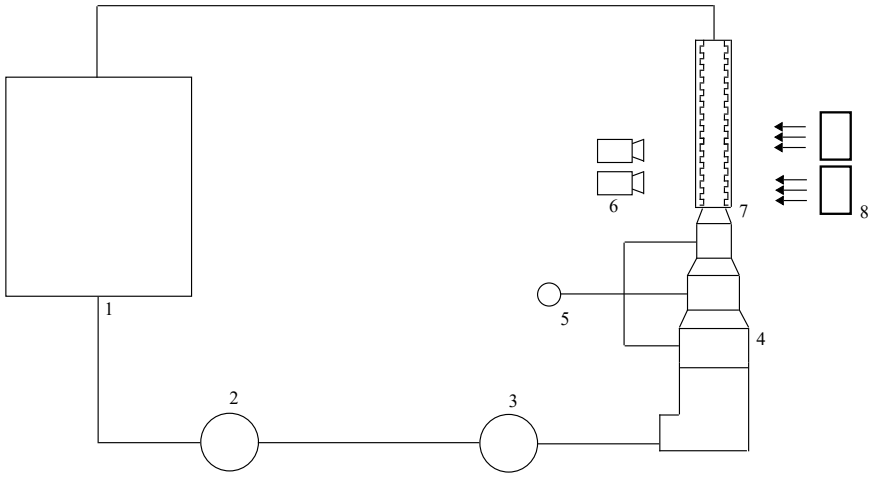

Figure 5.1: Schematic drawing of the experimental setup. 1. Water tank and phase separator, 2. water pump, 3. flow meter, 4. droplet generation section, 5. oil syringe pump, 6. two cameras, 7. breakage section, 8. illumination.

5.2.1 Turbulent Energy Dissipation Rate Estimation

The pressure drop in a pipe due to wall friction can be given as [5]

$$\Delta P = 2f\rho\frac{L}{D_p}u^2 \tag{5.1}$$

where ΔP is the pressure drop, f is the Fanning friction factor, ρ is the fluid density, L is the distance for which the pressure drop is considered, D_p is the diameter of the pipe and u is the cross sectional averaged fluid velocity in the channel. The pressure drop corresponds to a loss in kinetic energy which is dissipated to heat. The average turbulent kinetic energy dissipation rate can be given as

$$\bar{\epsilon} = \frac{\Delta P}{\rho L}u = \frac{2fu^3}{D_p} \tag{5.2}$$

The right hand side expression was used by Hesketh et al. [78] to estimate the dissipation rate in pipe flow during single bubble experiments. The friction factor f can be estimated by the Haaland equation [79]

$$\frac{1}{\sqrt{f}} = -3.6 \log \left[\frac{6.9}{\mathrm{Re}} + \left(\frac{\varepsilon/D}{3.7} \right)^{1.11} \right] \tag{5.3}$$

where ε is the characteristic length of the wall roughness. Solving for ε/D, this ratio is determined to be ~ 0.05. However, the relationship between the characteristic length of the wall roughness ε and the length of large protrusions placed in a repeating pattern is not known. It was assumed that the protrusion would need to be larger than the estimated characteristic length, and the protrusions were set to 10% of the channel diameter. Obviously, the flow characteristics and dissipation rate of this channel geometry required a more thorough investigation, hence the LDV investigations in Paper 1 was performed. Before the LDV investigation of the channel, changing the channel geometry represented a minor inconvenience both economically and practically. Thus, some initial oil particle experiments were performed. As these initial experiments showed breakup, the channel geometry was known to produce sufficient turbulence for breakage.

5.3 Challenges and Adaptions

5.3.1 Pressure fluctuations

The first attempted droplet generation section is shown in Figure 5.2. A glass cannula could be inserted at the red caps, allowing the droplet generation to take place in different area averaged velocities. The droplet generation in this setup was challenging, as the flow exhibited a recirculation and secondary flow pattern in this region. Moreover, the positive displacement pump induced rapid pressure fluctuations in the flow. The flow conditions caused the pressure where the droplets were generated to dynamically change. This pressure change caused the oil/water interface in the cannula to move, possibly due to elasticity in the tube connecting the cannula to the syringe pump. The result was jetting of oil and limited control of the size and number of droplets generated. The design of the cannula was adapted to account for this challenge and the final cannula design is shown in Figure 5.3. A small inner diameter caused the pressure fluctuations to have less of an impact on droplet generation, probably due to higher capillary pressure in the cannula. Another improvement was achieved by exchanging the tube connected to the syringe pump for a tube with a smaller diameter and made from a more rigid material. The resulting system provided reasonable stable drop sizes.

In addition to designing a better injection system, four components were installed in the loop to dampen the pressure fluctuations upstream of the section for droplet generation. The impact was not quantified, but collectively the components dampened the pressure fluctuations to a level which did not affect droplet generation. Three of the installed components may be seen in Figure 5.4. As large pressure drops causes the fluctuations in the pressure to dampen, a valve was installed. This valve appears to have

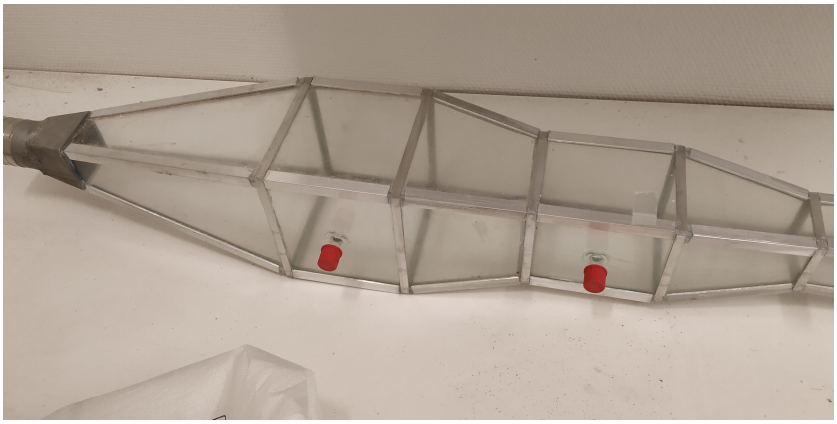

Figure 5.2: First version of the droplet generation section.

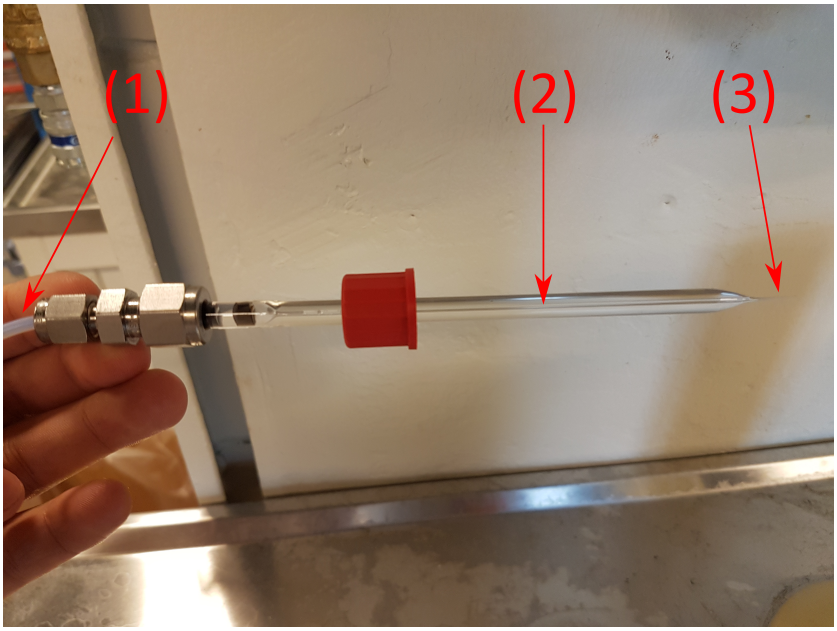

Figure 5.3: Final cannula design with important features highlighted. (1) denotes the small rigid tube connected to the syringe pump, (2) denotes the small inner diameter and (3) denotes a small outer diameter at the tip.

had the smallest impact of the four components considered. A better approach was to install a grid in the flow, inducing an significant amount of turbulence which smoothed the flow and the pressure downstream of the grid. The two remaining components installed were less intrusive. A section of tube in the loop was exchanged for a less rigid tube placed in a spiral. The combination of spiral form and ductile material dampened pressure fluctuations by allowing the spiral to contract and expand with the pressure variances. A pressure dampener was also considered, but commercial equipment was not available at this low level of pressure oscillation. Thus, a stand pipe filled with air was installed. At high pressures, water is stored in the stand pipe, while the water exits the pipe at low pressures. The result is a more even flow of water with less pressure fluctuations.

Despite the improvements made to dampen the pressure fluctuations, the droplet generation section needed to be redesigned to obtain consistent sizes of the droplets generated. The final design can be seen in Figure 5.5. This new design still relied on three different cross sectional areas for droplet generation, but the upstream design was significantly changed. The tube from the pump was connected to a channel of much larger cross-section, causing a recirculation area where the flow was redistributed. The large cross-section channel is long, allowing the flow to achieve steady state before reaching the droplet generation section. While the pressure fluctuations are still present, they are now so small that they no longer impact the droplet generation.

5.3.2 Maintenance

The new droplet generation section solved the challenge of pressure fluctuations, but also provided a new challenge. The new design did not allow for the entire facility to be drained of water. Eventually, algae started growing on the walls in the droplet generation section and upstream. The algae affected visibility through the glass and detached from the walls to impact the system and flow conditions. Attempts to remove the algae by chemical agents did not work and thus the experimental facility had to be adapted. By constructing large openings, brushes could be introduced to remove the algae mechanically. To avoid further algae buildup, additional holes were added to completely drain the droplet generation section when the facility was not in use. The modifications allowed the droplet generation section to fully dry every day, which significantly inhibited the algae generation.

The stainless steel tank utilized as a gravity separator exhibits no algae problems, hence the aluminum used in the new droplet generation section is likely a critical component of the algae generation.

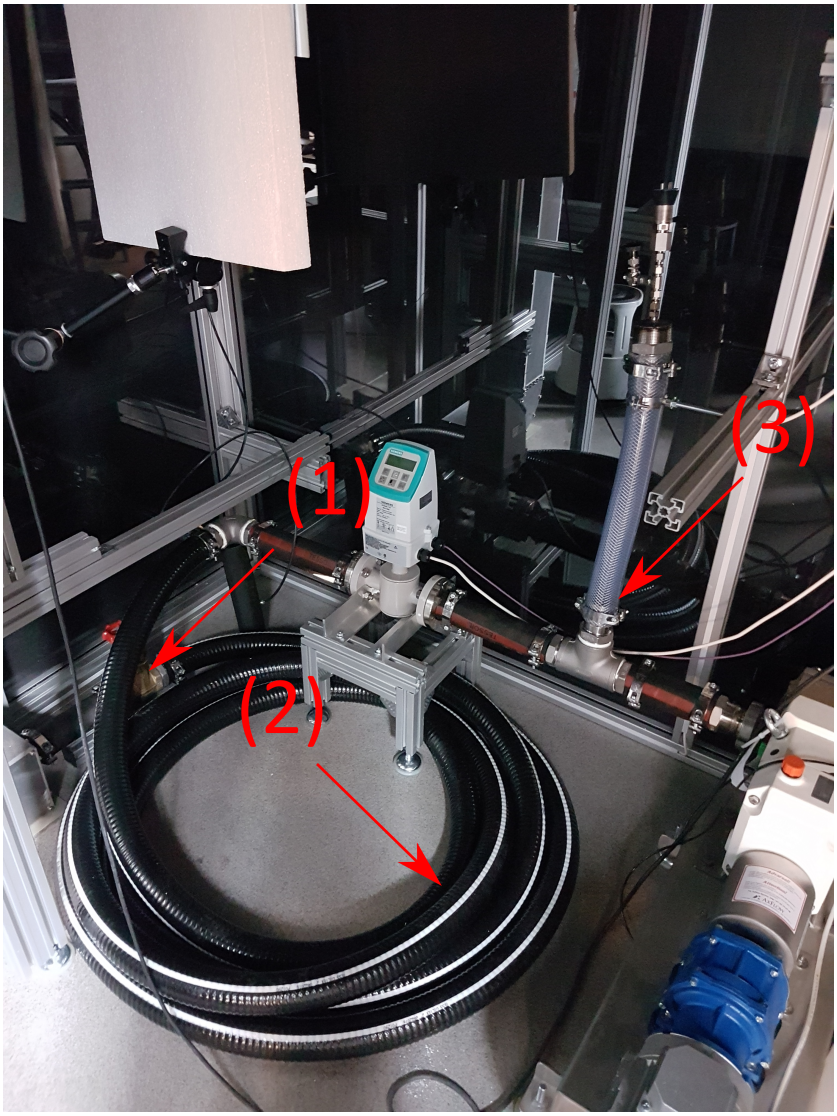

Figure 5.4: Several components for dampening of pressure fluctuations. (1) denotes a valve which causes a pressure drop. (2) denotes a tube in a spiral where the combination of spiral form and ductile material causes pressure fluctuations to be dampened. (3) denotes a stand pipe in which functions as a general pressure dampener.

Figure 5.5: Final droplet generation section

Chapter 6

Paper 1

Chemical Engineering Science 195 (2019) 159–178

Contents lists available at ScienceDirect

Chemical Engineering Science

journal homepage: www.elsevier.com/locate/ces

Dissipation rate estimation in a rectangular shaped test section with periodic structure at the walls

Nicolas La Forgia *, Eirik Helno Herø, Jannike Solsvik, Hugo Atle Jakobsen

Department of Chemical Engineering, Norwegian University of Science and Technology (NTNU), Trondheim, Norway

HIGHLIGHTS

- Evaluation of different methods for the estimation of turbulent dissipation rate.
- Experimental validation of second order structure function models.
- Experimental characterization of turbulent flow in a square-shaped test section.

ARTICLE INFO

Article history:
Received 15 August 2018
Received in revised form 9 November 2018
Accepted 16 November 2018
Available online 17 November 2018

Keywords:
Droplet breakage
Experimental investigation
Turbulence measurement
Dissipation rate

ABSTRACT

An experimental study of turbulent flow concerning the characterization of turbulence by two-point correlation and estimations of the turbulent dissipation rate is presented. The fluid used is deionized water and the test section used was a square shaped channel of 24 mm by 30 mm on the cross section with a length of 1 m. The test section also presented periodic baffle structure at two of the walls for enhancing and maintaining turbulence. The study consisted in the measurement of the velocities at different positions of the channel using Laser Doppler Velocimetry instrument (LDV), the velocity measurement obtained were used for estimating two point correlations using the Taylor's frozen hypothesis. Finally, the results from the two-point correlation were used for estimating the turbulent dissipation rate. Considering the difference in the methods for calculating the dissipation rate, a comparison of the accuracy of each method is presented. It was found that the methods presented in this work showed similar results and trends of the dissipation rate with respect to changes in flow condition and distance to the channel walls. However, better accuracy was obtained by estimating the dissipation rate using the second order structure function and the Kolmogorov's two-third law.

1. Introduction

Turbulence flow are present in many industrial processes, and have become a key parameter in the study of phase interaction in multiphase flows. One particular case of importance for the oil industry is the study of breakage and coalescence of oil droplets in turbulent water. In this case, models for droplets breakage and coalescence are used for the design and modeling of separation processes. While these models concentrate in the evolution of the different phases in the mixture, one key parameter is related to the characterization of the turbulence. Nevertheless, due to the stochastic behavior of the turbulent phenomena the interaction between phases can be difficult to model. As a consequence, most models are based on the statistical probability measured through larger amounts of individual measurement.

A review of droplet breakage mechanisms in static mixer can be found in the work of Lemenand et al. (2013), where shear, elongation and turbulent fluctuation mechanisms are discussed and compared. One important contribution to the modelling of dispersed phase distribution in multiphase flow was presented by Coulaloglou and Tavlarides work (Coulaloglou and Tavlarides, 1976), in which the foundation for models of droplet breakage and coalescence in turbulent flow for use with Population Balance Equation (PBE) was established. The phenomenological model was derived from a theoretical perspective and validated with the available experimental data where the breakage frequency and coalescence frequency were related to an estimated turbulent dissipation rate. While the model proposed presented good agreement with experimental observations, the authors also concluded that in order to

* Corresponding author.
E-mail addresses: nicolas.la-forgia@ntnu.no (N. La Forgia), eirik.h.hero@ntnu.no (E.H. Herø), jannike.solsvik@ntnu.no (J. Solsvik), hugo.a.jakobsen@ntnu.no (H.A. Jakobsen).

https://doi.org/10.1016/j.ces.2018.11.039
0009-2509/

improve the model more measurements with uniform turbulent condition and where coalescence and breakage could be observed independently were needed. Following the same principle, Azizi and Al Taweel (2011) investigated breakage in a mixer where the volume-average dissipation rate was estimated from measurement of pressure drop in combination with a model for describing the spatial variation of dissipation rate. More recently, models for drop breakage derived in term of the turbulence energy spectrum has been proposed. Han et al. (2014) suggested that the breakage frequency is parent drop size dependant, and thus influenced by the entire energy spectrum distribution using the energy spectrum models proposed by Pope (2000) and by Hinze (1975). The authors found a good agreement between their model predictions and the experimental data of Andersson and Andersson (2006b) and Maaß and Kraume (2012). Solsvik and Jakobsen (2016a,b) proposed a model for the second order structure function based on Pope's energy spectrum model which allowed the evaluation of the breakage and coalescence for the entire energy spectrum range. More recent, Gong et al. (2018) proposed a model for studying the coalescence of droplet in turbulent flow by considering the contribution of multiscale turbulent eddies. The structure function model for turbulence were compared with data from direct numerical simulation and with previous models, where the authors claim to have obtained a better accuracy in representing the second order structure function compared to the model of Han et al. (2014) and Solsvik and Jakobsen (2016a,b). Nevertheless, none of these models were compared with experimental measurement.

While different approaches are available for relating the turbulent phenomena to breakage and coalescence in multiphase flows, there is still lack of accurate experimental data regarding the turbulence characteristics and, as a result, models for turbulence had been used instead. In addition, these models require input of turbulent parameters such as the dissipation rate and the turbulent kinetic energy. However, the turbulent dissipation rate, kinetic energy and energy spectrum are not variables that can be directly measured, and must be experimentally determined which in most cases result in determining two-point correlation from the velocity fluctuation (Pope, 2000; Davidson, 2015). These correlations require measurement of the velocity fluctuation at two points while varying the distance between them. This procedure requires the use of multiple instruments, however, simplification can be made by adopting the Taylor's frozen hypothesis (Taylor, 1938) for constructing two-point correlation based on measurements from a single point.

While the amount of experimental data available in the literature is low, the focus is on models of breakage and coalescence with less focus on the turbulent characterization. Bouaifi et al. (2004) used PIV measurements and CFD simulations using the commercial software Fluent. They compared the commercial software predictions for the axial velocity component with the velocity measured with the PIV and concluded that the low-Reynolds number $k-\epsilon$ turbulence model presented a good agreement with the experiments. Nevertheless, this comparison would only reveal the ability of the model to reproduce the velocity field and not the velocity fluctuation that are required for the turbulence characterization. This work was continued by Andersson et al. (2004) where measurements and simulations of breakage and coalescence were investigated. Here the authors used the PIV technique for obtaining the turbulent kinetic energy and the turbulent dissipation rate which were obtained by direct calculation through the velocity gradients obtained by the PIV method, however the accuracy of the results were not presented. Andersson and Andersson (2006a) investigated and discussed breakup mechanisms and the dynamics of fluid particle deformation by means of high speed camera and using CFD simulations and PIV method for characterizing the turbulence. Andersson and Andersson (2006b) proposed a model for fluid particle breakage using the dissipation rate estimated by CFD simulations. Maaß et al. (2012a) used the commercial software STAR-CD for estimating the local dissipation rate in a stirred tank for studying breakage phenomena. The model used was based on a $k-\epsilon$ model which showed better prediction at higher flow velocities. Maaß et al. (2010) used the Population Balance Equation (PBE) for investigating the prediction of drop size in stirred tanks. In the PBE model, the authors used the agitation power to calculate the power number accounting the average turbulence dissipation rate. Maaß et al. (2012b) studied the prediction of droplet size distribution in breakage dominated stirred systems by hindering the coalescence phenomena. In this case, the dissipation rate was calculated by CFD simulations. Maaß and Kraume (2012), performed experimental investigations of single drop breakage where the dissipation rate were calculated as in Maaß et al. (2012a). Håkansson et al. (2017), performed experimental investigation to estimate local fragmenting stresses in rotor-stator mixer using two different approach based on PIV measurements. While both methods can provide valuable information, both approaches presented disadvantages related with the low resolution of the PIV method. Mortensen et al. (2018), experimentally study the effects of slot width on the local dissipation rate of turbulent kinetic energy using a PIV method coupled with a sub-resolution modelling for studying breakage phenomena in roto-stator mixer.

Very few works acknowledged the importance and difficulties in estimating the turbulence parameters. In the work of de Jong et al. (2009), seven different methods for estimating the dissipation rate has been compared using a PIV instrument for the characterization. The uncorrected results obtained using second and third order structure function and the scaling argument presented similar results. However, the uncorrected results obtained using the direct method (measuring the velocity derivatives from the PIV experiments) and the large-eddy PIV method developed by Sheng et al. (2000) results in larger values. The results obtained from the spectral fitting resulted larger values that the second and third structure function methods and the scaling argument but the values were lower than the direct and large-eddy PIV methods. The large-eddy PIV is similar to the direct method but employs the Smagorinsky model (Smagorinsky, 1963) for estimating the subgrid stress T_{ij}. In particular, these two methods require a good approximation of the velocity derivatives which can be affected by the spatial resolution of the PIV method. The results were corrected using models obtained from literature that allowed a reduction in the gap between different methods. The corrections diminished the values obtained by the direct method and large-eddy PIV and increased slightly the values from the second and third order structure function method and the scaling argument. Vejražka et al. (2017) performed experimental measurement of the breakage of air bubbles in a turbulent water flow. The turbulent flow was characterized through the use of the dissipation rate by measuring the velocity field by a PIV system. The local dissipation rate was estimated using a large-eddy PIV technique, a second order structure function method and a scaling argument. The results from the measurement of the dissipation rate from the different techniques presented similar trends with the variation of the flow rate and distances, nevertheless there was a large discrepancy in the values obtained, in which the second order structure function presented systematically lower values for the dissipation rate followed by the large-eddy PIV and finally by the scaling argument.

Lemenand et al. (2017a), performed experimental investigation of micro-mixing by chemical probe in homogeneous and isotropic turbulence. The turbulent characteristic was generated by means

of an oscillating grid, where the dissipation rate was estimated using a scaling argument based on a three axis LDV measurements. The authors compared the dissipation rate obtained with two different models, showing that the scaling argument used underestimate the dissipation rate compared to the models used. They conclude that the constant of the scaling argument could be greater. In the work of Lemenand et al. (2017b), the turbulent dissipation rate was obtained by linear fitting of the energy spectrum model for the inertial sub-range of Kolmogorov (1941) using a reconstruction of the energy spectrum based on LDV measurements.

In this paper, measurement of different statistical parameter for characterizing the turbulence in a square channel is presented. It is focused on providing accurate measurements for characterizing the evolution of the turbulence in the channel under different flow conditions. Different parameters were studied; including the turbulent dissipation rate, the second order structure function, third order structure function and the longitudinal autocorrelation function. Several methods are available for estimating dissipation rate from these correlations. These methods will be presented and compared considering the method accuracy and the statistical error in each case.

The design of the experimental apparatus used in this work were previously presented in Shi et al. (2017), where the design of the wall structures for the turbulence enhancing were investigated using Large Eddy Simulation method using the commercial software Fluent. The experimental apparatus was designed to study the breakage probability of oil droplet in turbulent flow. More recent, measurement for fully developed turbulent flow were presented and compared with the results from the simulations (Herø et al., 2018). The results from the simulations and the dissipation rate estimated from the measurements presented a good agreement. Nevertheless, the injection of oil droplet in a fully developed turbulent flow is difficult to achieve with this design, as a consequence the turbulence needed to be characterized for the entire channel in order to account the evolution of the turbulent flow around the channel inlet.

2. Turbulent flow characterization

Turbulent flow are characterized by the fluctuating behavior of the velocity field. This means that prediction of the flow condition at any time becomes a difficult task. The use of time average or ensemble average operators over the velocity field can provide information on the magnitude and energy of the turbulence fluctuations which can be used for constructing two-points correlations and for estimating turbulent dissipation rate (Pope, 2000; Davidson, 2015). Here, the velocity of a particular spatial point can be separated in a mean velocity component and a fluctuation component:

$$U(\bar{x},t) = \overline{U}(\bar{x}) + U'(\bar{x},t) \tag{1}$$

where $U(\bar{x},t)$ is the instantaneous velocity, $\overline{U}(\bar{x})$ is a time average mean velocity and $U'(\bar{x},t)$ is the velocity fluctuation.

The evolution of turbulence can be represented by correlating the velocity fluctuations at two different spatial positions. The correlation between spatial positions is stronger when the position is close and tends to vanish as the distance between points increases. This dependence on the position can be used in estimating the turbulent dissipation rate. The calculation of the correlations requires the simultaneous measurements of the velocities at two different positions. While the measurement at two different positions can be obtained using two instruments, the simultaneous condition can be difficult to achieve. An alternative approach is to use the Taylor's frozen hypothesis (Taylor, 1938), which assumes that the turbulent fluctuations of the velocity advect with the fluid. This means that the velocity at a different position in the stream-wise direction can be estimated from the conversion from velocity measurements at one position but differents times. The velocity at the new position can be expressed as:

$$U_x(x+r,t_0) = U_x(x,t_0 - r/\bar{U}_x) \tag{2}$$

where U_x is the velocity in the stream-wise direction, x is the position in the stream-wise direction, r is the distance between the two points in the stream-wise direction, t_0 is the initial time, and $r/\bar{U}_x$ corresponds to the time that the flow takes to advect the velocity fluctuation. Different two-point correlations can be used for characterizing the turbulent flow. The longitudinal correlation function is based in the product of the velocities at different positions in the stream-wise direction. An ensemble average is used with the product of the two velocities in order to construct the auto correlation matrix:

$$Q_{ij}(\bar{x},\bar{r},t) = < U_i'(\bar{x},t)U_j'(\bar{x}+\bar{r},t) > \tag{3}$$

If Q_{ij} does not depend on time, then it is said that the turbulence is statistically steady. In addition, if it is independent of the position $\bar{x}$, then it is said that the turbulence is statistically homogeneous. If the flow condition does not change over time, it can be assumed that the flow is statistically steady. Nevertheless, the condition for statistically homogeneous is more difficult to achieve specially at flows with turbulence generated at the walls (Pope, 2000).

It should be noted that at large $\bar{r}$, $Q_{ii}(\bar{x})$ tends to 0. Moreover, when the distance $\bar{r}$ approaches 0, then this result in:

$$Q_{ii}(\bar{x},t) = < U_i'(\bar{x},t)^2 > = U_{i,rms}'^2 \tag{4}$$

With this property, a dimensionless form can be found, which for the particular case of the stream wise direction this leads to the longitudinal auto correlation function:

$$f(r) = Q_{xx}(r)/U_{x,rms}'^2 \tag{5}$$

Where $f(r)$ is the longitudinal auto correlation function. This dimensionless function can be used to estimate the integral length scale:

$$l = \int_0^\infty f(r)dr = \frac{1}{U_{x,rms}'^2}\int_0^\infty Q_{xx}(r)dr \tag{6}$$

This parameter gives an estimation of the region in which the velocities are appreciably correlated.

A different approach is to construct the second and third order longitudinal structure function:

$$\left\langle [\Delta v(r)]^2 \right\rangle = \left\langle \left[U_x'(x+r) - U_x'(x)\right]^2 \right\rangle \tag{7}$$

$$\left\langle [\Delta v(r)]^3 \right\rangle = \left\langle \left[U_x'(x+r) - U_x'(x)\right]^3 \right\rangle \tag{8}$$

In the case of the second order structure function, the correlation approaches 0 when r tends to 0 and start developing until it reach its maximum value $< [\Delta v(r)]^2 > \approx 2U_{x,rms}'^2$. It is normally interpreted as a measure of the cumulative kinetic energy contained in eddies of size r and less (Pope, 2000).

A relation between longitudinal auto correlation and the second order structure function can be given as:

$$\left\langle [\Delta v(r)]^2 \right\rangle = 2u'^2(1 - f(r)) \tag{9}$$

Another approach is to work in the wavenumber space where the energy spectrum can be interpreted as the distribution of energy of the different vortex size, and the energy is transmitted from the larger scales to the smaller scales where the dissipation of energy takes place. Different sub-ranges can be identified; the dissipation sub range, the inertial sub range and the energy containing eddies sub range. Early breakage and coalescence models like Coulaloglou and Tavlarides (1976) assumed a particular relation between the interaction of turbulent energy and droplet size by accounting the contribution of the inertial sub range of the energy spectrum. In the inertial sub range, the turbulence can be described in terms of the turbulent dissipation rate by means of the well-known Kolmogorov's two-thirds law (Kolmogorov, 1941) and the Kolmogorov's four-fifths law (Kolmogorov, 1962), which relates the evolution of second order structure function and the third order structure function to the dissipation rate.

The Kolmogorov's two-third law can be described by:

$$\left\langle [\Delta v(r)]^2 \right\rangle = \beta \epsilon^{2/3} r^{2/3} \tag{10}$$

where $\beta = 2$. And the Kolmogorov's four-fifth law can be expressed as:

$$\left\langle [\Delta v(r)]^3 \right\rangle = -4/5 \epsilon r \tag{11}$$

The model for the energy spectrum of Kolmogorov for the inertial sub range follows:

$$E(\kappa) = C \epsilon^{2/3} \kappa^{-5/3} \tag{12}$$

where κ is the wavenumber $\kappa = 2\pi/r$. By measuring these two-point correlations, the value of the dissipation rate can be obtained.

The dissipation rate follows from calculating the rate works of viscous stress on Navier-Stokes equation for a Newtonian fluid (Davidson, 2015):

$$\dot{W} = \int u_i (T_{ij} dS_j) = \int \frac{\partial}{\partial x_j} (u_i T_{ij}) dV \tag{13}$$

where $\dot{W}$ is the rate of work, T_{ij} is the stress tensor, dS is a surface differential and dV is a volume differential. The stress tensor for Newtonian fluids can be defined as:

$$T_{ij} = \rho \nu \left(\frac{\partial u_i}{\partial x_j} + \frac{\partial u_j}{\partial x_i} \right) = 2 \rho \nu S_{ij} \tag{14}$$

where S_{ij} is defined as the stress tensor:

$$S_{ij} = \frac{1}{2} \left(\frac{\partial u_i}{\partial x_j} + \frac{\partial u_j}{\partial x_i} \right) \tag{15}$$

here it can be seen that S_{ij} and in consequence T_{ij} are symmetric. Eq. (13) can then be decomposed in:

$$\frac{\partial}{\partial x_j} [u_i T_{ij}] = \left(\frac{\partial T_{ij}}{\partial x_j} u_i + T_{ij} \frac{\partial u_i}{\partial x_j} \right) \tag{16}$$

where the first term is related with the net work of viscous force ($f_i u_i$), and the second term correspond to the rate of change of internal energy of the fluid. Using this relation, the dissipation rate can be defined as:

$$\epsilon = \frac{T_{ij} S_{ij}}{\rho} = 2 \nu S_{ij} S_{ij} \tag{17}$$

The calculation of the dissipation rate through Eq. (17) is called the direct method. Measurement using PIV instruments can provide information on a two-dimensional velocity field from which the velocity derivatives can be extracted in order to apply the direct method. The third velocity field in PIV can be estimated for using this method. Nevertheless, the accurate estimation of the velocity derivatives requires a very fine spatial resolution in order to resolve the turbulent dissipation scales. The large-eddy PIV method developed by Sheng et al. (2000) uses the Smagorinsky model (Smagorinsky, 1963) for estimating the unresolved smaller scales through the calculation of the sub grid stress T_{ij} in Eq. (17).

LDV methods provides measurement of velocity in one spatial position, however, by means of the Taylor's frozen hypothesis, information on the velocity in the stream wise direction can be obtained. The estimation of the velocity can be used to obtain the velocity derivative for the stream-wise direction. In order to solve the direct method, assumptions must be used for the remaining unknown velocity derivatives. One common approximation is to assume isotropic flow, from which the equation of the dissipation rate for isotropic flow can be simplified (Taylor, 1935):

$$\epsilon = 2 \nu S_{ij} S_{ij} = 15 \nu \left(\frac{\partial u_x}{\partial x} \right)^2 \tag{18}$$

nevertheless, the error in estimating the velocity derivative can still be large depending on the spatial resolution for each experiment.

A different approximation is based on a scaling argument where it is assumed the turbulent dissipation rate equals the energy passed down the cascade from largest eddies to smaller eddies, and since viscous dissipation is concentrated at smaller scales this leads to the following approximation:

$$G \approx \epsilon \approx u_{rms}^2 \frac{u'_{rms}}{l} = \frac{u_{rms}^3}{l} \tag{19}$$

where G is the generation of turbulence, u_{rms}^2 is a measure of the kinetic energy and l/u'_{rms} is a measure of the turnover time of the largest eddies. Then the estimation of the dissipation rate from the scaling argument follows:

$$\epsilon = \frac{A u_{rms}^3}{l} \tag{20}$$

where the prefactor A is a constant parameter with value ($A \approx 1$).

As mentioned before, the use of the turbulent dissipation rate in the classical breakage and coalescence models were related to the inertial sub range solely. However, more recent developments on breakage and coalescence modeling include the effects from the entire energy spectrum (Han et al., 2014; Solsvik and Jakobsen, 2016a). In this case, the entire energy spectrum cannot be described only in terms of the turbulent dissipation rate. Several models for energy spectrum have been reviewed in the work of Solsvik and Jakobsen (2016b). In particular, Pope (2000) proposed an empirical model for the entire energy spectrum:

$$E(\kappa) = C \epsilon^{2/3} \kappa^{-5/3} f_L(\kappa L) f_\eta(\eta \kappa) \tag{21}$$

where f_L and f_η are non-dimensional functions, C is the Kolmogorov's constant ($C = 1.62$), and L is the integral scale defined as:

$$L = \frac{k^{3/2}}{\epsilon} \tag{22}$$

where k is the turbulent kinetic energy:

$$k = \frac{3}{2} u_{rms}^2 \tag{23}$$

The function f_L and f_η follows:

$$f_L(\kappa L) = \left(\frac{\kappa L}{\left[(\kappa L)^2 + c_L \right]^{1/2}} \right)^{5/3 + p_0} \tag{24}$$

$$f_\eta(\kappa \eta) = e^{-\beta \left(\left[(\kappa \eta)^4 + c_\eta^4 \right]^{1/4} - c_\eta \right)} \tag{25}$$

where ($p_0 = 2, \beta = 5.2$), c_L and c_η are positives parameter, and η is the Kolmogorov's micro length scale defined in Tennekes and Lumley (1972) as:

$$\eta = \left(\frac{\nu^3}{\epsilon}\right)^{1/4} \tag{26}$$

where ν is the kinematic viscosity. The function f_η concern the micro scale as is related with the fluid viscosity, while the function f_L is related to the energy containing sub range by accounting the turbulent kinetic energy k through the integral length scale L. It should be noted that the energy spectrum proposed by Kolmogorov for the inertial sub range has contribution on the entire energy range in the model proposed by Pope, where it follows that the dissipation rate could be considered as the main parameter affecting the entire energy spectrum.

The estimation of the values for C_L and C_η has been proposed in the work of Solsvik (2017), where the parameters are presented as functions of the Kolmogorov's constant C:

$$c_\eta(Re_\lambda, C) = \exp\left(\frac{14.043 - 4.222C}{Re_\lambda^{1.986-0.363C}}\right) - [0.089 + 0.339C] \tag{27}$$

$$c_L(Re_\lambda, C) = \exp\left(-\frac{4.478 + 18.362C}{Re_\lambda^{1.075-0.07C}} - 1.342 + 2.024C\right) - 1.913 + 2.169C \tag{28}$$

where Re_λ is the Taylor-scale Reynolds number which is related with the integral scale Reynolds number Re_L:

$$Re_\lambda = \sqrt{\frac{20}{3}} Re_L^{1/2} \tag{29}$$

$$Re_L = \frac{k^2}{\epsilon\nu} \tag{30}$$

Based on Pope's model, Solsvik and Jakobsen (2016a) presented an analytical solution for the second order structure function considering the energy spectrum model from Pope in the energy containing range and inertial sub-range, and then extended to the dissipation range by including a semi empirical formula proposed by Sawford and Hunt (1986):

$$\left\langle [\Delta v(r)]^2 \right\rangle = \frac{4}{3} k \left(\frac{r^2}{r_d^2 + r^2}\right)^{2/3} (1 - [T_1(r) + T_2(T_3(r)T_4(r) - T_5(r))])$$

$$T_1(r) = \frac{2}{[s(r)]^2} F\left((-\tfrac{1}{3})^{1/2}, \left(\tfrac{3}{2}\frac{[s(r)]^2}{4}\right)\right)$$

$$T_2 = 3^{3/2}\Gamma(2/3)$$

$$T_3(r) = 27 \times 2^{1/3} [s(r)]^{2/3} \Gamma(2/3)$$

$$T_4(r) = \frac{1}{352\pi} F\left(\left(\tfrac{7}{3}\right)^{11/6}, \left(\tfrac{17}{6}\frac{[s(r)]^2}{4}\right)\right)$$

$$T_5(r) = \frac{2^{2/3}}{2\pi[s(r)]^{2/3}} K_{4/3}(s(r))$$

$$s(r) = \frac{Kr}{C_L^{1/2} \kappa L}$$

$$c_L = (C \times 1.262)^3$$

$$r_d = (15 C_K)^{3/4}$$

where $C_K = 2$, F is the hypergeometric function, K is the Bessel function, and Γ is the gamma function.

More recently, Gong et al. (2018) proposed an alternative empirical model for the second order structure function for the entire energy spectrum:

$$\left\langle [\Delta v(r)]^2 \right\rangle = \begin{cases} C_K \left(\frac{r^2}{r^2 + r_d^2}\right) (\epsilon r)^{2/3} f_L(\kappa L) & \text{for} \quad r \leqslant L \\ C_K \left(\frac{L^2}{L^2 + r_d^2}\right) (\epsilon L)^{2/3} f_L(\kappa L) & \text{for} \quad r > L \end{cases} \tag{32}$$

where f_L is given by Eq. (24). The parameter c_L was taken from Eq. (28).

In addition, the second order structure function can be obtained by integrating the energy spectrum model from Pope (2000). The integration follows (Davidson, 2015):

$$\left\langle [\Delta v(r)]^2 \right\rangle = \frac{4}{3} \int_0^\infty E(\kappa) \left[1 - 3\frac{\sin(\kappa r)}{(\kappa r)^3} + 3\frac{\cos(\kappa r)}{(\kappa r)^2}\right] d\kappa \tag{33}$$

3. Experimental setup

The experimental setup was developed in order to study the breakage of oil droplets in turbulent water flow. The design presents a baffle structure on the channel walls for enhancing the turbulence generation. The design of these structures was simulated using the Fluent software, where the Large Eddy Simulation model was employed. The details of this numerical simulation can be found in the work of Shi et al. (2017).

The experimental setup is presented in Fig. 1. It is a closed loop circuit using destilled water as continuous phase. The fluid is driven from a reservoir tank by a mechanical pump (model MDL-0670 from SPX Flow Technology), then pass through a flow meter (model SITRANS F M MAG 5000 from Siemens) connected to an acquisition card (NI USB-6221 from national instrument) which has a sampling frequency of 250 kHz. Before reaching the measurement section the flow pass through three sections with different cross-sectional areas. The first section presents the largest area while the third section presents the smallest area. Finally, the flow circulates the test section and is recovered in the reservoir tank.

The test section presents a rectangular cross section were two walls are made with glass and the other two walls presents a periodic squared shaped structure for enhancing and sustain the turbulence. The two walls with glass allows the visualization of the fluid flow and the utilization of the Laser Doppler Velocimetry (LDV) measurement. The cross sectional evolution of the three reduction section before the test section help to avoid turbulence before the test section, meaning that turbulence should be generated in the channel walls at the beginning of the test section. In Fig. 2 a view of the test section can be observed along its main dimension, the structures at the wall for creating and enhancing turbulence are presented in black.

The experiments consisted in measurements of the velocity of the fluid at different positions of the channel using a laser Doppler velocimetry (LDV) instrument. Using this technique, the mean value and velocity fluctuation are measured at different points in space. Then the different two-point correlations were calculated. Finally, the dissipation rate was estimated using the different relations presented in the previous section.

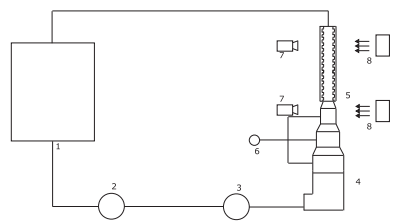

Fig. 1. Schematic drawing of experimental setup. 1. Water tank, 2. Pump, 3. Flowmeter, 4. Droplet generation channel, 5. Breakage channel, 6. Syringe pump with oil, 7. Camera, 8. Illumination.

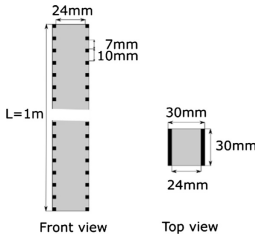

Fig. 2. The section view.

In the present paper, oil droplets were not used during the turbulent characterization. However, when experiments involves the use of oil droplets these are separated by gravity in the water reservoir. The volume of water in the reservoir is approximately around 800–900 liters, and the amount of oil used during experiments is small which means that the oil can be separated by gravity and collected at the top of the water tank where it is removed manually.

3.1. Laser Doppler Velocimetry

A laser Doppler velocimetry (LDV) model Fiberflow from Dantec Dynamics was used for the measurements. The instrument measures single point velocities by the Doppler Shift of laser beams reflected by seeding particles in the fluid media. With two pairs of laser beams, it was possible to get two velocity directions, stream-wise and normal to the baffled walls. To map a plane in the center between the two glass sides the probe emitting the laser beams was mounted on an automatic traverse system such that it could move stream wise and between the baffled channel sides. In each point, a dataset of velocities was obtained.

3.2. Experimental procedure

The measurement procedure consisted in selecting the flow condition (flow rate). Then, using the measurement from the flow-meter, the pump was adjusted to achieve the targeted condition. Then using two motorized stages, the laser were positioned at different locations of the channel. The positioning of the laser were performed in order to map the entire visible area of the channel. For this reason, a grid of points were constructed and measurements were performed at each point.

The grid of points were constructed using 17 points in the stream axis and 11 points in the perpendicular direction (wall distance). The first point in the stream wise direction was located at 100 mm from the channel entrance and the last point at 900 mm. The points perpendicular to the wall were measured in term of the distance to the wall starting at 0.5 mm of distance and to the middle of the channel at a distance of 12 mm from the wall.

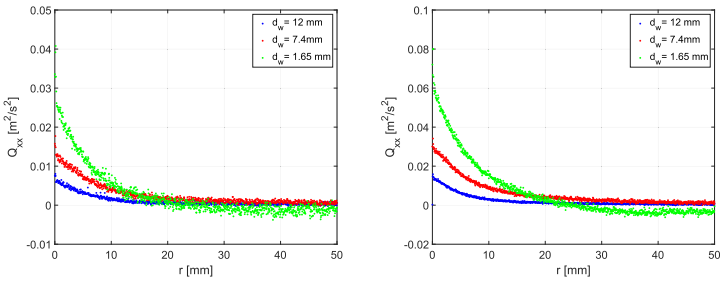

(a) Cross sectional averaged velocity $1.0m/s$. (b) Cross sectional averaged velocity $1.5m/s$.

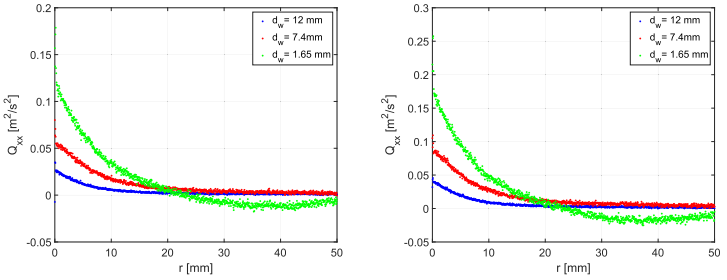

(c) Cross sectional averaged velocity $2.0m/s$. (d) Cross sectional averaged velocity $2.5m/s$.

Fig. 3. Velocity correlation function for different flow conditions at 600 mm from the channel inlet. The different measurements correspond to different distances to the channel wall.

3.3. Instrument error

The flow condition was measured using a flow meter that has an accuracy of 0.4% of the measured flow rate. The measurements of the flow presented also a statistical error which could be related to pump oscillations and instrument fluctuations of $\pm 15\,\mathrm{mm}/s$. This value was approximately constant at the different flow conditions, meaning that the relative error in the flow is larger for lower flow rate. Nevertheless, the error of the mean diminishes with the number of sampling, where with a sampling frequency of 250 kHz, the error of the mean results 500 times smaller for the mean value with a sampling period of one second. Finally, considering that the minimum flow rate used corresponded to a mean cross sectional velocity of 1.0 m/s, the statistical error can be neglected in comparison with the instrument accuracy.

Using the accuracy in the flow measurements, the error in the measurement of the mean flow follows:

$$\frac{\delta U}{U} \approx 0.004 \tag{34}$$

here U is the mean cross sectional velocity.

The error in the velocity measurements is related with the accuracy of the LDV instrument. Systematics error can be improved with calibration of the LDV instruments (Iyer and Woodmansee, 2005). However, since no calibration were done an uncertainty of 10% will be used for estimating the errors. Nevertheless, the focus of this study is on the velocity fluctuations, and since systematic errors affects the mean value, then it is expected that systematic errors would not affect the measurements of the velocity fluctuation.

$$\frac{\delta u}{u} = 0.1 \tag{35}$$

The error in the estimation of the distance between two measurement points r necessary for estimating two points correlations is related with the fluid velocity at each position and the time interval between particles detected by the LDV system:

$$r = \frac{\Delta t}{u} \tag{36}$$

where u is the mean velocity at a given position. Considering that the uncertainties from the time measurement and the mean velocity measurement are random and independent, we can apply the square root of sum of squares of relative error for the error propagation of r:

$$\frac{\delta r}{r} = \sqrt{\frac{\delta \Delta t^2}{\Delta t} + \frac{\delta u^2}{u}} \tag{37}$$

For estimating the error on the time interval, we considered the precision in which the LDV measured time. At the maximum fluid velocities used (2.5 m/s), the maximum frequency for particle detection were approximately 2000 particles per second, which

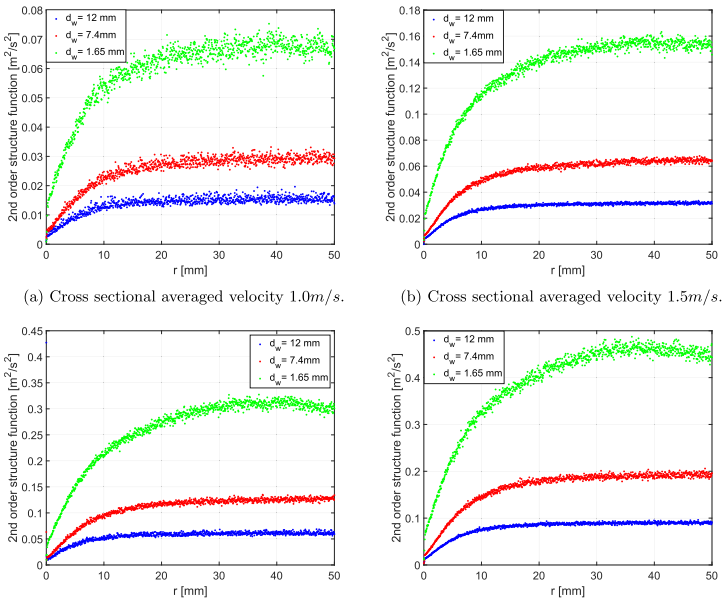

(a) Cross sectional averaged velocity $1.0m/s$. (b) Cross sectional averaged velocity $1.5m/s$.

(c) Cross sectional averaged velocity $2.0m/s$. (d) Cross sectional averaged velocity $2.5m/s$.

Fig. 4. Second order structure function for different flow conditions at 600 mm from the channel inlet. The different measurements correspond to different distances to the channel wall.

gives on average 0.5 ms between particles. Considering that the instrument can report time interval with a 1 μs resolution, it was consider this as the instrument error and therefore:

$$\frac{\delta\Delta t}{\Delta t} < \frac{1\ \mu s}{500\ \mu s} = 0.002 \tag{38}$$

It should be noted that at lower pumping speed, the time between particles increase and therefore the error in the detection of time interval decreases. The error for r from Eq. (37) results:

$$\frac{\delta r}{r} = 0.1 \tag{39}$$

4. Measurements

The measurements consisted in acquiring the velocity fluctuation for different flow conditions and at different positions in the channel. The flow conditions are expressed in terms of the average cross sectional velocity of the flow. The velocity used were 1.0 m/s, 1.5 m/s, 2.0 m/s and 2.5 m/s. From the measured instantaneous average velocity at each position, the root mean square of the velocity was computed, which was later used for estimating the dissipation rate. For each position, the amount of samples used for the averaging procedure were $N = 200,000$.

4.1. Velocity fluctuation

The velocity fluctuation is a statistical quantity that is computed as an average of many samples. Since the mean value of the velocity fluctuation is zero, then it can be related with the measurement of the standard deviation of the velocity measurement:

$$\left(u'_{rms}\right)^2 = \langle u'^2 \rangle = \sigma^2 \tag{40}$$

where σ is the standard deviation of the measurement of the velocity. The error of the estimation of $\langle u'^2 \rangle$ follows the error estimation of the standard deviation (Taylor, 1997):

$$\delta\sigma = \sigma \frac{1}{\sqrt{2(N-1)}} \tag{41}$$

where N is the number of samples used in the averaging procedure ($N = 200,000$). Using this relation, then the relative error of u'_{rms} follows:

$$\frac{\delta u'_{rms}}{u'_{rms}} = \frac{\delta\sigma}{\sigma} = \frac{1}{\sqrt{2(N-1)}} = 0.0016 \tag{42}$$

In Fig. 20 in Appendix A, the root mean square of the velocity fluctuations are presented for different flow conditions and positions in the channel. It can be observed that the velocity fluctuations start developing at the walls and increases from the start of the channel until approximately the middle of the channel. Then

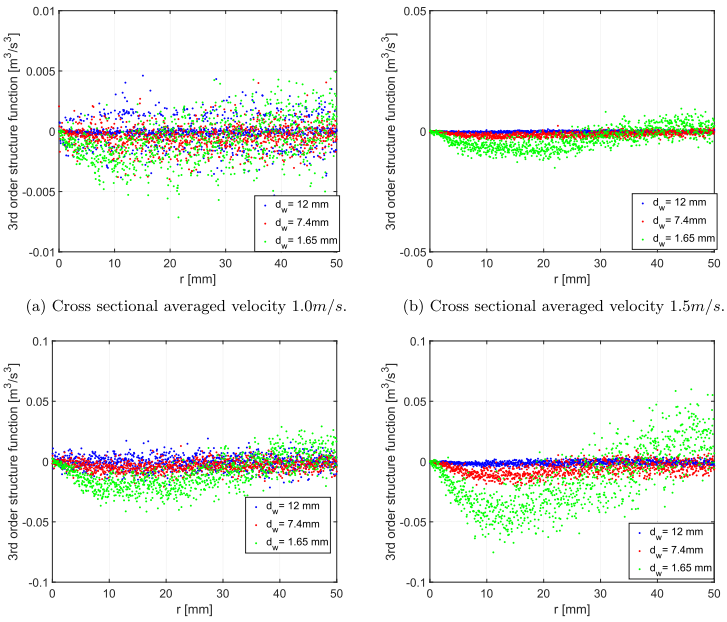

(a) Cross sectional averaged velocity $1.0m/s$.

(b) Cross sectional averaged velocity $1.5m/s$.

(c) Cross sectional averaged velocity $2.0m/s$.

(d) Cross sectional averaged velocity $2.5m/s$.

Fig. 5. Third order structure function for different flow conditions at 600 mm from the channel inlet. The different measurements correspond to different positions along the channel length.

it appears to be independent with the distance to the channel inlet, and close to the end of the channel (at distance 900 mm), it decreases slightly.

Another source of error in the velocity fluctuations is produced by the abrupt change in the mean velocity profile close to the channel wall. The LDV instrument measures the instantaneous velocities of seeding particles that pass through the laser beam. The seeding particles that are detected in each measurement can be associated to a volume around the measurement point defined by the laser beam size, and since the velocity field close to the wall has large velocity gradient, then the velocity measurement of the LDV will be affected by the large velocity distribution inside the volume of detection, resulting in overestimation of the root mean square of velocity fluctuation. In addition, since the amount of particles detected is correlated with the traveling velocity of these particles, the distribution of velocities may not be homogeneous inside the measuring volume. These two sources of error will be translated in larger estimation of the mean velocity and the velocity fluctuation close to the channel wall, resulting in overestimation of the turbulent dissipation rate estimated by the scaling argument.

4.2. Longitudinal autocorrelation function

The values for the longitudinal autocorrelations function result from the ensemble average over a large set of data. The data obtained is separated according to the distance r calculated using the Taylor's Frozen hypothesis. First, a value for r is calculated according to the time between the velocity measurements. Then with this set of velocity and distances, the distances were grouped into smaller regions in order to obtain an average value. Each group were selected using a distance between points of $\Delta r = 0.5$ mm, this value was selected taking into consideration the amount of samples to be averaged in each group and the accuracy in resolving the given direction. On one hand, narrower groups could lead to higher position accuracy at the expense of decreasing in the accuracy of the averaged velocity fluctuation measurement. On the other hand, wider groups provide more samples to increase the accuracy of the averaged velocity fluctuations while the position accuracy decreases.

In Fig. 3, an example of the relation between distance and the autocorrelation function Q_{xx} is shown for different flow conditions and distances to the channel wall. The flow selected corresponds to a fully developed flow situated approximately in the middle of the channel at a distance of 600 mm from the inlet of the channel. From this measurement, it can be observed that the correlation is larger for those positions closer to the channel wall, and it can be observed that the fluctuation of the correlation is also larger for these cases. This last observation could be related with the abrupt change in the velocity profile close to the channel wall.

The standard deviation of the mean value of Q_{xx} can be estimated as Taylor (1997):

$$\delta\overline{Q}_{xx}(r) = \frac{\delta Q_{xx}(r)}{\sqrt{N_r(r)}} \tag{43}$$

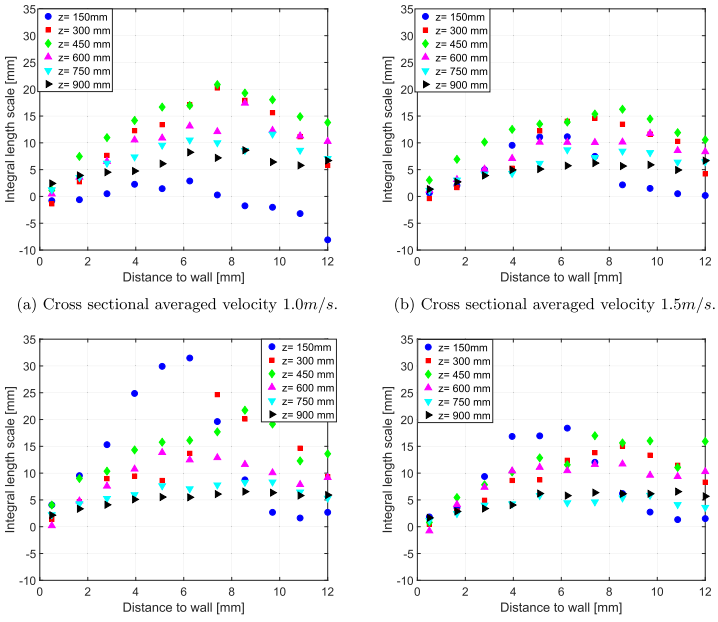

(a) Cross sectional averaged velocity $1.0m/s$. (b) Cross sectional averaged velocity $1.5m/s$.

(c) Cross sectional averaged velocity $2.0m/s$. (d) Cross sectional averaged velocity $2.5m/s$.

Fig. 6. Integral length scale for different flow conditions. The different measurements correspond to different positions along the channel length.

where $\delta\overline{Q}_{xx}$ denotes the error of the mean value, $\delta Q_{xx}(r)$ can be estimated through the standard deviation of the averaging procedure performed in each group of r, and $N_r(r)$ is the number of samples used in the averaging procedure, where different samples number correspond to different values of r.

4.3. Second order structure function measurements

Using the same procedure as for the longitudinal autocorrelation function, an ensemble average of the difference between velocities at two different points in the same stream-wise direction was calculated using a set of data grouped in sections of $\Delta r = 0.5$ mm. The results for the case with fully develop flow at a distance of 600 mm from the inlet of the channel is shown in Fig. 4. It can be seen that in line with the previous case, the turbulence intensity is larger closer to the channel walls, with larger fluctuation of the correlation for the same case.

4.4. Third order structure function measurements

The measurement of the third order structure function can be observed in Fig. 5. Here the observed fluctuation in the measured values of the correlation are larger than for the previous two cases, and therefore the expected accuracy that can be obtained from using this correlation should be lower than using the second order structure function measurements. In addition, the data fluctuation that can be observe for low velocities would make it more difficult to perform a curve fitting of the data. Nevertheless, it can be observed that at higher velocities the dependency of the third order structure function with the distance is more clear and in particular closer to the channel wall where it is expected to observe stronger turbulence intensities, showing that the third order structure function can still be a useful tool for the characterization of the turbulence.

5. Integral length scale estimation

The integral length scale has been estimated to be used in Eq. (20) to compute the turbulent dissipation rate. The integral length scale is obtained by integration of the velocity autocorrelation function according to Eq. (6), using the estimation of Q_{xx} and u'_{rms}. The values obtained can be observed in Fig. 6 for different positions of the channel and different flow conditions. It can be observed that the values are in the same range and with very little variation at different velocities or distance to the wall, presenting minimum values close to the channel wall and the middle of the channel. Lower value of the integral length scale close to the channel wall could be due to the presence of smaller turbulent structures. When these structures moves into the flow, they interacts with other structure and as a result, they could increase their size. This could explains why the integral length scale measurements shows first an increase with the distance to the channel wall. The decrease of the integral length scale close to the middle of the channel could be related with the loss of energy due to dissipation.

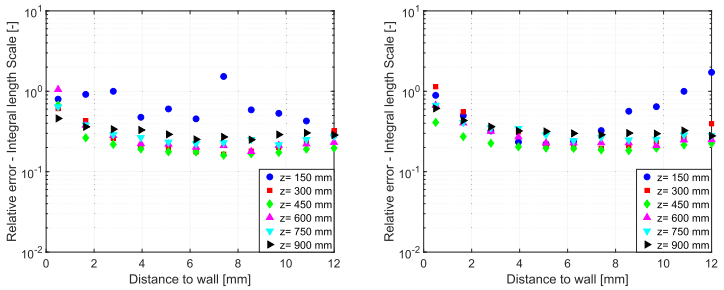

(a) Cross sectional averaged velocity $1.0m/s$. (b) Cross sectional averaged velocity $1.5m/s$.

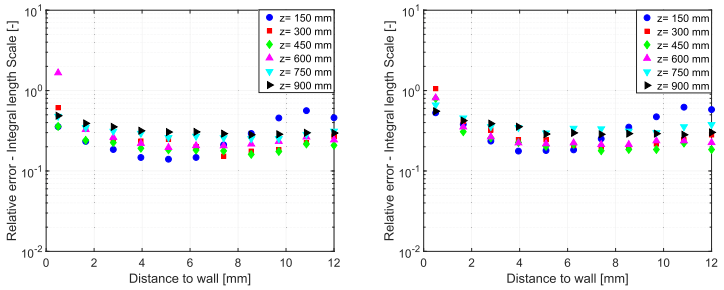

(c) Cross sectional averaged velocity $2.0m/s$. (d) Cross sectional averaged velocity $2.5m/s$.

Fig. 7. Estimated error for the integral length scale for different flow conditions. The different measurements correspond to different positions along the channel length.

In addition, entrance effects affect the integral length scale estimation in the middle of the channel, since the turbulence levels are smaller in the middle of the channel close to the entrance of the test section. This last hypothesis is sustained by the fact that this effect is observed greater for the channel position closer to the entrance of the test section.

Since the integral length scale (l) is an estimated parameter, it is of great importance to discuss the error propagation in detail. In particular, the error propagation accounts for the error produced by the integration procedure, in which the values of $Q_{xx}(r)$ were estimated over several measurements, and presents an error estimation for each value of r. The error estimation for the integration of a generic function f can be expressed as:

$$\delta\left(\int f(x)dx\right) \approx \delta\left(\sum f(x_i)\Delta x_i\right) \tag{44}$$

However, in order to simplify the error estimation, the error for each point will be assumed to be uncorrelated and similar. With these assumptions, the error of the integration can be estimated as:

$$\begin{aligned}\delta\left(\int f(x)dx\right) &\approx \Delta x\sqrt{\sum (\delta f)^2} \\ &\approx \Delta x\sqrt{N_x}\delta f\end{aligned} \tag{45}$$

where Δx is the discretization in the longitudinal direction r, N_x is the amount of integration points and δf is the assumed constant error of the function f at each integration point. Applying this assumptions to the error propagation of Eq. (6) and assuming a limit for the numerical integration at a distance of approximately 10 times the integral length scale, then we obtain the following relation:

$$\frac{\delta \bar{l}}{l} = 2\frac{\delta u'_{rms}}{u'_{rms}} + 10\frac{\delta \overline{Q}_{xx}}{u'^2_{rms}\sqrt{N_x}} \tag{46}$$

Here $\overline{Q}_{xx}$ is the constant value used as the estimation of the error of $Q_{xx}(r)$ for the different values of r. The contribution from the velocity fluctuation can be neglected compared to the error contribution from Q_{xx}. The results from applying Eq. (46) can be seen in Fig. 7. It can be observed that the error in the estimation of the integral length scale is considerable.

6. Dissipation rate calculations and error estimation

The dissipation rate can be estimated using different methods as presented in Section 2. First, we estimated the turbulent dissipation using the scaling argument presented in Eq. (20). The results from estimating the dissipation rate are presents in Fig. 8, where it can be observed that the dissipation rate is larger closer to the channel wall where the turbulent flow is generated by the structures at the wall, and decreases with the distance to the wall as the turbulent flow propagates through the flow. It can also be observed some increase along the center of the channel (wall

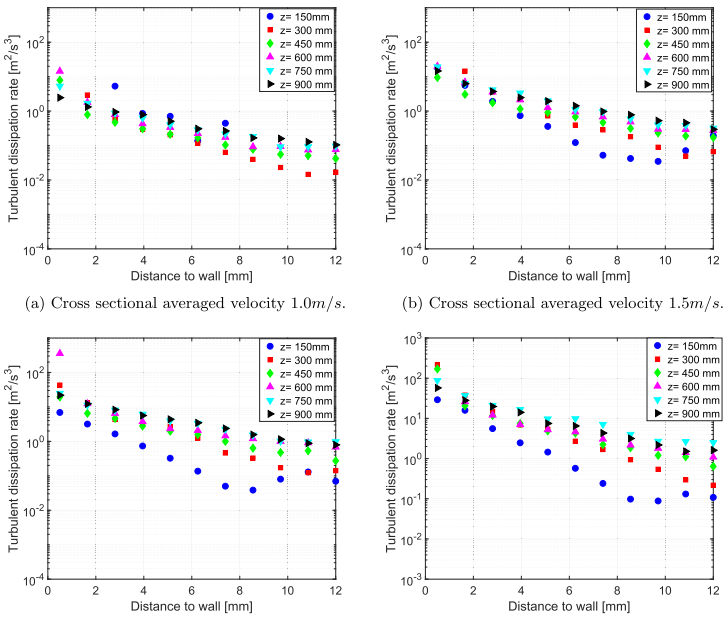

(a) Cross sectional averaged velocity $1.0m/s$.

(b) Cross sectional averaged velocity $1.5m/s$.

(c) Cross sectional averaged velocity $2.0m/s$.

(d) Cross sectional averaged velocity $2.5m/s$.

Fig. 8. Dissipation rate estimated using the integral length scale (scaling argument) for different flow conditions. The different measurements correspond to different positions along the channel length.

distance of 12 mm) as the effects of the entrance effects reduces and the turbulent flow becomes more developed. As expected, it can be observed that the turbulent dissipation rate increase with the mean flow rate.

The error propagation of Eq. (20) results in:

$$\frac{\delta\epsilon}{\epsilon} = 3\frac{\delta u'_{rms}}{u'_{rms}} + \frac{\delta l}{l} \tag{47}$$

The error in the estimation of the velocity fluctuation term is negligible compared with the error in the estimation of the integral length scale. However, as we have acknowledged in Section 4.1 the estimation of the velocity fluctuation could be overestimated, and since a power law relates the velocity fluctuation with the turbulent dissipation rate, then we expect the calculation of this to be overestimated close to the channel walls. Fig. 9 shows the error estimated for the turbulent dissipation rate constructed using Eq. (47) for different flow conditions, channel positions and distances to the wall, where it can be observed a larger error closer to the channel walls.

In addition, the scaling argument presents another source of error through the constant parameter A. This parameter value should be in the range 1—1.2. However, many researchers use this as an adjustment parameter and use values outside this range. In this work, the value adopted correspond to $A = 1.1 \pm 0.1$, meaning that the method present an error of 10% given by the range of A.

Another method for obtaining the dissipation rate uses the second order structure function. Considering the turbulent inertial subrange, the dissipation rate can be calculated using the Kolmogorov's two-third law presented in Eq. (10). The approach consists in performing a linear fitting of the second order structure function versus $r^{2/3}$ for the measurement points that correspond to the inertial subrange. The results from the linear fitting provides

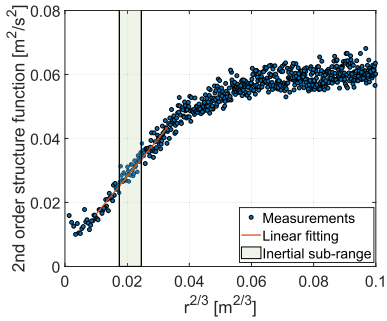

Fig. 10. Linear fitting example using the second order structure function in the inertial sub range. The measurement correspond to the center line of the channel at a distance of 600 mm from the channel inlet. The mean cross sectional velocity was 2.0 m/s.

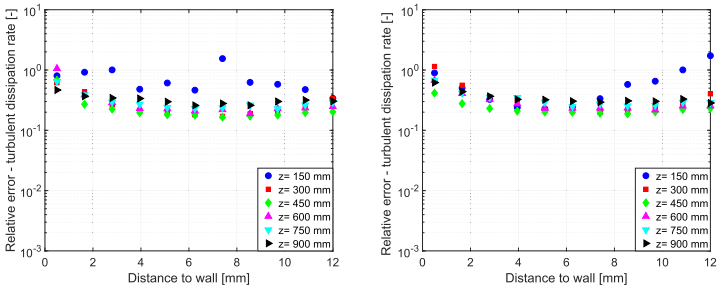

(a) Cross sectional averaged velocity $1.0m/s$. (b) Cross sectional averaged velocity $1.5m/s$.

(c) Cross sectional averaged velocity $2.0m/s$. (d) Cross sectional averaged velocity $2.5m/s$.

Fig. 9. Estimated error for the dissipation rate calculated using the integral length scale (scaling argument) for different flow conditions. The different measurements correspond to different positions along the channel length.

the value of $\beta\epsilon^{2/3}$, from which the value of the dissipation rate can be easily obtained. An example of this procedure can be seen in Fig. 10, here the measurements were performed at the center line of the channel, from a distance of 600 mm from the inlet of the test section and with a mean cross sectional velocity of 2.0 m/s.

Considered the following a linear representation:

$$y = a + bx \tag{48}$$

Then, using the least squares linear fitting (Taylor, 1997), the coefficients a and b can be obtained. In addition, information of the statistical error of the coefficient a and b can be obtained in the form of σ_a and σ_b respectively.

$$a = \frac{\sum x_i^2 \sum y_j - \sum x_i \sum y_j^2}{\Delta} \tag{49}$$

$$b = \frac{N\sum x_i y_i - \sum x_i \sum y_j}{\Delta} \tag{50}$$

$$\Delta = N\sum x_i^2 - \left(\sum x_i\right)^2 \tag{51}$$

The error on the coefficient follows:

$$\sigma_y = \sqrt{\frac{1}{N-2}\sum (y_i - a - bx_i)^2} \tag{52}$$

$$\sigma_a = \sigma_y \sqrt{\frac{\sum x^2}{\Delta}} \tag{53}$$

$$\sigma_b = \sigma_y \sqrt{\frac{N}{\Delta}} \tag{54}$$

Here σ_b reflects the estimated error from the linear fitting from the y coordinate which in this case is the error of $\left\langle [\Delta v(r)]^2 \right\rangle$. Nevertheless, an error was estimated for this quantity since each point is based in an average procedure over several measurements from where a standard deviation was obtained. Then the largest error of these two method were selected. In Fig. 11, the dissipation rate are presented for different flow conditions and channel positions, where it can be observed that the results obtained with this method are in the same range than the measurements obtained with the scaling argument presented in Fig. 8. Nevertheless, from the comparison between the two methods it can be observe that with this method, the effects of the entrance length are more clearly represented. Here, the turbulent dissipation rate for those positions closer to the entrance presents smaller values close to the middle of the channel (wall distance of 12 mm), and as the distance to the entrance increases, the turbulent dissipation rate converges approximately to the same value.

Using the error estimation from the linear fitting presented in Eq. (54), the relative error of the dissipation rate from Eq. (10) follows:

$$\frac{\delta\epsilon}{\epsilon} = \frac{3}{2}\sigma_B \tag{55}$$

The results from applying Eq. (55) can be observed in Fig. 12. It can be observed that with this method the relative error is larger in the center of the channel. This effect is related with the lower turbulence intensities at the middle of the channel that

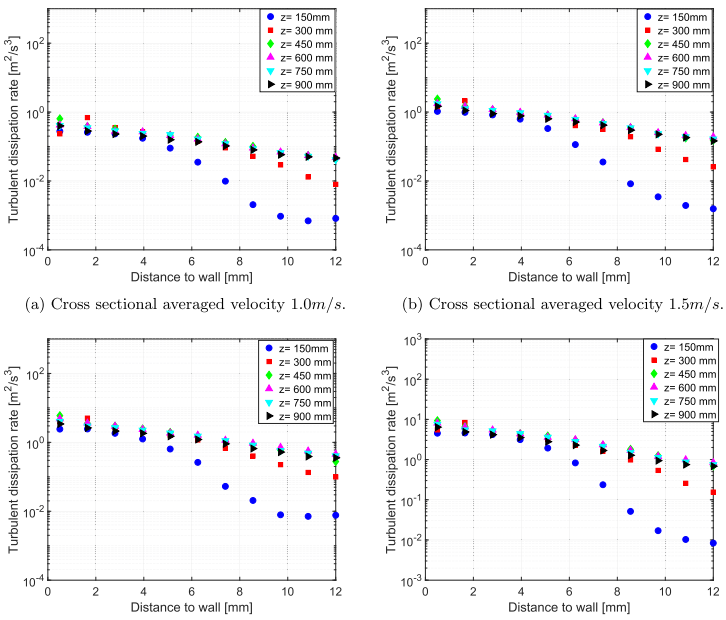

(a) Cross sectional averaged velocity $1.0m/s$.

(b) Cross sectional averaged velocity $1.5m/s$.

(c) Cross sectional averaged velocity $2.0m/s$.

(d) Cross sectional averaged velocity $2.5m/s$.

Fig. 11. Dissipation rate estimated using the second order structure function for different flow conditions. The different measurements correspond to different positions along the channel length.

contribute to an increase in the relative error of the turbulent dissipation rate. This effect is more evident for the positions close to the entrance of the channel where the dissipation rate presents lower values. The error produced with this method is considerable smaller than the error obtained using the integral length scale, due to the error produced in the integration of Q_{xx} which is considerable.

A similar method consists in using the third order longitudinal structure function, from which the dissipation rate can be obtained through Kolmogorov's four-fifth law presented in Eq. (11). A linear fitting is employed as presented in Eq. (48), in which the parameter y correspond to the third order structure function and the parameter x to the position. An example of fitting the data with this procedure is presented in Fig. 13, where the measurements were performed at the center line of the channel, from a distance of 600 mm from the inlet of the test section and with a mean cross sectional velocity of 2.0 m/s. From the linear fitting we obtain the coefficient a, b and σ_a σ_b using the same procedure as with the second order structure function. The dissipation rate obtained are shown in Fig. 14. Here it can be observed the effects of the higher fluctuations of the third order structure function (see Fig. 5) in the estimation of the turbulent dissipation rate. While the values of turbulent dissipation rate obtained are in the same range with the other two methods, it can be clearly see that the results from the second order structure function presents less fluctuation and with a smoother transition between the data generated at different flow conditions and channel position. While this effect can be observed for the different flow condition, it is more evident at lower velocities.

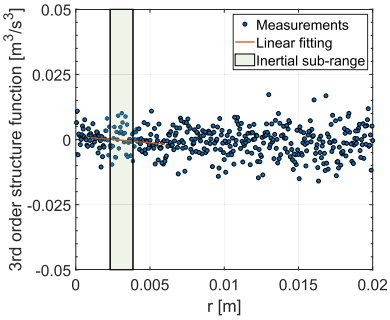

Fig. 13. Linear fitting example using the third order structure function in the inertial sub range. The measurement correspond to the center line of the channel at a distance of 600 mm from the channel inlet. The mean cross sectional velocity was 2.0 m/s.

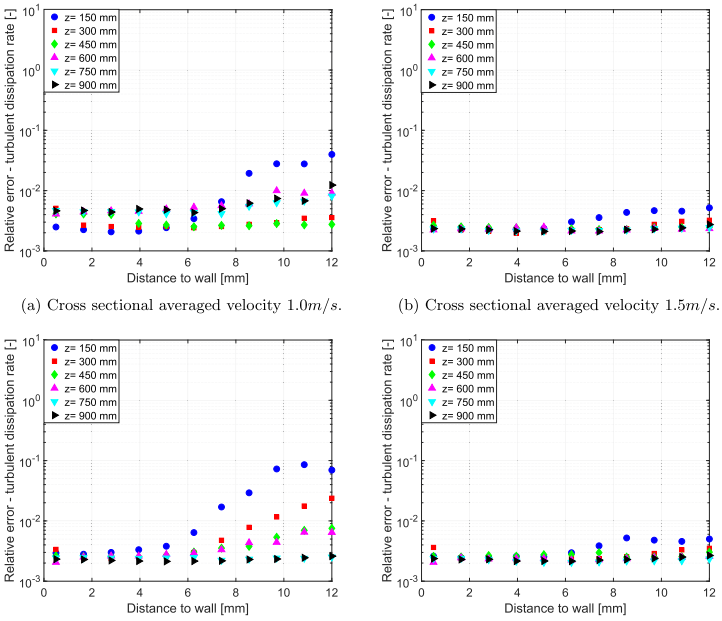

(a) Cross sectional averaged velocity $1.0m/s$. (b) Cross sectional averaged velocity $1.5m/s$.

(c) Cross sectional averaged velocity $2.0m/s$. (d) Cross sectional averaged velocity $2.5m/s$.

Fig. 12. Error estimation for the dissipation rate estimated using the second order structure function for different flow conditions. The different measurements correspond to different positions along the channel length.

Similarly as with previous case, the coefficient σ_b obtained from the linear fitting was compared with the estimated error of the third order structure function and the larger value was then used for estimating the error of the dissipation rate:

$$\frac{\delta\epsilon}{\epsilon} = \frac{5}{4}\sigma_b \tag{56}$$

The estimated error can be seen in Fig. 15. In this case the relative error is larger than using the second order structure function and apparently slightly better that the error from the scaling argument methods. Here the larger fluctuation of the third order structure function contributed to the increase in the error of the estimation of the dissipation rate by mean of the error propagation. This effects is more pronounced at lower velocities and closer to the center of the channel where the turbulent intensity are lower and where it was observed higher fluctuation of the third order structure function presented in Fig. 5.

7. Second order structure function models

In Section 2 different methods for turbulent characterization were presented, where the second order structure function was introduced as a mean for obtaining the turbulent dissipation rate. In order to obtain the turbulent dissipation rate the second order structure function was used in the inertial sub range using Kolmogorov's two-third law presented in Eq. (10). Nevertheless, the second order structure function presents information on the entire energy spectrum, which can be used in the development of models for breakage and coalescence that included the contribution from the entire spectrum of turbulence. In Fig. 16, a comparison obtained from measurement of the second order structure function and the models from Solsvik and Jakobsen (2016a), Gong et al. (2018) and from the numerical integration of Pope's energy spectrum (Pope, 2000) is presented for different flow conditions. The measurement were performed at the centerline of the test section and at a distance of 600 mm from the inlet of the channel. The models were evaluated using the dissipation rate measured using Eq. (10) and using an estimation for the turbulent kinetic energy presented in Eq. (23) based on the measurement of u'_{rms}. With the estimation of k, then integral scale was obtained using Eq. (22). It can be observed that the methods describe fairly well the evolution of the structure function. At higher correlation distances ($r > 20$ mm), it can be observed that the measurements are better described by Solsvik and Jakobsen model and by the numerical integration of Pope's energy spectrum presented in Eq. (33), with the model of Gong et al. over predicting the measurements. However, in the inertial sub-range, the model from Gong et al. and the model from Solsvik and Jakobsen presents similar results which also approximate the measurements better than the numerical integration of the energy spectrum.

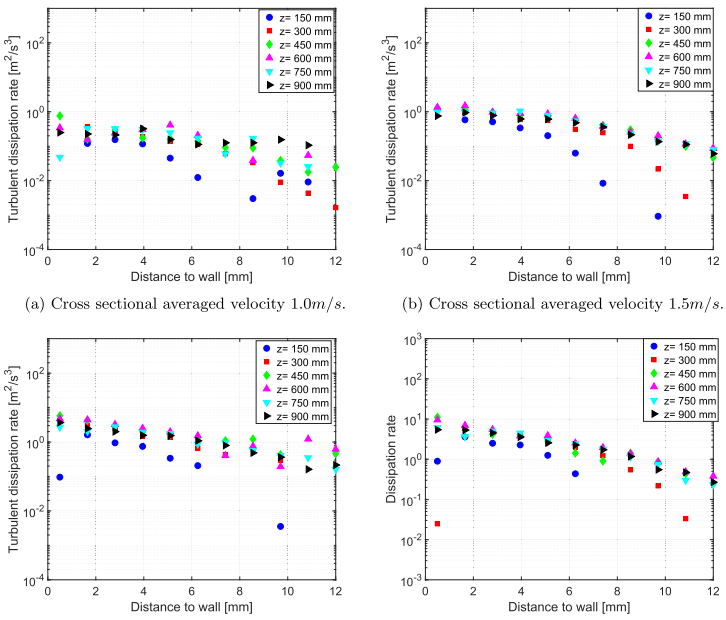

(a) Cross sectional averaged velocity $1.0 m/s$.

(b) Cross sectional averaged velocity $1.5 m/s$.

(c) Cross sectional averaged velocity $2.0 m/s$.

(d) Cross sectional averaged velocity $2.5 m/s$.

Fig. 14. Dissipation rate estimated using the third order structure function for different flow conditions. The different measurements correspond to different positions along the channel length.

8. Results

In Section 4, measurement of the dissipation rate were presented for different methods where the error for each case was discussed. Based on the results obtained, it was found that the estimation of the dissipation rate using the second order structure function presented the smallest uncertainty.

Nevertheless, the other two methods provided results in the same range of values predicting with similar trend the evolution of the turbulent dissipation rate for different wall distance and flow condition. These results are summarized in Fig. 17, where the results from the different methods are presented for different flow conditions and at a distance of 600 mm from the inlet of the channel. Here, the measurement from the different method shows similar results at the middle of the channel. However, closer to the channel wall, the dissipation rate calculated from the scaling argument presented deviation compared to the other two methods which presents similar results in this region. This observation was addressed in Section 4.1 where it was discussed that the velocity fluctuation was overestimated close to the channel walls and this is reflected in an overestimation of the dissipation rate using the scaling argument. It can also be observed than the estimations using the third order structure function presents a little more fluctuation than the other two methods, nevertheless it is expected considering the larger uncertainty obtained with this method compared with the second order structure function.

Measurement of the turbulent dissipation rate were performed for different positions in the channel and flow conditions. The methods used corresponded to the second order structure function presented in Eq. (10). The methods was chosen due to presenting the best accuracy from the methods reviewed in this work. The results are presented in Fig. 18, where the dissipation rate is presented for different flow conditions and positions in the test section. It can be observed that the dissipation rate intensity is stronger at the channel walls and propagates into the flow as the distance to the inlet of the channel increases.

The dependence of the dissipation rate with the distance to the channel wall was observed in Fig. 17 where the logarithm of the dissipation rate presented a linear behavior with the distance to the channel wall. Using these observation, an empirical correlation for the turbulent dissipation rate and the turbulent kinetic energy was found for different flow conditions and distance to the channel walls. The correlation was obtained for the measurement at a distance of 600 mm where we assume a turbulent flow fully developed since the effects that the distance to the channel entrance has on the turbulent dissipation rate can be neglected (see Fig. 18). The correlation obtained follows:

$$\epsilon(d_w, Re_d) = \exp\left(-32.2972 - 5.42\left[\frac{d_w}{d_h}\right]\right) Re_d^{3.114} \tag{57}$$

$$k(d_w, Re_d) = \exp\left(-23.1252 - 3.77\left[\frac{d_w}{d_h}\right]\right) Re_d^{2} \tag{58}$$

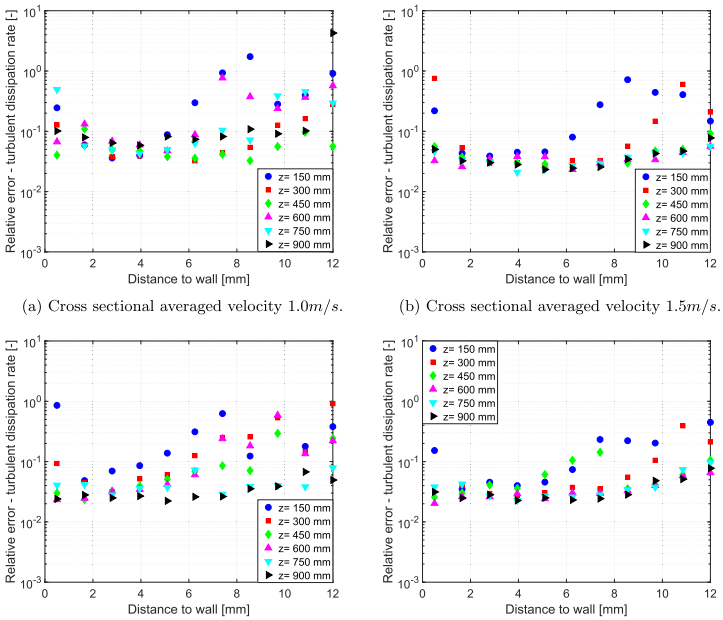

(a) Cross sectional averaged velocity $1.0m/s$. (b) Cross sectional averaged velocity $1.5m/s$.

(c) Cross sectional averaged velocity $2.0m/s$. (d) Cross sectional averaged velocity $2.5m/s$.

Fig. 15. Error estimation for the dissipation rate determined using the third order structure function for different flow conditions. The different measurements correspond to different positions along the channel length.

where d_w is the distance from the channel walls, d_h is the hydraulic diameter, and Re_d is the Reynolds number based on the hydraulic diameter:

$$Re_d = \frac{Ud_h}{\nu} \tag{59}$$

A comparison between the measured data and the results from the empirical correlation is presented in Fig. 19, where it can be observed that the error of this method is in the range of $\pm 20\%$.

9. Conclusions

We have presented measurements of the turbulent dissipation rate for a rectangular channel using Laser Doppler Velocimetry for direct velocity measurements. The estimation of the dissipation rate presented contains a comparison between the Kolmogorov's two-thirds law, the Kolmogorov's four-fifths law and a scaling argument. We have considered the statistical nature of turbulent flow and performed an uncertainty analysis of each method where we showed the dependence of each method with the measurements statistics. With several available methods for calculating the dissipation rate, it is important to note the uncertainty in the value presented, such that later modeling attempts may treat the information correctly.

The methods for estimating the turbulent dissipation rate are statistical methods that required the use of two-points correlations. These were obtained by using direct velocity measurement with the LDV and by applying the Taylor's frozen hypothesis for transforming a time dependent velocity into a spatial velocity field required for the calculation of two-point correlation. The two point correlation used were the velocity autocorrelation function, the second order structure function and the third order structure function.

We observed that the methods presented in this work showed similar results and trends with respect to changes in flow condition and distance to the channel walls. It was also observed that a significant larger increase in the estimated turbulent dissipation rate was observed close to the channel wall in the scaling argument method compared to the other methods. However, the deviation in this estimation could be explained by acknowledging the uncertainty of the velocity fluctuation measurements close to the channel wall, which greatly affects the estimation of the scaling argument. The comparison between the uncertainties in the estimation for each method also showed that by using the Kolmogorov's two-thirds law a smaller statistical uncertainty was achieved.

The measurement of the second order structure function were compared with the models from Solsvik and Jakobsen (2016a) and Gong et al. (2018). The relevance of these two models is founded in the possibility of implementing breakage and coalescence models for the entire energy spectrum. The results from the comparison showed a good agreement with both methods for

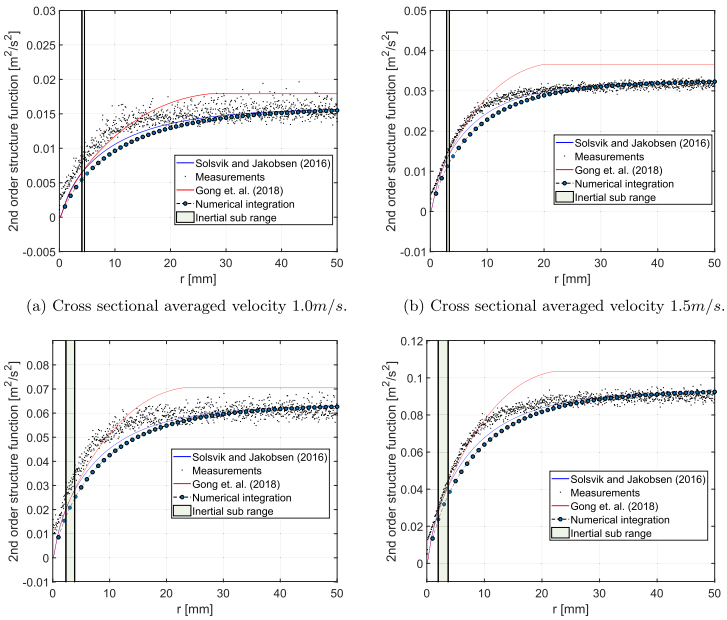

(a) Cross sectional averaged velocity $1.0m/s$.

(b) Cross sectional averaged velocity $1.5m/s$.

(c) Cross sectional averaged velocity $2.0m/s$.

(d) Cross sectional averaged velocity $2.5m/s$.

Fig. 16. Second order structure function model comparison at different flow conditions at a distance to the channel inlet of 600 mm. The measurement were obtained at the centerline of the channel.

the inertial and energy containing sub-range. The accuracy required for the comparison between measurement of the second order structure function and the models from Solsvik and Jakobsen (2016a) and Gong et al. (2018) for the dissipation sub-range was not achieved, and as a consequence the validity of this two models in this sub-range were not discussed in this work.

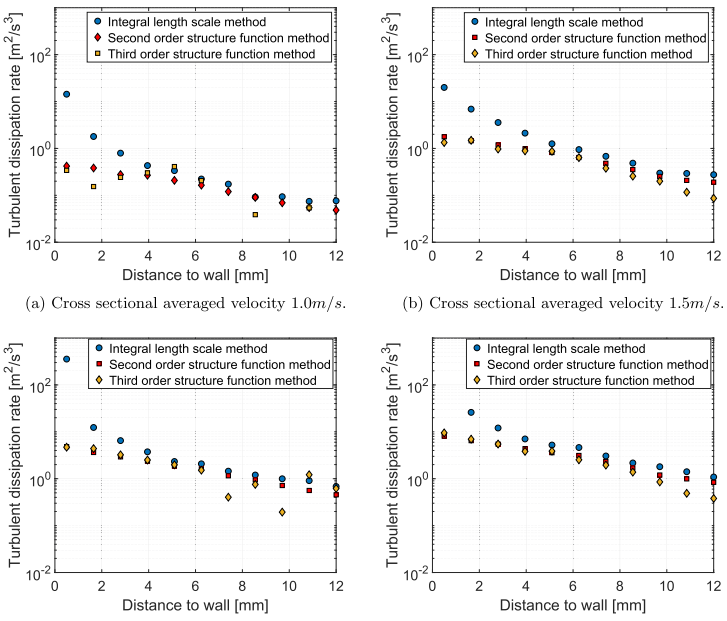

(a) Cross sectional averaged velocity $1.0m/s$. (b) Cross sectional averaged velocity $1.5m/s$.

(c) Cross sectional averaged velocity $2.0m/s$. (d) Cross sectional averaged velocity $2.5m/s$.

Fig. 17. Comparison of the dissipation rate obtained from the different methods for different flow conditions at a distance of 600 mm from the channel inlet.

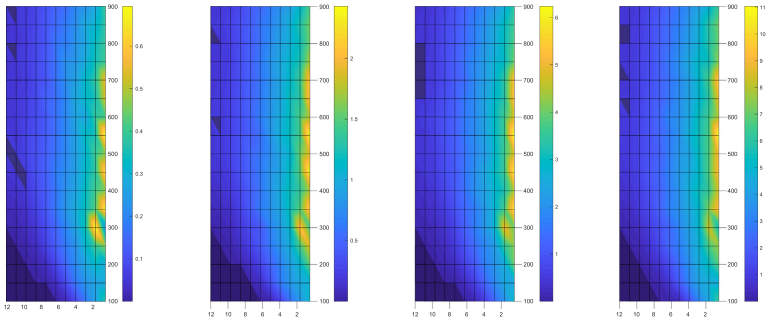

(a) Cross sectional averaged velocity $1.0m/s$. (b) Cross sectional averaged velocity $1.5m/s$. (c) Cross sectional averaged velocity $2.0m/s$. (d) Cross sectional averaged velocity $2.5m/s$.

Fig. 18. Dissipation rate estimated using the second order structure function for different flow condition.

Finally, an empirical correlation for the dissipation rate for fully developed turbulent flow was presented. A comparison between measurement and the empirical correlation presented an estimated error in the range of $\pm 20\%$.

Declaration of interests

The authors declare that they have no known competing financial interests or personal relationships that could have appeared to influence the work reported in this paper.

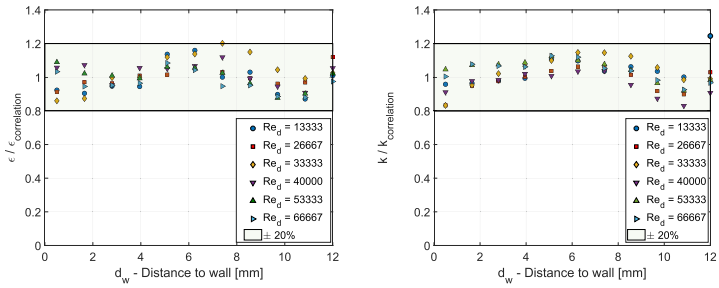

(a) Dissipation rate comparison.

(b) Turbulent kinetic energy comparison.

Fig. 19. Comparison between measurements of turbulent dissipation rate and turbulent kinetic energy measurements with estimation using the empirical correlations from Eq. (58).

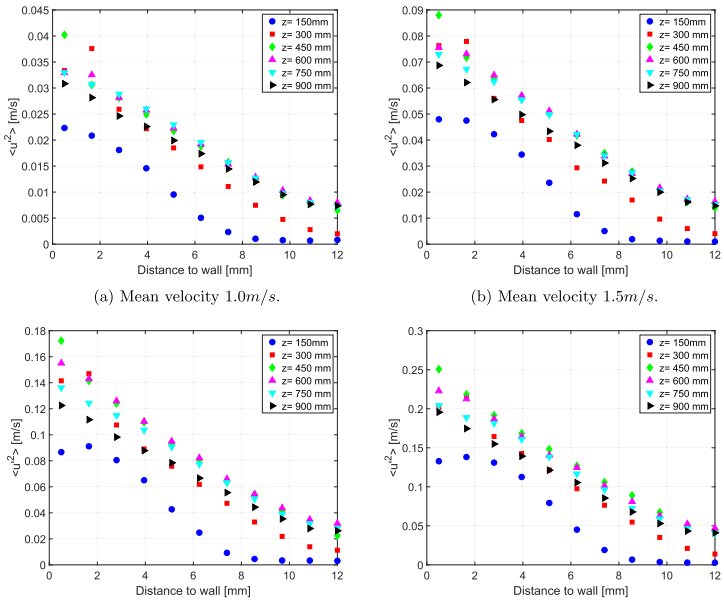

(a) Mean velocity $1.0 m/s$.

(b) Mean velocity $1.5 m/s$.

(c) Mean velocity $2.0 m/s$.

(d) Mean velocity $2.5 m/s$.

Fig. 20. Velocity fluctuations for different flow conditions. The different measurements correspond to different positions along the channel length.

Acknowledgement

This work was carried out as a part of SUBPRO, a Research-based Innovation Centre within Subsea Production and Processing. The authors gratefully acknowledge the financial support from SUBPRO, which is financed by the Research Council of Norway, major industry partners and NTNU.

Appendix A. Complementary measurements

See Fig. 20.

References

Andersson, R., Andersson, B., 2006a. On the breakup of fluid particles in turbulent flows. Am. Inst. Chem. Eng. J. 52, 2020–2030.
Andersson, R., Andersson, B., 2006b. Modelling the breakup of fluid particles in turbulent flows. Am. Inst. Chem. Eng. J. 52, 2031–2038.
Andersson, R., Andersson, B., Chopard, F., Noren, T., 2004. Development of a multi-scale simulation method for design of novel multiphase reactors. Chem. Eng. Sci. 59, 4911–4917.
Azizi, F., Al Taweel, A., 2011. Turbulently flowing liquid-liquid dispersions. Part I: drop breakage and coalescence. Chem. Eng. J. 166 (2), 715–725.
Bouaifi, M., Mortensen, M., Andersson, R., Orciuch, W., Andersson, B., Chopard, F., Noren, T., 2004. Experimental and numerical investigation of a jet mixing in a multifunctional channel reactor. Passive and reactive system. Chem. Eng. Res. Des. 82, 274–283.
Coulaloglou, C., Tavlarides, L., 1976. Drop size distributions and coalescence frequencies of liquid-liquid dispersions in flow vessels. Am. Inst. Chem. Eng. J. 22 (2), 289–297.
Davidson, P.A., 2015. Turbulence: An Introduction for Scientists and Engineers. Oxford University Press.
de Jong, J., Cao, L., Woodward, S., Salazar, J., Collins, L., Meng, H., 2009. Dissipation rate estimation from piv in zero-mean isotropic turbulence. Exp. Fluids 46 (3), 499–515.
Gong, S., Han, L., Luo, H., 2018. A novel multiscale theoretical model for droplet coalescence induced by turbulence in the framework of entire energy spectrum. Chem. Eng. Sci. 176, 377–399.
Håkansson, A., Mortensen, H.H., Andersson, R., Innings, F., 2017. Experimental investigation of turbulent fragmenting stresses in a rotor-stator mixer. Part 1. Estimation of turbulent stresses and comparison to breakup visualizations. Chem. Eng. Sci. 171, 625–637.
Han, L., Gong, S., Li, Y., Gao, N., Fu, J., Luo, H.A., Liu, Z., 2014. Influence of energy spectrum distribution on drop breakage in turbulent flows. Chem. Eng. Sci. 117, 55–70.
Herø, E.H., La Forgia, N., Shi, J., Solsvik, J., Jakobsen, H.A., On the turbulent dissipation rate in experimental investigation of single droplet breakage in fluid-liquid system. In: 6th International Conference on Population Balance Modelling, Ghent, 2018.
Hinze, J.O., 1975. Turbulence. McGraw-Hill, NewYork.
Iyer, V.A., Woodmansee, M.A., 2005. Uncertainty analysis of laser-doppler-velocimetry measurements in a swirling flowfield. Am. Inst. Aeronaut. Astronaut. J. 43 (3), 512–519.
Kolmogorov, A.N., 1941. The local structure of turbulence in incompressible viscous fluid for very large reynolds numbers. Dokl. Akad. Nauk SSSR 30 (4), 299–303 (English translation in Proc R Soc London Ser A 434:9–13 (1991)).
Kolmogorov, A.N., 1962. A refinement of previous hypotheses concerning the local structure of turbulence in a viscous incompressible fluid at high reynolds number. J. Fluid Mech. 13, 82–85.
Lemenand, T., Dupont, P., Della Valle, D., Peerhossaini, H., 2013. Comparative efficiency of shear, elongation and turbulent droplet breakup mechanisms: review and application. Chem. Eng. Res. Des. 91, 2587–2600.
Lemenand, T., Della Valle, D., Habchi, C., Peerhossaini, H., 2017a. Micro-mixing measurement by chemical probe in homogeneous and isotropic turbulence. Chem. Eng. J. 314, 453–465.
Lemenand, T., Della Valle, D., Dupont, P., Peerhossaini, H., 2017b. Turbulent spectrum model for drop-breakup mechanisms in an inhomogeneous turbulent flow. Chem. Eng. Sci. 158, 41–49.
Maaß, S., Kraume, M., 2012. Determination of breakage rates using single drop experiments. Chem. Eng. Sci. 70, 146–164.
Maaß, S., Metz, F., Rehm, T., Kraume, M., 2010. Prediction of drop sizes for liquid-liquid systems in stirred slim reactors - Part I: Single stage impellers. Chem. Eng. J. 162, 792–801.
Maaß, S., Gabler, A., Zaccone, A., Paschedag, A., Kraume, M., 2012a. Experimental investigations and modelling of breakage phenomena in stirred liquid/liquid systems. Chem. Eng. Res. Des. 85, 703–709.
Maaß, S., Paul, N., Kraume, M., 2012b. Influence of the dispersed phase fraction on experimental and predicted drop size distribution in breakage dominated stirred systems. Chem. Eng. Sci. 76, 140–153.
Mortensen, H.H., Innings, F., Håkansson, A., 2018. Local levels of dissipation rate of tubulent kinetic energy in a rotor-stator mixer with different stator slot widths - an experimental investigation. Chem. Eng. Res. Des. 130, 52–62.
Pope, S.B., 2000. Turbulent Flows. Cambridge University Press.
Sawford, B., Hunt, J., 1986. Effects of turbulence structure, molecular diffusion and source size on scalar fluctuations in homogeneous turbulence. J. Fluid Mech. 165, 373–400.
Sheng, J., Meng, H., Fox, R.O., 2000. A large eddy piv method for turbulence dissipation rate estimation. Chem. Eng. Sci. 55, 4423–4434.
Shi, J., Herø, E.H., Solsvik, J., Jakobsen, H.A., Experimental and numerical study on single droplet breakage in turbulent flow. In: 12th International Conference on CFD in Oil & Gas, Metallurgical and Process Industries, Trondheim, 2017.
Smagorinsky, J., 1963. General circulation experiments with the primitive equations: 1. The basic experiment. Mon. Weather Rev. 91 (3), 99–162.
Solsvik, J., 2017. Turbulence modeling in the wide energy spectrum: explicit formulas for reynolds number dependent energy spectrum parameters. Eur. J. Mech.-B/Fluids 61, 170–176.
Solsvik, J., Jakobsen, H.A., 2016a. Development of fluid particle breakup and coalescence closure models for the complete energy spectrum of isotropic turbulence. Ind. Eng. Chem. Res. 55 (5), 1449–1460.
Solsvik, J., Jakobsen, H.A., 2016b. A review of the statistical turbulence theory required extending the population balance closure models to the entire spectrum of turbulence. Am. Inst. Chem. Eng. J. 62 (5), 1795–1820.
Taylor, G.I., 1935. Statistical theory of turbulence. I. Proc. R. Soc. A 151 (873), 421–444.
Taylor, G.I., 1938. The spectrum of turbulence. Proc. R. Soc. London. Ser. A Math. Phys. Sci. 164 (919), 476–490.
Taylor, J.R., 1997. An Introduction to Error Analysis. University Science Books.
Tennekes, H., Lumley, J.L., 1972. A First Course in Turbulence. The MIT Press.
Vejražka, J., Zedníková, M., Stanovský, P., 2017. Experiments on breakup of bubbles in a turbulent flow. Am. Inst. Chem. Eng. J. 64 (2), 740–757.

Chapter 7

Paper 2

Eirik H. Herø*
Nicolas La Forgia
Jannike Solsvik
Hugo A. Jakobsen

Determination of Breakage Parameters in Turbulent Fluid-Fluid Breakage

Numerous sets of single-particle breakage experiments are required in order to provide a sufficient database for improving the modeling of fluid particle breakage mechanisms. This work focuses on the interpretation of the physical breakage events captured on video. In order to extract the necessary information required for modeling the mechanisms of the fluid particle breakage events in turbulent flows, a well-defined image analysis procedure is necessary. Two breakage event definitions are considered, namely, initial breakup and cascade breakup. The reported breakage time, the number of daughter particles created, and the daughter size distribution are significantly affected by the definition used. For each breakage event definition, an image analysis procedure is presented.

Keywords: Droplet breakage, Image analysis, Multiphase flow, Population balance equation, Turbulence

Received: October 31, 2018; *revised:* February 07, 2019; *accepted:* February 11, 2019

DOI: 10.1002/ceat.201800610

Supporting Information available online

1 Introduction

Several industries are interested in dispersed-phase properties. In the oil and gas industry, one of the challenges is separation of phases in a liquid-liquid system, e.g., oil in water. Many of the separators use gravity, buoyancy, or other forces related to dispersed-phase size, with larger drops separated faster than smaller drops. In the simulation of these systems, a framework able to predict the dispersed-phase droplet size distribution is required. The population balance equation (PBE) [1, 2] dynamically describes the change of the dispersed-phase particles as they are transported, coalescing and breaking. The present study focuses on breakage events in turbulent flow.

For an overview of the PBE and fluid-particle breakage, the reader is referred to the Supporting Information. In summary, the parameters needed from experimental investigations are mother drop size D[1)], breakage probability P_b, breakage time t_b, average number of daughters ν, and daughter size distribution function P_D, as well as the continuous-phase flow properties, in particular the turbulent kinetic energy dissipation rate ε. Furthermore, it is important to know the fluid properties of both the dispersed phase and continuous phase, and system properties, e.g., densities and interfacial tension.

The existing experimental work on the breakage event can be divided into macroscopic dispersed-phase analysis, e.g., Coulaloglou and Tavlarides [3], and single-fluid particle analysis. Macroscopic investigations provide little information about local breakage functions [4], while the number of single fluid particle experiments is relatively scarce. Further complicating matters, many authors reporting fluid-particle experiments provide no clear definition of the measured parameters, i.e., how the parameters are actually interpreted and measured in the experiments. Identifying the parameters, from a video or otherwise, is not a trivial task and different procedures give rise to deviating values. An overview is given in Tab. 1, although the variation may be partly explained by the difference in experimental setups.

Several of the recent experimental investigations reported utilize high-speed imaging to capture the breakage event. Examples include Galinat et al. [5, 6], who conducted breakage experiments with single oil drops in a channel with an orifice using 1.5–3 mm diameter *n*-heptane drops. Data on the droplets were extracted from video through commercial software, using the pixels in the contour of the droplets. The breakage probability, daughter size, and daughter distribution were presented and correlated to the Weber number. Unfortunately, the different parameters determined were not specifically defined in the article.

Similarly, Andersson and Andersson [7] did not specify their definition of the breakage parameters when they studied a single oil drop, 1 mm dodecane or octanol, passing through a static mixer. Neither did they specify how they identified the measured breakage parameters from images. The turbulence energy dissipation rate was found by computational fluid dynamics (CFD), with a large eddy simulation, and experimentally by particle image velocimetry. The volume average dissipation

1) List of symbols at the end of the paper.

Eirik H. Herø, Dr. Nicolas La Forgia, Dr. Jannike Solsvik, Prof. Hugo A. Jakobsen
eirik.h.hero@ntnu.no
Norwegian University of Science and Technology (NTNU) Faculty of Natural Science, Department of Chemical Engineering, Seem Sælandsvei 4 Kjemiblokk 5, 7491 Trondheim, Norway.

Table 1. Selected single-drop experiments in literature.

Reference	Experimental setup	Breakage definition	Average number of daughter drops	Breakage time [ms]
Galinat et al. [5, 6]	Orifice pipe flow	Unknown	2–11.5	45–65
Andersson and Andersson [7]	Static mixer	Unknown	2–9	4–11
Maass et al. [9, 10]	Mimic stirred tank	Initial breakup	2–2.4	12–35
Solsvik and Jakobsen [12]	Stirred tank	Breakup cascade	2–9+	5–160

rate, found to be 1.3–16.4 m^2s^{-3} depending on the continuous phase flow rate, was presented.

In the work of Maaß and co-workers (e.g., [8–10]), single oil drops were investigated in a stirred tank and a channel with a single blade inducing turbulence, mimicking the flow around an impeller in a stirred tank. The videos were analyzed with commercial software [8] through an unknown procedure. The size of the mother drops, toluene or petroleum, were reported from 0.54–3.1 mm. The breakup events were linked to the volume average turbulent energy dissipation rate of 0.3–1.8 m^2s^{-3} and the local maximum of 3.4–91.1 m^2s^{-3}. Maaß et al. [9] do indirectly define the parameters determined, stating that successive breakups are not considered. In addition, Maaß and Kraume [10] provided a decent attempt at statistical treatment of several breakage parameters. For the single-blade setup, the breakage time was counted from the instant the drop passed the blade until the instance of fragmentation [10].

Nachtigall et al. [11] continued the work with an increased focus on statistical analysis. MATLAB was used to automatically extract the droplets' projected area and perimeter and the shape and axes of drops were investigated. In addition, the breakage time was defined in two separate ways, i.e., deformation and oscillation time. The deformation time is defined as starting with the last instance of a spherical mother drop and ending with the instance of fragmentation. In the oscillation time, the start is instead defined as the instance in which the mother drop passes the stirrer blade.

Solsvik and Jakobsen [12] investigated single fluid particle breakage in a stirred tank using several oils, i.e., toluene, petroleum, *n*-dodecane, and 1-octanol, with sizes ranging from 0.6 to 4.0 mm. The videos were manually investigated for extraction of mother drop size, daughter numbers, and breakage time. The breakup events were linked to the volume average dissipation rate, being 1.14 m^2s^{-3}. Solsvik and Jakobsen [12] considered a breakup cascade to be a single event, thus the definition of the reported parameters deviate from that of Maaß and co-workers [8–10] and Nachtigall et al. [11].

From the literature, two clear definitions of the breakage event exist, namely, the initial breakup, e.g., Maaß et al. [9], and the breakup cascade, as originally suggested by Solsvik et al. [13]. In the initial breakage definition, the event ends at the initial instantaneous breakup of the mother drop and the possible breakup cascade of the daughter drops are not considered. Thus, the breakage time, daughter size, and daughter number are only dependent on the first breakup. Conversely, in the breakup cascade, the breakup event can be a sequence of breakups. When deformed daughters undergo breakup, they are considered dependent on the breakup of the initial mother drop. The definition adopted significantly affects the reported values for the breakage time, the daughter size distribution, and the average number of daughters. Therefore, the present work aims to outline an algorithm for the extraction of the breakage parameters from video.

2 Experimental Setup

In order to investigate single-droplet breakage, an experimental facility has been constructed. A schematic is displayed in Fig. 1. The main part of the setup is a square channel, hereafter referred to as the breakage channel, which is 1 m long with a

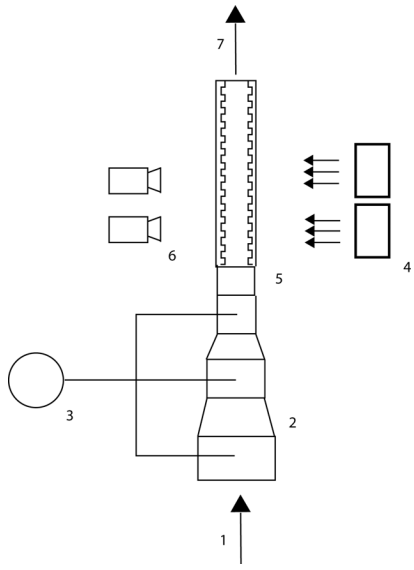

Figure 1. Schematic drawing of the experimental setup. 1. Water inlet, 2. droplet generation section, 3. oil syringe pump, 4. illumination, 5. breakage channel, 6. two cameras, 7. water outlet.

cross section of 30 mm by 30 mm. It consists of two sides of glass and two sides of metal. The two glass sides allow the breakage event to be observed by two high-speed cameras of the type Photron FASTCAM Mini AX100 540K M3 and illuminated by backlight. The two metal sides are equipped with transverse square rods to increase the turbulence generated at the wall, which in turn intensify the general turbulence level in the channel. The rods are of size 3 mm by 3 mm and placed with a centerline distance of 10 mm.

An example of a breakage event in one camera can be seen in Fig. 2, in which the rods on the channel walls are visible. The geometry allows for a flow pattern in the center of the channel with low shear and high turbulence intensity, which have been experimentally investigated and mapped by laser Doppler velocimetry and are presented in La Forgia et al. [14].

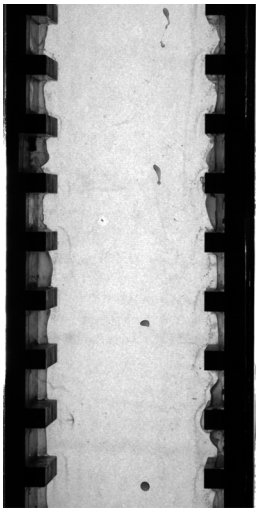

Figure 2. Collage of part of a breakup event observed by one camera.

Directly downstream of the breakage channel is a section for generating single oil droplets, hereafter referred to as the droplet generation section, which is similar to the setup used by Maaß and co-workers, e.g., in [9]. The droplet generation section has three different regions, each with different cross-sectional areas. This allows for three different flow conditions for drop generation for each mean flow condition, i.e., turbulence level, in the breakage channel. For the creation of an oil droplet, a glass cylinder with a needle tip is inserted in one of the three regions. The size of the oil drop generated is determined by the size of the tip and the flow conditions of the section. Further, the glass cylinder is connected to a syringe pump with a 10-mL syringe.

Single 1-octanol drops are investigated with the algorithm proposed in the following section. The oil is dyed with black sudan, a non-water-soluble dye, for increased contrast in the images. The resulting properties are as follows: density ρ, 825 kg m^{-3}; interfacial tension σ_I, 8.20 mN m^{-1}; dynamic viscosity μ, 9.09 mPa s. The continuous phase is clean reverse-osmosis water at an area average flow speed of 1.5 m s^{-1}. The two cameras each have a resolution of 1024 × 1024 and record at 4000 frames per second. Together they cover a region from 191 to 535 mm downstream of the inlet of the breakage channel, for a total length of 344 mm. The smallest drops detectable with this setup are about 0.17 mm, provided the contrast between the drop and continuous phase is high enough.

3 Image Analysis

The image analysis considers both of the breakup event definitions suggested in literature, i.e., the initial breakage definition and the cascade breakage definition. In order to compare the two definitions, each observed breakup event is interpreted through both the initial and the cascade breakage definition. Thus, the image analysis returns two separate sets of breakage parameters, one for each definition.

In order to establish the start of a breakage event, consider an initially stable drop. At this instance in time, it has a spherical shape. Then, the energy needed for breakup to occur is obtained by, e.g., collision with a turbulent eddy. The drop goes through a continuous deformation process and breaks into smaller drops stable at the new energy level. Thus, in either of the breakage event definitions, the start of the event is considered the instant of mother drop deformation, provided this deformation leads to a breakup. In the initial breakage definition, the event ends at initial breakup, i.e., the first instant of more than one drop. Possible successive breakups of the daughter drops are considered separate and independent breakage events.

In the cascade breakage definition, on the other hand, the breakage event is considered finished at final breakup of intermediary daughters. In order for a daughter to be considered intermediary, it must undergo a continuous deformation or, in other terms, it must not obtain a spherical and stable shape. The difference of the two definitions is illustrated in Fig. 3. From the start instant of the breakage event, the continuous-phase flow properties are found, while the size and number of daughter drops are observed from the end instance. Further, the breakage time is the time between the two instants.

To extract the breakage parameters from 2D video, the following algorithm is applied. Each frame is subtracted an image without a drop, i.e., the value of each pixel is subtracted the value of the corresponding pixel in an image with no drop. In the resulting image, each pixel without a drop present has a low greyscale value, while the pixels containing a drop have a higher greyscale value. Then, every pixel above a given greyscale value, dependent on light intensity in the video, is considered part of a drop. The procedure is illustrated in Fig. 4. Connected pixels are considered part of the same drop, and the area and position of the drops in the image are found from the pixels they occupy. In order to investigate the shape, the perimeter of

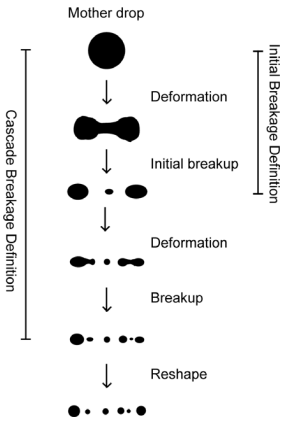

Figure 3. Illustration of the breakup cascade definition versus the initial breakup definition.

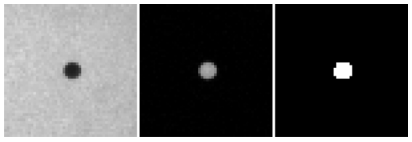

Figure 4. Image analysis; original grayscale image, subtracting background in grayscale and binary image.

the area is computed, as well as the minor axis and major axis of an ellipse with the same normalized second central moments as the area.

The shape of the drop from the image is 2D, while the real shape of the drops is 3D. In order to determine the drop as stable or not stable, i.e., spherical or not spherical, the 2D shape is first determined to be circular or not circular, as the projected area of a sphere is a circle. Two criteria are tested to identify circularity: first, the major and minor axes of the shape should be equal; second, the actual perimeter of the drop shape is compared to the circumference of a circle with the same area as the drop. These two measures should be equal as well. If both the criteria are fulfilled, the drop is assumed circular in the plane. Yet, the drop may still be deformed in the third dimension and not spherical. However, as this deformation is unlikely to be stable in time, the drop is assumed spherical if it is found to be circular and it has the same area and perimeter for a few, e.g., five consecutive frames.

The start of the breakage event is taken to be the first frame in which the mother drop is deformed by a deformation that eventually leads to breakup. Thus, the start of the breakage event is a frame of a deformed, i.e., not spherical drop which has been found to be circular for a number of the previous frames, e.g., five. In the initial breakage definition, the breakage end is taken to be the first frame with more than one drop, i.e., the first frame with countable pixels between daughter drops, and further breakups are not considered. However, in the cascade breakage definition, the breakage end is the frame of the last intermediary daughter breakup. Daughter drops are considered intermediary if they are deformed, i.e., not considered spherical, between the breakup of the mother drop and the breakup of the daughter drop itself.

From the breakage start and breakage end instants, the breakage time is calculated from the number of frames in between and the frame rate of the video. The number of daughters is the number of distinct drops at breakage end, i.e., the number of different regions of connected pixels. An example is demonstrated in Fig. 5, where the difference in breakage time t_b and number of daughter particles ν due to the breakage event definition is illustrated. Further, determining daughter sizes poses a significant challenge. A simplified and uncertain size determination is made from the ratio of the individual daughter's area to the total area of all daughter drops. For example, if a daughter makes up half of the collective drop areas in the image, it is assumed to be half the size of the mother drop.

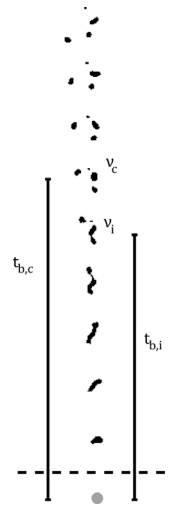

Figure 5. Output from image analysis and illustration of how the definition of the breakup event affects breakage time t_b and number of daughter particles ν. Cascade breakup is denoted by subscript c and initial breakup is denoted by subscript i.

The turbulent energy dissipation rate is found from the continuous-phase average value at the position of the mother drop at breakage start. In the cases that the mother drop travels through large gradients in turbulence level, e.g., traveling close

to the wall, the initial turbulent energy dissipation rate may not be representative. Thus, in such cases, a trajectory maximum value of the turbulent energy dissipation rate is also reported.

The breakage probability is determined from a set of experiments. The outcome of every single drop experiment is categorized as either a breakup event or no breakup event. After the whole series of experiments have been characterized in this way, the breakage probability is determined from the ratio of breakup events to the total number of drops observed.

4 Results and Discussion

Although the use of high-speed cameras is common in the experimental work on droplet breakage reported in the literature, the interpretation of breakage parameters from the images is generally not provided or described in a vague manner. Sect. 3 outlines the framework used for extracting the breakage parameters from the video of the physical events in this work. In this section, the application of the image analysis to the current setup is discussed.

A single binary breakage event is depicted in Fig. 6. Each image is a region of 50 pixels by 50 pixels taken from the full image. First, a spherical mother drop undergoes a continuous deformation, starting at 0.25 ms, until separating after 37.5 ms. Then the daughters obtain a spherical shape and the further development is not considered. In this special case, due to no daughters undergoing further breakage before becoming spherical, the cascade breakage definition coincides with the initial breakage definition and the breakage parameters obtained are the same. The breakage start is taken to be the start of deformation, i.e., 0.25 ms, and breakage end at separation, i.e., 37.5 ms, which gives a breakage time of 37.25 ms. From the breakage end image, the daughter number is found to be 2. Finally, the mother drop size follows from the time instance before deformation start, in which it was determined to be spherical. The daughter sizes are then found from their relative projected area of 62 % and 38 %, and taken to be 62 % and 38 % of the mother drop size.

Figure 6. Sequence of images of an event leading to binary breakage.

Conversely, Fig. 7 demonstrates an event of in which the breakage parameters of the two breakage definitions are significantly different. In order to highlight the determined information in each image, the binary image of the image algorithm is presented alongside. An originally spherical mother drop starts to deform at 0.25 ms. At 18 ms, the first separation into multiple drops is observed and this time instance taken to be the end of the breakage event in the initial breakage definition. However, several of the drops are still significantly deformed and found to break up until 28.25 ms. Thus, this time instance is taken to be the end of the breakage event in the cascade breakage definition. Further, in the initial breakage event definition, this event has a breakage time of 17.25 ms and four daughters, while in the cascade breakage event definition, this event has a breakage time of 28 ms and nine daughters.

Ideally, the breakage events are checked for volume conservation. In order to do so, the daughter sizes must be determined exclusively from the information available after breakup. In one possible method, the daughters are assumed spherical and their projected area assumed circular. Then, from the projected area of the daughter, the diameter of an area equivalent circle is found, which is taken to be the size of the daughter. In the event that the daughter drops are observable at a stable and spherical shape, this method provides a better estimation of the daughter sizes compared with the method suggested in Sect. 3. However, in the initial breakage event definition, the daughter drops may have a significantly deformed shape, as seen in Fig. 7.

Additionally, the deformed daughter drops undergoing further breakage may not ever obtain a spherical shape. Thus, this method of determining daughter sizes is particularly challenging and may lead to significantly deviating values of volume conservation. On the other hand, in the cascade breakage event definition, the assumption that the daughters are spherical is more realistic. Furthermore, near-spherical daughters may be identified from images after breakage end.

The resolution, both spatial and temporal, is an important factor determining the experimental uncertainty of the image analysis process. Firstly, at 4000 frames per second, there is a gap of 0.25 ms between each observation of the event. Subsequently, the instance of breakage start or breakage end may be determined to be almost 0.25 ms after the true value. Furthermore, the spatial resolution represents a tradeoff: on the one hand, it is beneficial to observe as much of the channel as possible to capture the whole cascade of all events; on the other hand, the two cameras have a set resolution of 1024×1024 pixels, which means that a certain zoom is required to capture the details of the breakage event.

At low spatial resolution, detection and identification of the correct breakage end are further challenged, due to each pixel being considered either a drop or not, e.g., two drops might be separated, but this is not detectable in the image. Furthermore, very small daughters of approximately 1 pixel in size may not be detectable continuously in subsequent images, due to changes in light intensity or due to the drop occupying only a small part of each pixel, in turn leading to a greyscale value below the threshold of detection.

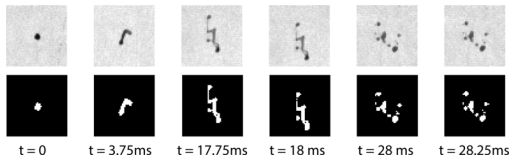

Figure 7. Sequence of images of an event leading to multiple breakage.

Additionally, special care must be taken if the drop moves towards the wall. While the channel flow allows for a predictable turbulence level and low streamwise gradients in the turbulent energy dissipation rate in the center section of the channel, drops moving close to the wall experience an increase in both shear and turbulence intensity. Thus, drops not broken before entering a region 1.5 mm from the rods on the wall are not considered to break from the turbulence alone, and while the events are recorded, they are not considered compatible with the events of drops broken outside of this region. In the particular event of a breakage in the center channel region, in which a possible intermediary daughter drop of the breakage cascade is transported into the wall region, no further breakage of the daughter drop is considered.

Further, special care is also taken for a deforming drop leaving the field of view of the cameras. In such cases, the event is either considered finished or disregarded. If the drop leaving is a mother drop, it is considered to be an event with no breakage. On the other hand, if the drop is a possible intermediary daughter in the cascade breakage definition, the daughter is only considered finished breaking if it has been observed for at least 10 ms. When it has been observed less, the event is not considered for the cascade breakage, yet still counted in the initial breakage dataset.

Ideally, a program could interpret each event automatically. Unfortunately, daughter drops not detectable in continuous images, due to overlap or small size, make automatic determination of the breakage cascade particularly challenging.

5 Conclusions

The image analysis of fluid particle breakage videos has been discussed. Specific definitions and physical interpretation of the breakage parameters are given, and the procedure for extracting the parameters from a series of images is elucidated.

The choice of breakage event definition, i.e., initial breakup or cascade breakup, is of significant importance to the reported values of breakup time, daughter distribution size, and average number of daughters. While two definitions of the breakage event are considered in the literature, the experimental investigation should aim to provide the breakage parameters of both definitions. The accuracy of the experimental data is dependent on being extracted from the correct definition of the breakage event, and as such, both sets of data are relevant until one of the definitions of the breakage event can be reconciled with the physical breakage phenomena.

The determination of daughter sizes is a particular challenge. In the initial breakage event definition, the available information of each drop obtainable from 2D imaging is limited. Thus, coarse assumptions must be made. Conversely, while the cascade breakage event definition is challenging to implement automatically, it has the advantage of observing each daughter drop in a stable state, allowing volume conservation verification.

Acknowledgment

This work was carried out as a part of SUBPRO, a research-based innovation center within Subsea Production and Processing. The authors gratefully acknowledge the financial support from SUBPRO, which is financed by the Research Council of Norway, major industry partners, and NTNU.

The authors have declared no conflict of interest.

Symbols used

D	[m]	droplet diameter
P_b	[–]	breakage probability
P_D	[m^{-1}]	daughter size distribution function
t_b	[s]	breakage time

Greek letters

ε	[$m^2 s^{-3}$]	turbulent kinetic energy dissipation rate
μ	[mPa s]	dynamic viscosity
ν	[–]	average number of daughters
ρ	[$kg\ m^{-3}$]	density
σ_I	[$mN\ m^{-1}$]	interfacial tension

Abbreviation

PBE	population balance equation

References

[1] D. Ramkrishna, *Population Balance: Theory and Applications to Particulate Systems in Engineering*, Academic Press, San Diego, CA **2000**.

[2] H. A. Jakobsen, *Chemical Reactor Modeling*, 1st ed., Springer-Verlag, Berlin **2008**.

[3] C. A. Coulaloglou, L. L. Tavlarides, *Chem. Eng. Sci.* **1977**, *32 (11)*, 1289–1297. DOI: https://doi.org/10.1016/0009-2509(77)85023-9

[4] J. Solsvik, S. Tangen, H. A. Jakobsen, *Rev. Chem. Eng.* **2013**, *29 (5)*, 241–356. DOI: https://doi.org/10.1515/revce-2013-0009

[5] S. Galinat, O. Masbernat, P. Guiraud, C. Dalmazzone, C. Noïk, *Chem. Eng. Sci.* **2005**, *60 (23)*, 6511–6528. DOI: https://doi.org/10.1016/j.ces.2005.05.012

[6] S. Galinat, L. Garrido Torres, O. Masbernat, P. Guiraud, F. Risso, C. Dalmazzone, C. Noïk, *AIChE J.* **2006**, *53*, 56–68. DOI: https://doi.org/10.1002/aic.11055

[7] R. Andersson, B. Andersson, *AIChE J.* **2006**, *52*, 2020–2030. DOI: https://doi.org/10.1002/aic.10831

[8] S. Maaß, A. Gäbler, A. Zaccone, A. R. Paschedag, M. Kraume, *Chem. Eng. Res. Des.* **2007**, *85 (5)*, 703–709. DOI: https://doi.org/10.1205/cherd06187

[9] S. Maaß, S. Buscher, S. Hermann, M. Kraume, *Biotechnol. J.* **2011**, *6*, 979–992. DOI: https://doi.org/10.1002/biot.201100161

[10] S. Maaß, M. Kraume, *Chem. Eng. Sci.* **2012**, *70*, 146–164. DOI: https://doi.org/10.1016/j.ces.2011.08.027
[11] S. Nachtigall, D. Zedel, M. Kraume, *Chin. J. Chem. Eng.* **2016**, *24*, 264–277. DOI: https://doi.org/10.1016/j.cjche.2015.06.003
[12] J. Solsvik, H. A. Jakobsen, *Chem. Eng. Sci.* **2015**, *131*, 219–234. DOI: https://doi.org/10.1016/j.ces.2015.03.059
[13] J. Solsvik, S. Maaß, H. A. Jakobsen, *Ind. Eng. Chem. Res.* **2016**, *55 (10)*, 2872–2882. DOI: https://doi.org/10.1021/acs.iecr.6b00591
[14] N. La Forgia, E. H. Herø, J. Solsvik, H. A. Jakobsen, *Chem. Eng. Sci.* **2019**, *195*, 159–178. DOI: https://doi.org/10.1016/j.ces.2018.11.039

Chapter 8

Paper 3

Chemical Engineering Science: X 8 (2020) 100082

Contents lists available at ScienceDirect

Chemical Engineering Science: X

journal homepage: www.elsevier.com/locate/cesx

Single drop breakage in turbulent flow: Statistical data analysis

Eirik H. Herø *, Nicolas La Forgia, Jannike Solsvik, Hugo A. Jakobsen

Department of Chemical Engineering, Norwegian University of Science and Technology, Sem Sælandsvei 4, Kjemiblokk 5, 7491 Trondheim, Norway

ARTICLE INFO

Article history:
Received 17 June 2020
Received in revised form 27 August 2020
Accepted 25 September 2020

Keywords:
Breakage
Fluid particle
Turbulence
Statistical analysis
Population balance equation

ABSTRACT

To improve breakage models in the population balance framework, single octanol droplet experiments have been performed in a channel flow and recorded by high-speed camera. The study investigates impact of mother drop size on the breakage time, breakage probability, average number of daughters and the daughter size distribution for known turbulence characteristics. Each breakage event is associated with an individual turbulence level, based on the local flow characteristics. A clearly defined statistical analysis is presented. Using 95% confidence intervals, the precision of each of the determined properties is described quantitatively. Furthermore, the confidence intervals are a tool for determining whether an increased number of experiments will yield a significant increase in the precision, considered against the sources of error. It is found that 35–50 breakage events are sufficient to obtain confidence intervals of desired precision.

1. Introduction

The dispersed phase properties in multiphase flows are of interest for several fields of industry. Some examples of industrial applications of low turbulence level flows are channel or pipe flow, bio- and chemical-reactor flows, as well as phase separation equipment like gravity separators. To determine the separation of a dispersed phase, or to determine the interfacial mass transfer of a system, information on the size distribution of the dispersed phase is critical. The transient breakage phenomenon must be well understood for predictive simulation of such systems. Even so, the knowledge of the turbulent breakage phenomenon is scarce, likely owing to technological limitations and labor intensive experimental procedures.

One simulation tool available for multiphase flow systems is the population balance equation, PBE. There is a need for experiments on single fluid particle breakage in order to improve or validate breakage models within this framework. This need has previously been acknowledged by e.g. Andersson and Andersson (2006b) and Solsvik and Jakobsen (2015). The experimental data is needed on the source term constitutive equations, which are given here as:

- The breakage frequency $b(D_m)$. Which is found through investigating:
  - The breakage time $t_B(D_m)$, which is the time it takes for a drop of size D_m to break.
  - The breakage probability $P_B(D_m)$, which is the probability that a drop of size D_m will break.
- The average number of daughter drops $\nu(D_m)$, which is the average number of drops produced upon the breakup of a drop of size D_m.
- The daughter size distribution function $P_{DSD}(D_m, D_d)$, which is the probability that a drop of size D_d is produced upon breakup of a drop of size D_m.

Here, D_m is the diameter of the mother drop, i.e. the breaking drop, and D_d is the diameter of a daughter drop. In the context of this article, a mother drop may also refer to a drop not breaking. For simplicity, the source term constitutive equations are written as functions of the drop diameters only. Additionally, they may depend on the turbulent kinetic energy dissipation rate, TDR, ϵ, the viscosity, μ, the density, ρ, of each phase, the interfacial tension, γ, and the turbulent kinetic energy, TKE, k, in addition to other parameters.

Experiments on breakage in dense dispersions, in which many fluid particles are investigated simultaneously, are challenging or impossible to use in validation of local breakage functions (Solsvik et al., 2013). Unfortunately, the number of studies on single fluid particle breakage is low. In addition, the use of different experimental setups and different procedures makes it difficult to compare the available experimental data. The studies in the literature vary in the number of considered events, the statistical procedure employed, the turbulence level and the method of determination of the turbulence level. The studies also use different oils as the dispersed phase and use either tap or distilled water

* Corresponding author.
E-mail address: eirik.h.hero@ntnu.no (E.H. Herø).

https://doi.org/10.1016/j.cesx.2020.100082
2590-1400/

Nomenclature

Latin Letters

$\hat{b}$	estimated breakage frequency [1/s]
$\bar{x}$	mean value
$\boldsymbol{r}$	space coordinate vector [m]
$\boldsymbol{v}_r$	velocity vector [m/s]
ΔN	number of breaking drops
ΔN_B	true number of drops breaking
ΔP	Pressure drop [Pa]
$\Delta P_{DSD}{}'$	discrete daughter size distribution function [1/m^3]
$\Delta P_{DSD}*$	dimensionless discrete daughter size distribution function [-]
ΔV_d	daughter size range
$\hat{P}$	true probability of a favorable outcome
AB	separation distance [m]
b	breakage frequency [1/s]
B_B	birth due to breakage [1/(m^3 m s)]
B_D	death due to breakage [1/(m^3 m s)]
c	parameter
c_L	model parameter
$D*$	Dimensionless daughter diameter
$D*_{max}$	dimensionless drop, complimentary to $D*_{min}$ in (24)
$D*_{min}$	dimensionless smallest drop breaking in (24)
D_c	critical diameter [m]
D_d	daughter drop diameter [m]
D_m	mother drop diameter [m]
D_{max}	in (3), largest drop size present [m]
E	energy [J]
E_c	critical energy [J]
E_s	Surface energy [J]
F	hypergeometric function
f_n	number density function [1/(m^3 m)]
h	breakage yield distribution function [1/m]
K	Bessel function
k	turbulent kinetic energy [m^2/s^2]
L	integral length scale [m]
N	number of observations
N	total number of drops
$P*$	estimated probability
P_B	breakage probability
P_{DSD}	daughter size distribution function [1/m]
$P_{DSD}*$	Dimensionless daughter size distribution function
Q	true probability of an unfavorable outcome
r_d	model distance [m]
S	standard deviation
s	function
t	time [s]
t_B	breakage time [s]
T_n	function, n = 1, 2, 3, 4, 5
u_B	characteristic breakup velocity [m/s]
V_d	daughter drop volume [m^3]
V_m	mother drop volume [m^3]
$z_{\alpha/2}$	normal distribution coefficient
Re_λ	Taylor scale Reynolds number
We	Weber number

Greek Letters

α	confidence interval size
β	Komogorov constant
$\Delta\sigma$	surplus stress [Pa/m^2]
ϵ	turbulent energy dissipation rate [m^2/s^3]
η	Kolmogorov micro scale [m]
Γ	gamma function
γ	interfacial tension [N/m]
Λ	dimensionless critical diameter [m]
μ	dynamic viscosity [kg/(m s)]
μ	true mean
ν	average number of daughters
ν	kinematic viscosity, in Section 2.5 [m^2/s]
ω	confidence interval limit
$\overline{\delta u^2}$	second order longitudinal velocity structure function [m^2/s^2]
ρ	fluid density [kg/m^3]
ρ_c	continuous phase density [kg/m^3]
ρ_d	dispersed phase density [kg/m^3]
σ	standard deviation
σ_s	surface restoring stress [Pa/m^2]
σ_t	turbulent stress [Pa/m^2]

Abbreviations

CFD	Computational Fluid Dynamics
PBE	Population Balance Equation
TDR	Turbulent Kinetic Energy Dissipation Rate
TKE	Turbulent Kinetic Energy

for the continuous phase, which results in different fluid and system properties. In particular, both the interpretation of the studies and the comparison between the studies are challenging due to different or unclear definitions of the breakage event. Partly, this is due to a controversy in the literature regarding the breakage event definition. Solsvik et al. (2016a) outlined two definitions of the breakage event. One is the initial breakage definition, in which the breakage event is considered to end at the first fragmentation. This is employed in the studies of Maaß et al. (2011); Maaß and Kraume (2012) and Nachtigall et al. (2016). The other breakage event definition is the breakage cascade definition, in which the breakage event end at the final fragmentation of intermediate daughter drops. The cascade breakage definition is used in the investigation of Solsvik and Jakobsen (2015) and seemingly also in the daughter size distribution investigations of Maaß et al. (2007). The breakage definition employed has a significant impact on the breakage time, the number of daughters and their size distribution, as the cascade breakage definition considers the time after initial breakage.

Furthermore, the studies in literature investigate different phenomena of the breakage event. Galinat et al. (2005) investigated the breakage probability, daughter size distribution and average number of daughters of single oil droplet breakage in an orifice flow. The number of experiments performed is unclear, but at least 50 to 80 drops where observed for each of the twelve flow conditions. These different flow conditions were obtained by changing the orifice opening and the continuous phase velocity. Further, Galinat et al. (2005) used single drops of heptane or heptane colored with red sudan as the dispersed phase, while the continuous phase was tap water. Due to fluctuations in the diameter of the generated mother drop under the same experimental conditions, the mother drops were divided into classes. The mother drop diameters were between 1.5 to 3 mm and the classes had a width of 0.25 mm. From these mother drop diameter groups, groups based on a Weber number was constructed, where the Weber number was expressed as $\mathrm{We} = \Delta P D_m/\gamma$. Here, ΔP is the pressure drop over the orifice, from which the TDR levels can be found to be between 1 and 20 m^2/s^3, depending on the flow condition, while

Table 1
Fluid and system properties reported in previous studies.

Reference	Continuous phase	Dispersed phase	γ x10^{-3} [N/m]	ρ [kg/m^3]	μ x10^{-3} [kg/(m s)]
Galinat et al. (2005)	Tap water			996	0.82
		Heptane	47	683.7	0.45
		Colored heptane	23.6		
Galinat et al. (2007)	Tap water with glycerin			1100	
		Colored heptane	24.4		
Andersson and Andersson (2006a,b)		Dodecane	53	750	1.5
		Octanol	8.5	819	6.5
Maaß et al. (2007) and		Petroleum		760	1.9
Zaccone et al. (2007)	Unspecified water		2		
	Colored water		28		
Maaß et al. (2011) and	Unspecified water				
Maaß and Kraume (2012)		Toluene	32	870	0.55
		Petroleum	38.5	790	0.65
Nachtigall et al. (2016)		Petroleum		760	1.7
	Unspecified water		43.2		
	Water with SDS		5.9		
		Paraffin oil		861	127
	Unspecified water		53.3		
	Water with SDS		8.4		
Solsvik and Jakobsen (2015)	Distilled water				
		Toluene	33	866.7	0.6
		Petroleum	44.5	754	1.14
		n-Dodecane	41.5	745	1.38
		1-Octanol	8.4	822	7.52
Ashar et al. (2018)	Deionized water			988	1
		Rapeseed oil	20	920	70

no TKE values or relations were given. Finally, the results are presented as functions of the Weber number, although the number of experiments within each Weber number group is not given. The breakage probability was also linked directly to the mother drop size for four different flow conditions. No statistical analysis was presented for the daughter size distribution and the breakage probability, but the average number of daughters are presented as average values with standard deviation. Later, Galinat et al. (2007) performed additional experiments with water-glycerin as the continuous phase, and colored heptane as the dispersed phase. 70 experiments where performed for each of the twelve flow conditions, with the TDR level varying between 0.9 and 2.5 m^2/s^3. In the study, the mother drop diameter was between 1.4 to 2.0 mm. No breakage definition was given in either studies by Galinat et al. (2005, 2007). The reported fluid and system properties of all the considered studies can be seen in Table 1 and a simplified overview of selected studies can be seen in Table 2.

Andersson and Andersson (2006a,b) studied single oil dodecane or octanol drop breakage in a static mixer. The continuous phase was water, for which the properties was not specified. In their study, the breakage time was reported as a function of the TDR level, and presented as an average value with standard deviation. However, no further statistical analysis was presented. In addition, the daughter number distribution of dodecane drops was presented for two different TDR levels. For each reported value, approximately 50 breakage events were considered and the mother drop diameter was kept constant at 1 mm [1]. PIV-experiments and Large Eddy Simulation was used to determine the turbulent characteristics. Depending on the continuous phase flow rate, the volume average the TDR levels was found to be 1.13, 3.69 and 8.54 m^2/s^3, while the TKE level was found to be 17, 37 and 64 m^2/s^2. Finally, the employed breakage definition is not mentioned.

Maaß et al. (2007) and Zaccone et al. (2007) investigated oil drop breakage in a channel flow with an impeller blade, mimicking stirred tank flow. They investigated the daughter size distribution for different daughter numbers and reported the daughter number distribution. The dispersed phase was petroleum and the continuous phase was an unspecified type of water, with and without coloring by sudan-black. Further, the TDE was determined from CFD simulations with a k-ϵ model, where the local maximum near the impeller was found to be 26.1 m^2/s^3. The TKE was not given. For each of the mother drop diameters 0.56, 1 and 2 mm, the number of investigated events are given as 284, 503 and 184. In addition, a required number of events were reported, however, it is not clear what the significance of this number is or how it was determined. Later, Maaß et al. (2011) and Maaß and Kraume (2012) used the same setup to investigate the daughter number distribution and breakage frequency, the latter as breakage time and breakage probability. The mother drops were toluene with diameters of 0.62, 1.0, 2.0 and 3.0 mm, as well as petroleum drops of 0.54, 0.7, 1.0, 1.3, 1.9 and 3.1 mm. For each of the mother drop sizes, the number of total events where between $\sim$ 750 and $\sim$ 1320, of which the number of breakage were between $\sim$ 240 and $\sim$ 780. The results on breakage time and breakage probability were presented with average values and standard deviation. Additionally, the development of the mean value with the number of experiments were investigated. This showed that the values were stable, thus there were more than enough experiments performed. Later, and in the same setup, Nachtigall et al. (2016) investigated the breakage time with emphasis on the deformation process. The mother drops where all 1 mm in diameter and either petroleum or paraffin oil, while the continuous phase was either water or water mixed with sodium dodecyl sulfate. The different combinations of dispersed and continuous phases allowed for the impact of the interfacial tension to be investigated. In the study, the number of events with breakage was between 364 and 917, while the total number of events was between 1021 and 1486. Furthermore, the experimental results are presented as whisker-and-box plots, but no further statistical analysis was presented.

Solsvik and Jakobsen (2015) investigated single oil droplet breakage in a stirred tank. In their study, the breakage time was presented as function of the mother drop size, along with the distribution of daughter drop numbers. Toluene, petroleum, n-

[1] Personal communication

Table 2
Overview of selected single drop experimental studies. *Standard deviation is only shown when determining an average value, e.g. not for breakage probability or daughter size distributions.

Reference	Investigated values	Mother Drop Diameter, D_m [mm]	TDR ϵ [m^2/s^3]	Statistical Treatment
Galinat et al. (2005, 2007)	P_B, ν, P_{DSD}	1.5–3	~1–20	Average values with standard deviation*
Maaß et al. (2007)	P_{DSD}	0.56–2	26.1	None
Maaß and Kraume (2012)	t_B, P_B	0.54–3.1	~ 2.3–12.3	Analysis of the development in the mean value
Andersson and Andersson (2006a,b)	t_B, ν	1	1.13–8.54	Average values with standard deviation*
Solsvik and Jakobsen (2015)	t_B, ν	0.6–4.0	1.14	None
Ashar et al. (2018)	P_B, ν	0.07–0.55	535–2480	Average values with uncertainty

dodecane and 1-octanol was used as the dispersed phase and distilled water was used as the continuous phase. The diameter of the mother drops was varying between 0.6 to 4 mm, and thus divided into groups with a width of 0.5 mm. There were between 180 to 250 breakage events for each oil, but greatly varying in numbers within each mother drop group. Here, the number of breakage events were between 1 and 71. The TDR level was determined from the power input and given as a volume average of the entire tank, at 1.14 m^2/s^3. No information on the TKE was given. Furthermore, no statistical method was presented.

Ashar et al. (2018) studied single droplet breakage in a stirred tank and investigated the breakage probability and the average number of daughters. The results were reported as functions of a turbulent Weber number and presented as average values with uncertainty. However, the statistical procedure was not given. A deformation time was also presented, which was defined as the time from turbulent vortex interaction until the maximum deformation. This is believed to be the time of energy transfer from the turbulent vortex to the breaking drop. As this maximum deformation occurs at an earlier time instance than the instance of first fragmentation, the deformation time is shorter than the initial breakage time. While not explicitly defined, the daughter number appears to be calculated according to the cascade breakage definition. In the study, the mother drops were rapeseed oil drops with a diameter between 0.07 and 0.55 mm, and deionized water was used as the continuous phase. In total, 285 breakage events were investigated for two different TDR levels, 535 and 2480 m^2/s^3. The TDR level was determined from a procedure arising from PIV analysis, and given as a local average value of the volume near the impeller. The TKE is not given.

Although it may initially appear otherwise, the studies presented above follow a similar procedure when reporting their results. An investigated parameter, e.g. breakage probability, is plotted against another variable, e.g. mother drop diameter. The other variables are assumed constant, where the TDR level is taken to be that of the single phase flow field of the continuous phase. It should be noted that when reporting the results by Weber number instead of the drop diameter, it is not possible to regain the dependency on ϵ and D_m, except if either ϵ or D_m is kept constant. Thus, the data cannot be used to validate most of the currently available models.

Based on the studies presented here, some generalizations of the status of single fluid particle breakage investigations are possible. Firstly, no investigation covers all of the information needed to model the terms in the PBE. That is, information on the breakage frequency, b, average number of daughters, ν, and daughter size distribution, P_{DSD}, have not all simultaneously been extracted from the same experimental data set. Consequently, subsequent model validation must rely on experimental data from different experimental setups and procedures, a strategy which does not ensure consistency.

Second, most of the previous studies employ a volume average TDR level, while the breakage models are developed considering local turbulence characteristics. The regions of breakage in the employed experimental facilities have large gradients in the turbulence level, thus the difference in local and average turbulence level may be significant. In turn, the reported turbulence characteristics may not be sufficiently accurate to represent the turbulence characteristics responsible for the breakage event. Additionally, there are two other weaknesses related to the flow conditions. Weakness one, the regions of breakage have a significant presence of mean flow shear, which possible impact on the breakage cannot be distinguished from the impact of the level of turbulence. Weakness two, no value of the TKE is associated with the breakage. Thus, the impact of the entire range of turbulence cannot be computed, only the impact of the inertial subrange of turbulence. How to model the entire range of turbulence has been shown by Solsvik and Jakobsen (2016a), and a summary is shown in Section 2.5.

Finally, the studies commonly presented the determined average value with a standard deviation, and no clear statistical analysis is available. As experimental procedures are subject to many sources of error, the statistical analysis, along with a discussion on uncertainty, is important in regards to the accuracy and precision of the results. Accuracy and precision are considered to be different concepts within uncertainty analysis, and the difference is shown graphically in Fig. 1. If measurements are repeated, a high accuracy yields values that are near the true value, while a high precision yields nearly the same value from each measurement. The statistical analysis, when resulting in a 95% confidence interval, is a tool for describing the precision of the data. However, it does not address the accuracy. This can be better understood by considering the plausible errors sources, which are usually divided into random errors and systematic errors. Random errors are largely due to changing initial conditions between each experiment. As the name implies, random errors are considered to be randomly applied. Systematic errors, on the other hand, arise from the experimental procedure and assumptions, and are generally not considered to be randomly applied. In a simplified view, the random errors may be assumed to be accounted for by the statistical analysis, while the systematic errors are not accounted for. Thus, systematic errors may skew the data in such a way that the confidence interval does not contain the true value. That is, while the experimentally determined value may be precise, it does not need to be accurate. It is possible to account for systematic errors if the impact on the results is known and quantified. Unfortunately, quantification of the systematic errors is rarely possible in complex experimental procedures. Nevertheless, performing a statistical analysis is particularly important due to the labor intensive

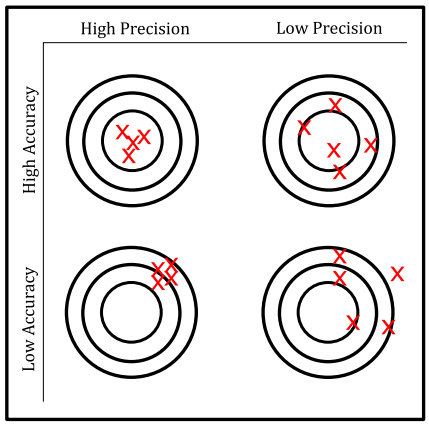

Fig. 1. The difference between accurate and precise experimental techniques.

methodology of the state of the art single droplet breakage experiments. The gain in precision from additional experiments must be considered against the increased workload. An increased number of experiments may lead to only a small increase in the precision, but may lead to additional aspects of the breakage phenomenon not being investigated. This may be part of the reason that no investigation covers all the information needed to model the source term constitutive equations in the PBE.

The purpose of this work is to obtain data on and elucidate the breakage phenomenon in general, and the impact of mother drop size in particular. An experimental facility has been constructed with a design that offers low gradients in the turbulence level of the continuous phase. As the local turbulence level is known, due to the investigation by La Forgia et al. (2018), each breakage event may be associated with relevant and local turbulent characteristics. This allows for a quantified difference in turbulence level between investigated events. Furthermore, the design allows for video capture of the entire breakage event, such that the videos may be investigated according to the procedure outlined in Herø et al. (2019). The resulting data should be consistent, as the breakage frequency, b, the average number of daughters, ν, and the daughter size distribution P_{DSD} are determined from the same events. Furthermore, this study employs a transparent statistical methodology as a tool to discuss the precision of the data. This statistical procedure is also used to identify whether additional experiments are beneficial.

2. Turbulent breakage models

The PBE is a common and powerful simulation tool. It is a framework that dynamically describes the change in the number density distribution of the dispersed phase (Ramkrishna, 2000). Simplified to consider only accumulation, convection and breakup, the PBE in terms of the number density function, f_n, can be written as (Jakobsen, 2014)

$$\frac{\partial f_n(D_m,\boldsymbol{r},t)}{\partial t}+\nabla\cdot[\boldsymbol{v}_r(\boldsymbol{r},D_m,t)f_n(D_m,\boldsymbol{r},t)] = -B_D(D_m,\boldsymbol{r},t)+B_B(D_m,\boldsymbol{r},t) \quad (1)$$

$$B_D(D_m)=b(D_m)f_n(D_m) \quad (2)$$

$$B_B(D_m)=\int_{D_m}^{D_{max}}\nu P_{DSD}(D_m,D_d)b(D_d)f_n(D_d)dD_d \quad (3)$$

Here, $\boldsymbol{r}$ is the space coordinate vector, t is the time, $\boldsymbol{v}_r$ is the velocity vector and D_m and D_d are denoting the drop diameters of the mother and daughter drop. Further, b is the breakage frequency, ν is the average number of daughter particles and P_{DSD} is the daughter size distribution function. The two latter quantities may be combined to the breakage yield redistribution function, h. Finally, the terms on the right hand side of (1) are the sink and source terms that represent the breakage death, (2), and breakage birth of drops, (3), of diameter D_m due to breakage events.

In order to use the PBE in simulations, e.g. coupled with computational fluid dynamics, the terms of (2) and (3) must be modeled. If experimental data are to improve these models, it is critical to consider how the models are developed. The mechanisms considered and the model interpretation of the breakage phenomenon should coincide with the interpretation of the data from physical experiments. Thus, two classic and commonly used models are presented in this section.

2.1. Coulaloglou and Tavlarides

In developing their model, Coulaloglou and Tavlarides (1977) assumed a drop would break due to local pressure fluctuations only. Further, they assumed binary breakage, locally isotropic turbulence and that the size of the droplet diameter falls within in the inertial subrange of turbulence. The basic assumption is that a breakup occurs if a drop collides with a turbulent eddy of sufficient energy. The breakage frequency, $b(D_m)$, which is required in both (2) and (3), is determined as the reciprocal of a breakage time, $t_B(D_m)$, multiplied by the fraction of drops breaking, $\frac{\Delta N(D_m)}{N(D_m)}$. This fraction of drops breaking is interpreted as the breakage probability $P_B(D_m)$, i.e. the probability that a drop will break. Thus, the breakage frequency relation becomes

$$b(D_m)=\frac{1}{t_B(D_m)}\frac{\Delta N(D_m)}{N(D_m)}=\frac{1}{t_B(D_m)}P_B(D_m) \quad (4)$$

The breakage probability is assumed proportional to the fraction of the turbulent eddies that collides with the drop, where the energy of the turbulent eddy is larger than the drop surface energy. Further, this fraction of turbulent eddies is assumed to be described by the Maxwell–Boltzmann 2D energy distribution, thus

$$P_B(D_m)=\int_{E_c(D_m)}^{\infty}P(E(D_m))dE=\exp\left(-\frac{E_c(D_m)}{E(D_m)}\right) \quad (5)$$

in which $E(D_m)$ is the turbulent energy associated with eddies of size D_m and $E_c(D_m)$ is the critical value that the turbulent energy $E(D_m)$ must overcome. $E_c(D_m)$ is taken as the surface energy

$$E_c(D_m)\propto\gamma D_m^2 \quad (6)$$

in which γ is the interfacial tension and D_m is the diameter of the drop. The energy of the turbulent eddies is taken to be

$$E(D_m)\propto\rho_d D_m^3\overline{\delta u^2}(D_m) \quad (7)$$

where ρ_d is the density of the dispersed phase. The second order longitudinal velocity structure function, $\overline{\delta u^2}(D_m)$, is determined from Kolmogorov theory

$$\overline{\delta u^2}(D_m)=\overline{|u(r+D_m,t)-u(r,t)|^2}=\beta(\epsilon D_m)^{2/3} \quad (8)$$

Thus, inserting (6) and (7) in (5) the expression becomes

$$P_B(D_m) = \exp\left(-\frac{c_1\gamma}{\rho_d\epsilon^{2/3}D_m^{5/3}}\right) \tag{9}$$

in which c_1 is a parameter. The breakage time was estimated by assuming the eventual centers of mass of the daughter drops behave like two turbulent eddies. If AB is the initial separation distance, the separation distance $AB\prime$ of the two masses at time t are given as

$$[AB\prime(t)]^2 \propto (AB\ \epsilon)^{2/3}t^2 \tag{10}$$

Further, if both AB and the distance at breakage are proportional to the mother drop diameter, the equation can be solved for t_B as

$$t_B(D_m) = c_2 D_m^{2/3}\epsilon^{-1/3} \tag{11}$$

in which c_2 is a parameter. Finally, the breakage frequency was determined from (4) by combining expressions for the breakage time, (11), and the fraction of drops breaking, (9)

$$b(D_m) = c_2^{-1}D_m^{-2/3}\epsilon^{1/3}\exp\left(-\frac{c_1\gamma}{\rho_d\epsilon^{2/3}D_m^{5/3}}\right) \tag{12}$$

In the source term, (3), two additional functions are required; the average number of daughters, ν, and the daughter size distribution function, $P_{DSD}(D_m, D_d)$. As aforementioned, binary breakage is assumed, thus the average number of daughters are known. Further, the daughter size distribution function is assumed to fit a normal distribution in which the variance is set so that $> 99.6\%$of droplets formed lie in the volume range 0 to D_m. The resulting normal distribution has a maximum for equal sized daughter drops and a low probability for a significant size difference. In terms of diameter the expression becomes (Solsvik et al., 2013)

$$P_{DSD}(D_m, D_d) = \frac{2.4}{D_m^3}\exp\left(-\frac{4.5\left(2D_d^3 - D_m^3\right)^2}{D_m^6}\right)3D_d^2 \tag{13}$$

While in terms of volume, the expression becomes (Coulaloglou and Tavlarides, 1977)

$$P_{DSD}(V_m, V_d) = \frac{2.4}{V_m}\exp\left(-\frac{4.5(2V_d - V_m)^2}{V_m^2}\right) \tag{14}$$

2.2. Martinez-Bazan et al.

The Martínez-Bazán et al. (1999a,b) breakage frequency model represents a novel attempt to represent the fluid particle-turbulence interaction in terms of the directly measurable turbulent stress quantity, i.e. the second order structure function. Most of the predecessor breakage frequency models rely on the more abstract drop-eddy collision or interactions frequencies which are difficult to validate due to the vague definition of the eddy concept. The MB model avoids the eddy concept. Thus, the model may be considered more fundamental in nature. In developing their model, Martínez-Bazán et al. (1999a,b) assumed that a bubble deforms and breaks if the turbulent stresses of the surrounding fluid flow is sufficiently large. That is, this stress, σ_t, has to be at least larger than the bubble surface restoring stress, σ_s. They assumed locally isotropic turbulence, that the bubble diameter falls within the inertial subrange of turbulence, and binary breakage. As such, the model shares similarities with the model of Coulaloglou and Tavlarides (1977). The breakage frequency is given as

$$b(D_m) \propto \frac{1}{t_B(D_m)} \tag{15}$$

that is, compared to Coulaloglou and Tavlarides (1977), the breakage frequency is purely determined from the inverse of an expression for breakage time. This breakage time is defined as

$$t_B(D_m) \propto \frac{D_m}{u_B} \tag{16}$$

in which D_m is the bubble size and u_B is a characteristic breakup velocity. This velocity is assumed proportional to the square root of the difference between the turbulent stress, σ_t and the bubble surface restoring stress σ_s as

$$u_B \propto \sqrt{\sigma_t - \sigma_s} \tag{17}$$

in which σ_t is found as

$$\sigma_t = 1/2\rho_c\overline{\delta u^2}(D_m) = 1/2\rho_c\beta(\epsilon D_m)^{2/3} \tag{18}$$

where ρ_c is the density of the continuous phase. Further, σ_s is found as

$$\sigma_s = \frac{6E_s(D_m)}{\pi D_m^3} = 6\frac{\gamma}{D_m} \tag{19}$$

where $E_s(D_m)$ is the surface energy defined as $E_c(D_m) = \pi\gamma D_m^2$. Thus, the expression for the breakage time becomes:

$$t_B(D_m) \propto \frac{D_m}{\sqrt{\beta(\epsilon D_m)^{2/3} - 12\gamma/(\rho_c D_m)}} \tag{20}$$

and finally the expression for breakage frequency becomes:

$$b(D_m) = c_3\frac{\sqrt{\beta(\epsilon D_m)^{2/3} - 12\gamma/(\rho_c D_m)}}{D_m} \tag{21}$$

In the event that the bubble surface restoring stress, σ_s, is larger or equal to the turbulent stress, σ_t, breakup is assumed not to occur and the breakage frequency is set to zero. Thus, for a given system there is a critical diameter, D_c, where the bubble surface stress is equal to the turbulent stress. From (18) and (19)

$$D_c = \left(\frac{12\gamma}{\beta\rho_c}\right)^{3/5}\epsilon^{-2/5} \tag{22}$$

Due to the assumption of binary breakage the only remaining expression required in (3) is the daughter size distribution function, P_{DSD}. Martínez-Bazán et al. (1999a,b) postulated that the probability of forming two bubbles of diameter $D_{d,1}$ and $D_{d,2}$ is weighted by the product of the surplus stress associated with the diameters $D_{d,1}$ and $D_{d,2}$, defined as

$$\Delta\sigma(D_{d,n}) = \frac{1}{2}\rho_c\beta(\epsilon D_{d,n})^{2/3} - 6\gamma/D_m \tag{23}$$

in which n is either 1 or 2 and D_m is the diameter of the mother bubble. If a bubble of diameter $D_{d,1}$ is formed, the diameter of the second bubble is given from volume conservation. The original daughter size distribution function was not volume conserving, thus it was later updated by Martínez-Bazán et al. (2010). Written in dimensionless form, such that $P^*_{DSD}(1, D^*)\cdot D_m = P_{DSD}(D_m, D_d)$, the updated daughter size distribution function is given as

$$P^*_{DSD}(1, D^*) = \frac{D^{*2}\left[D^{*2/3} - \Lambda^{5/3}\right]\left[\left(1 - D^{*3}\right)^{2/9} - \Lambda^{5/3}\right]}{\int_{D^*_{min}}^{D^*_{max}} D^{*2}\left[D^{*2/3} - \Lambda^{5/3}\right]\left[\left(1 - D^{*3}\right)^{2/9} - \Lambda^{5/3}\right]dD^*} \tag{24}$$

in which $D^* = D_d/D_m$and $\Lambda = D_c/D_m$. The minimum diameter, D_{min}, is the smallest diameter of a daughter bubble for which the turbulent stress is equal to the restoring surface pressure, i.e. $\sigma_t(D_{min}) = \sigma_s(D_{min})$. The maximum diameter, D_{max}, is the complimentary diameter that conserves the mass of the mother bubble. From this, the dimensionless quantities are obtained as $D^*_{max} = D_{max}/D_m$ and $D^*_{min} = D_{min}/D_m$. The resulting daughter size distribution function behave similarly to the model of Coulaloglou and

Tavlarides (1977) in which equal sizes daughters are the most likely outcome of a breakage event.

The model of Martínez-Bazán et al. (1999a,b, 2010) were originally designed considering very high Reynolds number flows, thus breakage was frequent and $P_B(D_m) \sim 1$. Solsvik et al. (2017) suggested to add a breakage probability to the breakage frequency, analogous to the model of Coulaloglou and Tavlarides (1977), in order to expand the model to be valid also for lower Reynolds number flows. The breakage probability was defined as a shifted version of (5):

$$P_B(D_m) = \exp\left(-\frac{E_c(D_m - D_c)}{E(D_m - D_c)}\right) \tag{25}$$

in which E_c and E are defined by (6) and (7), respectively. For bubbles smaller than the critical diameter D_c, the breakage probability was set to zero.

The model of Martínez-Bazán et al. (1999a,b, 2010) was originally designed considering a gas–liquid system. Later, Eastwood et al. (2004) investigated liquid–liquid breakage in the same experimental setup. They found that the breakage frequency was underpredicted for fluid particles with non-negligible density and viscosity at low Weber numbers. However, model adaptions, e.g. Revuelta et al. (2006) and Solsvik et al. (2013), have been found to provide good agreement with data from liquid–liquid experiments. Some examples can be seen in the appendix of Solsvik et al. (2013).

2.3. Model constraints

In the models of Coulaloglou and Tavlarides (1977) and Martínez-Bazán et al. (1999a,b, 2010) the breakage frequency goes trough a maximum for increasing mother drop diameter. This behavior was criticized by for example Tsouris and Tavlarides (1994), who argued that the breakage frequency should increase monotonously. Later, experimental data have suggested that this maximum is possible, e.g. Maaß and Kraume (2012). Subsequently, the behavior of the breakage frequency is still a matter of debate. Further, both the model of Coulaloglou and Tavlarides (1977) and the model of Martínez-Bazán et al. (1999a,b, 2010) assume binary breakage. As this assumption is possibly erroneous, other authors have considered a different average number of daughters in their model derivations, e.g. Konno et al. (1983) and Han et al. (2011, 2013, 2015). Of particular interest is the framework proposed by Diemer and Olson (2002) which allows for any average number of daughters, also non-integers. The main drawbacks of the framework are the prediction of equal sized daughters, which might be erroneous, and the need for fitting of model parameters to the specific system in order to be volume and number conserving.

In the available frameworks, the average number of daughters, ν, needs to be known a priori in order to design the daughter size distribution function, P_{DSD}. The constraints on the daughter size distribution function must satisfy the normality or number conservation condition

$$\int_0^{D_m} P_{DSD}(D_m, D_d) dD_d = 1 \tag{26}$$

I.e. all daughters exists in the interval $[0, D_m]$. Further, the breakage yield redistribution function, $h(D_m, D_d) = \nu P_{DSD}(D_m, D_d)$, should be volume conserving;

$$\int_0^{D_m} D_d^3 h(D_m, D_d) dD_d = D_m^3 \tag{27}$$

which is mass conserving given constant density.

2.4. Other models

Several adaptations of the model of Coulaloglou and Tavlarides (1977)(e.g. Konno et al., 1983; Vankova et al., 2007; Maaß and Kraume, 2012) and the model of Martínez-Bazán et al. (1999a,b, 2010)(e.g. Håkansson et al., 2009; Solsvik et al., 2013) exist. While the models change parameters values, add some criteria for breakage or otherwise modify the originally proposed models, they do not change the concepts and breakage event definition. Thus, the experimental data needed for validation of the original models proposed by Coulaloglou and Tavlarides (1977) and Martínez-Bazán et al. (1999a,b, 2010) may also be used for validation of the adapted models.

Furthermore, another group of models within the PBM framework exists. Instead of (1), the PBM is formulated considering sections of the internal coordinate, in what is often referred to sectional models. Of particular relevance are the models proposed by Luo and Svendsen (1996) and Andersson and Andersson (2006b), and recently Xing et al. (2015) and Liao et al. (2018). Special care should be taken as to what framework the models are based on as the models are not directly interchangeable. While the models are possible to reformulate, the procedure is not trivial. Interested readers are referred to Lasheras et al. (2002), Mitre et al. (2010) or Solsvik et al. (2013). However, the if more fundamental form of the breakage frequency, b, average number of daughters, ν, and daughter size distribution P_{DSD} are investigated experimentally, the results can be used in validating models of both frameworks.

Reviews of most of the available breakage models have been published by Lasheras et al. (2002), Liao and Lucas (2009) and Solsvik et al. (2013).

2.5. Coulaloglou and Tavlarides in the entire range of the turbulence spectrum

Recently, some authors (e.g. Solsvik and Jakobsen, 2016a,b; Solsvik et al. 2017; Karimi and Andersson, 2018, 2019) have presented methods to expand several models from only considering the inertial subrange of turbulence, into considering the entire range of the turbulence spectrum. This change in modeling of turbulent stress is of critical importance when comparing model results with experimental data, in particular when the droplet size falls outside of the inertial subrange of turbulence.

Solsvik and Jakobsen (2016a) showed that the model of Coulaloglou and Tavlarides (1977) could be expanded to consider the full range of turbulence. First, they recognized that the expression for breakage time, (11), could be written as

$$t_B(D_m) = c_4 \frac{D_m}{\sqrt{\overline{\delta u^2}(D_m)}} \tag{28}$$

Thus, the breakage time depends on the expression for the second order longitudinal structure function. The expression for breakage probability, (9), already depend on the second order longitudinal structure function through (7). Similarly, the resulting expression for breakage probability becomes

$$P_B(D_m) = \exp\left(-\frac{c_5 \gamma}{\rho_d D_m \overline{\delta u^2}(D_m)}\right) \tag{29}$$

Thus, the expressions for breakage time and breakage probability, and subsequently the breakage frequency, can be expanded to be valid for the entire range of turbulence if the expression for the second order longitudinal structure function is valid in the entire range of turbulence. Such an expression can be given as, Solsvik and Jakobsen (2016b),

$$\overline{\delta u^2}(D_m) = \frac{4}{3}k\left(\frac{D_m^2}{r_d^2 + D_m^2}\right)^{2/3} \cdot (1 - [T_1(D_m) + T_2(T_3(D_m)T_4(D_m) - T_5(D_m))]) \quad (30)$$

where k is the TKE and r_d is given by

$$r_d = (15\beta)^{3/4}\eta \quad (31)$$

where β is the Kolmogorov constant and $\eta = (\nu/\epsilon)^{1/4}$ is the Kolmogorov micro scale, in which ν is the kinematic viscosity. The different T_n expressions are given as:

$$T_1(D_m) = \frac{2}{[s(D_m)]^2} F\left(\left(-\frac{1}{3}\right)^{\frac{1}{2}}, \left(\frac{3}{2}\right) \middle| \frac{[s(D_m)]^2}{4}\right) \quad (32)$$

$$T_2 = 3^{3/2}\Gamma\left(\frac{2}{3}\right) \quad (33)$$

$$T_3(D_m) = 27 \cdot 2^{1/3}[s(D_m)]^{2/3}\Gamma\left(\frac{2}{3}\right) \quad (34)$$

$$T_4(D_m) = \frac{1}{352\pi} F\left(\left(\frac{7}{3}\right)^{\frac{11}{6}}, \left(\frac{17}{6}\right) \middle| \frac{[s(D_m)]^2}{4}\right) \quad (35)$$

$$T_5(D_m) = \frac{2^{2/3}}{2\pi[s(D_m)]^{2/3}} K_{\frac{2}{3}}(s(D_m)) \quad (36)$$

in which F is the hypergeometric function, K is the Bessel function and Γ is the gamma function. Further,

$$s(D_m) = D_m / \left(c_L^{-1/2} L\right) \quad (37)$$

where c_L is a model parameter value which can be estimated from, Solsvik (2017),

$$c_L(\mathrm{Re}_\lambda) = \exp\left[-\frac{4.478 + 18.362\beta}{\mathrm{Re}_\lambda^{1.075 - 0.070\beta}}\right] - 1.913 + 2.169\beta \quad (38)$$

Finally, $L = \frac{k^{3/2}}{\epsilon}$ is the integral length scale and Re_λ is the Taylor scale Reynolds number given as;

$$\mathrm{Re}_\lambda = \sqrt{\frac{20}{3}\frac{k^2}{\epsilon\nu}} \quad (39)$$

3. Experimental setup and procedure

An experimental facility has been constructed to investigate turbulent breakage of oil droplets in water, as previously described in La Forgia et al. (2018) and Herøet al. (2019). The facility is constructed as a loop, as can be seen from Fig. 2. A pump (numbered 2 in the sketch) is placed downstream from a water tank (1) and upstream of a droplet generation section 4. In the droplet generation section, a single oil droplet can be produced, which travels downstream into the main test section (7), or breakage section. In the end, the water and oil drop return to the tank, which also serves as a gravity separator.

The breakage section consists of a square vertical channel in which droplets may be observed by two cameras (6). To facilitate this observation, the channel consists of two glass walls. The two remaining walls have periodic rods in order to increase the turbulence level. The channel itself is 1 m long and has a cross-sectional area of 30 mm x 30 mm. The rods have a cross-sectional area of 3 mm x 3 mm and are placed every 10 mm in the channel. The resulting flow pattern and turbulence level has been investigated using laser doppler velocimetry in La Forgia et al. (2018). In the droplet generation section, downstream of the breakage section, single spherical 1-octanol (Sigma–Aldrich, product number 472328) droplets are generated from a glass cannula connected to a syringe pump (5) of the type KDS Legato 180. The oil is dyed with Sudan Black B (RAL Diagnostics) and the resulting properties are density $\rho = 825$ kg/m^3, dynamic viscosity $\mu = 9.09 \cdot 10^{-3}$ kg/(m s) and interfacial tension $\gamma = 8.20$mN/m. The continuous phase is clean reverse-osmosis water, where the water pump of type MDL-0670 from SPX Flow Technology provides an area average velocity of 1 m/s.

The two cameras are of the type Photron FASTCAM Mini AX100 540 K M3, which have a maximum resolution of 1024 x 1024, which is only fully used in one direction. The two cameras record from 40 mm to 400 mm above the channel entry for a total section length of 360 mm, i.e. the full channel length is not recorded. Further, the two cameras are connected and synchronized in time. The resulting images are overlapping in a small area and semi-automatically converted to one image through MATLAB. The resolution gives the pixel size as 0.175 mm by 0.175 mm, thus a drop at 1 mm diameter has almost 6 pixels covering its diameter. Moving with a speed of 1 m/s, the centroid of a drop moves 0.25 mm, or ~ 1.4 pixel side lengths, between two frames. The cameras records at 4000 frames per second and this high framerate is beneficial on several accounts. Firstly, the accuracy of the determined breakage times is dependent on the frame rate. Secondly, the average number of daughters and the daughter size distribution in the initial breakage definition can only be accurately determined at high framerates. Solsvik et al. (2016a) showed that the number of daughters in the initial breakage definition was tending towards two for increasing framerate. However, their setup did not allow for more than 1450 frames per second, which was not enough to discern exactly two daughters per breakage. Finally, post processing the images automatically is simpler when the drops travel a short distance between the frames. There is often a trade-off between the resolution selected and the framerate of the camera. In the current study, the framerate at maximum resolution was considered sufficient for the accuracy required. At this framerate, the initial breakage definition always results in two daughters. Thus, the tradeoff between framerate and resolution has not been further analyzed.

Three LED lamps, of the type Multiled LT-V9-15 by GS Vitec, provide the illumination required. The lamps are run continuously, i.e. not synchronized with the cameras. The light is diffused by opaque paper in order to obtain a more even light distribution.

The size of the droplet generated in the generation section is dependent on cannula tip surface area and the continuous flow past the cannula tip. Due to fluctuations in the latter, the droplets are generated with some variation in their size. Such behavior has previously been reported in comparable setups, e.g. Galinat et al. (2005) and Maaß et al. (2009). Due to this fluctuation in size, it was in the present work necessary to divide the experimental data into four size groups based on the mother drop diameter after the experiments have been performed. In this way, the impact of mother drop size on breakage time, t_B, breakage probability, P_B, average number of daughters, ν, and the daughter size distribution P_{DSD}, can be investigated. As such, the standard deviation is not as much an error as it is a measurement of how similar the grouped drops are. As the smallest drop sizes are most difficult to produce consistently, as well as the drops that have the lowest breakage probability, this group is made with the largest size range. The resulting mean diameter and number of events of each group can be seen in Table 3. As the number of breakage events are different in each mother drop size group, the impact of this number on the statistical precision can be investigated. Furthermore, the number of breakage events are comparable to the studies discussed in Section 1.

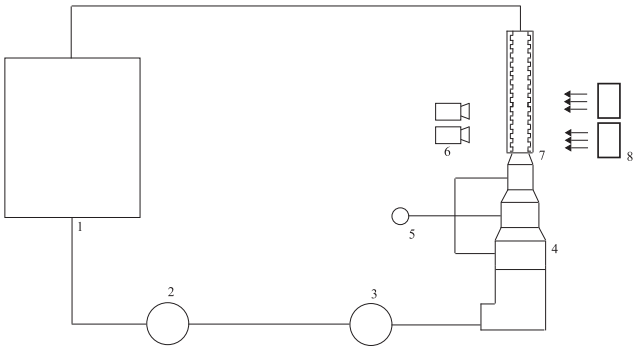

Fig. 2. Schematic drawing of the experimental setup. 1. Water tank and phase separator, 2. water pump, 3. flow meter, 4. droplet generation section, 5. oil syringe pump, 6. two cameras, 7. breakage section, 8. illumination.

All events are interpreted through both initial breakage definition and cascade breakage definition, as outlined in the following Sections 3.1 and 3.2. Thus, two sets of interpreted data are produced from the same experimental raw data. In order to discriminate between breakup in the center of the channel and the high shear region near the walls, a region of wall breakage is defined as drops breaking with their centroid within a horizontal distance of 1.5 mm from the tip of a rod. The value of 1.5 mm is an estimation based on two criteria. Mainly, a distance of 1.5 mm is 5% of the channel width. Thus, the two regions, one on each side of the channel, cover a total of 10% of the channel. Additionally, a spherical drop with its centroid at the 1.5 mm line would not touch the baffle, unless the drop is 3 mm or larger in diameter. Drops of this size is much larger than the biggest drops considered in this study. The breakage events in this region are not included in the data, as the number of events were too few and the impact of shear forces on the breakage events cannot be discerned from that of the turbulence level. When interpreting an event through the cascade breakage definition some daughter drops may enter the wall breakage region. In this case, any proceeding breakups of this particular daughter are not considered to be part of the breakage event. The event is otherwise interpreted following the proposed procedure. Similarly, when a deformed daughter drop leave the field of view, the breakage event is assumed to have ended for this daughter.

3.1. Image analysis

The procedure for extracting data from high speed videos have been described in detail by Herøet al. (2019). In this work, the procedure is employed with a minor modification in the determination of daughter drop sizes. This difference is described and discussed further in Section 4.9, in which a short discussion on the determination of the breakage event start is included. The procedure may be outlined as follows. Each frame of the high speed video is subtracted an image in which there is no drop and the resulting image is converted to a binary image by a gray-level threshold. From the pixels of the binary image, the position, sizes and number of drops in each image can be found. The procedure is implemented and performed in MATLAB, requiring substantial manual input.

The image analysis considers both the initial breakage definition and the cascade breakage definition. First, the start and end instances of the breakage event must be determined;

- Breakage event start is when a spherical mother drop starts to deform, and this deformation process is directly related to a fragmentation of the drop.
- Breakage event end for the initial breakage definition is when the mother drop fragments.
- Breakage event end for the cascade breakage definition is when the final intermediary daughter fragments.

When these two instances are known for a breakage event, the breakage time can be computed as the time period between them. The number of daughters and their sizes are found at the breakage end instance. The TDR level is assumed equal to that of the continuous phase. This TDR level has previously been determined by laser doppler velocimetry, see La Forgia et al. (2018), such that each position of the channel is associated with a local turbulence level. In the case of breakage, the TDR level is taken to be that of the position at breakage start. Thus, it is assumed that a single turbulent vortex-drop interaction is occurring at this position and time instance. For the cases where the drop did not break, the TDR level is taken as the maximum TDR level along the recorded drop path.

It is noted that, by the breakage event definitions applied in this study, the breakage end instance is not an equilibrium state. Both broken and unbroken drops may break, in new independent breakage events, after leaving the test section.

As an example of the breakage definitions applied, Fig. 3 shows an image sequence of a binary breakage, in which a mother drop is broken into two unequal sized drops. In this case the end criteria of the initial breakage definition and cascade breakage definitions coincide, and subsequently the determined breakage time, daughter number and daughter sizes are equal.

Table 3
Mother diameter with standard deviation and number of events investigated.

Mother diameter [mm]	Total number of events	Number of events with breakage
1.0 ± 0.2	284	35
1.48 ± 0.08	379	115
1.87 ± 0.05	148	53
2.23 ± 0.06	154	83

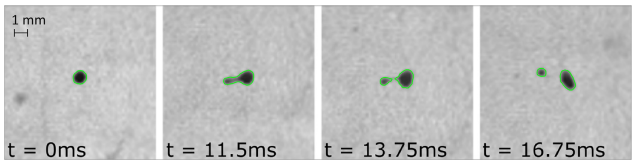

Fig. 3. Binary breakup resulting in two daughters of different size. The mother drop was 0.91 mm in diameter.

Conversely, Fig. 4 shows an example of a sequence of breakups. The initial mother drop is deformed with a long thin thread between two forming daughters, this thread later breaking up into several small daughters. In turn, as the two breakage event definitions differ in the interpretation of the end instance, the resulting breakage time, daughter number and daughter size distribution are different. It should be noted that the two definitions always coincide with regard to the breakage probability.

For completeness, Fig. 5 shows an equal sized breakage, which is a common outcome of the experiments. As above, the two breakage definitions differ in the interpretation of the end instance. In the interpretation according to the initial breakage definition, there are two near equal sized droplets. In the cascade breakage definition, there are still two near equal sized daughters, but also an additional small droplet.

3.2. Interpretation of image analysis data

After the individual videos have been analyzed, the breakage time, t_B, breakage probability, P_B, average number of daughters, ν, and the daughter size distribution P_{DSD} must be determined from the resulting set of data. In this study, these values are determined for each of the mother size groups seen in Table 3. The breakage time is found as the average value of all the drops breaking, while the breakage probability is determined from the fraction of drops breaking to the total number of drops in the mother size group, also those not breaking. Afterwards, the determined breakage time and breakage probability values are combined to the breakage frequency according to (4), i.e. the breakage frequency is not explicitly determined. The number of daughter particles are found as the average number of daughters that are produced from the breakage events of the corresponding mother drop size group. Thus, in this procedure, the breakage time, the breakage probability and the number of daughter particles are a single average value for each mother drop size group. The procedure of obtaining the daughter size distribution function from the experimental data set is not immediately obvious. The first step is to approximate the probability of a daughter appearing in a particular daughter size range with a width of ΔV_d;

$$\Delta P^*_{DSD}(V_m, V_d) = \frac{\text{Number of particles in range}[V_d - \Delta V_d/2,\ V_d + \Delta V_d/2]}{\text{Total number of particles in range}[0,\ V_m]} \tag{40}$$

Following this procedure, the discrete variable $\Delta P^*_{DSD}(V_m, V_d)$ should sum to one. In order to fulfill the constraints in Section 2.3, (40) must be divided by the daughter size range, ΔV_d to obtain another discrete function, $\Delta P\prime_{DSD}(V_m, V_d)$;

$$\Delta P\prime_{DSD}(V_m, V_d) = \Delta P^*_{DSD}(V_m, V_d) \cdot \frac{1}{\Delta V_d} \tag{41}$$

Finally, a continuous function should be fitted to the discrete $\Delta P\prime_{DSD}(V_m, V_d)$ values to obtain a continuous $P_{DSD}(V_m, V_d)$. It follows that to compare (40) directly with a P_{DSD}, e.g. a P_{DSD} computed from a model, the P_{DSD} must be multiplied by ΔV_d. Here, and for the rest of this work, the daughter size distribution is considered by volume instead of diameter for two reasons. Firstly, the shape of the daughter size distribution is in the literature generally discussed on volume form. Secondly, daughter size distributions by volume are significantly more intuitive. Two drops each at 50% of the volume of the mother drop, would correspond two drops both at $\sim 80\%$ of the diameter of the mother drop. If the daughter size distribution function is desired as a function of diameter, it may be obtained through the fundamental relation given by:

$$P_{DSD}(D_m, D_d)\, dD = P_{DSD}(V_m, V_d)\, dV \tag{42}$$

which is given in e.g. Martínez-Bazán et al. (2010).

3.3. Statistical data treatment

The state of the art single fluid particle experiments are relying on manual and often extremely time consuming approaches. Thus, the statistical treatment of the different parameters are of critical importance. Historically, statistic relevance are attributed experimental investigations with a high number of repetitions, e.g. Maaß and Kraume (2012). Obviously, larger data sets provides an increased precision in the estimates of the quantity investigated, yet this precision is seldom quantified. While the standard deviation provide much information of the nature of the experimental data, models and their validation rely on the statistical mean values. The true mean can be more accurately described by specifying a suitable confidence interval. Moreover, the statistical treatment of the data is seldom discussed in previous works, thus the interpretation of error bars and uncertainties are not clear.

In the following procedure, all of the parameters that the estimated quantities may depend on are assumed constant. The

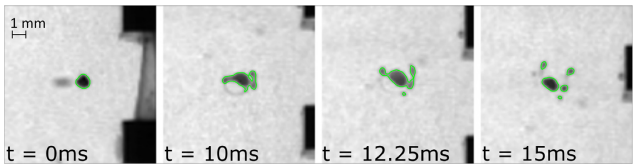

Fig. 4. Breakup resulting several daughters after cascading breakages. The mother drop was 0.89 mm in diameter.

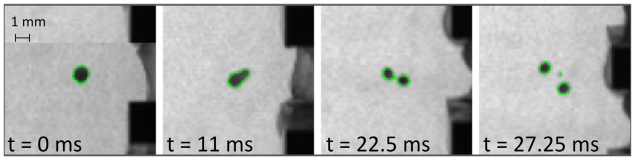

Fig. 5. Breakup sequence resulting two near equal sized daughters and a small drop. The mother drop was 0.99 mm in diameter.

mother drop size, the turbulence level, the interfacial tension, etc., are considered constant for each mother drop size group. The concepts applied can be found in text books on experimental statistics (e.g., Box et al., 2005; Wheeler and Ganji, 2010). Breakage time and the average number of daughter drops are average values, thus the mean, $\bar{x}$, and standard deviation, S, of the data sets may be calculated through the well known relations:

$$\bar{x} = \frac{\sum_{i=1}^{N} x_i}{N} \tag{43}$$

$$S = \left(\frac{\sum_{i=1}^{N} (x_i - \bar{x})^2}{N-1} \right)^{1/2} \tag{44}$$

in which x_i is the value determined in each individual experiment and N is the number of experiments with breakage events. The mean can be assumed to be randomly sampled and belong to a normal distribution of means. That is, the raw data itself may not be normally distributed, but the mean value is assumed to be normally distributed. If the standard deviation in the raw data, often denoted σ, is approximated as S, the standard deviation of the distribution of means are given by $\frac{S}{\sqrt{N}}$. Finally, the $1-\alpha$ confidence interval can be found as

$$\mu = \bar{x} \pm z_{\alpha/2} \frac{S}{\sqrt{N}} \tag{45}$$

In which μ is the true mean value and $z_{\alpha/2}$ is a constant denoting the size of the confidence interval. In a two sided 95%-confidence interval the value of $z_{\alpha/2}$ is $z_{2.5} = 1.96$. In other words, the 95% confidence interval limits, denoted ω, can be computed according to

$$\omega = \pm z_{2.5} \frac{S}{\sqrt{N}} \tag{46}$$

Breakage probability is a binomial distribution as each experiment is either breaking or not. The mean of a binomial distribution is $\mu = N\widehat{P}$ and the standard deviation is

$$\sigma = \sqrt{N\widehat{P}Q} \tag{47}$$

in which N is the number of experiments, including those without breakage events, $\widehat{P}$ is the true probability of breakage occurring and $Q = \widehat{P} - 1$ is the probability of no breakage. At large N and when $\widehat{P}$ is not near either of the extrema 0 or 1, the binomial distribution may be approximated by a normal distribution. Assuming that the calculated experimental probability P^* can be used as an estimate of the true probability $\widehat{P}$ in the standard deviation, the confidence interval of the true number of drops breaking, ΔN_B, can be given as

$$\Delta N_B = NP^* \pm z_{\alpha/2} \frac{\sqrt{NP^*(1-P^*)}}{\sqrt{N}} \tag{48}$$

which, divided by N yields the confidence interval of the breakage probability;

$$\widehat{P} = P^* \pm z_{\alpha/2} \frac{\sqrt{P^*(1-P^*)}}{N} \tag{49}$$

Thus, the probability estimate is computed as

$$P^* = \frac{\text{Number of favorable outcomes}}{\text{Total number of experiments}} \tag{50}$$

and the 95% confidence interval limits as

$$\omega_{P^*} = \pm z_{2.5} \frac{\sqrt{P^*(1-P^*)}}{N} \tag{51}$$

The estimated breakage frequency can be determined according to (4) by the use of the mean value for breakage time and the estimated breakage probability:

$$\bar{b} = \frac{1}{\bar{t}_B} P^* \tag{52}$$

Then, the 95% confidence interval limits can be determined from the confidence interval limits of both the breakage time and the breakage probability. Denoting the interval limits as ω, the expression becomes:

$$\frac{\omega_b}{\bar{b}} = \left[\left(\frac{\omega_{\bar{t}_B}}{\bar{t}_B} \right)^2 + \left(\frac{\omega_{P^*}}{P^*} \right)^2 \right]^{1/2} \tag{53}$$

Investigating the daughter size distribution function can be done in the same way as the breakage probability. If each daughter size range is considered individually, then the probability that a daughter will appear in the considered daughter size range is binomial. Thus, (50) and (51) can be applied to the results from (40). In this procedure, the sample size N is the number of observed daughters.

In summation, the average breakage time and average number of daughters are computed according to (43), while the standard deviation is computed according to (44). Finally, the confidence interval limits are computed according to (46). The breakage probability and the probability of a daughter appearing in each of the daughter size ranges are computed according to (50), with confidence intervals computed from (51).

4. Results and discussion

4.1. Turbulent quantities

As discussed in Section 3, each experimental run must be associated with the local TDR level in order to validate the model con-

Table 4
TDR level and standard deviation associated with the droplet size groups. The area average velocity of the continuous phase is 1 m/s.

Mother Drop Diameter [mm]	TDR [m^2/s^3]	TDR Breaking [m^2/s^3]	TDR Not Breaking [m^2/s^3]
1.0 ± 0.2	0.2 ± 0.1	0.19 ± 0.09	0.2 ± 0.1
1.48 ± 0.08	0.1 ± 0.1	0.14 ± 0.09	0.1 ± 0.1
1.87 ± 0.05	0.10 ± 0.07	0.09 ± 0.08	0.10 ± 0.07
2.23 ± 0.06	0.09 ± 0.08	0.06 ± 0.07	0.12 ± 0.09

Table 5
TKE level and standard deviation associated with the droplet size groups. The area average velocity of the continuous phase is 1 m/s.

Mother Drop Diameter [mm]	TKE [m^2/s^2]	TKE Breaking [m^2/s^2]	TKE Not Breaking [m^2/s^2]
1.0 ± 0.2	0.02 ± 0.01	0.024 ± 0.009	0.02 ± 0.01
1.48 ± 0.08	0.02 ± 0.01	0.02 ± 0.01	0.02 ± 0.01
1.87 ± 0.05	0.016 ± 0.007	0.015 ± 0.009	0.016 ± 0.008
2.23 ± 0.06	0.01 ± 0.01	0.010 ± 0.008	0.019 ± 0.01

Table 6
TDR level and TKE level, both with 95% confidence intervals. The area average velocity of the continuous phase is 1 m/s.

Mother Drop Diameter [mm]	TDR [m^2/s^3]	TKE [m^2/s^2]
1.0 ± 0.2	0.15 ± 0.03	0.022 ± 0.004
1.48 ± 0.08	0.13 ± 0.02	0.020 ± 0.002
1.87 ± 0.05	0.10 ± 0.02	0.016 ± 0.002
2.23 ± 0.06	0.09 ± 0.02	0.014 ± 0.002

cepts. With the continuous phase area average velocity of 1 m/s, the corresponding TDR characteristic for the mother drop diameter groups, as defined in Table 3, are given in Table 4. Table 4 classifies the TDR level into average of all events, the average of breakage events and the average of events where the drops are not breaking. It can be seen that, within each mother drop size group, the TDR level associated with the breaking drops are comparable to the TDR level associated with non-breaking. Thus, the average TDR level of all events within each mother drop size group are hereafter taken as representative values of the TDR level for the entire group. It should be noted that the largest mother size group has the largest difference in the associated TDR level with breaking and non-breaking drops. The TKE level, found through the same procedure as the TDR level, can be seen in Table 5.

When comparing with models the average turbulence characteristics of each group is of interest, which should be at the highest precision available. Thus, (46) have been employed on the TDR level and the TKE level to obtain the average values and confidence intervals shown in Table 6. While the experimental conditions are clearer shown in Table 4 and Table 5, the values shown in Table 6 are better suited for comparison with models. The increased precision allows to discriminate between the value of 0.15 or 0.2, etc., which lead to significantly different model results.

To investigate the turbulent stress, σ_t, compared to the surface restoring stress, σ_s, a Weber number, i.e. a dimensionless group, may be defined as;

$$\mathrm{We} = \frac{\sigma_t}{\sigma_s} \tag{54}$$

in which the turbulent stress may be approximated through the second order structure function, $\overline{\delta u^2}$, as:

$$\sigma_t \approx \rho_c \overline{\delta u^2}(D_m) \tag{55}$$

where ρ_c is the continuous phase density. In the inertial subrange of turbulence the second order structure function can be approximated through the relation:

$$\overline{\delta u^2}(D_m) \approx \beta(\epsilon D_m)^{2/3} \tag{56}$$

where $\beta = 2$. To account for the entire range of turbulence, the second order structure function may instead be approximated by the expression (30) presented in Section 2.5. Finally, the surface restoring stress can be defined as

$$\sigma_s = \gamma / D_m \tag{57}$$

where γ is the interfacial tension. The Weber numbers of each mother drop size group, as presented in Table 3, are shown in Table 7, which considers both the inertial range and the entire spectrum of turbulence. To compute the entire spectrum as described by Solsvik and Jakobsen (2016a) the TKE is needed, as shown in Table 6. As can be seen from Table 7, the two procedures for determining the turbulent stress results in relatively similar Weber numbers in the current setup. Thus, it is likely that the drop sizes are close to the inertial subrange of turbulence.

Considering that there are breakage events in each mother drop size group, see Table 3, it can be seen that there are breakages for Weber numbers below 1. Some models, like that of Martínez-Bazán et al. (1999a,b, 2010) in Section 2.2, predict no breakage in this case. Thus, it is not possible to compare the model prediction of the breakage time, t_B, the breakage probability, P_B, the average number of daughters, ν, and the daughter size distribution P_{DSD} with the experimental results. It is noted that the model of Martínez-Bazán et al. (1999a,b, 2010) is developed considering very high TDR levels, in the region of $100 - 3000$ m^2/s^3. Thus, it is not unexpected that the model does not accurately predict breakage behavior in the low turbulence level of this study. Nevertheless, the data presented in Table 7 show that breakage takes place also when $\mathrm{We} < 1$. Hence, a breakage model for these fluid and flow conditions should also predict this outcome.

It is noted that investigations of the Weber number should be considered an order of magnitude analysis and not an exact limit. I.e., at large Weber numbers breakage is likely to be prominent, while less common for low Weber numbers. It does not follow that no breakage occurs for $\mathrm{We} < 1$. This can be further illustrated by considering that the expressions for σ_t and σ_s given above are not universal. As an example, the expression for σ_s could have a prefactor of 1, 2, 4 or 6 depending on the derivation, see e.g. Solsvik et al. (2013).

The continuous phase turbulence characteristics are time averaged in this analysis. Thus, the real dynamic interaction between the drop and the turbulent vortex is lost. In transient flows, the TDR level and TKE level experience fluctuations that may be relatively large. In turn, the turbulence level causing breakup may be higher than the averaged values reported in this article. However, experimental investigations of the actual dynamic turbulence-droplet interactions are extremely challenging. An option may be to employ direct numerical simulations, as suggested by Andersson and Helmi (2014). Nevertheless, determining the breakage frequency, b, the average number of daughters, ν, and daughter size distribution, P_{DSD}, based on the local time average turbulence characteristics are certainly of value for development and validation of CFD-PBE simulations. Especially as commonly employed turbulence models, such as Reynolds Averaged Navier–Stokes models, determine time averaged turbulence characteristics. Even with the use of Unsteady Reynolds Averaged Navier–Stokes, the turbulence characteristics are averaged over some time period.

It is noted that the standard deviation within each group of turbulence level in Table 6 is large, thus uncertainty is introduced when employing the average value as the turbulence level. This uncertainty is likely also present in previous experimental studies, where the average TDR level of a finite volume is taken as the turbulence level of all experiments. It is further noted that some

Table 7
Turbulent Weber number associated with the droplet size groups.

Mother drop diameter [mm]	1.0	1.48	1.87	2.23
We - Inertial Range	0.34	0.60	0.75	0.93
We - Entire Spectrum	0.35	0.68	0.84	1.04

Table 8
Selected cascade breakage times taken from regressional fit of the data in Solsvik and Jakobsen (2015).

Mother drop diameter	1 mm	1.5 mm	2 mm
Petroleum	~ 10 ms	~ 20 ms	~ 35 ms
Octanol	~ 20 ms	~ 40 ms	~ 60 ms

authors, e.g. Foroushan and Jakobsen (2020), have investigated the breakage phenomenon through an instability analysis. That is, instead of considering a single turbulent vortex-droplet interaction, the breakage event is considered to be due to a series of interactions. While this treatment leads to an increased complexity, it might be the correct interpretation of the turbulence-droplet interaction. If that is the case, the determined turbulence characteristics in this study might not be sufficient to explain the relation between the turbulence level and the breakage phenomenon.

4.2. Breakage time

Only a limited number of experimental single droplet studies report breakage time, t_B, fewer yet investigate the impact of mother drop size, D_m. Currently, the effect of mother drop size on average breakage time is not sufficiently validated by single drop experiments. A selection of representative values from the study of Solsvik and Jakobsen (2015) are presented in Table 8. In their investigation of breakup in a stirred tank, they found that, for a given stirrer speed and oil, the breakage time is increasing with increasing mother drop size. This trend is consistent with the models presented in Section 2. On the other hand, when Maaß and Kraume (2012) investigated channel flow around a stirrer blade, they did not observe a clear trend. Some representative values from the latter study are given in Table 9. Interestingly, they found that the longest average breakage times were for the smallest drop sizes, contrary to the model concepts in Section 2 and to the results of Solsvik and Jakobsen (2015). Maaß and Kraume (2012) employed the initial breakage definition with a slight modification. In their procedure, the breakage event start instance was taken as the instance of the drop passing the stirrer blade. However, this instance does not necessarily correspond to the instance of the beginning of a breakage, see Section 3.1. Due to a recirculating flow pattern behind the stirrer blade, a drop could pass the stirrer blade and stay spherical, before breaking at a later time instance. Maaß and Kraume (2012) recognized the weakness themselves. Based on the interpreted videos, it was stated the phenomenon of recirculating drops was more frequent in experiments on the smallest drop sizes, which was given as the explanation for why the smallest drop sizes had the longest average breakage times. Maaß and Kraume (2012) claimed that the distribution of breakage time was a β-distribution. Thus, the problem of the average value being saturated by long breakage time was avoided by utilizing the peak of the β-distribution as the breakage time measurement. This breakage time estimate did follow the trend of increasing breakage time with increasing mother drop size. In summary, there is a general belief that, for a given system, an increase in mother drop size should increase the breakage time. As noted in Section 1, it is challenging with direct and quantitative comparison between different experimental studies due to differences in the experimental setup, such as flow condition, dispersed phase and breakage event definition.

In this study, the average breakage time of each mother drop group, see Table 3, has been determined for both the initial breakage definition and the cascade breakage definition. The results are shown in Fig. 6 and Fig. 7, respectively. As expected, due to the cascade breakage definition including the time after the initial breakage definition, the cascade breakage times are significantly longer than the initial breakage times.

By both the breakage event definitions, the average breakage time show a trend of increasing breakage time with increasing mother drop diameter. This is consistent with the cascade breakage results of Solsvik and Jakobsen (2015), although the breakage times of this study are longer. The difference in the determined breakage time may be dependent on mainly two factors. First, the discrepancy with the petroleum results may be partly due to different system properties when working with different oils. Secondly, Solsvik and Jakobsen (2015) used a stirrer with an volume average TDR level at 1 m^2/s^3, which is higher than the values seen in Table 6 by a factor of approximately 5 to 10. Additionally, the TDR level in the breakup region near the impeller blade is likely much higher than 1 m^2/s^3 (Solsvik and Jakobsen, 2015), as the TDR level is not uniform in the stirrer. Thus, some of the difference may be due to the turbulent intensity of the setup in this study being significantly lower than that of Solsvik and Jakobsen (2015). This may have an impact on the results, as it is likely that the breakage time decreases with increasing turbulence levels, as shown by e.g. Andersson and Andersson (2006a) and consistent with (11) and (20) of Section 2.

In order to compare the model of Coulaloglou and Tavlarides (1977) with the experimental results of this study, (11) is computed. First, the mother drop size and TDR level is taken from Table 6. Then, the parameter c_2 is fitted to a linear equation, with the constant term set to zero. The procedure is performed in MATLAB by using the fit function and the "poly1" method. This yields the value of c_2 as 1.54 when employing the initial breakage definition. This is close to the value determined by Maaß and Kraume (2012), who found the value of c_2 to be ~ 1.1. Their breakage definition was similar to the initial breakage definition. When employing the cascade breakage definition instead, the value of c_2 was found to be 2.39. Coulaloglou and Tavlarides (1977) found the original value of c_2 to be ~ 2.98, when comparing with data from dense dispersion experiments. As such, neither of the parameter values are very different from previously determined values.

Additionally, the data is compared to the Coulaloglou and Tavlarides model adaption of Solsvik and Jakobsen (2016a), which is valid for the entire range of turbulence. Fitting the parameter c_4 in (28) using the same procedure as described above, yields the values of c_4 as 2.30 and 3.57 for the initial and cascade breakage definitions, respectively. The value of c_4 is determined experimentally for the first time. However, Solsvik and Jakobsen (2016a) showed that the value of c_4 is not equal to the value of c_2, which is in line with the present results.

From the Fig. 6 it can be seen that the predictions of the model of Coulaloglou and Tavlarides (1977) and the model adaption of Solsvik and Jakobsen (2016a), plotted as triangles and circles respectively, are very similar. Additionally, the model predictions are in reasonable agreement with the experimentally determined initial breakage time. However, the predicted breakage time of the largest mother drop size group is significantly lower than the average value of the experimental results. While the predicted breakage time is within the standard deviation, it is outside the 95% confidence interval. This mother drop size group had a large difference in the turbulence level associated with breakage events and non breakage events. Thus, it is possible that the discrepancy between model prediction and experimental value of the largest

Table 9
Selected average breakage times from Maaß and Kraume (2012).

Mother drop diameter	0.65 mm	1.0 mm	2.0 mm	3.0 mm
Toluene	19.7 ms	12.4 ms	14.3 ms	16.1 ms
Mother drop diameter	0.535 mm	1.0 mm	1.9 mm	3.1 mm
Petroleum	34.0 ms	16.0 ms	13.9 ms	16.6 ms

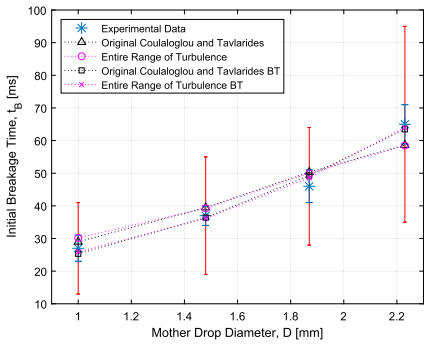

Fig. 6. Average breakage time considering the initial breakage definition plotted with 95%-confidence interval in blue and standard deviation in red. The confidence interval is computed according to (46). The model predictions are computed using (11) by Coulaloglou and Tavlarides (1977) and (28) by Solsvik and Jakobsen (2016a). BT denotes model predictions utilizing the turbulence associated with breakage events only.

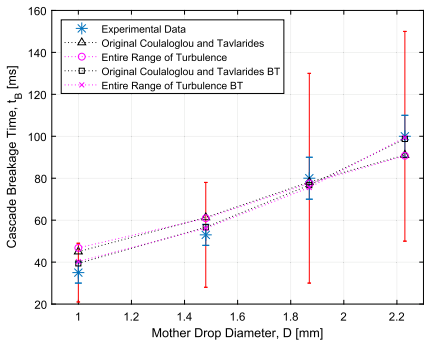

Fig. 7. Average breakage time considering the cascade breakage definition plotted with 95%-confidence interval in blue and standard deviation in red. The confidence interval is computed according to (46). The model predictions are computed using (11) by Coulaloglou and Tavlarides (1977) and (28) by Solsvik and Jakobsen (2016a). BT denotes model predictions utilizing the turbulence associated with breakage events only.

mother drop size group is partly due to the procedure employed when associating turbulence level with the mother drop size groups. In light of this, an additional model fitting is performed in which the turbulence level associated with breakage events only is employed, instead of the average turbulence level of all events. As such, different values for c_2 and c_4 are obtained. Considering the initial breakage definition values, the value of c_2 is found to be 1.46 and the value of c_4 is 2.15. The resulting model predictions are plotted as squares and exes in Fig. 6. As can be seen from the figure, this provides a much better fit to every point on the graph.

For the breakage time determined considering the cascade breakage definition, Fig. 7, the predictions of the model of Coulaloglou and Tavlarides (1977) and the model adaption of Solsvik and Jakobsen (2016a) are plotted as triangles and circles. It can be seen from the figure that the model predictions are similar to each other. However, the model predictions are in general less accurate than for the initial breakage time, as seen in Fig. 6. In the same procedure as above, the model parameters are fitted to the turbulence level associated with the breakage events only. The following model predictions are plotted as squares and exes. It can be seen from the figure, that these model predictions represent a better parameter estimation. In this procedure, the value of c_2 is determined to be 2.26 and the value of c_4 is found to be 3.35.

Unfortunately, it is not clear how the turbulence level associated with the breakage events only can be associated with the breakage probability. The determination of breakage probability requires consideration of both the events with breakage and the events in which breakage does not occur. While it is intuitive that the breakage time is dependent on the turbulence level causing breakage, a consistent model for the breakage frequency uses only one turbulence level, i.e. the same turbulence value for both breakage time and breakage probability. Thus, the turbulence level associated with the breakage events only is not further employed in this study. The good fit obtained when parameter fitting with this turbulence level may be an indication of a need for improvement of the procedure, which may warrant further study.

4.3. Breakage probability

The breakage probabilities determined from (50) are shown in Fig. 8, with the 95%-confidence interval included in red. The standard deviation from (47) is not shown, as the breakage probability is determined from the number of drops breaking divided by the number of experiments. Thus, the standard deviation does not provide additional insight into the probability investigated. As can be seen from Fig. 8, the breakage probability is increasing monotonously with droplet diameter. This general trend is in agreement with previous experimental investigations. Both Galinat et al. (2005, 2007), for an orifice flow, and Ashar et al. (2018), for a stirred tank, showed that there exists a critical Weber number below which there is no breakage and that the probability increases monotonously with increasing Weber number. In their experimental setups, increasing the Weber number translates to either increasing the diameter of the mother drop or increasing the average flow conditions, i.e. continuous phase volume flow or stirrer speed. Maaß and Kraume (2012) reported the same trend; for petroleum the breakage probability was ~ 0.55 and ~ 0.8 for mother drop diameter of 1 mm and 2 mm, respectively, while the breakage probabilities for toluene drops of the same size were ~ 0.6 and ~ 0.75.

The predicted breakage probability of the models of Coulaloglou and Tavlarides (1977), given by (9), and Solsvik and Jakobsen (2016a), given by (29), is also shown in Fig. 8. Following the same

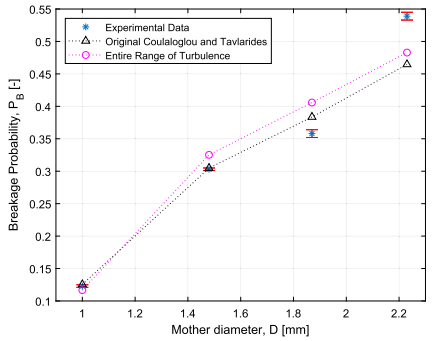

Fig. 8. Breakage probability plotted in blue. The 95%-confidence interval, computed according to (49), is plotted in red. The model predictions are computed using (9) by Coulaloglou and Tavlarides (1977) and (29) by Solsvik and Jakobsen (2016a).

procedure as in the previous section, the parameter c_1 is fitted in MATLAB, yielding the value 0.59. Previously, Maaß and Kraume (2012) found the value of c_1 to be 0.39, while Coulaloglou and Tavlarides (1977) found the value to be 0.106. The fitted value of c_5 in (29) is 1.25. The value of c_5 is determined experimentally for the first time. However, Solsvik and Jakobsen (2016a) showed that the value of c_5 is not equal to the value of c_1. It can be seen from Fig. 8 that the model predictions are reasonable for the two smallest mother drop sizes, but less accurate for the two largest ones. The reason for this behavior is not clear.

4.4. Breakage frequency function

Even though the breakage frequency, b, is what is used in modeling the breakage death and breakage birth terms of the PBE, the only single droplet study previously investigating this value is the study by Maaß and Kraume (2012). In general, their results suggests that when increasing the mother drop size, the breakage frequency trends to rapidly increase at first, before going through a maximum value and slowly decrease. This was assumed to happen under the same turbulence conditions. Some representative breakage frequency values from the study by Maaß and Kraume (2012) are $\sim 175\ s^{-1}$ and $\sim 75\ s^{-1}$ for toluene mother drop sizes of 1 mm and 2 mm, respectively, and for petroleum the breakage frequency was determined as $\sim 120\ s^{-1}$ and $\sim 80\ s^{-1}$.

The breakage frequency estimated in this study, computed using (52), can be seen in Fig. 9. Compared to that of Maaß and Kraume (2012), the breakage frequency is significantly lower. Which is expected, as the breakage time of this study is longer, Section 4.2, and the breakage probability is lower, Section 4.3. This can likely be attributed to the different flow conditions and fluid properties employed in this study.

From Fig. 9 it can also be seen that the breakage frequency based on the cascade breakage time is lower than the frequency based on the initial breakage time, which is due to the cascade breakage time by definition being larger than the initial breakage time. Furthermore, it appears that the breakage frequency is increasing at first, before it stabilizes or slightly declines, which in turn is a similar to the trend reported by Maaß and Kraume (2012). Considering the initial breakage definition, the experimental results are also in reasonable agreement with the model predictions of Coulaloglou and Tavlarides (1977) and the model predictions of Solsvik and Jakobsen (2016a).

Although the breakage time and breakage probability estimates of the largest mother drop size group was both predicted inaccurately, the breakage frequency of this size group is well predicted. Of course, this may be a coincidence. Nevertheless, the different experimental breakage frequency data are well predicted by the models. A possible reason for the high accuracy is the association of the local turbulence level with the breakage event instead of a volume average approach. From the data based on the local turbulence level approach, the disruptive turbulent force is accurately modeled and the resulting model prediction is close to the measured values. This result highlights the importance of associating the turbulence level with local values, even for a low gradient system as employed in this study.

4.5. Average number of daughters

Similarly to the breakage time, the average number of daughter drops produced from a breakage event, ν, is significantly dependent on the breakage definition employed. In the current study, the number of daughters for the initial breakage definition was always determined to be two. I.e. due to the high frame rate used in the experiments, it was always possible to identify a frame in which a drop was broken into two daughters, before possibly continuing the breakage process. Solsvik et al. (2016a) suggested that the number of daughters of the initial breakage would tend to two as the framerate increased, which appears to be supported by the data presented in this work.

In the cascade breakage definition the average number of daughters depend on the mother drop diameter, as seen in Fig. 10. Both the average number of daughters and the standard deviation is increasing with increasing mother drop diameter. Interestingly, the number is significantly larger than the binary outcome determined from the initial breakage definition, even for the smallest mother drop diameters. The trend of this study correspond to that of the previous investigations of Galinat et al. (2005, 2007) and Ashar et al. (2018). Even though these authors report significantly higher turbulence levels in their setups,

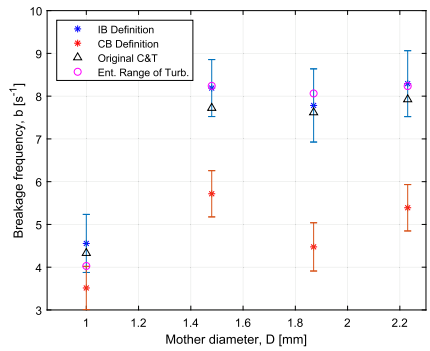

Fig. 9. Breakage frequency, computed using (52), plotted with an estimated 95%-confidence interval, computed using (53). "IB definition" and "CB definition" denotes the breakage frequency determined with breakage time from the initial breakage definition and the cascade breakage definition, respectively. The model predictions are computed using (12) by Coulaloglou and Tavlarides (1977), denoted as "Original C&T", and according to the procedure of Solsvik and Jakobsen (2016a), as presented in 2.5, denoted as "Ent. Range of Turb.".

Galinat et al. (2005, 2007) found the average number daughters to be ~ 3 to ~ 8 and Ashar et al. (2018) found it to be ~ 3 to ~ 7. Galinat et al. (2005) also reported a high standard deviation, which is increasing with increasing mother drop size.

In the models available in the literature, the average number of daughter drops produced upon breakage is a constant which must be given before any simulations are performed. While the binary breakage assumption appears to hold for the initial breakage framework, it does not hold for the cascade breakage framework. If the cascade breakage definition is advantageous in order to describe the breakage phenomenon, then the breakage models should determine the average number of daughters as a function dependent on the mother drop size, the local flow conditions and the system properties. Additionally, the models should be able to predict non-integer values for average number of daughters.

The underlying probability distribution of daughter numbers is of interest in order to elucidate the resulting average number of daughters and the high standard deviation. Fig. 11 shows the probability of daughter number for each mother drop diameter. For the smallest mother drop diameter binary, tertiary and quaternary breakage are the most frequent outcome and there are no events of seven or more daughters. As the mother drop increases, cases with higher number of daughters appear and the curve is flattened while binary and tertiary breakage are still the most common outcome of any breakage event. The same trends, i.e. distribution of daughter number dependent on mother drop size, are previously reported by Solsvik and Jakobsen (2015) and Solsvik et al. (2016a). In those studies, all but the smallest drop sizes have an even distribution in the range 2 to 11 daughter drops.

4.6. Daughter size distribution

In contrast to the breakage frequency and the daughter number, the daughter size distribution function is not only an average value, but a function for each mother drop size. The shape of the daughter size distribution is usually considered from a theoretical point of view with the assumption of binary breakage. Depending the strategy employed in model derivation, the daughter size distribution can be considered to have a variety of shapes. Considered on volume form, some of the common shapes include bell-, U-, bimodal- or uniformly-shaped. The discussion of the shape is significantly influenced by the binary breakage assumption and few alternative formulations exists. One alternative is the model by Diemer and Olson (2002), in which any average number of daughters is possible and the daughters are most likely to be near equal in size. Other models have been proposed by Han et al. (2011, 2013, 2015) and Solsvik et al. (2016b), in which the daughter number may be 2, 3 or 4. Also for these models, the daughters are most likely to be near equal in size.

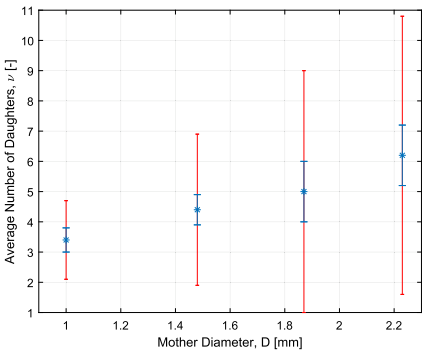

Fig. 10. Cascade breakage average number of daughters with a 95%-confidence interval in blue, computed using (46), and standard deviation in red.

As with the breakage time and average number of daughters, the choice of breakage definition greatly impacts the experimentally determined daughter size distribution. First, the initial breakage definition is considered, and the resulting daughter size distributions, calculated according to (40), is shown in Fig. 12. The smallest mother drop size group, Fig. 12a has the highest likelihood of equal breakage, but otherwise a near uniform distribution. Then the two middle size groups, Fig. 12b and c, have nearly uniform distributions. Finally, the largest mother drop size group, Fig. 12d, show that it is more likely with a small and a large drop, i.e. a U-shape. Generalized, the trend in the daughter size distribution, as the mother drop size increases, appears to be a uniform distribution with a weak preference of equal breakage, then a uniform distribution before eventually obtaining a relatively small preference for the U-shape. Also from the Fig. 12, it can be seen that for every mother drop size group there is no daughter size that is not apparent. The biggest difference is found for the U-shape of the largest mother drop size group, Fig. 12d, where the least common outcome is $\sim 6\%$ and the most common outcome is $\sim 19\%$.

The model predictions from (14) by Coulaloglou and Tavlarides (1977) are included in the Fig. 12 for completeness. According to the procedure in Section 3.2, the model predicted daughter size distribution function is computed from (41). The model framework assumes two daughters, which coincides with the experimental results. However, the assumption of equal sized breakage dominating is not accurate. While equal sized breakage obviously is present to obtain a uniform distribution, it is not more frequent than unequal sized breakage. As such, the model is not accurately predicting any of the experimentally determined distributions. The best fit is obtained for the shape of the smallest mother drop size group and becomes worse for increasing mother drop size. This behavior is expected based on the discussion above.

The resulting daughter size distributions of the cascade breakage definition, Fig. 13, are very different from the initial breakage definition. For each mother drop size group, there is a large probability of obtaining the smallest class of drops. This probability is the lowest for the smallest mother drop size group and increases as the mother drop size increases, which is also related to an increase in the average number of daughters. Such a large probability of small drops are previously not reported in literature(e.g. Galinat et al., 2005, 2007; Maaß et al., 2007). From the investigated videos, it appears that breaking drops often deforms into a dumbbell shape, with two soon-to-be daughter drops connected by a thin thread. As the breakup progresses, this results in two larger drops and a number of smaller drops originating from the thread. In some cases, the larger daughter drops undergo the process again, yielding even more small drops.

As for the initial breakage definition, the model predictions from (14) by Coulaloglou and Tavlarides (1977) are included in the Fig. 13. For the cascade breakage definition, the discrepancy between the assumed binary breakage of the model and the experimental data is large. As such, the model fails to predict the experimental data. This is due to the small size of many of the daughter drops, which is considered unlikely to be produced by the model prediction. Thus, a different breakage model is needed to determine the daughter size distribution function in the cascade breakage event definition. Currently, there are no existing models that predict multiple unequal sized breakage events. However, such a model is needed in order to predict the current experimental data.

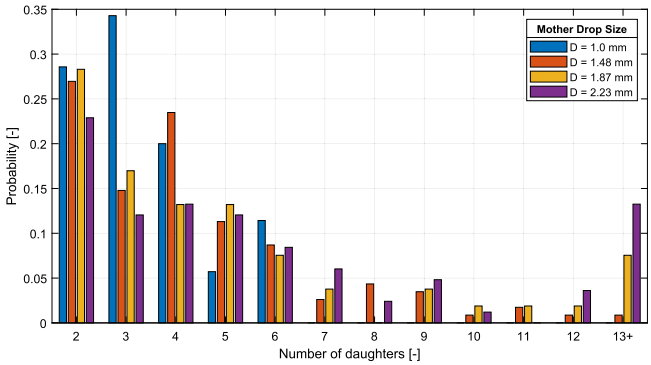

Fig. 11. Distribution of number of daughters in the cascade breakage definition.

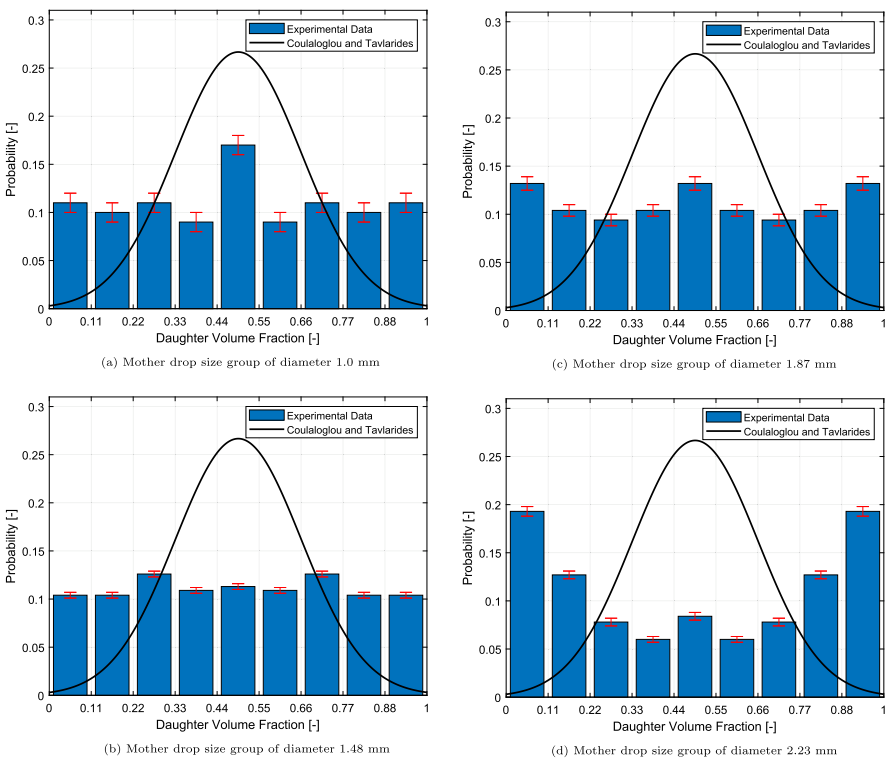

(a) Mother drop size group of diameter 1.0 mm

(c) Mother drop size group of diameter 1.87 mm

(b) Mother drop size group of diameter 1.48 mm

(d) Mother drop size group of diameter 2.23 mm

Fig. 12. Daughter size distributions, calculated according to (40) and utilizing the initial breakage definition. Confidence interval calculated from (51). The model predictions are computed from (14) by Coulaloglou and Tavlarides (1977), in accordance with (41).

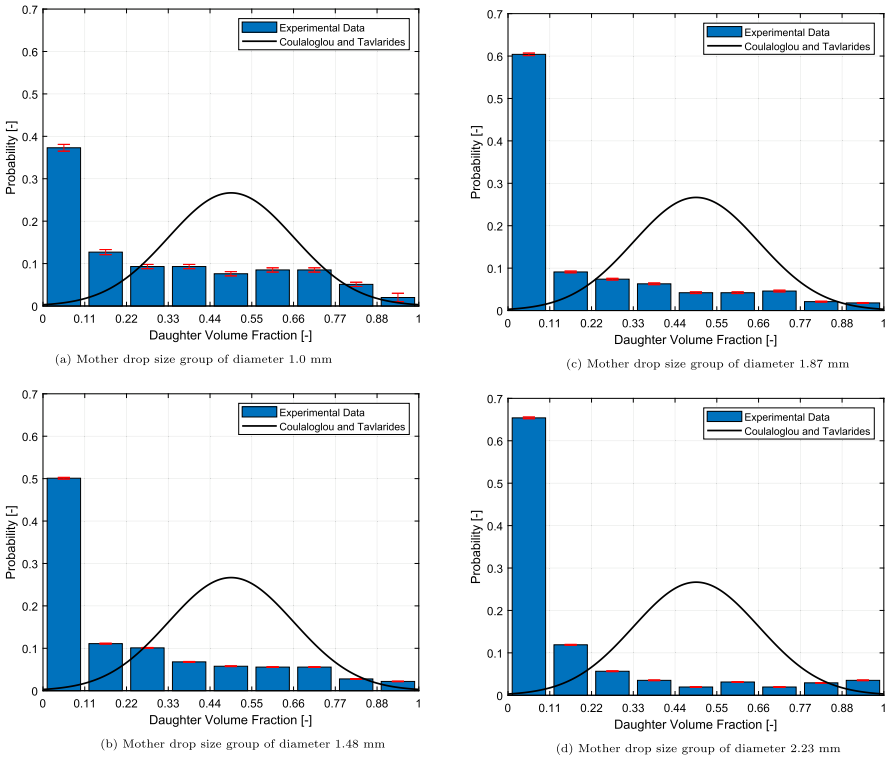

(a) Mother drop size group of diameter 1.0 mm

(c) Mother drop size group of diameter 1.87 mm

(b) Mother drop size group of diameter 1.48 mm

(d) Mother drop size group of diameter 2.23 mm

Fig. 13. Daughter size distributions, calculated according to (40) and utilizing the cascade breakage definition. Confidence interval calculated from (51). The model predictions are computed from (14) by Coulaloglou and Tavlarides (1977), in accordance with (41).

Neither the initial breakage definition, nor the cascade breakage definition has one general daughter size distribution curve valid for all of the mother drop size groups. Considering the cascade breakage definition the probability of the smallest drops is increasing significantly with increasing mother drop size. Which is obvious considering that the average number of daughters is increasing significantly, thus the number of smaller drops increase simultaneously. Contrary to these experimental data, breakage models give the shape of the daughter size distribution before any simulations are performed. However, the shape of the daughter size distribution is likely dependent on the mother drop size, the local flow conditions and the system properties. A predictive breakage model should account for these dependencies.

It is noted that the currently employed procedure for determining the daughter size distribution is different from previous investigations. Maaß et al. (2007) grouped the breakage events by the number of daughters produced upon breakage. As such, one daughter size distribution function is determined for binary breakage, one for tertiary breakage, and so on. Thus, Maaß et al. (2007) obtained unique daughter size distribution functions for each integer value of the average number of daughters. This approach could be used to validate models such as Han et al. (2011, 2013, 2015), where unique equal size daughter size distribution functions are available for the average number of daughters as 2, 3 or 4. However, for a given system, different daughter numbers and sizes may be the outcome of different breakage events, i.e. there is a presence of binary breakage, tertiary breakage, quartary breakage and so on, each with a different daughter size distribution. It is not clear how the different daughter size distribution functions of Maaß et al. (2007) should be combined to obtain the daughter size distribution function corresponding to the average number of daughters.

In the present study, all daughter drops produced from breakage events of the given mother drop size group is considered collectively, regardless of whether a given daughter originated from a binary breakage, tertiary breakage, etc. This results in one daughter size distribution per mother drop size group. As such, the presence of different outcomes of the breakage event is incorporated in the determined distribution function. The current procedure is similar to that of Galinat et al. (2005), although they did not use single droplet experiments for this determination.

4.7. Statistical treatment

The experimental data might be subject to a number of sources of error. This may include experimental lab procedure, data processing or assumptions, among others. Random errors contributes to the standard deviation in the experimental data and increases the size of the confidence interval. Systematic errors are present regardless of the individual experiment and usually considered not to be randomly applied. For example, if the thread of oil between two soon-to-be daughter drops is very thin, the thread might not be visible by the camera and the breakage assumed to have ended. Subsequently, some breakage times may be predicted to be shorter than the true value, but none are predicted to be longer. As such, it mostly impacts the determined mean value and not the standard deviation. If the impact of systematic errors is large enough, the true mean may fall outside the confidence interval from the statistical analysis. It follows that the employment of the statistical analysis is no guarantee that the true mean value is within the confidence interval. Furthermore, performing a very large number of experiments in order to obtain a small confidence interval is, in most experimental studies, not beneficial. At a certain number of experiments, the statistical precision is close to the total uncertainty arising from the experimental procedure, thus repeating the experiment under the same conditions, e.g. drop size, oil type and flow conditions, provides limited additional information. Instead, other aspects of the breakage phenomenon should be investigated.

Before investigating the determined statistical uncertainty, a short discussion on the uncertainties in the experimental procedure is required. While the models are defined as point values, the experimental data is taken from a volume. Ideally, the experimental data should be determined as representative for points, which would translate to a very small experimental volumes. This is practically impossible on several accounts. First, there are practical limitations. Due to fluctuations in the channel flow and in the droplet generation channel, the droplets will have an almost random horizontal motion. Thus, the droplets are traveling along different trajectories despite having nearly equal initial conditions. The amount of experiments needed to be able to validate every single point would be extremely large. This is even further complicated by the randomness of the turbulence level, which means that breakage can happen at different vertical positions, even for droplets transported along the same trajectory. Second, the association of each breakage with a single location is disputable, as each experimental breakage event clearly has a duration in which the droplet or droplets are transported. While it appears to be natural to associate the breakage with the position at the breakage event start instance, this is not determined from the PBE model framework considered. In summation, the procedure of considering a larger volume is a necessary simplification. It does, however, include some uncertainty which cannot be quantified.

4.7.1. Breakage time

From the figure showing the initial breakage time, Fig. 6, and the figure showing the cascade breakage time, Fig. 7, it can be seen that the standard deviation in breakage time for each mother drop size group is significant. This is expected, as each mother drop within each group might be slightly different in size, break in different positions, i.e. turbulence level, or experience different instantaneous turbulent conditions. On the other hand, the confidence intervals are fairly small. As the trends are similar for the initial breakage definition and the cascade breakage definition, only the cascade breakage definition will be considered in the following discussion. The standard deviation in the breakage time, as seen in Fig. 7, is $40\%, 47\%, 63\%$ and 50% when given in relative values. In contrast, the 95% confidence intervals are $14\%, 9\%, 13\%$ and 10%. Thus, the mean values are more precisely determined statistically, than what appears to be the case when only considering the standard deviation. Furthermore, it does not appear beneficial to determine the statistical uncertainty below $\sim 10-15\%$ with the current procedure, when considering the large variation in TDR level and the uncertainties discussed in the start of this section. As such, additional experiments under the same conditions are not required. This decision is also influenced by the feasibility of improving the confidence intervals.

From (46) it can be seen that the size of the confidence interval limits is dependent on the standard deviation and the number of experiments. When performing experiments, the standard deviation approaches a constant value. When this constant value is obtained, the confidence interval is only dependent on the factor $N^{-1/2}$, which has a diminishing effect on the confidence interval limits as N increases. For example, at $N = 30$, the value of $N^{-1/2}$ is ~ 0.18, while at $N = 40$, the value of $N^{-1/2}$ is ~ 0.16. Assuming that the standard deviation was constant at 30 experiments, the ten additional experiments from 30 to 40 experiments only shortened the confidence interval limits by $\sim 2\%$ of the value of the standard deviation. This is shown graphically in Fig. 14, which shows the mean value, standard deviation and confidence interval of the cascade breakage time plotted as a function of the number of experiments performed for the 1.48 mm mother drop size group. As can be seen from the figure, the mean value appears to be relatively stable after 20 experiments. However, it is possible to improve the standard deviation by performing approximately 10 additional experiments. From this point onward, the standard deviation is near constant. The confidence interval can still be improved with additional experiments, but this does have a diminishing effect per experiment performed, as explained above. The mean value does experience some oscillation after 20 experiments, but this is within even the final confidence interval limits.

4.7.2. Breakage probability

Breakage probability, Fig. 8, is the only function in the expression for breakage frequency that requires data of the drops not breaking. As such, the experimental value is determined from a larger set of data than e.g. breakage time. It is therefore expected that the confidence intervals for the breakage probability are smaller

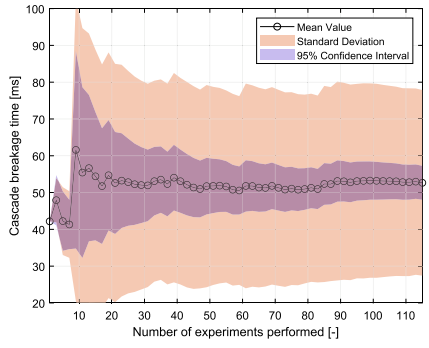

Fig. 14. Plot of the cascade breakage time of the 1.48 mm mother drop size group from Table 3. It shows the development in determined mean value, standard deviation and confidence interval of the cascade breakage time, by the number of experiments performed. The values are calculated for every two experiments from the first until the final 115.

than the confidence intervals for the breakage times, i.e. the breakage probability is more precise from a purely statistical point of view. The small confidence interval is a strong indication that the determined breakage probability is unlikely to change significantly if an increased number of experiments are performed.

4.7.3. Breakage frequency

The breakage frequency is not determined directly, rather it is determined from the breakage time and breakage probability. The same is true for the uncertainty in the breakage frequency. It is directly related to the uncertainty in the breakage time and breakage probability by (53). As such, it is not necessary with an additional discussion of the uncertainty in the breakage frequency when the uncertainty in both breakage time and breakage probability have been discussed extensively.

4.7.4. Average number of daughters

In the Fig. 10, showing the average number of daughters, there are sizeable standard deviations and subsequently large confidence intervals. Which, from Fig. 11 is reasonable, as there is a rather flat distribution for most of the mother drop sizes. The standard deviation in a flat distribution is always large. Thus, it follows that additional experiments are not likely to significantly improve the statistical precision of the average number of daughters. Instead, different aspects of the breakage phenomenon should be investigated.

4.7.5. Daughter size distribution

The daughter size distribution is a special case, as it is a distribution for each mother drop size group instead of an average value. Due to the presentation of the distribution in bins, as in Fig. 12 and in Fig. 13, there are two precisions to consider; the number of bins and the confidence interval of each bin. As such, when deciding whether to continue with the same experimental conditions or change, one must also consider whether the number of bins is sufficient. As for the breakage time, breakage probability and daughter number, the choice of precision must be weighted against the error sources in the experimental work.

In comparison to the initial breakage, the cascade breakage daughter sizes have increased precision due to the daughters often being observed in a near spherical shape, as the sequence of breakages normally has ended. For the cases where the cascade ends in many daughters, the determination of the size of the initial breakage daughters is very challenging, as the initial breakage daughters often are severely deformed in the few video frames they are visible. In short, in the current experimental procedure, the initial breakage definition is not optimal to determine the daughter size distribution when successive breakages are common. On the other hand, the procedure of scaled volume, as outlined in Section 4.9, is accurate if the initial breakage daughter drops of a single breakage can be assumed to deform in a similar manner. Unfortunately, based on the investigated videos, this is a course, and not quantified, assumption.

From the Fig. 13, showing the daughter size distribution when considering the cascade breakage definition, it can be seen that the confidence intervals are very small. With the nine bins used in this study, the statistical precision cannot be meaningfully improved by additional experiments. With this number of bins, near equal and equal size breakage end up in the same bin and the size of each bin is $\sim 11\%$ of the mother drop size, a reasonable precision considering the uncertainties and error sources discussed above.

4.8. Experimental setup design

A survey on the design process of the current experimental facility is included here to elucidate the main challenges in designing the facility. The facility was designed to obtain experimental data for increased physical understanding of the breakage process and validation of breakage models in the PBE framework. A systematic study of previous experimental facilities, both within droplet breakage experiments and homogeneous turbulence, was performed. Three main points were identified as critical in order to obtain the required quality and quantity of data.

1. Observation of the entire breakage event
   The entire breakup should be continuously observed for two reasons. First, this ensures that the breakage definitions are correctly applied. Second, the obtained experimental results cover all of the necessary data to validate the breakage time, t_B, the breakage probability, P_B, the average number of daughters, ν, and the daughter size distribution P_{DSD}. Thus ensuring a coherent dataset that may be used for validate breakage models.
2. Known local turbulence level
   From Section 2 it can be seen that the breakage models rely on the impact of the local turbulence level. Thus, in order to associate the breakages with a representative turbulence characteristic, the facility should have known local turbulence levels. Additionally, the accuracy of the determined turbulence level is increased with low gradients in the turbulence level. In an ideal facility for investigating turbulent breakage, the breakup would happen in homogeneous and isotropic turbulence. However, 3D isotropic turbulence is not experimentally feasible. In setups with 2D isotropic turbulence, e.g. after static mixer (Azizi and Al Taweel, 2011) or near oscillating grids (Shy et al., 1997; Yan et al., 2007), the turbulence level is rapidly decaying in the third direction. The setups also has high shear forces in the area generating the turbulence. In conclusion, it is challenging to inject a droplet into a region of sufficiently high turbulence level. As an added challenge, the facility would be challenging to automate.
3. Repeatable and reproducible
   In order to obtain enough data within a reasonable time, the experimental runs should be easily repeatable. Firstly, the facility operation should be automated. In order to obtain this automation, it is critical to ensure a reliable injection of dispersed phase drops. The criterion of repeatability also means that designs which require substantial cleaning between one or few experiments are disregarded. Likewise, designs in which the continuous phase cannot be reused, which will lead to a very large consumption of the continuous phase, are disregarded.

Considering only points 1 and 2 above, it would be beneficial to also observe the breakage in the third dimension. However, this is challenging due to increased complexity in the facility design, automation and image analysis. In turn, this significantly increases the time required to perform each experiment. However, it is noted that observation of all three dimensions has been performed, for gas bubbles in a stirred tank, by Krakau and Kraume (2019).

Some important lessons has been learned from the operation of the facility. First, the facility is designed as a loop with a 1000 liter tank functioning as both continuous phase storage and gravity separator, separating the small oil droplets from the water. While the separation works as intended, the inlet generated air bubbles. Despite the size of the tank, these bubbles reentered the loop and interfered with the image analysis. The situation was remedied by installing a partially holed plate near the inlet of the tank, which acts as a momentum breaker and redistributes the inlet flow over a larger area.

In order to create the continuous phase flow, the setup uses a positive displacement pump. This gives a reasonably stable mass flow, but also give rise to pressure fluctuations. These fluctuations manly interfere with the size of the injected droplets, giving rise to a fluctuation in the generated droplet size. The problem can be mitigated by geometric considerations in the design of the facility, as some flow patterns dampen pressure fluctuations. In this particular case, a sudden expansion of the cross sectional area was installed before the droplet generation section. Additional solutions include installation of a pressure dampener, although no commercial pressure dampeners are available at such low pressure levels. A simple solution is to implement a T-section which allows a volume of air to be compressed. Additionally, an adjustment that may mitigate pressure fluctuations is to implement a coiled tube in the loop. As the flow is going through the coil, the pressure fluctuations are dampened by the oscillation of the coil.

The droplet size is also influenced by the surface finish of the cannula tip area, where a courser surface finish yields a larger fluctuation in the droplet size generated. Due to this dependence on surface finish, less fluctuation in droplet size is experienced with regular cleaning of the cannula tip.

Finally, still water is an excellent breeding grounds of algae. In particular when high intensity light is present, as is the case in high speed imaging facilities. Thus, it is critical to have a procedure for easy cleaning of the setup, as well as easy exchanging of water. As algae settles on the walls, the ability to drain the experimental section of water is highly advantageous to avoid algae buildup on the wall during periods in which the facility is not in use.

4.9. Image analysis algorithm

As mentioned in Section 3.1, the procedure employed in this paper differentiate from the algorithm presented in Herø et al. (2019) on the determination of daughter drop sizes. Daughter drops are often recorded with irregular shapes. Thus, calculating the diameter from the projected area, assuming the drop to be spherical, and calculating the volume from this diameter can lead to a total volume which is larger than the volume of the original mother drop. In a few extreme cases, this estimated volume is 100% larger than the mother drop volume in the initial breakage definition, and 50% larger in the cascade breakage definition. In order to determine the daughter sizes, the daughter drops are associated with a fraction, which is subsequently associated to the mother drop size. In Herø et al. (2019), it was suggested obtain this fraction from the projected area of each daughter drop divided by the total projected area of daughter drops. In this work the daughter drop size is estimated by a volume fraction instead, as volume scales differently than area and it is the volume that is to be conserved. For each daughter drop, the projected area is assumed circular and a diameter is calculated, then this diameter is used to estimate the volume of the corresponding daughter drop, assuming it to be spherical. From this, the volume fraction of a particular daughter drop relative to all the daughter drops is found. Subsequently, the daughter drop volume is approximated as the same fraction of the mother drop volume.

The determination of the breakage event start instance is essentially an attempt to determine the instance of a single critical turbulent vortex-drop interaction, or the start of this interaction. The application of the described procedure is elucidated here in order to increase the readers understanding of the video interpretation process. The procedure is based on determining the start instance of the oscillation in the projected area, normal to the camera, that is related to the breakage event. In practice, the determination of the breakage event start is performed after the determination that a breakage event has taken place. From the instance of fragmentation, i.e. when two drops can be discerned, one can move backwards in time on the video until a near spherical drop is detected. In this procedure, oscillations denote changes to the projected drop area where the drop is significantly deformed from spherical, i.e. becoming ellipsoidal or irregularly shaped. Thus, very small perturbations of near spherical mothers are not considered. As an example, consider a low complexity breakage event in which a non-oscillating mother drop starts to deform and break. Such a breakage event can be seen in Fig. 15. The figure shows the mother drop projected area, normalized by the initial mother drop projected area, frame by frame leading up to a breakage of the drop. The arrow indicates the determined breakage event start instance. The small changes in projected area before the arrow are not considered to be related to the breakage event. These oscillations are assumed either to be due to very small perturbations in the projected area of the drop, artifacts from the image analysis or a combination of the two effects.

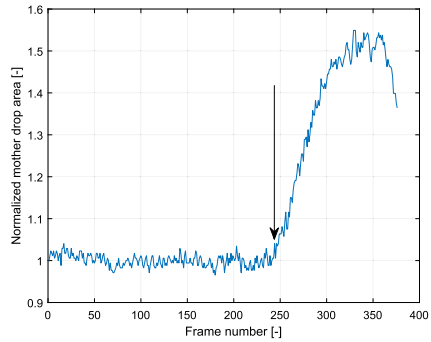

Fig. 15. A breakage event with only one oscillation before breakage. The arrow denotes the instance of the start of breakage. The mother drop area is normalized by the area of the mother drop in the first frame.

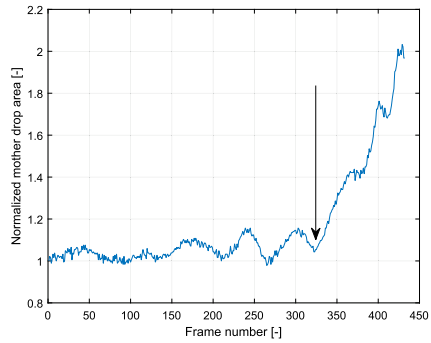

Fig. 16. A breakage event with several oscillations before breakage. The arrow denotes the instance of the start of breakage. The mother drop area is normalized by the area of the mother drop in the first frame.

However, in many breakage events, the mother drop is going through several smaller oscillations before undergoing a significantly larger deformation directly before breakage. Subsequently, the determination of the instance of one vortex-drop interaction

is less clear. Dampened oscillations are not considered part of the vortex-drop interaction, as the energy appears to be dissipated. Thus, another vortex-drop interaction is considered responsible for the breakage event. An example of such an event may be seen in Fig. 16. The first oscillations are seemingly dampened, hence they are considered unrelated to the breakage event, as the drop undergoes a significantly larger deformation during the breakage event. This large deformation is assumed to be due to a single vortex-droplet interaction, therefore the breakage event start instance is assumed to be at the instance before this deformation. In Fig. 16 this instance is indicated by the arrow. This breakage event start instance is also an instance of spherical mother drop, which ideally, but not always, has been spherical for several frames. It is noted that the drop in Fig. 16 is visibly oscillating from around frame 150 until the breakage event takes place.

5. Conclusions

Single octanol drop breakage experiments in turbulent flow have been performed. The droplets were inserted into a channel flow and the following breakage events were captured by high speed cameras. The videos obtained were interpreted by adopting both the initial breakage definition and cascade breakage definition. Furthermore, the design of the channel allows for breakage events to occur in a turbulent flow with low gradients.

The impact of mother drop size on the breakage phenomenon were investigated. While the flow considered is characterized by a level of turbulence that is lower than for comparable breakage investigations previously reported in literature, the results show similar trends. With a specified constant flow rate in the channel, an increase in mother drop size induces an increase in breakage time and breakage probability. Considering the initial breakage definition, the number of daughter drops was always two and the daughter size distribution was close to uniform. However, when considering the cascade breakage definition, the number of daughters increased with increasing mother drop size. The corresponding daughter size distributions had a large probability of very small drops which only increase with increased number of daughters. Due to the various shapes of the daughter size distribution for the different mother drop size groups, breakage models should determine the shape of the daughter size distribution dependent on the mother drop size, the local flow conditions and the system properties. For the cascade breakage definition, also the average number of daughters should be determined in this way.

A statistical analysis have been employed in order to quantify the quality of the data and to address the requirement of statistically valid data. In particular, the analysis show that adequate statistical precision could be obtained, in this study, with as few as 35 to 50 breakage events. Due to the uncertainties inherent in the experimental procedure, further increasing the statistical precision, i.e. increase the number of investigated events, is not cost effective. Instead, investigations should focus on obtaining data with different system properties or, if possible, increase the accuracy and precision of the experimental procedure. Furthermore, the statistical analysis show that, for this study, the breakage probability is determined with lower uncertainty than the breakage time, while the average number of daughters is less precise than the daughter size distribution functions.

Each breakage event is associated with a local turbulence level. As data from different experiments are combined in order to obtain the average breakage time, the breakage probability, the average number of daughter and the daughter size distributions, the resulting average turbulence level is relevant to the events considered. Furthermore, the turbulence level has a quantified standard deviation that can be used to describe the uncertainty of the procedure.

In general, more single drop breakage data from experiments is still needed to elucidate the breakage phenomenon. In the experimental facility, different fluid and system properties might be investigated. For example, investigating different continuous flow velocities, i.e. turbulence level, or different oils. In addition, efforts should be made into determining whether the initial breakage definition or the cascade breakage definition best describes the breakage phenomenon. Finally, the data should be used for discriminating between breakage models.

Each mother drop size group has a different turbulent kinetic energy dissipation rate levels associated with it, and the difference in turbulence level between two events can be large. This may have an impact on the results and subsequently the investigated trends. Thus, the impact of mother drop size might warrant further study. Possibly, the problem could be mitigated by investigating a smaller volume, such that the breakages happen under less varying conditions. However, decreasing the volume would lead to an increase in the needed number of experiments, as each volume would need enough data to be statistically relevant.

CRediT authorship contribution statement

Eirik H. Herø: Conceptualization, Methodology, Software, Formal analysis, Investigation, Data curation, Writing - original draft. **Nicolas La Forgia:** Conceptualization, Methodology, Software, Investigation, Writing - review & editing. **Jannike Solsvik:** Conceptualization, Writing - review & editing. **Hugo A. Jakobsen:** Conceptualization, Writing - review & editing, Supervision.

Declaration of Competing Interest

The authors declare that they have no known competing financial interests or personal relationships that could have appeared to influence the work reported in this paper.

Acknowledgment

This work was carried out as a part of SUBPRO, a research based innovation center within Subsea Production and Processing. The authors gratefully acknowledge the financial support from SUBPRO, which is financed by the Research Council of Norway, major industry partners, and NTNU.

References

Andersson, R., Andersson, B., 2006a. On the breakup of fluid particles in turbulent flows. AIChE J. 52 (6), 2020–2030. https://doi.org/10.1002/aic.10831. http://doi.wiley.com/10.1002/aic.10831.

Andersson, R., Andersson, B., 2006b. Modeling the breakup of fluid particles in turbulent flows. AIChE J. 52 (6), 2031–2038. https://doi.org/10.1002/aic.10832. http://doi.wiley.com/10.1002/aic.10832. arXiv:arXiv:1402.6991v1.

Andersson, R., Helmi, A., 2014. Computational fluid dynamics simulation of fluid particle fragmentation in turbulent flows. Appl. Math. Model. 38 (17–18), 4186–4196. https://doi.org/10.1016/j.apm.2014.01.005.

Ashar, M., Arlov, D., Carlsson, F., Innings, F., Andersson, R., 2018. Single droplet breakup in a rotor-stator mixer. Chem. Eng. Sci. 181, 186–198. https://doi.org/10.1016/j.ces.2018.02.021. https://linkinghub.elsevier.com/retrieve/pii/S0009250918300836.

Azizi, F., Al Taweel, A.M., 2011. Hydrodynamics of liquid flow through screens and screen-type static mixers. Chem. Eng. Commun. 198 (5), 726–742. https://doi.org/10.1080/00986445.2011.532748.

Box, G.E.P., Hunter, J.S., Hunter, W.G., 2005. Statistics for Experimenters. Wiley-Interscience, Hoboken.

Coulaloglou, C.A., Tavlarides, L.L., 1977. Description of interaction processes in agitated liquid-liquid dispersions. Chem. Eng. Sci. 32 (11), 1289–1297. https://doi.org/10.1016/0009-2509(77)85023-9.

Diemer, R., Olson, J., 2002. A moment methodology for coagulation and breakage problems: Part 3—generalized daughter distribution functions. Chem. Eng. Sci. 57 (19), 4187–4198. https://doi.org/10.1016/S0009-2509(02)00366-4. https://www.sciencedirect.com/science/article/pii/S0009250902003664.

Eastwood, C.D., Armi, L., Lasheras, J.C., 2004. The breakup of immiscible fluids in turbulent flows. J. Fluid Mech. 502, 309–333. https://doi.org/10.1017/S0022112003007730.

Foroushan, H.K., Jakobsen, H.A., 2020. On the dynamics of fluid particle breakage induced by hydrodynamic instabilities: a review of modelling approaches. Chem. Eng. Sci. 219, 115575. https://doi.org/10.1016/j.ces.2020.115575. https://linkinghub.elsevier.com/retrieve/pii/S000925092030107X.

Galinat, S., Masbernat, O., Guiraud, P., Dalmazzone, C., Noïk, C., 2005. Drop break-up in turbulent pipe flow downstream of a restriction. Chem. Eng. Sci. 60 (23), 6511–6528. https://doi.org/10.1016/j.ces.2005.05.012.

Galinat, S., Torres, L.G., Masbernat, O., Guiraud, P., Risso, F., Dalmazzone, C., Noik, C., 2007. Breakup of a drop in a liquid-liquid pipe flow through an orifice. AIChE J. 53 (1), 56–68. https://doi.org/10.1002/aic.11055. http://doi.wiley.com/10.1002/aic.11055. arXiv:arXiv:1402.6991v1.

Håkansson, A., Trägårdh, C., Bergenståhl, B., 2009. Dynamic simulation of emulsion formation in a high pressure homogenizer. Chem. Eng. Sci. 64 (12), 2915–2925. https://doi.org/10.1016/j.ces.2009.03.034. https://linkinghub.elsevier.com/retrieve/pii/S0009250909002164.

Han, L., Luo, H., Liu, Y., 2011. A theoretical model for droplet breakup in turbulent dispersions. Chem. Eng. Sci. 66 (4), 766–776. https://doi.org/10.1016/J.CES.2010.11.041. https://www.sciencedirect.com/science/article/pii/S0009250910007037.

Han, L., Gong, S., Li, Y., Ai, Q., Luo, H., Liu, Z., Liu, Y., 2013. A novel theoretical model of breakage rate and daughter size distribution for droplet in turbulent flows. Chem. Eng. Sci. 102, 186–199. https://doi.org/10.1016/J.CES.2013.06.046. https://www.sciencedirect.com/science/article/pii/S0009250913004697.

Han, L., Gong, S., Ding, Y., Fu, J., Gao, N., Luo, H., 2015. Consideration of low viscous droplet breakage in the framework of the wide energy spectrum and the multiple fragments. AIChE J. 61 (7), 2147–2168. https://doi.org/10.1002/aic.14830. http://doi.wiley.com/10.1002/aic.14830.

Herø, E.H., Forgia, N.L., Solsvik, J., Jakobsen, H.A., 2019. Determination of breakage parameters in turbulent fluid-fluid breakage. Chem. Eng. Technol. 42 (4), 903–909. https://doi.org/10.1002/ceat.201800610.

Jakobsen, H.A., 2014. Chemical reactor modeling. Springer, Berlin.

Karimi, M., Andersson, R., 2018. An exploratory study on fluid particles breakup rate models for the entire spectrum of turbulent energy. Chem. Eng. Sci. 192, 850–863. https://doi.org/10.1016/J.CES.2018.08.016. https://www.sciencedirect.com/science/article/pii/S0009250918305852?via%3Dihub.

Karimi, M., Andersson, R., 2019. Dual mechanism model for fluid particle breakup in the entire turbulent spectrum. AIChE J., e16600 https://doi.org/10.1002/aic.16600.

Konno, M., Aoki, M., Saito, S., 1983. Scale effect on breakup process in liquid-liquid agitated tanks. J. Chem. Eng. Jpn. 16 (4), 312–319. https://doi.org/10.1252/jcej.16.312.

Krakau, F., Kraume, M., 2019. Three-dimensional observation of single air bubble breakup in a stirred tank. Chem. Eng. Technol. https://doi.org/10.1002/ceat.201900033. ceat.201900033. https://onlinelibrary.wiley.com/doi/abs/10.1002/ceat.201900033.

La Forgia, N., Herø, E.H., Solsvik, J., Jakobsen, H.A., 2018. Dissipation rate estimation in a rectangular shaped test section with periodic structure at the walls. Chem. Eng. Sci. 195, 159–178. https://doi.org/10.1016/j.ces.2018.11.039.

Lasheras, J., Eastwood, C.D., Martínez-Bazán, C., Montañés, J., 2002. A review of statistical models for the break-up of an immiscible fluid immersed into a fully developed turbulent flow. Int. J. Multiph. Flow 28 (2), 247–278. https://doi.org/10.1016/S0301-9322(01)00046-5.

Liao, Y., Lucas, D., 2009. A literature review of theoretical models for drop and bubble breakup in turbulent dispersions. Chem. Eng. Sci. 64 (15), 3389–3406. https://doi.org/10.1016/j.ces.2009.04.026.

Liao, Y., Oertel, R., Kriebitzsch, S., Schlegel, F., Lucas, D., 2018. A discrete population balance equation for binary breakage. Int. J. Numer. Meth. Fluids 87 (4), 202–215. https://doi.org/10.1002/fld.4491. http://doi.wiley.com/10.1002/fld.4491.

Luo, H., Svendsen, H.F., 1996. Theoretical model for drop and bubble breakup in turbulent dispersions. AIChE J. 42 (5), 1225–1233. https://doi.org/10.1002/aic.690420505. http://www.ncbi.nlm.nih.gov/pubmed/19947509 http://doi.wiley.com/10.1002/aic.690420505.

Maaß, S., Kraume, M., 2012. Determination of breakage rates using single drop experiments. Chem. Eng. Sci. 70, 146–164. https://doi.org/10.1016/j.ces.2011.08.027.

Maaß, S., Gäbler, A., Zaccone, A., Paschedag, A.R., Kraume, M., 2007. Experimental investigations and modelling of breakage phenomena in stirred liquid/liquid systems. Chem. Eng. Res. Des. 85 (5 A), 703–709. https://doi.org/10.1205/cherd06187.

Maaß, S., Wollny, S., Sperling, R., Kraume, M., 2009. Numerical and experimental analysis of particle strain and breakage in turbulent dispersions. Chem. Eng. Res. Des. 87 (4), 565–572. https://doi.org/10.1016/j.cherd.2009.01.002. https://linkinghub.elsevier.com/retrieve/pii/S0263876209000057.

Maaß, S., Buscher, S., Hermann, S., Kraume, M., 2011. Analysis of particle strain in stirred bioreactors by drop breakage investigations. Biotechnol. J. 6 (8), 979–992. https://doi.org/10.1002/biot.201100161.

Martínez-Bazán, C., Montañés, J.L., Lasheras, J.C., 1999. On the breakup of an air bubble injected into a fully developed turbulent flow. Part 1. Breakup frequency. J. Fluid Mech. 401, S0022112099006680. doi:10.1017/S0022112099006680. http://www.journals.cambridge.org/abstract_S0022112099006680.

Martínez-Bazán, C., Montañés, J.L., Lasheras, J.C., 1999. On the breakup of an air bubble injected into a fully developed turbulent flow. Part 2. Size PDF of the resulting daughter bubbles. J. Fluid Mech. 401, S0022112099006692. doi:10.1017/S0022112099006692. http://www.journals.cambridge.org/abstract_S0022112099006692 http://www.journals.cambridge.org/abstract_S0022112099006680.

Martínez-Bazán, C., Rodríguez-Rodríguez, J., Deane, G.B., Montaes, J.L., Lasheras, J.C., 2010. Considerations on bubble fragmentation models. J. Fluid Mech. 661, 159–177. https://doi.org/10.1017/S0022112010003186.

Mitre, J., Takahashi, R., Ribeiro, C., Lage, P., 2010. Analysis of breakage and coalescence models for bubble columns. Chem. Eng. Sci. 65 (23), 6089–6100. https://doi.org/10.1016/J.CES.2010.08.023. https://www.sciencedirect.com/science/article/pii/S0009250910004902.

Nachtigall, S., Zedel, D., Kraume, M., 2016. Analysis of drop deformation dynamics in turbulent flow. Chin. J. Chem. Eng. 24 (2), 264–277. https://doi.org/10.1016/j.cjche.2015.06.003.

Ramkrishna, D., 2000. Population balances: Theory and applications to particulate systems in engineering. Academic Press, San Diego.

Revuelta, A., Rodríguez-Rodríguez, J., Martínez-Bazán, C., 2006. Bubble break-up in a straining flow at finite Reynolds numbers. J. Fluid Mech. 551, 175–184. https://doi.org/10.1017/S0022112005008505. http://www.journals.cambridge.org/abstract_S0022112005008505.

Shy, S.S., Tang, C.Y., Fann, S.Y., 1997. A nearly isotropic turbulence generated by a pair of vibrating grids. Exp. Thermal Fluid Sci. 14 (3), 251–262. https://doi.org/10.1016/S0894-1777(96)00111-2.

Solsvik, J., 2017. Turbulence modeling in the wide energy spectrum: explicit formulas for Reynolds number dependent energy spectrum parameters. Eur. J. Mech. B. Fluids 61, 170–176. https://doi.org/10.1016/j.euromechflu.2016.10.011. https://linkinghub.elsevier.com/retrieve/pii/S0997754616303211.

Solsvik, J., Jakobsen, H.A., 2015. Single drop breakup experiments in stirred liquid-liquid tank. Chem. Eng. Sci. 131, 219–234. https://doi.org/10.1016/j.ces.2015.03.059.

Solsvik, J., Jakobsen, H.A., 2016a. Development of fluid particle breakup and coalescence closure models for the complete energy spectrum of isotropic turbulence. Ind. Eng. Chem. Res. 55 (5), 1449–1460. https://doi.org/10.1021/acs.iecr.5b04077. http://pubs.acs.org/doi/10.1021/acs.iecr.5b04077.

Solsvik, J., Jakobsen, H.A., 2016b. A review of the statistical turbulence theory required extending the population balance closure models to the entire spectrum of turbulence. AIChE J. 62 (5), 1795–1820. https://doi.org/10.1002/aic.15128. http://doi.wiley.com/10.1002/aic.15128.

Solsvik, J., Tangen, S., Jakobsen, H.A., 2013. On the constitutive equations for fluid particle breakage. Rev. Chem. Eng. 29 (5), 241–356. https://doi.org/10.1515/revce-2013-0009.

Solsvik, J., Maaß, S., Jakobsen, H.A., 2016a. Definition of the single drop breakup event. Ind. Eng. Chem. Res. 55 (10), 2872–2882. https://doi.org/10.1021/acs.iecr.6b00591.

Solsvik, J., Skjervold, V.T., Han, L., Luo, H., Jakobsen, H.A., 2016b. A theoretical study on drop breakup modeling in turbulent flows: The inertial subrange versus the entire spectrum of isotropic turbulence. Chem. Eng. Sci. 149, 249–265. https://doi.org/10.1016/J.CES.2016.04.037. https://www.sciencedirect.com/science/article/pii/S0009250916301968#bib11.

Solsvik, J., Skjervold, V.T., Jakobsen, H.A., 2017. A bubble breakage model for finite Reynolds number flows. J. Dispersion Sci. Technol. 38 (7), 973–978. https://doi.org/10.1080/01932691.2016.1216440. https://www.tandfonline.com/doi/full/10.1080/01932691.2016.1216440.

Tsouris, C., Tavlarides, L.L., 1994. Breakage and coalescence models for drops in turbulent dispersions. AIChE J. 40 (3), 395–406. https://doi.org/10.1002/aic.690400303. http://doi.wiley.com/10.1002/aic.690400303.

Vankova, N., Tcholakova, S., Denkov, N.D., Vulchev, V.D., Danner, T., 2007. Emulsification in turbulent flow: 2. Breakage rate constants. J. Colloid Interface Sci. 313 (2), 612–629. https://doi.org/10.1016/j.jcis.2007.04.064. https://linkinghub.elsevier.com/retrieve/pii/S0021979707005413.

Wheeler, A.J., Ganji, A.R., 2010. Introduction to Engineering Experimentation. Pearson Higher Education, Upper Saddle River.

Xing, C., Wang, T., Guo, K., Wang, J., 2015. A unified theoretical model for breakup of bubbles and droplets in turbulent flows. AIChE J. 61 (4), 1391–1403. https://doi.org/10.1002/aic.14709. http://doi.wiley.com/10.1002/aic.14709.

Yan, J., Cheng, N.S., Tang, H.W., Tan, S.K., 2007. Oscillating-grid turbulence and its applications: a review. J. Hydraul. Res. 45 (1), 26–32. https://doi.org/10.1080/00221686.2007.9521740.

Zaccone, A., Gäbler, A., Maaß, S., Marchisio, D., Kraume, M., 2007. Drop breakage in liquid–liquid stirred dispersions: Modelling of single drop breakage. Chem. Eng. Sci. 62 (22), 6297–6307. https://doi.org/10.1016/J.CES.2007.07.026. https://www.sciencedirect.com/science/article/pii/S000925090700526X#bib6.

Chapter 9

Paper 4

Chemical Engineering Science: X 12 (2021) 100111

Contents lists available at ScienceDirect

Chemical Engineering Science: X

journal homepage: www.elsevier.com/locate/cesx

Single oil drop breakage in water: Impact of turbulence level in channel flow

Eirik H. Herø *, Nicolas La Forgia, Jannike Solsvik, Hugo A. Jakobsen

Department of Chemical Engineering, Norwegian University of Science and Technology, Sem Sælandsvei 4, Kjemiblokk 5, 7491 Trondheim, Norway

ARTICLE INFO

Article history:
Received 29 March 2021
Received in revised form 4 August 2021
Accepted 10 August 2021
Available online xxxx

Keywords:
Breakage
Fluid particle
Turbulence
Population balance equation
Weber number

ABSTRACT

Single octanol droplet fragmentations in channel flow have been investigated by use of high speed imaging. The resulting raw data have been analyzed, interpreted and used to elucidate the fluid particle breakage phenomena, enabling improved understanding and motivating development of more universal population balance equation closures. The breakage kernel functions considered are the breakage time, the breakage probability, the average number of daughters and the daughter size distribution. These functions have been determined from the same set of data ensure consistency. The impact of the drop size and the turbulent energy dissipation rate on the different kernel functions were investigated. The breakage probability and average number of daughters functions correlate reasonably with the Weber number. Similarly, the breakage time correlates adequately with known model concepts. However, the correlations may not be considered universal as the parameter values obtained are not in agreement with values reported in the literature.

1. Introduction

Multiphase flow is important for many industrial applications. For the relevant industries, predictive modeling of the dispersed phase transient behavior would be beneficial, e.g. when designing new equipment. Modeling of the dispersed phase is possible through the population balance equation, PBE, framework. However, as the underlying mechanisms of the dispersed phase breakage phenomena are not well understood, available models do not exhibit the required predictiveness. Large amounts of experimental data are required in order to improve the understanding of the breakage phenomena and enable the development of more universal breakage models. In this study, the breakup phenomena are investigated in a liquid-liquid system by observing single octanol drops in a turbulent channel flow of water.

1.1. PBE modeling

In the PBE, constitutive equations are required for the source and sink terms. These constitutive equations comprise of underlying kernel functions, hereafter referred to as kernel functions. The kernel functions relevant for breakage is the breakage frequency, b, the average number of daughter drops, ν, and the daughter size distribution function, P_{DSD}. The breakage frequency is generally determined by the breakage time, t_B, and the breakage probability, P_B. The kernel functions may depend on the drop properties, such as the diameter of the mother drop, D_m, the different physical properties of the phases, such as the viscosity, μ, and the density, ρ, the system properties, such as the interfacial tension, γ, and flow characteristics such as the turbulent kinetic energy dissipation rate, ϵ, and the turbulent kinetic energy, k.

The PBE describes the change in the number density distribution function of the dispersed phase (Ramkrishna, 2000). On a simplified form, the PBE in terms of the number density function, f_n, can be given as (Jakobsen, 2014)

$$\frac{\partial f_n(D_m,\boldsymbol{r},t)}{\partial t}+\nabla\cdot[\boldsymbol{v}_r(\boldsymbol{r},D_m,t)f_n(D_m,\boldsymbol{r},t)] = -B_D(D_m,\boldsymbol{r},t)+B_B(D_m,\boldsymbol{r},t) \quad (1)$$

In which $\boldsymbol{r}$ is the place vector, t is the time, $\boldsymbol{v}_r$ is the velocity vector and D_m denotes the drop diameter of the mother drop. B_D and B_B denote the sink and source terms for breakage death and breakage birth, respectively. These sink and source terms may be expressed as:

$$B_D(D_m)=b(D_m)f_n(D_m) \quad (2)$$

$$B_B(D_m)=\int_{D_m}^{D_{max}}\nu P_{DSD}(D_m,D_d)b(D_d)f_n(D_d)dD_d \quad (3)$$

* Corresponding author.
E-mail address: eirik.h.hero@ntnu.no (E.H. Herø).

https://doi.org/10.1016/j.cesx.2021.100111
2590-1400/

Nomenclature

Latin letters

$\bar{S}$	Rate of strain [1/s]
$\boldsymbol{r}$	space coordinate vector [m]
$\boldsymbol{v}_r$	velocity vector [m/s]
ΔP	pressure drop [Pa]
ΔP^*_{DSD}	dimensionless discrete daughter size distribution function [–]
ΔV_d	daughter size range
ΔV_d	range in daughter size [m^3]
Δx	displacement from channel centerline [m]
b	breakage frequency [1/s]
B_B	birth due to breakage [1/(m^3 m s)]
B_D	death due to breakage [1/(m^3 m s)]
c	parameter
C_k	Kolmogorv constant
c_L	model parameter
D_d	daughter drop diameter [m]
D_m	mother drop diameter [m]
D_{crit}	Hinze critical diameter [m]
E	Energy Spectrum [m^2 s^3]
F	hypergeometric function
f_L, f_η	Pope's model spectrum functions
f_n	number density function [1/(m^3 m)]
K	Bessel function
k	turbulent kinetic energy [m^2/s^2]
L	integral length scale [m]
N_B	number of breaking drops
N_{tot}	total number of drops
$p0$	Pope's model spectrum constant
P_B	breakage probability
P_{DSD}	daughter size distribution function [1/m]
P^*_{DSD}	dimensionless daughter size distribution function
r_d	model distance [m]
s	function
t	time [s]
t_B	breakage time [s]
T_n	function, n = 1, 2, 3, 4, 5
V_d	daughter drop volume [m^3]
V_m	mother drop volume [m^3]
Re_λ	Taylor scale Reynolds number
U	velocity during experiments [m/s]
We_S	Weber number formulated with the second order structure function

Greek letters

β	Komogorov constant
β_E	Pope's model spectrum constant
ϵ	turbulent energy dissipation rate [m^2/s^3]
η	Kolmogorov micro scale [m]
Γ	gamma function
γ	interfacial tension [N/m]
κ	Wave number [1/m]
μ_c	continuous phase dynamic viscosity [kg/(m s)]
μ_d	dispersed phase dynamic viscosity [kg/(m s)]
ν	average number of daughters
ν_c	continuous phase kinematic viscosity [m^2/s]
ν_d	dispersed phase kinematic viscosity [m^2/s]
$\overline{\delta u^2}$	second order longitudinal velocity structure function [m^2/s^2]
ρ_c	continuous phase density [kg/m^3]
ρ_d	dispersed phase density [kg/m^3]
σ_s	surface restoring stress [Pa/m^2]
σ_t	turbulent stress [Pa/m^2]
$\sigma_{s,v}$	stabilizing viscous stress [Pa/m^2]
$\sigma_{t,S}$	turbulent shear stress [Pa/m^2]

Abbreviations

CB	Cascade Breakage Definition
CI	Confidence Interval Limits
IB	Initial Breakage Definition
PBE	Population Balance Equation
SD	Standard Deviation

For convenience, the kernel functions are expressed as functions of droplet sizes only. The kernel functions must be modeled to close the PBE and many breakage model concepts and adaptions exists in the literature. For an extensive overview, interested readers are refereed to the reviews by Lasheras et al. (2002), Liao and Lucas (2009) and Solsvik et al. (2013).

To describe the turbulent energy, Pope (2000) formulated a model energy spectrum as

$$E(\kappa) = C_k \epsilon^{2/3} \kappa^{-5/3} f_L(\kappa L) f_\eta(\kappa\eta) \tag{4}$$

where $C_k = 1.5$, κ is the wavenumber, $L = \frac{k^{3/2}}{\epsilon}$ is the integral length scale, $\eta = (\nu_c^3/\epsilon)^{1/4}$ is the Kolmogorov micro scale and ν_c is the kinematic viscosity. The function $f_L(\kappa L)$ is given as

$$f_L(\kappa L) = \left[\frac{\kappa L}{\left[(\kappa L)^2 + C_L \right]^{1/2}} \right]^{5/3+p0} \tag{5}$$

and the function $f_\eta(\kappa\eta)$ is given as

$$f_\eta(\kappa\eta) = \exp\left[-\beta_E \left[(\kappa\eta)^4 + C_\eta^4 \right]^{1/4} - C_\eta \right] \tag{6}$$

Here, $p0 = 2$ and $\beta_E = 5.2$. C_L and C_η are parameters that can be estimated from (Solsvik, 2017)

$$C_L(\mathrm{Re}_\lambda, C_k) = \exp\left[-\frac{4.478 + 18.362 C_k}{\mathrm{Re}_\lambda^{1.075 - 0.070 C_k}} \right] - 1.913 + 2.169 C_k \tag{7}$$

$$C_\eta(\mathrm{Re}_\lambda, C_k) = \exp\left[-\frac{14.043 - 4.222 C_k}{\mathrm{Re}_\lambda^{1.986 - 0.363 C_k}} \right] - [0.089 + 0.339 C_k] \tag{8}$$

For Re_λ in the range 10^2 to 10^5. Re_λ is the Taylor scale Reynolds number given as

$$\mathrm{Re}_\lambda = \sqrt{\frac{20}{3} \frac{k^2}{\epsilon \nu_c}} \tag{9}$$

The second order structure function can be determined from the energy spectrum, Davidson (2004), and is often used in order to approximate the turbulent stress or force acting on a droplet. An underlying assumption is that only vortices of the same size as the droplet contribute to the breakup of the droplet. In the inertial subrange of turbulence, the Kolmogorov structure function is given as

$$\overline{\delta u^2}(D_m) = \beta (\epsilon D_m)^{2/3} \tag{10}$$

in which the Kolmogorov constant β can be set to 2, Batchelor (1951). This formulation of $\overline{\delta u^2}$ is limited to very large Taylor scale Reynolds numbers, Re_λ. Even then, it is only valid for droplet sizes in

the intertial subrange of turbulence. Therefore, (10) may not accurately describe $\overline{\delta u^2}$ in low Re_λ applications. Solsvik and Jakobsen (2016a) proposed a semi-empirical formulation for $\overline{\delta u^2}$ valid for the entire range of turbulence and any turbulent Re_λ, based on the model energy spectra by Pope (2000). The expression was given as

$$\overline{\delta u^2}(D_m) = \frac{4}{3}k\left(\frac{D_m^2}{r_d^2 + D_m^2}\right)^{2/3} \cdot (1 - [T_1(D_m) + T_2(T_3(D_m)T_4(D_m) - T_5(D_m))]) \tag{11}$$

where r_d is a crossover length scale, which is related to the transition between the dissipation subrange and the inertial subrange of turbulence. The expression for r_d is given by

$$r_d = (15\beta)^{3/4}\eta \tag{12}$$

The different T_n expressions are given as

$$T_1(D_m) = \frac{2}{[s(D_m)]^2}F\left(\left(-\frac{1}{3}\right)^{\frac{1}{2}}, \left(\frac{3}{2}\right)\middle|\frac{[s(D_m)]^2}{4}\right) \tag{13}$$

$$T_2 = 3^{3/2}\Gamma\left(\frac{2}{3}\right) \tag{14}$$

$$T_3(D_m) = 27 \cdot 2^{1/3}[s(D_m)]^{2/3}\Gamma\left(\frac{2}{3}\right) \tag{15}$$

$$T_4(D_m) = \frac{1}{352\pi}F\left(\left(\frac{7}{3}\right)^{\frac{11}{6}}, \left(\frac{17}{6}\right)\middle|\frac{[s(D_m)]^2}{4}\right) \tag{16}$$

$$T_5(D_m) = \frac{2^{2/3}}{2\pi[s(D_m)]^{2/3}}K_{\frac{1}{3}}(s(D_m)) \tag{17}$$

in which F is the hypergeometric function, K is the Bessel function and Γ is the gamma function. Finally, $s(D_m)$ is found from

$$s(D_m) = D_m/\left(c_L^{-1/2}L\right) \tag{18}$$

From the expression for $\overline{\delta u^2}$, e.g. Eq. (11), a turbulent inertial stress or disruptive force is defined as

$$\sigma_t = \rho_c\overline{\delta u^2}(D_m) \tag{19}$$

The restoring surface stress of a drop is defined as

$$\sigma_s = \gamma/D_m \tag{20}$$

The two stresses can be combined to a turbulent Weber number (Hinze, 1955)

$$\mathrm{We}_S = \frac{\sigma_t}{\sigma_s} = \frac{\rho_c\overline{\delta u^2}(D_m)D_m}{\gamma} \tag{21}$$

It should be noted that the derivation of a turbulent Weber number is not universal, as both (19) and (20) has been given with different prefactors. Eq. (19) can be found with a prefactor of 1, e.g. Galinat et al. (2005), or 1/2, e.g. Andersson and Andersson (2006). Eq. (20) have been expressed in several variations, with 1 in Hinze (1955), 2 in Karimi and Andersson (2019), 4 in Ashar et al. (2018) and 6 in Martínez-Bazán et al. (1999a,b).

Shinnar (1961) formulated a viscous shear stress as

$$\sigma_{t,S} = \mu_c\bar{S} \tag{22}$$

where $\bar{S}$ is the local rate of strain due to velocity gradients. The shear stress is considered as an additional stress to the conventional turbulent inertial stress (19). For the dissipating subrange of turbulence, Shinnar (1961) expressed $\bar{S}$ as the Kolmogorov local rate of strain, $\bar{S} = \sqrt{\epsilon/\nu_c}$. Later, Håkansson et al. (2009) and Karimi and Andersson (2019) generalized the strain rate as $\bar{S} = \sqrt{\overline{\delta u^2}(D_m)}/D_m$. Then, the expression for the shear stress becomes

$$\sigma_{t,S} = \mu_c\frac{\sqrt{\overline{\delta u^2}(D_m)}}{D_m} \tag{23}$$

which is assumed valid when the expression for $\overline{\delta u^2}(D_m)$, e.g. Eq. (11), is valid. Both Shinnar (1961) and Karimi and Andersson (2019) noted that this stress is dominating around the Kolmogorov microscale and lower, but is otherwise small.

Hinze (1955) argued that the drop viscosity contributes a stabilizing effect, adversely affecting breakage. A stabilizing viscous stress may be formulated as (Calabrese et al., 1986)

$$\sigma_{s,\nu} = \mu_d\sqrt{\rho_c/\rho_d}\frac{\sqrt{\overline{\delta u^2}(D_m)}}{D_m} \tag{24}$$

Hinze (1955) argued that this effect was usually small, but could be critical in systems with particularly viscous dispersed phase. Later, Alopaeus et al. (2002) and Vankova et al. (2007) both achieved better model fits to experimental data by including the stabilizing effect of viscosity.

It is noted that alternative breakage phenomena have been investigated. Recently, Foroushan and Jakobsen (2020) published a review on the concept of energy accumulation and decay rates. In this view, droplets may break due to a series of interactions. Drop surface energy is both accumulated through vortex interactions and decaying through dampening oscillations, either until enough energy for breakage is achieved or no breakage take place due to a relatively large decay rate. It is possible that this phenomenon is relevant for the breakup mechanisms.

1.2. Breakage frequency models

1.2.1. Coulaloglou and Tavlarides

A well known model was proposed by Coulaloglou and Tavlarides (1977). They proposed the idea that the breakage frequency could be determined from breakage time, t_B, and breakage probability, P_B,

$$b(\epsilon, D_m) = \frac{1}{t_B(\epsilon, D_m)}P_B(\epsilon, D_m) \tag{25}$$

The probability of breakage was assumed proportional to the fraction of turbulent eddies, which has energy larger than the drop surface energy, that collide with the drop. The resulting expression became

$$P_B(D_m) = \exp\left(-\frac{c_1\gamma}{\rho_d\epsilon^{2/3}D_m^{5/3}}\right) \tag{26}$$

in which c_1 is a parameter, γ is the interfacial tension and ρ_d is the dispersed phase density. Further, Coulaloglou and Tavlarides (1977) determined the breakage time in the inertial range of turbulence as

$$t_B = c_2D_m^{2/3}\epsilon^{-1/3} \tag{27}$$

As shown by Solsvik and Jakobsen (2016b), the model of Coulaloglou and Tavlarides (1977) can be expanded to consider the full range of turbulence. The expression for breakage time, Eq. (27), can be written as

$$t_B(D_m) = c_3\frac{D_m}{\sqrt{\overline{\delta u^2}(D_m)}} \tag{28}$$

In addition, the expression for breakage probability, Eq. (26), can be written as

$$P_B(D_m) = \exp\left(-\frac{c_4\gamma}{\rho_d D_m \overline{\delta u^2}(D_m)}\right) \tag{29}$$

Thus, if the expression for $\overline{\delta u^2}$ is valid for the entire range of turbulence, then the breakage probability is assumed valid for the entire range of turbulence.

1.2.2. Coulaloglou and Tavlarides with viscous stabilization

Several authors, e.g. Chen et al. (1998) and Vankova et al. (2007), have added the drop viscosity as a stabilizing effect to the model of Coulaloglou and Tavlarides (1977). Following the same procedure and setting $\sigma_{s,v} = \mu_d \frac{\sqrt{\overline{\delta u^2}(D_m)}}{D_m}$, the following expression is obtained

$$b(D_m) = c_5 \frac{\sqrt{\overline{\delta u^2}(D_m)}}{D_m} \times \exp\left(-\frac{c_6\gamma}{\rho_d D_m \overline{\delta u^2}(D_m)} - \frac{c_7\mu_d}{\rho_d D_m \sqrt{\overline{\delta u^2}(D_m)}}\right) \tag{30}$$

In this formulation, the original model of Coulaloglou and Tavlarides (1977) is recovered for $c_7 = 0$, i.e. no viscous stabilization. In this model derivation, the surface tension and the drop viscosity are both assumed to be effects adversely affecting breakage. c_6 and c_7 must be non-negative parameters for this assumption to be valid.

1.2.3. Alopaeus et al.

Narsimhan et al. (1979) formulated a breakage frequency model where the breakages occurred due to oscillations resulting from relative velocity fluctuations. The eddy-drop collisions were assumed to form a Poisson process, and droplet breakage takes place when an eddy of sufficient energy collides with the drop. Written in terms of diameter their model took the form, Alopaeus et al. (2002)

$$b(D_m) = c_8 \operatorname{erfc}\left(\sqrt{\frac{c_9\gamma}{\rho_c \epsilon^{2/3} D_m^{5/3}}}\right) \tag{31}$$

The parameter c_8 has dimensions [1/s] and Narsimhan et al. (1979) expected it to depend on both D_m and ϵ. However, without sufficient experimental data, Narsimhan et al. (1979) assumed c_8 to be independent of the two variables for the model development. Later, Alopaeus et al. (2002) introduced a dependency of $\epsilon^{1/3}$ to c_8. In addition, they added the stabilizing effect of the drop viscosity (24). The resulting expression was

$$b(D_m) = c_{10}\epsilon^{1/3} \operatorname{erfc}\left(\sqrt{\frac{c_{11}\gamma}{\rho_c \epsilon^{2/3} D_m^{5/3}} + \frac{c_{12}\mu_d}{\sqrt{\rho_c \rho_d}\epsilon^{1/3} D_m^{4/3}}}\right) \tag{32}$$

Which can generalized with the second order structure function as

$$b(D_m) = c_{13}\epsilon^{1/3} \operatorname{erfc}\left(\sqrt{\frac{c_{14}\gamma}{\rho_c \overline{\delta u^2}(D_m)} D_m + \frac{c_{15}\mu_d}{\sqrt{\rho_c \rho_d \overline{\delta u^2}(D_m) D_m}}}\right) \tag{33}$$

As for the original model, the parameter c_{13} has dimensions, [$m^{3/2}$], and is likely problem dependent. In their study, Alopaeus et al. (2002) found no dependency of c_{13} on D_m.

1.3. Daughter size distribution functions

The product of the daughter size distribution and the average number of daughters must be number and volume conserving, Solsvik et al. (2013). In the model frameworks available in the literature, the common procedure is to assume the average number of daughters to be known a priori. Then, the daughter size distribution is designed.

For their model, Coulaloglou and Tavlarides (1977) assumed binary breakage. Then, the daughter size distribution was assumed to fit a normal distribution. In terms of volume, the expression for the daughter size distribution becomes (Coulaloglou and Tavlarides, 1977)

$$P_{DSD}(V_m, V_d) = \frac{2.4}{V_m} \exp\left(-\frac{4.5(2V_d - V_m)^2}{V_m^2}\right) \tag{34}$$

This procedure is commonly used; the model derivation assumes binary breakage and a universal shape of the daughter size distribution. Critically, it is assumed that the general shape of the daughter size distribution is neither dependent on the system properties nor the turbulent characteristics. That is, while the daughter size distribution may dependent on system properties or the turbulent characteristics, the shape may usually still be classified as a general shape such as the normal distribution given above. Other examples in the literature are the β distribution, e.g. Hsia and Tavlarides (1983), uniform, e.g. Narsimhan et al. (1979), U-shaped, e.g. Luo and Svendsen (1996) or M-shaped, e.g. Lehr et al. (2002).

Very few models allow for other outcomes than a binary breakage. One alternative is the model of Diemer and Olson (2002), where the average number of daughters can be any number, including non-integers. The model predicts equal size breakage as the most likely outcome of the breakage event. The drawback of this model system is that the daughter size distribution must be adjusted with shape factors to fulfill the number and volume conservation requirements. A few similar models have been proposed by Han et al. (2011, 2013, 2015) and Solsvik et al. (2016a). In these closures the daughter numbers are fixed at 2, 3 or 4. For each daughter number, the daughter size distribution is predetermined and not dependent on system properties or flow characteristics. Equal size breakage is the most likely outcome of the breakage event.

1.4. Previous experimental investigations

In the literature there are many dense dispersion experiments reported, considering many drops of the dispersed phase simultaneously. These studies rely on observing a dense dispersed phase at different time instances, sometimes also different space coordinates. From the resulting data it is possible to validate the results of a PBE simulation spanning the same time and space. However, the kernel functions can not be validated individually. For validation of the individual kernel functions, single droplet experiments are required. In such experiments, the entire breakage event of single droplets are observed by high speed imaging.

The number of single droplet studies available in the literature are few. In addition, the results are challenging to compare due to the use of different dispersed phases, continuous phase, experimental setup, determination of turbulence, etc. Moreover, in most of these studies only one or very few kernel functions are investigated simultaneously. That is, no study covers all the required kernel functions from the same breakage events simultaneously, with the exception of the study of Herø et al. (2020). Obtaining all the information needed to model the terms in the PBE simultaneously is an advantage, as model validation relying on experimental data from different experimental setups, procedures and breakage events does not ensure consistency.

A fundamental difference between these studies is the definitions employed when interpreting the data from an observed breakage event. As first outlined by Solsvik et al. (2016b), the def-

initions employed can be classified into either the initial breakage event definition or the cascade breakage event definition. The two definitions differ in what physical configuration is defined as the end of a breakage event. In the initial breakage event definition, the breakage event is considered ended when the breaking mother drop first separates. On the other hand, in the cascade breakage event definition the breakage event is considered ended when only stable daughter drops are formed. A more detailed explanation is given in Section 2.2. The choice of breakage definition greatly impacts the resulting breakage time, average number of daughters and daughter size distribution, as shown by Herø et al. (2020).

In the literature, only five studies investigate single drop breakage for different turbulence level under otherwise equal experimental conditions (Andersson and Andersson, 2006; Maaß and Kraume, 2012; Galinat et al., 2005; Galinat et al., 2007; Ashar et al., 2018). Thus, little experimental data is available to investigate the impact of the turbulence level on the breakage phenomena.

In the study by Andersson and Andersson (2006), breakup was observed in a static mixer. Investigating mother drops of 1 mm in diameter, the breakage time was determined for dodecane drops as 10.9 and 5.6 ms for ϵ at 1.13 and 3.69 m^2/s^3, respectively. When investigating octanol drops, the breakage time was determined to be 7.6 and 4.2 ms for ϵ at 3.69 and 8.54 m^2/s^3, respectively. The continuous phase in this study was tap water. In their work, no breakage definition is explicitly given.

Maaß and Kraume (2012) observed breakup in a channel flow around an impeller blade, mimicking a stirred tank reactor. The initial breakage event definition was employed in the study. To investigate the impact of ϵ, mother drops of 1 mm in diameter were observed at ϵ values of 2.3, 6.0 and 12.5 m^2/s^3. For toluene drops this resulted in a breakage time of 6.0, 4.7 and 3.7 ms, while for petroleum drops the breakage times were 4.4, 3.4 and 2.8 ms. Based on this, Maaß and Kraume (2012) showed that the breakage time for a given mother drop size agrees well with the model by Coulaloglou and Tavlarides (1977), Eq. (27). In their study, Maaß and Kraume (2012) also studied the impact of mother drop size on breakage time and breakage probability. The mother drops were toluene with diameters of 0.62, 1.0, 2.0 and 3.0 mm, as well as petroleum drops of 0.54, 0.7, 1.0, 1.3, 1.9 and 3.1 mm. The continuous phase in the study was water. In the same system, Maaß et al. (2011) investigated the impact of the mother drop diameter on the daughter number distribution. They also showed two daughter size distributions for binary breakages. Also in this study, the initial breakage event definition was employed.

The remaining three studies investigating varying turbulence levels, the results are only reported by the Weber number value (Galinat et al., 2005; Galinat et al., 2007; Ashar et al., 2018). As the studies have varying properties such as e.g. D_m, ϵ and γ, the experimental results dependence on ϵ can not be discerned from the other variables. This further complicates comparison of data obtained in the different studies.

Galinat et al. (2005) investigated single droplet breakage when transporting oil droplets through an orifice. In their setup, twelve flow conditions were obtained by varying either orifice opening or continuous phase velocity. Each flow condition was related to the theoretical pressure drop over the orifice. From this pressure drop, the ϵ can be found to be between 1 and 20 m^2/s^3. The oil drops were heptane with diameters between 1.5 and 3 mm, with and without red sudan for coloring. The continuous phase was tap water. Galinat et al. (2005) investigated the breakage probability, average number of daughters and daughter size distribution. Galinat et al. (2007) performed additional experiments in the same setup with water-glycerin as the continuous phase. Neither of the studies by Galinat et al. (2005, 2007) defined the breakage definition employed.

Ashar et al. (2018) investigated single droplet breakage in a stirred tank, where the breakage probability and the average number of daughters were reported as functions of the Weber number value. The dispersed phase were rapeseed oil and the continuous phase was deionized water. The mother drops had a diameter between 0.07 and 0.55 mm, and the experiments were run at ϵ values of 535 and 2480 m^2/s^3. The breakage event definition is not explicitly defined, but the daughter number appears to be calculated according to the cascade breakage event definition.

Other single drop studies in the literature vary other parameters than ϵ. Several of these studies are from the same setup as used by Maaß and Kraume (2012). Maaß et al. (2007) and Zaccone et al. (2007) investigated the daughter size distribution for different daughter numbers and reported the daughter number distribution for mother drop diameters of 0.56, 1 and 2 mm. The continuous phase was water, with and without sudan-black for coloring. The oil drops were petroleum. Nachtigall et al. (2016) investigated the deformation process and breakage time when combining different dispersed and continuous phases. In this way, they could investigate the impact of interfacial tension. The oils investigated were petroleum and paraffin oil, while the continuous phase was water with or without sodium dodecyl sulfate. The mother drops were 1 mm in diameter.

Solsvik and Jakobsen (2015) investigated the breakage time as a function of the mother drop size. Single toluene, petroleum, n-dodecane and 1-octanol drops were injected into a stirred tank filled with distilled water. The diameter of the mother drops were between 0.6 and 4 mm. Using a volume average value for the tank, ϵ was determined as 1.14 m^2/s^3. The cascade breakage definition was employed in this study.

In the study by Herø et al. (2020), all kernel functions were investigated as functions of mother drop size. The setup consist of a rectangular channel, with baffles for increased turbulence level. The dispersed phase was octanol drops with diameters between 1.0 and 2.23 mm and the continuous phase was distilled water. As ϵ was associated with individual breakages, the different ϵ levels were determined to be between 0.15 and 0.09 m^2/s^3, although all experiments were performed at an area averaged velocity of 1 m/s. Both the initial and the cascade breakage event definitions was employed, resulting in two separate sets of experimental data.

Although the experimentally determined kernel functions are difficult to directly compare between the studies, there are some general results. An increase in the mother drop size leads to an increase in the breakage time, the breakage probability and the average number of daughters, as well as a change in the daughter size distribution. On the other hand, an increase in ϵ decreases the breakage time. Finally, an increase in the Weber number value leads to an increase in the breakage probability and the average number of daughters, with a corresponding change in the daughter size distribution.

In this study single octanol drops are observed in a channel flow. Three different turbulence levels are investigated by changing the continuous phase mean flow. Analyzing the experimental data, the impact of ϵ on the breakage phenomena is investigated.

2. Experimental setup and procedure

2.1. Experimental facility

An experimental facility has been constructed to investigate breakage of oil droplets in water. A schematic drawing of the facility can be seen in Fig. 1. The facility has previously been described by La Forgia et al. (2018) and Herø et al. (2019, 2020).

To perform an experiment, a single oil drop (1-octanol, Sigma-Aldrich, product number 472328) is generated by a glass cannula connected to a syringe pump (KDS Legato 180). Next, the oil drop is transported by the continuous phase (reverse osmosis tap water) into the breakage section. Here, breakage events may be observed by two cameras (Photron FASTCAM Mini AX100 540 K M3) as two of the walls in the breakage channel is constructed in glass. The two remaining sides have periodic rods for increased turbulence generation. The channel is 1 m long with a cross-section of 30 mm by 30 mm and the rods are 3 mm by 3 mm spaced evenly every 10 mm. After the breakage channel, the oil and water is transported to a large tank that also serves as a gravity separator. The continuous phase flow is produced by a positive displacement pump (MDL-0670, SPX Flow Technology).

Each camera has a maximum resolution of 1024 x 1024, which is fully utilized only in the streamwise direction. The entire channel length is not observed. The cameras observe a region of the breakage channel which is 40 mm to 400 mm above the channel entry for a total length of 360 mm. The resolution gives the pixel size as 0.175 mm by 0.175 mm. The cameras are synchronized in time and record at 4000 frames per second. The observed region is backlit by three LED lamps (Multiled LT-V9-15 by GS Vitec). To obtain sufficient contrast of the oil drops in the images, the oil is dyed with Sudan Black B (RAL Diagnostics). The resulting properties are given in Table 1.

After the high-speed videos have been obtained, the videos must be processed to extract the data needed to validate the kernel functions. The full details of this procedure can be found in Herø et al. (2019, 2020) and a summary is given here. Through automatic image processing, the images of the video are individually treated to determine which pixels are part of a drop. Subsequently, the projected two-dimensional areas size, shape and position of the visible drops in each image are determined. Finally, the information from the individual images are combined to obtain continuous information of the drops. The procedure is executed in MATLAB, with several manual steps. Including manually observing the video to verify the MATLAB code, as well as determining the breakage event start and end instances according to the breakage event definitions given in the following section.

The turbulent characteristics were determined using laser doppler velocimetry, LDV, the procedure of which have previously been reported by La Forgia et al. (2018). In short, the channel was mapped every 50 mm in the streamwise direction. For the transverse direction, symmetry meant only half the channel needed to be characterized. Hence, the velocity was measured every 0.5 mm from the center of the channel to 0.5 mm from the baffle. As an LDV provides instantaneous velocities, k and ϵ must be calculated as time averaged values. Thus, the impact of the dynamics and intermittency of turbulence can not be investigated directly from this data. An error estimation of the turbulent quantities can be found in La Forgia et al. (2018).

Table 1
Properties of 1-octanol dyed with Sudan Black.

Density, ρ	Dynamic Viscosity, μ	Interfacial Tension, γ
825 kg/m^3	9.09 $\cdot 10^{-3}$ kg/(m s)	8.20 mN/m.

2.2. Breakage event definitions

The breakage events are interpreted by use of both the initial breakage event definition and the cascade breakage event definition. The definitions differ in the interpretation of the breakage event end time instance:

- Breakage event end for the initial breakage definition is when the mother drop fragments.
- Breakage event end for the cascade breakage definition is when the final intermediary daughter fragments.

Neither of the definitions of the breakage event end instances corresponds to an equilibrium state of the channel. The breakage event start is when a spherical mother drop starts to deform, and this deformation process is directly related to a fragmentation of the drop. The latter distinction is important as some mother drops undergoes small and dampening oscillations before a much larger deformations leads directly to breakage. These occasional oscillations are not considered to be part of the breakage, which may be an inaccurate according to the concept of energy accumulation and decay rates (Foroushan and Jakobsen (2020)). In the current interpretation and procedure, the breakage event start instance is

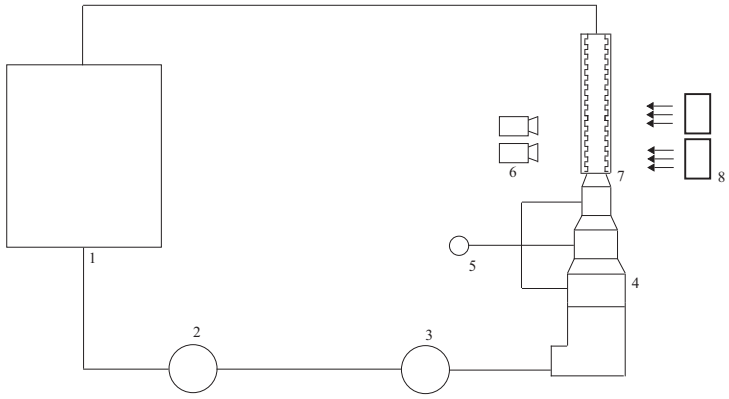

Fig. 1. Schematic drawing of the experimental setup. 1. Water tank and phase separator, 2. water pump, 3. flow meter, 4. droplet generation section, 5. oil syringe pump, 6. two cameras, 7. breakage section, 8. illumination.

assumed to occur at the instance of a single droplet-turbulent vortex interaction. This procedure was elucidated in Herø et al. (2020, Section 4.9, P. 21). At the breakage event end instance the number of daughters and their size distribution can be determined. The breakage time is determined as the time period between the start and end instances. ϵ and k is determined from the position at the breakage start. This position is associated with the time averaged continuous phase characteristics, which have been determined as described in Section 2.1.

The two breakage event definitions may result in different breakage time, average number of daughters and daughter size distribution as these are dependent on the breakage event end instance. On the other hand, the breakage probability coincides for the two definitions, as the determination of breakage probability is not dependent on the breakage event end instance.

Fig. 2 shows an image sequence of a breakage event. First, an initially spherical drop is deformed and breaks into two near equal daughters. At this instance, the breakage is ended according to the initial breakage event definition. One of the daughters continue with a deformation process and an additional smaller drop is produced. At this instance the event is considered ended in the cascade breakage event definition, as no more breakages occur.

2.3. Determination of data points

Several measurements under the same experimental conditions are required to investigate the kernel functions. The breakage probability is by definition a ratio with information from several experiments, which is also the case for the average number of daughters. The daughter size distribution is determined from the same events as the average number of daughters. Theoretically, the breakage time could be determined from a single breakage event. However, the effect of the instantaneous turbulence cannot be accounted for in the current procedure, as time averaged turbulence properties are employed. For this reason, several measurements are required to investigate the breakage time as well. It is noted that the instantaneous turbulence level probably has an effect on all the kernel functions. In the current study, experiments are grouped by their D_m value and the continuous phase area average velocity in the breakage channel during the experiments. These groups or size intervals are hereafter referred to as data points.

The data points investigated in this study, with values determined as described in Sections 2.1 and 2.2, can be seen in Table 2. In this work, every kernel function is determined through both the initial breakage definition and cascade breakage definition, for each data point. In Table 2, the data points have been given reference numbers for convenience. The data points collected at a cross sectional area averaged velocity of 1.0 m/s have previously been reported by Herø et al. (2020). The data points at 1.5 m/s and 2.0 m/s are not previously reported. As can be seen from the table, the data points have a varying number of assessed drops. This variation is found both in the drops undergoing breakage and the drops not breaking, N_B and N_{tot} - N_B, respectively. The variation in the number of assessed drops undergoing breakage is the result of a demand to obtain a reasonable statistical precision, rather than obtaining a predetermined number. It follows that the total amount of assessed drops in each data point varies as the probability of breakage varies for the data points.

While it is possible to quickly obtain videos where each video contains an observation of a single drop, the interpretation of the videos is time consuming and labor intensive. In particular, videos containing a breakage event require substantial manual input. Thus, the choice of the considered number of drops undergoing breakage is an important step in determining the individual data points. The data points obtained at 1.0 m/s were investigated to determine the number of experiments required for a reasonable statistical precision, in addition to investigate the general breakage phenomena. This number of experiments were found in the previous study by Herø et al. (2020) to be less than 35 drops undergoing breakage.

The procedure for determining the required number of assessed drops undergoing breakage for the data points at velocities 1.5 m/s and 2.0 m/s was based on the statistical analysis in Herø et al. (2020, P.19). In that study, it was shown that for this experimental system the largest confidence interval limits are found for the breakage times. This is especially due to large standard deviations in these values. When the number of assessed drops undergoing breakage approached 30, the standard deviation was stable and a significant increase in the precision in the confidence interval limits is time consuming. Hence, the procedure for the data points at velocities 1.5 m/s and 2.0 m/s required the confidence interval limits for the breakage time, according to the initial breakage event definition, to be $\lesssim 15\%$. This condition was checked when the number of assessed drops undergoing breakage investigated was more than 20. The resulting number of assessed drops required for the velocities 1.5 m/s and 2.0 m/s were lower than the data points obtained at 1.0 m/s.

As can be seen in Table 2, each data point is associated with unique D_m and ϵ values. Both D_m and ϵ are independent variables in the kernel functions. The experimentally determined kernel function values for the data points are compared in the results and discussion section. For this purpose the experimental data in Table 2 have been divided into three groups numbered A to C. Group A consists of the data points 1, 6 and 8, as these points have D_m values in the narrow range $\sim$1 to $\sim$1.1 mm. Similarly, group B consists of the two data points 5 and 7, which have intermediate D_m values in the narrow range of 0.86 and 0.87 mm. Group C consists of the data points 1, 2, 3 and 4, which have relatively low ϵ values in a narrow range of $0.09 - 0.15\ m^2/s^3$.

Another way of comparing data is to account for simultaneous changes in both D_m and ϵ by observing changes in the kernel function values with respect to variations in the Weber number value. In this study, the Weber number value is computed according to (21), where $\overline{\delta u^2}$ is determined using the full turbulent spectrum

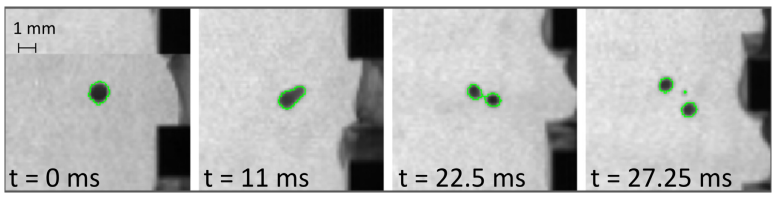

Fig. 2. Images from a breakage sequence of a 0.99 mm in diameter drop. The breakup results in two near equal sized daughters and one small daughter.

Table 2
The experimentally determined data points. # denotes an reference number for the given data point. U is the cross sectional area averaged velocity during the experiments, D_m is the mother drop diameter, N_B is the number of assessed drops undergoing breakage, N_{tot} is the total number of assessed drops, ϵ is the turbulent kinetic energy dissipation rate, k is the turbulent kinetic energy and We_S is the Weber number value according to (21) and (11). SD denotes the standard deviation and CI denotes the 95% confidence interval limits.

#	U [m/s]	$D_m \pm$ SD [mm]	N_B / N_{tot}	$\epsilon \pm$ CI [m^2/s^3]	k $\pm$ CI [m^2/s^2]	We_S
1	1.0	1.0 $\pm$ 0.2	35/ 284	0.15 $\pm$ 0.03	0.022 $\pm$ 0.004	0.530
2		1.48 $\pm$ 0.08	115/ 379	0.13 $\pm$ 0.02	0.02 $\pm$ 0.002	1.02
3		1.87 $\pm$ 0.05	53/ 148	0.1 $\pm$ 0.02	0.016 $\pm$ 0.002	1.29
4		2.23 $\pm$ 0.06	83/ 154	0.09 $\pm$ 0.02	0.014 $\pm$ 0.002	1.61
5	1.5	0.87 $\pm$ 0.04	25/ 26	0.41 $\pm$ 0.09	0.038 $\pm$ 0.006	0.858
6		1.13 $\pm$ 0.01	30/ 64	0.38 $\pm$ 0.07	0.038 $\pm$ 0.005	1.35
7	2.0	0.86 $\pm$ 0.03	30/ 34	0.9 $\pm$ 0.3	0.07 $\pm$ 0.01	1.52
8		1.02 $\pm$ 0.02	30/ 51	0.6 $\pm$ 0.2	0.06 $\pm$ 0.01	1.57

(11). γ is found in Table 1 and the continuous phase density is set as 1000 kg/m^3.

It is noted that the standard deviation and confidence interval limits of Table 2 are not measurements of the uncertainty in the conventional sense. In the procedure of this study, the D_m, ϵ and k are determined for each breakage event individually. In particular, each assessed drop is assigned individual turbulent characteristics values based on its trajectory in the experimental region. Hence, there may be some variation between the individually assessed drops, and between the average of breaking and the average of non-breaking drops. When the individual values are grouped into data points, the standard deviation and confidence interval limits are measurements of how similar the grouped variables are.

2.4. Interpretation of kernel functions

The kernel functions are determined according to the procedure given by Herø et al. (2019, 2020). In short, the breakage time and the average number of daughters is taken as the respective averages of the set of values determined from the individual experiments. Breakage probability is taken as the ratio of videos with breakage to the total number of videos. Hence, videos without breakage are required to determine the breakage probability. To associate a turbulence level with the experiments without breakage, the maximum ϵ level along the recorded drop path is taken. The breakage frequency is determined from the breakage probability and breakage time according to (25). The daughter size distribution is determined from:

$$\Delta P^*_{DSD}(V_m, V_d) = \frac{\text{Number of particles in range } [V_d - \Delta V_d/2,\ V_d + \Delta V_d/2]}{\text{Total number of particles in range} [0,\ V_m]} \tag{35}$$

in which ΔV_d is a range in the daughter sizes. ΔP^*_{DSD} is a discrete and dimensionless daughter size distribution, which has one value for each range of daughter sizes considered. Each determined value of ΔP^*_{DSD} corresponds to the integral of the kernel function P_{DSD} over the daughter size range, $[V_d - \Delta V_d/2,\ V_d + \Delta V_d/2]$ as seen above.

While the models are formulated in a Eulerian framework, the experimental data is essentially determined in an Langrangian framework, taken from a larger volume. This is a practically necessary simplification, the impact of which was discussed in Herø et al. (2020, P.19). It is noted that the breakage frequency is determined from the breakage time and the breakage probability. The breakage time is determined from local values associated with each breakage event while the breakage probability is determined as an average value of the whole test section. The limiting accuracy of the breakage probability function might require improvements, thus other approaches for determining this kernel function have been suggested in the literature (Vejražka et al. (2018), Håkansson (2020)).

3. Results and discussion

3.1. Turbulent forces

In this section, the three formulations of the turbulent stress, as described in Section 1.1, are investigated. The turbulent inertial stress (19) is computed using both formulations of the second order structure function, $\overline{\delta u^2}$. That is, the inertial subrange formulation (10) and the formulation valid for the entire range of turbulence (11). In addition, the formulation valid in the entire range of turbulence is used to compute a turbulent shear stress according to (23). The stresses are computed for each data point using the values in Table 2. The results are shown in Fig. 3, plotted against the determined ϵ of the data point. Note that the lines connecting the data points are introduced for ease of comparison. As the turbulent characteristics and D_m varies for each point, a first approach is to identify trends in the data.

From Fig. 3 it is clear that the shear stress (23), marked with stars, is very small compared to the inertial stresses (19). The value of the shear stress (23) is about 1% of the value of the inertial stress valid for the entire range of turbulence (19) and (11), marked with triangles, for each data point. As can be seen in the following sections, the 95% confidence interval limits of the kernel functions are significantly larger than 1%. Thus, the impact of the shear stress on the breakage phenomena is considered negligible in this study.

It can also be seen from Fig. 3 that the two formulations of $\overline{\delta u^2}$ results in different stresses. When considering the entire range of turbulence (11) the stresses are lower than when considering only the inertial subrange of turbulence (10). This indicates that the droplet sizes are not in the inertial subrange and the expression of $\overline{\delta u^2}$ is important for accurate determination of the turbulent stress.

This indication can be confirmed by computing the energy spectrum (4) and comparing with the droplet size. The resulting energy spectrum, and the drop position with respect to the inertial range, are similar for all data points. Data point 6 is chosen for visualization, and the energy spectrum for this point is shown in Fig. 4. As can be seen from the figure, the energy spectrum has a small inertial range (blue shaded area) and the droplet falls some value below this range, near the largest scales of the dissipation subrange.

In addition, Fig. 4 illustrates why the shear forces computed from (23) are very small. These forces are dominant from η and smaller scales, but the mother drop size is significantly larger than η.

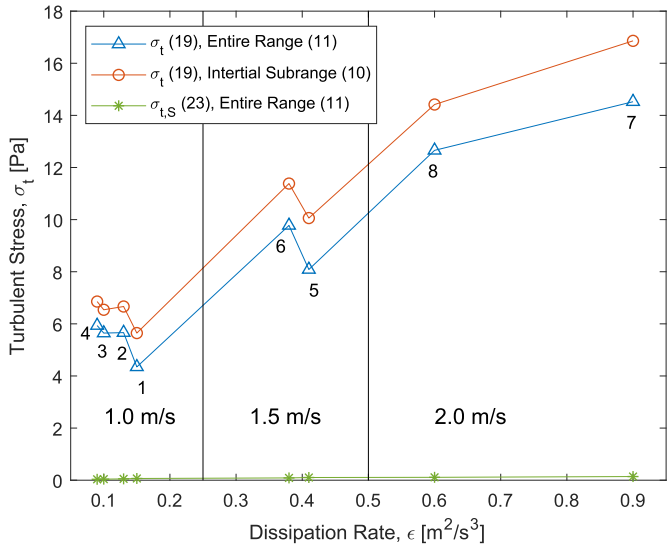

Fig. 3. Computed turbulent stresses, σ_t, for the different data points plotted against the determined ϵ of the data point. The numbers represent the reference number found in Table 2. The vertical lines separates the data points obtained under different area averaged velocities, denoted U in Table 2.

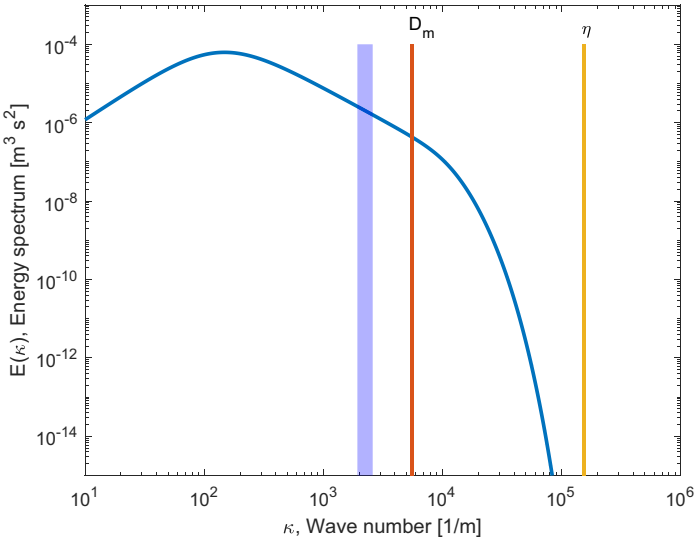

Fig. 4. Energy spectrum for data point 6 in Table 2, computed using (4). D_m denotes the wavenumber of the mother drop, while η denotes the wavenumber of the Kolmogorov micro scale. The blue shaded area is the inertial range, which according to Pope (2000), denotes the range from $L/6$ to 60η.

A final note on the turbulent forces; it was shown in Herø et al. (2020) that the model framework by Martínez-Bazán et al. (1999a, b, 2010) does not predict breakage for this low levels of turbulence.

3.2. Average number of daughters

When considering the initial breakage event definition, the average number of daughters, ν, is always determined to be two. Thus, the average number of daughters is not a function of the system properties or turbulent characteristics. This result is in line with the work of Herø et al. (2020), Maaß et al. (2011) and Solsvik et al. (2016b). The two latter studies suggested that for the initial breakage definition the average number of daughters will tend to two for high video frame rates. This result is also in line with the assumption that two drops are produced upon breakage. This assumption is commonly adopted when developing the breakage source term closure.

On the other hand, the average number of daughters according to the cascade breakage definition varies for the different data points. The average number of daughters formed after breakage is never two for any data point. However, binary breakage is observed in 10 out of 35 breakages (i.e. 10/35), 28/115, 16/53, 23/83, 5/25, 13/30, 8/30 and 5/30 for the data points 1 through 8, respectively. The determined average number of daughters can be seen plotted by the Weber number value in Fig. 5. The Weber number is used because the average number of daughters show a dependency on both D_m and ϵ. The combined effect appears to be well described by the Weber number value, as seen from the figure. It can also be seen that there is a very large standard deviation for each data point. This is due to the large number of possible outcomes of individual breakage events, as investigated in Herø et al. (2020). Similarly large standard deviations have previously been reported by Galinat et al. (2005).

In the study by Galinat et al. (2005), the average number of daughters ranged between ∼3–8 for Weber number values ranging between ∼17–65. Another study reporting the average number of daughters for different mean flow conditions is Ashar et al. (2018). For Weber number values in the range 0–8, the average number of daughters were 3, while for Weber number values larger than 32, the average number of daughters were 7. Note that the Weber number values in Ashar et al. (2018) have been multiplied by 4 when reported in this study. This is to account for the prefactor of 4 used by Ashar et al. (2018) in the surface stress (20) that results in a Weber number formulation which is 1/4 of the formulation in this study (21).

The data from these three studies imply that a similar range of average number of daughters are obtained in the breakage events, from ∼3 to ∼8, but for very different Weber number values. These Weber number value differences probably occur because the Weber number only contains some of the variables and physical properties having an impact on the average number of daughters. In particular, the Weber number definition does not include the dispersed phase viscosity, μ_d. As discussed in the introduction, the dispersed phase viscosity may be stabilizing deforming droplets. The difference in the dispersed phase viscosity for the three experimental studies mentioned above are significant, with the dispersed phase viscosities given as $4.5 \cdot 10^4$ kg/(m s), $9.09 \cdot 10^3$ kg/(m s) and $70 \cdot 10^3$ kg/(m s) for Galinat et al. (2005), the current study and Ashar et al. (2018), respectively. However, as will later be shown in Section 3.6, the dispersed phase viscosity does not

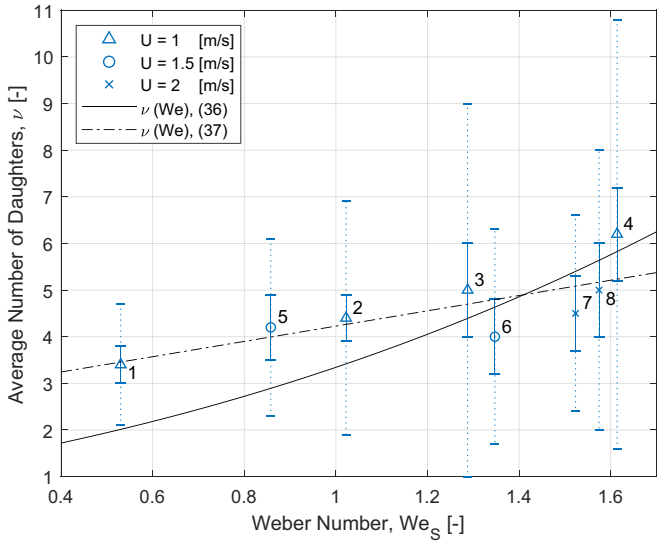

Fig. 5. Average number of daughters plotted against the Weber number calculated from the entire range of turbulence, as seen in Table 2. The solid errorbars denote the 95% confidence interval limits, while the dotted errorbars denote the standard deviation. The point marker of the data point symbolizes the cross sectional area averaged velocity during the experiments. Additionally, fitted model predictions are shown for (36) and (37).

affect the breakage frequency. While this is not conclusive on the viscosity's impact on the average number of daughters, alternative explanations may need to be considered.

An alternative reason for the differences in the Weber number values is the differences in the experimental setup and approximation of the disruptive force (19) in these studies:

- Based on the theoretical pressure drop in orifice flow (Galinat et al. (2005))
- Based on the rotor speed and PIV-measurements in a static mixer (Ashar et al. (2018))
- Based on LDV-measurements in a channel flow (this study)

Based on the results shown in Fig. 5, there appears to be a correlation between the average number of daughters and the Weber number value of the data point. Galinat et al. (2005) suggested that the correlation is on the form

$$\nu(\mathrm{We}_S) = (a\mathrm{We}_S + 1)^3 \tag{36}$$

where a was suggested to be 0.016, based on their results. In this study, a has been fitted in MATLAB using the *fit* function, yielding a value of 0.50. The resulting model prediction is plotted in Fig. 5 as a solid line.

As can be seen from the figure, the fit is reasonable, but less accurate for the lowest Weber number values. It should be noted that the model fit of (36) was less accurate for the small Weber number values also in the original study of Galinat et al. (2005). In this study, a linear function has been fitted to the results

$$\nu(\mathrm{We}_S) = a\mathrm{We}_S + b \tag{37}$$

Here a was determined to be 1.64 and b to be 2.59. The resulting model prediction is shown as a dashed and dotted line in Fig. 5. This relation appears to provide a reasonable fit, although a rigorous mechanistic model development would probably be more universal.

3.3. Daughter size distribution function

3.3.1. Initial breakage event definition

The daughter size distributions according to the initial breakage event definition, for the four novel data points of this study, are shown in Fig. 6. The bell shaped model prediction of (34) by Coulaloglou and Tavlarides (1977) is included in Fig. 6 for comparison purposes. While other models may fit an individual distribution more accurately, no single model framework can describe all the distributions.

The only W-distribution, when considering both the data given by Herø et al. (2020) and Fig. 6, can be seen in Fig. 6a. Here, the most frequent daughter volume fraction is equal sized. In addition it is common to observe one large and one smaller drop, when the volume fraction of the larger drop is at least 0.77. Other volume fractions are rarely produced upon breakage.

The daughter size distribution in Fig. 6b has an irregular shape where equal sized breakage is seldom observed. The lack of equal sized breakage is a significant difference from the other data points. The most common outcome is one drop of a size corresponding to the largest bin size and one complimentary small drop, while the remaining daughter size bins show a nearly uniform distribution.

Contrary to the two data points considered above, the daughter size distributions shown in the Figs. 6c and 6d have similar shapes. These daughter size distributions both exhibit a large frequency of one large and one small drop. Otherwise, the distributions are uniform with a small increase in the frequency of equal sized daughters.

The data points 1, 2 and 3 of Table 2 were all shown to have near uniform distributions in Herø et al. (2020). Data point number 4 was also more uniform than the distributions shown in Fig. 6.

From these results, it can be seen that the shape of the daughter size distribution function may change locally. This change may be due to variations in ϵ, D_m, Weber number value, system properties, etc. However, no pattern or correlation between the changing shape and these parameters have been identified.

A possible explanation for the lack of clear patterns in the daughter size distributions could be found in the experimental setup and procedure. The average number of daughters in the cascade breakage event definition is ∼4–5 for all data points, as discussed in Section 3.2. Thus, the initial daughters are often having irregular shapes, as these daughters undergo further deformation and breakup. When recording the projected 2D area of these shapes, an inaccuracy is introduced. The effect of this inaccuracy on the daughter size distribution is unknown. Conversely, it may be argued that the initial breakage definition is not able to describe the physical phenomena, as the initial breakage daughter drops are not stable drops produced upon breakage. Rather, the daughter drops are unstable intermediary daughters in a sequence, or cascade, of breakages. The view that the initial breakage definition could not correspond to the observed breakage phenomena was first reported by Solsvik et al. (2016b).

Maaß et al. (2007, 2011) has previously reported the daughter size distributions of binary breakages according to the initial breakage. In Maaß et al. (2007), one distribution is given by diameter, which complicates the discussion of shape. However, there appears to be a preference for droplet sizes of non-dimensional diameter of 0.8 or higher, which corresponds to volume fractions of 0.5 or higher. In Maaß et al. (2011) two daughter size distributions are given, each with a 1000 samples and 50 bins, for D_m values of 0.64 mm and 1.0 mm. Even at this accuracy, the distributions were not equal. Moreover, neighboring bins showed significant variations in height, as seen in the current study. Finally, the distribution of the largest D_m was best described by a U-distribution and the smallest D_m was best described by a uniform distribution.

3.3.2. Cascade breakage event definition

The daughter size distributions according to the cascade breakage event definition determined in this study are shown in Fig. 7. As can be seen from the figure, there are similar shapes for all of the data points. For the smallest daughters there is a large probability. Then, the probability lowers for increasing volume fraction of the daughter drop. The curve flattens and approaches an asymptotic value, such that the larger daughter droplet sizes have a near uniform distribution. The distributions vary in the probability of the smallest drops, the rate at which the distribution approaches the uniform distribution and the probability of the near uniform distribution of the largest daughter drop sizes. These results are very similar to the results for data points 1, 2, 3 and 4, given by Herø et al. (2020).

The distribution must be closely linked to or depend on the average number of daughters, such that the system is number and volume conserving. Given that the average number of daughters vary for each data point, as discussed in Section 3.2, the daughter size distributions should vary for the different data points. This can be seen in Fig. 7. Consider first Figs. 7a and 7b, where ν is 4.2 and 4, respectively. Here, the probability that a given daughter drop corresponds to the smallest bin is less than 0.5. In Fig. 7c, where ν is 4.5, the probability increases to above 0.5. Then, the probability that a given daughter drop corresponds to the smallest bin is further increased for ν equal to 5, as seen in Fig. 7d, where the probability is approaching 0.6. In addition, it can be seen that for all the distributions, the probability of a daughter drop size

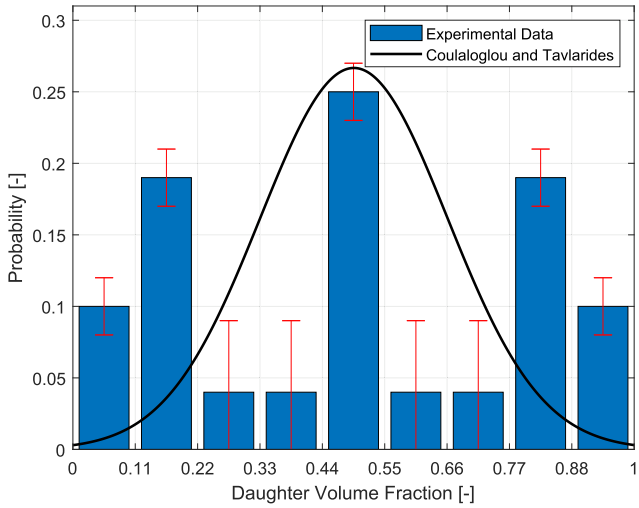

(a) Data point number 5. Mother drop diameter of 0.87 mm, U = 1.5 m/s

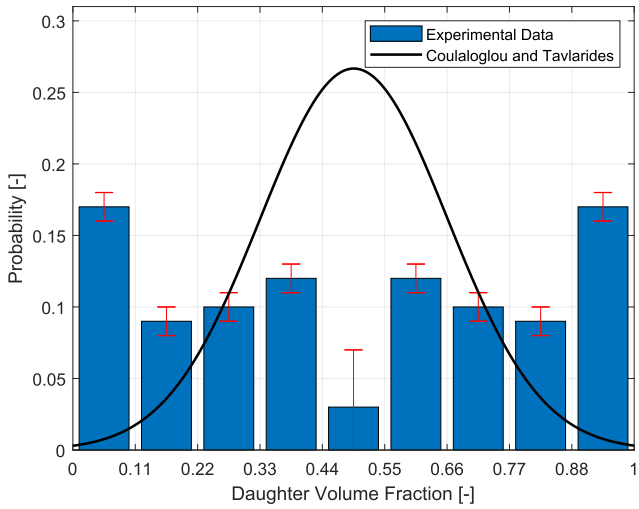

(b) Data point number 6. Mother drop diameter 1.13 mm, U = 1.5 m/s

Fig. 6. Daughter size distributions, calculated according to (35) and utilizing the initial breakage definition. The model predictions are computed from (34) by Coulaloglou and Tavlarides (1977).

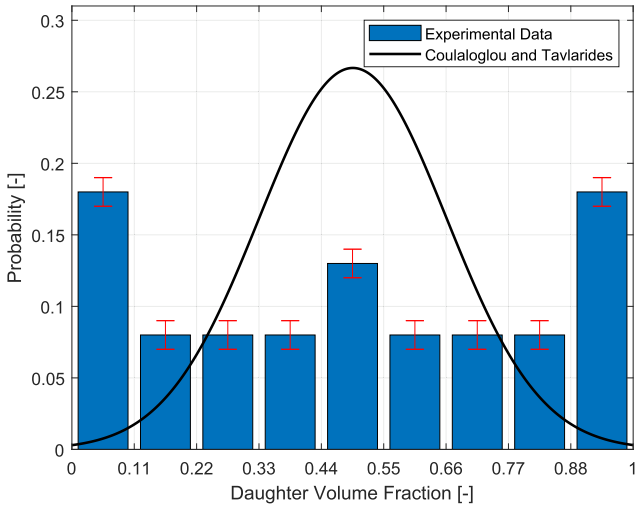

(c) Data point number 7. Mother drop diameter 0.86 mm, U = 2 m/s

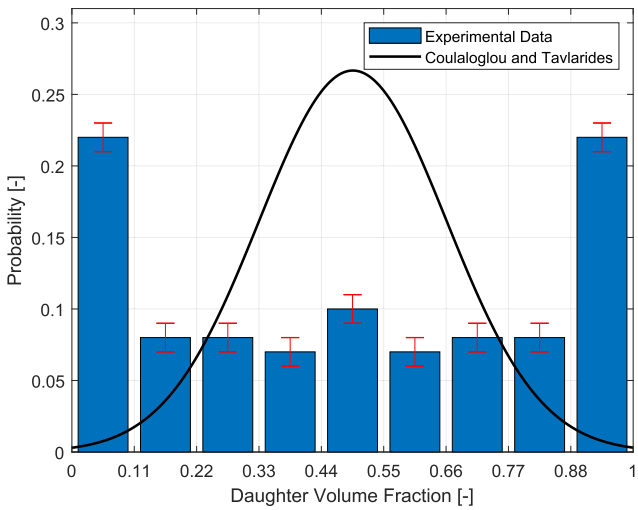

(d) Data point number 8. Mother drop diameter 1.02 mm, U = 2 m/s

Fig. 6 (*continued*)

corresponding to the second smallest bin stays approximately the same for all v. As the bins sum to 1, it follows that the rest of the bins decrease with increasing v.

The impact of v on the daughter size distribution can be compared over a wider range of v by comparing the daughter size distributions of the data points numbered 1, 4, 6 and 8 in Table 2. This

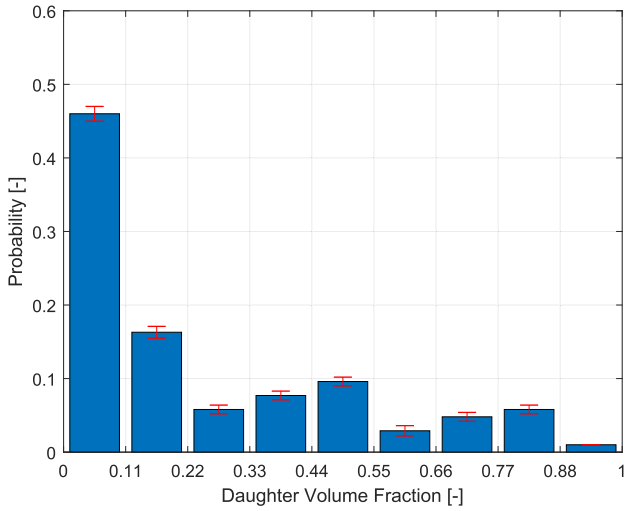

(a) Data point number 5. Mother drop diameter 0.87 mm, U = 1.5 m/s, $\nu = 4.2$

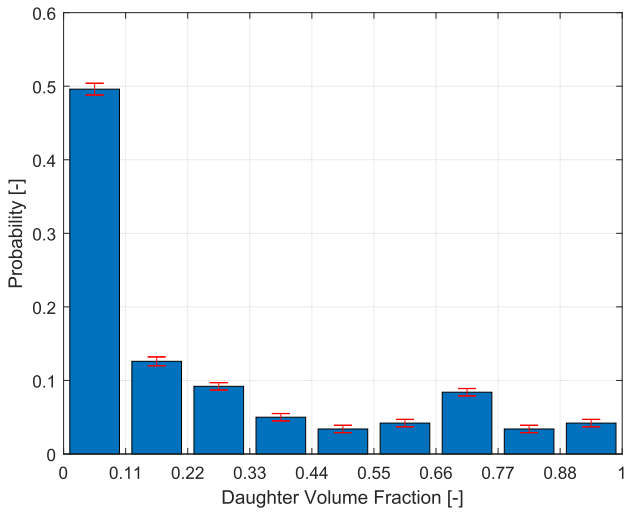

(b) Data point number 6. Mother drop diameter 1.13 mm, U = 1.5 m/s, $\nu = 4$

Fig. 7. Daughter size distributions, calculated according to (35) and utilizing the cascade breakage definition.

is shown in Fig. 8. Note that data points 1 and 4 are not given in Fig. 7, they were given in Herø et al. (2020). To obtain the plots shown in Fig. 8, the bins of the histograms are converted to points. For each bin, the height is taken as the y-coordinate of the corresponding point. The x-coordinate is found from the horizontal midpoint of the bin. The resulting points are plotted with straight lines

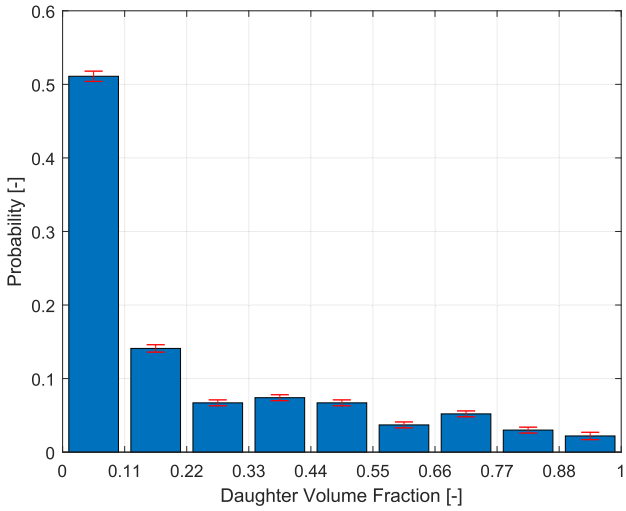

(c) Data point number 7. Mother drop diameter 0.86 mm, U = 2 m/s, $\nu = 4.5$

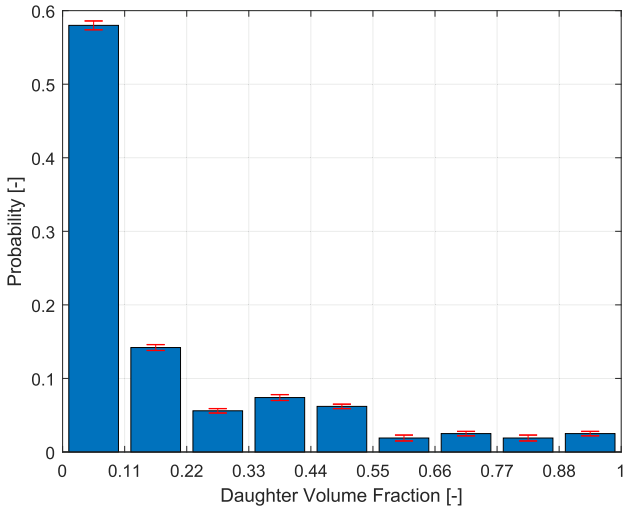

(d) Data point number 8. Mother drop diameter 1.02 mm, U = 2 m/s, $\nu = 5$

Fig. 7 (*continued*)

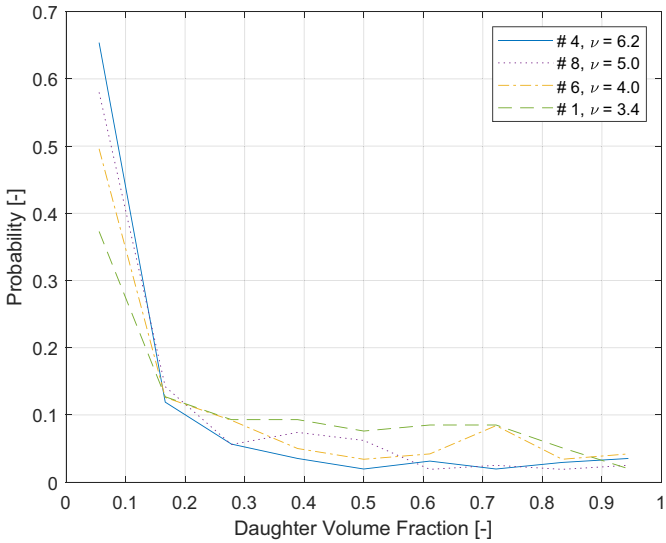

Fig. 8. Daughter size distributions of the data points numbered 1, 4, 6 and 8 in Table 2. The average number of daughters of the data point are shown in the legend.

between the points for ease of comparison. The procedure is repeated for each of the four data points investigated.

From Fig. 8 it is clear that an increase in ν leads to an increase in the probability of the smallest daughter drop size bin. That is, when a larger number of daughters are produced upon breakage, the additional daughters are mainly of the smallest drop size. This trend is in agreement with the experimental observations, where it is commonly observed that small daughter drops are formed from the thread between two larger daughter drops. For the remaining larger bins, the probability approach a uniform distribution. Possibly, there is a lower probability of obtaining the largest bin. However, Fig. 8 is not conclusive on this point.

To the authors knowledge, none of the existing models for the daughter size distribution predicts the general shape found in this study. Which is an obvious result for the models considering binary breakage, but also true for the few model concepts allowing for non-binary breakage. Moreover, the existing models do not account for differences in the shape due to different flow conditions. This may be explained partly by the lack of experimental data on the daughter size distribution. Apart from the study by Herø et al. (2020), the daughter size distribution function is seldom reported for single drop experiments in which the cascade breakage event definition has been employed. The one known example is the study by Galinat et al. (2005). In their study, the results are grouped in large groups by Weber number values, which makes comparison difficult. Additionally, their Weber number values are much larger than those reported in this study.

3.3.3. Average daughter size

For completion, the average daughter size is computed and shown in Table 3. As there are two breakage event definitions there are also two average daughter sizes, one for each definition. From the Table 3 it can be seen that the daughter sizes exhibit large standard deviations. These standard deviations are expected, as a large variety of different daughter sizes are observed, as seen in the previous sections.

For the average daughter sizes them self, the results are as expected. The initial breakage event definition always results in binary breakage. Hence, the average daughter size is about half the mother drop size. For the cascade breakage event definition, the range of average daughter sizes is narrow, 0.2–0.4 mm for all data points. This is also expected as all data points exhibit a large number of very small drops, as seen in Fig. 7.

3.4. Breakage time

3.4.1. Initial breakage event definition

The initial breakage time, the breakage time determined according to the initial breakage definition, is shown in Fig. 9. The breakage time is plotted against the ϵ values of the data points. Herø et al. (2020) found that the D_m value has a significant impact

Table 3
The average daughter size occurring after a breakage. IB denotes the Initial Breakage Event Definition and CB denotes the Cascade Breakage Event Definition. SD denotes the Standard Deviation.

Data point	Mother Drop Size [mm]	Average daughter size IB ± SD [mm]	Average daughter size CB ± SD [mm]
1	1.0	0.5 ± 0.3	0.2 ± 0.3
2	1.48	0.7 ± 0.4	0.3 ± 0.4
3	1.87	0.9 ± 0.6	0.4 ± 0.5
4	2.23	1.1 ± 0.7	0.4 ± 0.6
5	0.87	0.4 ± 0.3	0.2 ± 0.2
6	1.13	0.6 ± 0.4	0.3 ± 0.3
7	0.86	0.4 ± 0.3	0.2 ± 0.2
8	1.02	0.5 ± 0.3	0.2 ± 0.2

on the breakage time for similar ϵ values. The corresponding data points are Group C, which was defined in Section 2.3 as data points 1, 2, 3 and 4. In Fig. 9, these data points are in a descending order with respect to the D_m values. That is, data point 4 has the largest D_m value and data point 1 has the smallest D_m value. Thus, it can be seen that the breakage time decreases with decreasing D_m value.

In other words, to investigate the impact of ϵ on the breakage time, it is important to compare data points of similar D_m values. The data points in Group A are marked with an x in Fig. 9. These points are the three data points 1, 6 and 8, which all have a D_m values in the range 1.0 to 1.13 mm. Similarly, Group B is the two data points 5 and 7 which have D_m values in the range 0.86 to 0.87 mm. These two points are marked by a circle in the figure. Both sets of data points show a weak trend of decreasing breakage time with increasing ϵ values.

Model fitting is performed to further investigate the relationship between breakage time, ϵ and D_m. The parameter c_3 in (28), using the expression of $\overline{\delta u^2}$ valid in the entire range of turbulence (11) is fitted to the experimentally determined breakage time for seven of the eight data points. Data point 4 is not used in this fitting procedure. For this point, the ϵ associated with breakage events is significantly lower than the ϵ associated with non-breaking events, as shown by Herø et al. (2020). This is possible as each assed drop is assigned an individual ϵ value based on its trajectory in the experimental region, as discussed in Section 2.3. Due to the sensitivity of (28) to ϵ, including data point 4 would lead to a less accurate model fit for the seven remaining data points, for which this anomalous behavior is not present.

The fitting procedure is performed in MATLAB by using a linear equation on the form $y = ax$. Here, y is the experimentally determined breakage time of the data point and a is the parameter c_3. x is the expression $\frac{D_m}{\sqrt{\overline{\delta u^2}(D_m)}}$ in (28), using (11) for $\overline{\delta u^2}$ and computed with the ϵ, k and D_m values of the data point.

The value of the parameter c_3 found from the fitting procedure described above is 1.86. The value found by Herø et al. (2020) was 2.15. Other experimentally determined values of the parameter c_3 are not available in the literature. For comparison, the parameter in the inertial range formulation (27) is fitted to the same data using the same procedure as given above. The value of the parameter c_2 is found to be 1.43, which is very close to the value of 1.46 found by Herø et al. (2020). Maaß and Kraume (2012) found the value of this parameter to be ~1.1. The value of c_2 found in this study is thus in line with previous investigations.

The predictions of the fitted relations (27) and (28) are very similar for all data points. This is despite the different magnitude of the turbulent stresses, as discussed in Section 3.1. Thus, only the fitted (28) is included in Fig. 9. These model predictions are shown as squares with a dashed and dotted line. As can be seen from the figure, all predictions are within or close to the 95% confidence interval limits for the seven fitted data points. Hence, both models adequately describes the impact of ϵ on the breakage time for the given data points. The two models also account for the impact of the D_m value.

Few studies in the literature have determined the breakage time for different turbulence levels. Andersson and Andersson (2006) and Maaß and Kraume (2012) investigated drops of 1 mm in diameter. The area averaged ϵ was varied by changing the cross sectional area averaged velocity. Andersson and Andersson (2006) found that octanol drops have a breakage time of 10.9 and 5.6 ms

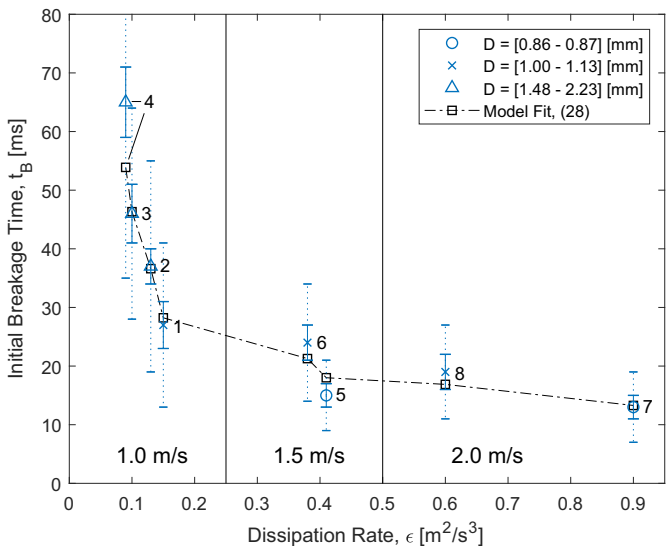

Fig. 9. Averaged breakage time considering the initial breakage definition for the data points in Table 2. For each data point, the solid line errorbars denote the 95% confidence interval limits, while the dashed lines errorbars denote the standard deviation. The vertical lines separates the data points obtained under different cross sectional area averaged velocities. The point symbols denotes the mother drop size of the data point. The model predictions by Coulaloglou and Tavlarides (1977), Eq. (28), are indicated by the dashed and dotted line with square symbols.

for ϵ values of 1.13 and 3.69 m^2/s^3, respectively. For dodecane drops the breakage time was 7.6 and 4.2 ms for ϵ values of 3.69 and 8.54 m^2/s^3. Maaß and Kraume (2012) performed experiments with three different cross sectional area averaged velocities, giving ϵ values of 2.3, 6.0 and 12.5 m^2/s^3, respectively. This resulted in breakage times for toluene drops of 6.0, 4.7 and 3.7 ms and for petroleum drops the breakage times were 4.4, 3.4 and 2.8 ms.

The breakage times in this study are significantly longer than those found by Andersson and Andersson (2006) and Maaß and Kraume (2012). This is likely due to the lower ϵ considered in this study, as well as different fluid and system properties. Moreover, the studies have further differences, such as different setups, breakage event definitions, etc. Due to these differences, it is difficult to directly compare the results and draw firm conclusions. Yet, it is clear that breakage time decreases as ϵ increases, in accordance with the model by Coulaloglou and Tavlarides (1977).

3.4.2. Cascade breakage event definition

The cascade breakage time, the breakage time determined according to the cascade breakage event definition, is shown in Fig. 10. Compared to the initial breakage time, each data point exhibits a longer breakage time when considering the cascade breakage event definition. This result is to be expected when considering the breakage event definitions as presented in Section 2.2. As was the case for the initial breakage time, Herø et al. (2020) showed that the cascade breakage time was significantly dependent on the D_m value. The corresponding data points are Group C, which was defined in Section 2.3 as data points 1, 2, 3 and 4. These data points have D_m values in the range 1.0–2.2 mm, where point 4 has the largest D_m value and point 1 has the smallest D_m value. Thus, it can be seen that the breakage time decreases with decreasing D_m value.

Due to the dependence of the breakage time on the D_m value, data points of similar D_m values must be considered when investigating the impact of ϵ on the breakage time directly from Fig. 10. Group A are marked by an x in the figure. These are the data points 1, 6 and 8, which have a D_m values in the range 1.0 to 1.13 mm. The data points in Group A could indicate a slightly decreasing trend of the breakage time with increasing ϵ. On the other hand, when considering the value of the 95% confidence interval limits, there may be no change in the data.

Group B contains the data points with D_m values in the range 0.86–0.87 mm and consists of the data points 5 and 7 from Table 2. This group is marked by circles in Fig. 10. These data points indicate the same trend in the data as Group A above; a very slight decrease or no change for the breakage time with increasing ϵ.

As was done for the initial breakage time, model fitting is performed to further investigate the relationship between breakage time, ϵ and D_m. The procedure is the same as described in Section 3.4.1. For c_3, the parameter found in (28), the value is determined to be 2.90. The value found by Herø et al. (2020) was 3.35. For the inertial range formulation (27) the parameter value of c_2 was determined to be 2.24. This is close to the value of 2.26 found by Herø et al. (2020). In the original study by Coulaloglou and Tavlarides (1977) this parameter value was found to be ∼6.33, when fitted to data from dense dispersion experiments.

The fitted relations (27) and (28) give very similar predictions for all data points. Thus, only the fit of (28) to the experimental data is included in Fig. 10, shown as squares with a dotted line. In general, the model predictions are in reasonable agreement with

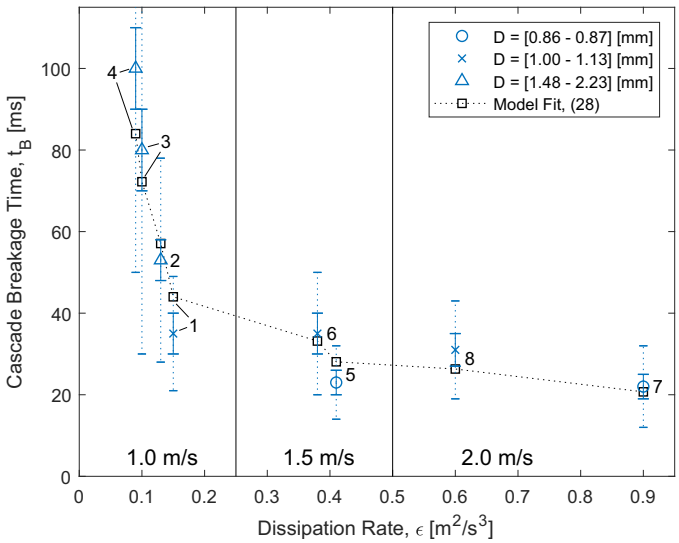

Fig. 10. Averaged breakage time considering the cascade breakage definition for the data points in Table 2. For each data point, the solid line errorbars denote the 95% confidence interval limits, while the dashed lines errorbars denote the standard deviation. The vertical lines separates the data points obtained under different cross sectional area averaged velocities. The point symbols denotes the mother drop size of the data point. The model predictions by Coulaloglou and Tavlarides (1977), Eq. (28), are indicated by the dotted line with square symbols.

the experimental data for the seven fitted data points, 1–3 and 5–8. However, the model predictions of the cascade breakage time are less accurate than the corresponding model predictions of the initial breakage time. For the cascade breakage time, three predictions of data points 1, 5 and 8 are outside the 95% confidence interval of the experimental data values. On the other hand, only the data point 5 was outside the confidence interval for the initial breakage time. It appears that the models do not accurately describe the change in breakage time with the changes the ϵ values. The expression (28) is better suited for determining the initial breakage time, than for the full breakup process in the cascade breakage event definition.

3.5. Breakage probability

The experimentally determined breakage probability is shown in Fig. 11. The breakage probability is the only source term constitutive equation that coincides for both the initial and the cascade breakage event definitions. While the breakage probability is plotted against the ϵ of the data point only, there is still a significant dependence on the D_m value. The D_m value of each data point may be seen in Table 2. For the four points in Group C, point 1, 2, 3 and 4, Herø et al. (2020) found that the breakage probability increased for increasing D_m value.

As was done for the breakage time, the impact of ϵ on the breakage probability can be investigated by considering data points with similar D_m value. Group A, marked by x in Fig. 11, contains the data points 1, 6 and 8 which all have D_m values in the range 1.0 to 1.13 mm. From these data points, it can be seen that there is a clear trend that increasing ϵ leads to increased probability. These result are in line with the current understanding of the breakage probability reported in the literature.

Very different results can be seen from Group B, representing the two data points 5 and 7 where the D_m values are in the range 0.86 to 0.87 mm. These data points are marked by a circle in Fig. 11. These data points exhibit much higher breakage probabilities than the other data points. This is despite the fact that these data points have the smallest droplet sizes, which is generally associated with a lower breakage probability. In addition, there is a trend of slightly decreasing breakage probability for increasing ϵ. Hence, the probabilities obtained for the data points in Group B do not follow the expected behavior for ϵ and D_m. These anomalous data points will be further discussed in Section 3.5.2.

The predictions of the model of Coulaloglou and Tavlarides (1977) were in reasonable agreement with the experimental data presented by Herø et al. (2020). Hence, the probability data is compared with the model to confirm that the anomalies of this study are not in line with expected behavior. That is, the results cannot be explained by the different combinations of D_m and ϵ for the different data points. Both the model version valid in the inertial subrange of turbulence (26) and the model version valid in the entire range of turbulence (29) are examined. To fit a linear function to the data in MATLAB, the natural logarithm is taken of the expressions in (26) and (29). The results are two equations on the form $y = ax$ where y is the logarithm of the experimentally determined breakage probability. x is the expression in the exponential of either (26) and (29), except the parameter which is denoted by a. The value of x is computed with the ϵ, k and D_m values of the corresponding data point, and the ρ_d and γ given in Section 2.

The value of c_1 is found to be 0.45 when fitting to all of the experimental data. This value is significantly different from the

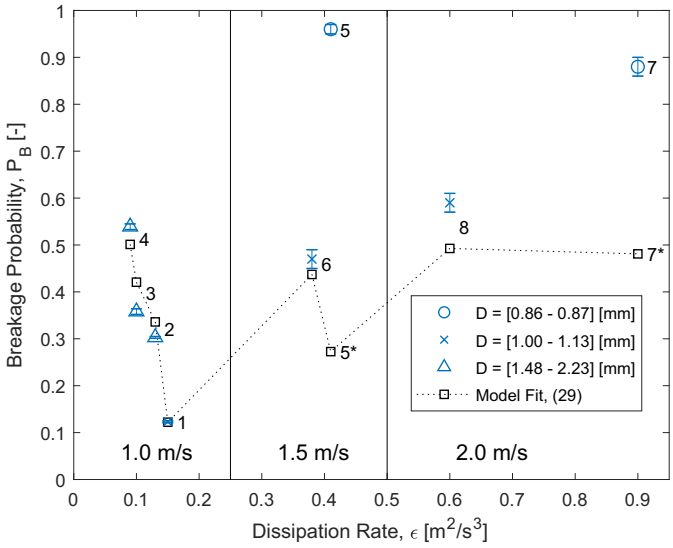

Fig. 11. Breakage probability plotted against the turbulent energy dissipation rate, ϵ, for the data points in Table 2. The errorbars denotes the 95% confidence interval limits and the point symbols denotes the mother drop size of the data point. The vertical lines separates the data points obtained under different cross sectional area averaged velocity. The model predictions of (29) by Coulaloglou and Tavlarides (1977) are indicated by the square symbols with dotted line.

value 0.59 found by Herø et al. (2020). Furthermore, including the anomalous data in the fitting provides generally poor fits to the experimental results. Instead, the parameters are fitted to the 6 non anomalous data points only, which are data points 1, 2, 3, 4, 6 and 8. This yields the parameter value of c_1 as 0.57. For c_4, the parameter value obtained when fitting the 6 remaining data points is 0.92, while the value of 1.25 was determined in Herø et al. (2020). It is noted that the parameter value of c_1 is debated in the literature. Previously, Maaß and Kraume (2012) reported a parameter value of c_1 to be 0.39, while Coulaloglou and Tavlarides (1977) found the value to be ∼0.182.

The predictions of the two fitted models are similar for each individual data point. Hence, only the fitted model predictions of (29) are shown in Fig. 11 as squares with a dotted line. The model predictions are higher than the experimental results for the two lowest breakage probabilities given by the data points 2 and 3. For the highest breakage probabilities, data points 4 and 5 through 8, the model predictions are lower than the experimental results. Nevertheless, the predictions are in reasonable agreement with the experimental data of the 6 fitted points. For the two anomalies, data points 5 and 7, the two models predict much lower breakage probabilities than the experimental results. The different behavior of these two data points are not explained by the physics represented by the models. A manual verification of the image analysis, and evaluations of alternative models, did not provide further understanding of the two data points.

3.5.1. Breakage probability by weber number values

The breakage probability has not previously been reported for varying ϵ. However, Galinat et al. (2005, 2007) and Ashar et al. (2018) reported the breakage probability against the Weber number values in studies where ϵ was one of the varying parameters. To compare to the data reported in these studies and to investigate the impact of the Weber number value on the breakage probability, the breakage probability has been plotted as a function of the Weber number value in Fig. 12. As above, the two data points corresponding to the smallest D_m values (data points 5 and 7) exhibit a different behavior than the other data points.

As can be seen from Fig. 12, the Weber number values of this study are in the range 0.6–2.2. Compared to the studies by Galinat et al. (2005, 2007) and Ashar et al. (2018), the breakage probability is high for such low Weber number values. In Galinat et al. (2005), the smallest Weber number value of ∼ 7.5 had very low probability of breakage. The breakage probability raised steadily and reached 1 for a Weber number value close to 50. Ashar et al. (2018) had similar results for low Weber number values, with the lowest data point at Weber number values equal to 0.8–3.2 exhibiting no breakages. With Weber number values in the range 3.2–6.4, the breakage probability was ∼0.09, rising to 0.6 for Weber number values in the range 16–24. Note that the Weber number values of Ashar et al. (2018) have been multiplied by 4, as discussed in Section 3.2. In general, the three studies agree that the breakage probability increases with increased Weber number value. On the other hand, similar Weber number values are not associated with similar breakage probability in the different studies. As discussed in Section 3.2, these deviations in Weber number values are probably due to the differences in the physical properties, μ_d in particular, or due to the differences in the experimental setup and approximation of the disruptive force (19) in these studies.

As shown by Galinat et al. (2005), the breakage probability of the model by Coulaloglou and Tavlarides (1977) (26) can be written as a function of the Weber number

$$P_B(\mathrm{We}_S) = a_1 \exp\left(-\frac{b_1}{\mathrm{We}_S}\right) \tag{38}$$

where a_1 and b_1 are parameters. Galinat et al. (2005) also suggested to multiply the exponent term with the Weber number raised to the power of a parameter

$$P_B(\mathrm{We}_S) = \mathrm{We}_S^{a_2} \exp\left(-\frac{b_2}{\mathrm{We}_S}\right) \tag{39}$$

where a_2 and b_2 are parameters. However, the results of this study, as seen in Fig. 12, appears to be close to linear. That is

$$P_B(\mathrm{We}_S) = a_3\mathrm{We}_S + b_3 \tag{40}$$

where a_3 and b_3 are parameters. These three functions have been fitted in MATLAB to the six data points that appears to be close to linear, data points 1, 2, 3, 4, 6 and 8. The resulting parameters can be seen in Table 4, along with the parameters determined by Galinat et al. (2005). Due to the significant differences in the experimental setup and procedure, the parameter values are very different for the two studies. The resulting model predictions have been plotted in Fig. 12. As can be seen from the figure, all of the models provide a similar fit, which is reasonable for the system. Any of the three models employed may describe the current system with reasonable accuracy.

3.5.2. Investigation of anomalies

We summarize the current findings before investigating the two data points referred to as anomalies. Firstly, the anomalous behavior is likely not due to viscous effects, as these forces are very small, as shown in Section 3.1. Secondly, if a data point is an anomaly when considering the breakage probability, it does not impact the other source term constitutive equations determined. As discussed previously, the breakage probability is the only source term constitutive equation determined from non-breaking drops. Any inaccuracies introduced by considering the non-breaking drops has no impact on the kernel functions determined from breaking drops only; v, P_{DSD} and t_B.

Finally, in the experimental procedure employed in this study, the only changes between the different experimental conditions are the continuous phase velocity and the size of the glass cannula used in generating the oil droplets. When determining a data point, the experiments under the same continuous phase velocity are considered. Then, the D_m value is measured when the drop enters the observed region of the breakage channel. Next, experiments with similar D_m values are considered collectively as a data point. In this procedure, different cannula sizes may be used within the same data point. However, the different cannulas are not likely to be the reason for the anomalous behavior. For the two data points at 2.0 m/s, data points 7 and 8 in Table 2, one point is an anomaly and the other point is not, even though the experimental conditions are very similar. Moreover, the individual experiments in these data points are from the same sequence of experiments in the lab. That is, the size of the continuously generated drops alternated between corresponding to data point 7 and corresponding to data point 8.

If the two anomalies are due to a experimental error or an inaccuracy introduced in the experimental procedure, it is natural to assume this would be linked to the methodology of determining breakage probability. In the PBE, as given on the form in (1), the breakage probability is a single point value. However, a large section of the channel is observed in the experimental procedure. The breakage probability is determined as the ratio of the number of drops breaking in this section to the total number of drops entering the section. Each mother drop observed in the considered

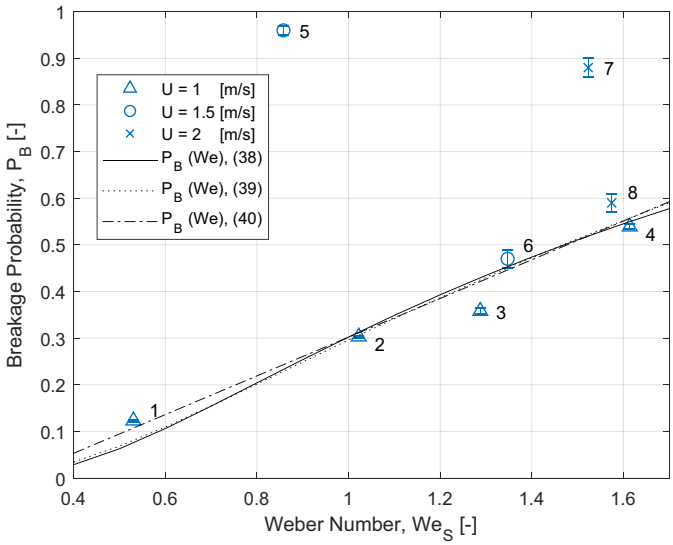

Fig. 12. Breakage probability plotted against the Weber number calculated from the entire range of turbulence, as seen in Table 2. The solid errorbars denote the 95% confidence interval limits. The point marker of the data point symbolizes the cross sectional area averaged velocity during the experiments. Additionally, fitted model predictions are shown for ()()()(38)–(40).

Table 4
Parameters determined when fitting the breakage probability to (38)–(40).

	a_1	b_1	a_2	b_2	a_3	b_3
This study	1.46	1.57	0.357	1.22	0.415	−0.113
Galinat et al. (2005)	2.6	11.2	0.29	55		

test section volume has an individual path. This means that the absolute transverse distance from the centerline of the channel may be different for the individual drops observed. Some drops may travel closer to the wall. This horizontal distance from the centerline is hereafter referred to as Δx. It is speculated that this distance to the wall impacts the probability of breakage.

In the investigation of Δx, each individual mother drop path for the four data points at U equal to 1.5 m/s and 2.0 m/s have been considered. For the drops undergoing breakage, Δx is found from the position at the breakage event start instance, as defined in Section 2.2. For the drops not undergoing breakage, Δx is found as the maximum recorded horizontal displacement of the entire observed trajectory of the drop. The resulting mean and median Δx for the data points are shown in Table 5. From the table, it is clear that the data points on average exhibit some displacement from the center of the channel. In the procedure of manually verifying each video containing an experimental sample, it has been observed that drops frequently exhibit some horizontal movement in the observed region of the breakage channel. The values in Table 5 are in line with these observations.

As can be seen from Table 5, the data points that exhibit expected breakage probabilities, 6 and 8, have a difference in the average Δx between breaking and non breaking drops of ∼1 mm. That is, the breaking drops travel, on average, ∼1 mm closer to the wall. Compared to the channel width of 30 mm, 1 mm is not a big difference. Conversely, the breaking drops of data point 8 travel ∼1 mm further from the wall than the breaking drops of data point 7, yet exhibits higher breakage probabilities.

For the data points considered anomalies, 5 and 7, Table 5 shows that there are only minor differences in the average Δx. For both breaking and non breaking drops, the mean values are in the range 7.2 to 7.5 mm. Compared to data points 6 and 8, the Δx of the data points 5 and 7 are ∼2–3 mm closer to the wall. It is not clear whether these differences in Δx between anomalous and not anomalous data points are large enough to explain the significant difference in breakage probability. If the breakage probability is very sensitive to the Δx, this is a systematic error in the procedure of determining the breakage probability. It is noted that the recorded ϵ of each experimental sample is dependent on the droplet trajectory, as described in Section 2.3. Thus, if a significant number of drops travel close to the wall, this is reflected in the corresponding ϵ of the data point. Moreover, the data point 5 does exhibit a similar variation in ϵ from the start point to the instance of first separation as the data point 6. The same is the case comparing the data points 7 and 8. Additionally, if there is a sensitivity to Δx instead of ϵ, it could be argued that none of the data points should agree with the model by Coulaloglou and Tavlarides (1977). As discussed previously, the model shows reasonable agreement with the experimental results for the data points 1, 2, 3, 4, 6 and 8.

Table 5
The mean and median of the critical horizontal distance from channel center. For breakage events, subscripted *B*, the distance is defined horizontal displacement at the breakage event start instance. For experiments without breakage, subscripted *N*, the distance is defined as the maximum displacement observed.

#	D_m	U	Mean Δx_B	Median Δx_B	Mean Δx_N	Median Δx_N
5	0.87 mm	1.5 m/s	7.5 mm	7.3 mm	7.5 mm	7.5 mm
6	1.13 mm	1.5 m/s	5.8 mm	6.2 mm	4.5 mm	3.8 mm
7	0.86 mm	2.0 m/s	7.4 mm	7.3 mm	7.2 mm	6.1 mm
8	1.02 mm	2.0 m/s	4.7 mm	5.3 mm	3.7 mm	2.8 mm

As mentioned, the size of the continuously generated drops alternated between corresponding to data point 7 and corresponding to data point 8, and it is further noted that these two data points exhibit different Δx. To investigate whether this may be due to the process of generating droplets, the displacement at the first observed position, Δx_0, is investigated for the data points 5, 6, 7 and 8. The determined Δx_0 for the data points are 6.4 mm, 3.2 mm, 6.4 mm and 2.8 mm, respectively. From this information, it is seen that the larger Δx of the data points 5 and 7, compared to data points 6 and 8, might be caused by the larger displacement of the drops at their first observed position. This may be due to an observed, but not quantified phenomena during droplet generation. Droplets form on the tip of the glass cannula, and detaches due to the continuous fluid flow past the cannula tip. After the detachment, the drops exhibit a transverse movement to the low pressure area downstream of the cannula, possibly due to a cannula wake effect. It is speculated that this transverse movement of the drops is larger for the smaller drop sizes.

Tomiyama et al. (2002) investigated the path and deformation of air bubbles in stagnant water. These bubbles were generated by vertically placed cannulas. In the study, Tomiyama et al. (2002) showed that the bubble generation caused an initial deformation, and that this deformation was critical for the following bubble path through the stagnant liquid. While drops are generally less deformed than bubbles, the initial deformation may be an effect during the droplet generation in the current study. In combination with a cannula wake effect, this initial deformation effect could explain why data points 7 and 8 exhibit different Δx and Δx_0.

It is proposed that the history of the drop motion, which is affected by the droplet generation, may be relevant to the breakage probability. It follows that the history of the drop motion may be relevant to all aspects of the breakage phenomena. This view is not compatible with the assumption that a breakage event is solely dependent on a single turbulent vortex-droplet interaction. In this interpretation, the mother drop is in equilibrium before it is interacting with the vortex. Moreover, this interaction is only containing sufficient energy for breakup when the vortex has similar size as the drop. However, the single vortex assumption has received criticism. One example is Andersson and Helmi (2014), who used large eddy and volume of fluid simulations to show that a droplet may interact with vortices of different sizes and more than one vortex simultaneously. A different argument was presented by Foroushan and Jakobsen (2020). They argued that droplets break due to a series of interactions rather than a single interaction. In this view, drop surface energy is both accumulated through vortex interactions and decaying through dampening oscillations, either until enough energy for breakage is achieved or no breakage take place due to a relative large decay rate. In this case, the initial deformation, as described by Tomiyama et al. (2002), and the wake effect described above may contribute with energy relevant to the breakup.

Obviously, the outliers may be due to a still undiscovered mechanism. As these data points correspond to the smallest D_m values, this means that the diameter of the mother drop is critical for the breakage probability. Further elucidation of the phenomena discussed in this section is required to draw firm conclusions on the anomalous data in this work.

3.5.3. Maximum stable drop size

Hinze (1955) formulated an expression for a theoretical maximum stable drop diameter, D_{crit}, in a system. First, the disruptive force (19) was set equal to the stabilizing force (20) multiplied by a constant $C_{H,1}$

$$\sigma_t = C_{H,1}\sigma_s \tag{41}$$

Using the second order structure function valid in the inertial subrange (10) the expression for D_{crit} was found to be

$$D_{crit} = C_{H,2}(\gamma/\rho_c)^{3/5}\epsilon^{-2/5} \tag{42}$$

Where Hinze (1955) found the value of $C_{H,2}$ to be 0.725. As seen in Section 3.1, the inertial subrange formulation is not accurate in the current study. Therefore, (41) is in this work solved with the second order structure function valid in the entire turbulent range (11). It can be shown that $C_{H,1} = \beta(C_{H,2})^{5/3} \sim 1.17$, which can be used in solving the more complex formulation of (41) using (11) numerically. This is done in MATLAB using the function *fminsearch*. The resulting maximum stable drop sizes are seen in Table 6.

From Table 6 and Fig. 11, it can be seen that mother drops larger than the maximum stable drop size has an increased probability of breakage compared to drops smaller than the maximum stable drop size. From the data points 1–4, it may appear that the breakage probability is linked to the difference in maximum stable drop size and mother drop size. However, data points 6 and 8 exhibits higher breakage probabilities than expected according to this theory.

It is noted that the anomalous behavior of data points 5 and 7 are not further elucidated by this procedure. Moreover, as given in Section 2.2, neither of the definitions of the breakage event end instances corresponds to an equilibrium state of the channel.

3.6. Breakage frequency

The breakage frequency is determined by combining the previously discussed breakage time, Section 3.4, and breakage probability, Section 3.5, according to (25). The results are affected by the same factors as when discussing the breakage time and breakage

Table 6
Maximum stable drop sizes according to (41).

Data Point	Mother drop size, D_m [mm]	Maximum stable drop size, D_{crit} [mm]	Difference, D_{crit}-D_m [mm]
1	1	1.5	0.5
2	1.48	1.6	0.12
3	1.87	1.75	−0.12
4	2.23	1.85	−0.38
5	0.87	1.0	0.13
6	1.13	1.05	−0.08
7	0.86	1.0	0.14
8	1.02	1.0	−0.02

probability individually. As there are two sets of breakage times, one set for each breakage event definition, there are two breakage frequencies. Note that the inverse of the breakage time is used in (25), thus the impact of ϵ and D_m is also inverted. For example, the breakage frequency according to the initial breakage event definition is higher than that of the cascade breakage event definition, because the initial breakage time is shorter than the cascade breakage time.

The breakage frequencies determined in this study is shown in Fig. 13. Fig. 13a shows the breakage frequency determined according to the initial breakage event definition, and Fig. 13b shows the breakage frequency determined according to the cascade breakage event definition. It can clearly be seen from the figures that the breakage frequency increases with increased ϵ. This behavior is expected, as increased ϵ increases breakage probability and lowers breakage time, as seen in the previous sections.

Fig. 13 also shows an unexpected result for the data points 1, 2, 3 and 4, defined as Group C in Section 2.3. For these data points the D_m value is varied, but the breakage frequency is similar. These points had very different breakage times and breakage probabilities, as discussed in Section 3.4 and Section 3.5, respectively. That is, while the D_m value was critical for both the breakage time and breakage probabilities individually, it is not critical for the breakage frequency for the given system properties and flow characteristics.

The model by Coulaloglou and Tavlarides (1977) have been fitted to both the breakage time and breakage probability in Sections 3.4 and 3.5. For the initial breakage time the parameter c_3 was determined as 1.86, while the cascade breakage time parameter c_3 was determined to be 2.9. The breakage probability parameter c_4 is the same for both definitions, i.e. 0.92. The fitted functions for breakage time and breakage probability can be combined to obtain the breakage frequency, according to (25). The resulting model predictions for each data point are plotted in Fig. 13 as a dotted line with square symbols. From the figure, it is clear that the model predictions for the data points 5 and 7 are inaccurate. This result is expected, due to the inaccurate breakage probability for these data points. On the other hand, the model predictions for the remaining data points are adequate for both breakage definitions. In fact, the model predictions for the breakage frequency appears to be better than the individual predictions of breakage time and probability.

The model based on Coulaloglou and Tavlarides with viscous stabilization (30) have been model fitted to the breakage frequency using the *fit* function in MATLAB. In this procedure, $\overline{\delta u^2}$ and D_m are given as the independent variables in the model. The anomalous data points are not included in the fitting procedure. The only constraint on the fitting is that the parameters must be non-negative. This results in c_7 being predicted to be zero and the original model by Coulaloglou and Tavlarides is recovered.

Fitting the model of Alopaeus et al. (2002), Eq. (33), requires $\overline{\delta u^2}, D_m$ and ϵ to be given as independent variables. This is done in the *lsqnonlin* function in MATLAB, where the residual of the model prediction is subtracted the experimentally determined breakage frequency values. The parameters are constrained to be non-negative and the anomalous data points are not included. As was the case for the viscous stabilization of Coulaloglou and Tavlarides, the fit of (33) returns the parameter governing the viscous stabilizing effect, c_{15}, as zero. Hence, it is unlikely that the drop viscosity is an important stabilizing force in this study. The remaining parameters values were in the initial breakage case determined to be $1.47 \cdot 10^2$ and 1.22 for c_{13} and c_{14}, respectively. For the cascade breakage case the values were determined to be 65.6 and 0.859. These values are debated in the literature; Alopaeus et al. (2002) found the values to be c_{13} = 3.68, $c_{14} = 7.75 \cdot 10^{-2}$, while the values reported by Maaß and Kraume (2012) were $c_{13} = 1.6 \cdot 10^2$ and $c_{14} = 1.6 \cdot 10^{-1}$.

The prediction of the fitted model of Alopaeus et al. (2002), Eq. (33), can be seen in Fig. 13. The model reasonable accounts for the impact of ϵ, but appears to lack the dependency of D_m, as suspected by Narsimhan et al. (1979). Hence, the model is less accurate than the model by Coulaloglou and Tavlarides (1977), despite being directly fitted to the breakage frequency.

3.7. Implications of modeling work

In this study, the breakage kernel functions are investigated experimentally to elucidate the fluid particle breakage phenomena. The aim is to enable improved understanding and motivating development of more universal population balance equation closures and models. Hence, we summarize our findings on this subject in this section.

In the Sections 3.2, 3.4 and 3.5 model parameters were fitted to the experimental results and compared to previously determined parameter values. As these parameter values are different, it is obvious that the model parameters are not universal. For example, the model parameter c_1 in the breakage probability (26) was determined in Section 3.5 as 0.57, while previous values were reported as 0.39 and 0.182 by Maaß and Kraume (2012) and Coulaloglou and Tavlarides (1977), respectively. Similar patterns can be seen for all parameter values in this study. Nevertheless, reasonable model predictions are achieved in the individual studies. It follows that the parameters are reasonably constant for small variations in the independent variables of the kernel functions, e.g. D_m and ϵ. On the other hand, large variations in D_m and ϵ results in new parameter values.

Much work is needed before models such as the one proposed by Coulaloglou and Tavlarides (1977) can be reformulated to be mechanistically correct with universal parameters. It is proposed as a first task that further experiments on the different kernel functions are performed, where the independent variables ϵ, D_m or k are varied over a wider range of values. In the current work, significantly changing these independent variables has proven difficult due to practical limitations with the experimental setup. However, if an independent variable is varied across a significant range, it would be possible to investigate the universal sensitivity of the kernel functions to the independent variable. The important independent variables are mother drop diameter, turbulent kinetic energy dissipation rate and turbulent kinetic energy. The ranges for which these variables are of industrial interest may be $D_m \in \left[10^{-6} - 10^{-2}\right]$ mm and $\epsilon \in [0.1 - 10000]$ m^2/s^3, with consistent values of k. For universal model development, experimental data is also needed from different experimental designs, as well as different fluid and system properties.

Based on the fitting of models to the breakage frequency, as seen in Section 3.6, it is clear that the pertinent stresses in the current system are the inertial stress (19) and restoring surface stress (20). The viscous stabilizing stress (24) is not found to be important, but it may be important for dispersed phases of higher viscosity. The generalized viscous shear stress (23) is also negligible in this study, as the drops are larger than the Kolmogorov microscale, η. Currently, there is some ambiguity to the use of the second order structure function in the formulation of the viscous shear stress. Shinnar (1961) originally formulated the viscous shear stress considering droplets smaller than η, where there are small or no inertial forces. For these droplets, the velocity gradient of the smallest turbulent scales exerts a shear force, which is determined from ϵ

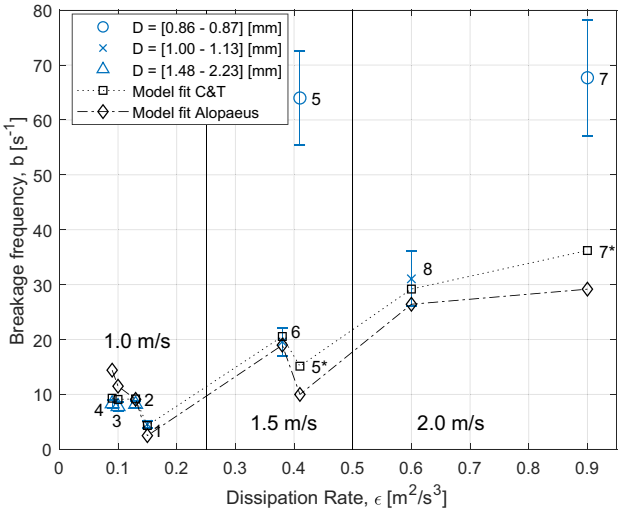

(a) Initial breakage event definition

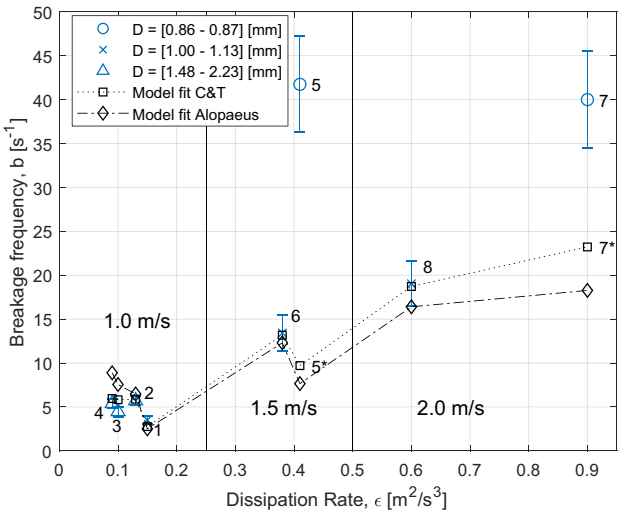

(b) Cascade breakage event definition

Fig. 13. Breakage frequency for both breakage event definitions for the data points in Table 2. The error bars denotes the 95% confidence interval limits and the point markers represents the range of the mother drop size of the data point. The vertical lines separate the data points obtained under different cross sectional area averaged velocity. The model predictions by Coulaloglou and Tavlarides (1977), Eq. (25), are indicated by the dotted line with square symbols. The model predictions of Alopaeus et al. (2002), Eq. (33), are indicated by dotted and dashed line with diamond symbols.

and viscosity only and valid in the viscous subrange of turbulence. The extending of the viscous shear stress to all scales of turbulence appears to be based on the view of Walstra and Smulders (1998). They claimed that, for all scales and ranges of turbulence, eddies of comparable size to the drop act by inertial forces, which is in agreement with classical Kolmogorov theory. In addition, Walstra and Smulders (1998) claimed that eddies larger than the drops contribute by viscous mechanisms. While this may be true, it is not clear how these larger viscous mechanisms may then be described by the second order structure function for the same size as the drop.

4. Conclusions

In this study it is shown that most of the source term kernel functions are dependent on both D_m and ϵ. Moreover, the employed breakage event definition is critical to the results.

In the initial breakage definition the average number of daughters are always two. Contrary to most inherent model assumptions for binary breakage models, the daughter size distribution changes for different system and flow conditions. However, no clear dependencies on D_m or ϵ are found. For the cascade breakage definition on the other hand, there is a clear dependence on the Weber number for both the average number of daughters and the daughter size distribution. An increase in the Weber number is followed by an increase in the average number of daughters, with a linear correlation. Nevertheless, the general shape of the daughter size distribution function remains similar for the average number of daughters. An increase in the average number of daughters leads to an increase in the number of the smallest daughter sizes, with a corresponding decrease in several of the largest daughter sizes. It is noted that the average number of daughters does not correspond to binary breakage for any data point.

The breakage probability shows a clear dependency on the Weber number, which may be either linear or exponential in nature. The exception is the two data points corresponding to the smallest D_m values, which exhibit very high breakage probabilities. No definite reason is found for these anomalies.

To model the breakage phenomena, predictive models must account for the physical conditions during breakage, which impacts every source term kernel function. The model of Coulaloglou and Tavlarides (1977) is fitted to show a reasonable agreement with the breakage time, breakage probability and ultimately the breakage frequency. However, a different model framework is required to model the average number of daughters and the daughter size distribution. These kernel functions vary with the physical system properties and flow characteristics, which the model of Coulaloglou and Tavlarides (1977) does not account for.

While the model may be fitted to predict the experimental results, the parameter values are different from the values reported in the literature. Hence, the models do not appear to be universal. Additional experimental investigations are required in order to obtain improved understanding and enabling development of more predictive models. Preferably, these investigations should cover a wider range in the independent variables. At present, experimental investigations cover very narrow ranges in the variables.

CRediT authorship contribution statement

Eirik H. Herø: Conceptualization, Methodology, Software, Formal analysis, Investigation, Data Curation, Writing – original draft. **Nicolas La Forgia:** Conceptualization, Methodology, Software, Investigation, Writing – review & editing. **Jannike Solsvik:** Conceptualization, Writing – review & editing. **Hugo A. Jakobsen:** Conceptualization, Writing – review & editing, Supervision.

Declaration of Competing Interest

The authors declare that they have no known competing financial interests or personal relationships that could have appeared to influence the work reported in this paper.

Acknowledgment

This work was carried out as a part of SUBPRO, a research based innovation center within Subsea Production and Processing. The authors gratefully acknowledge the financial support from SUBPRO, which is financed by the Research Council of Norway, major industry partners, and NTNU.

References

Alopaeus, V., Koskinen, J., Keskinen, K.I., Majander, J., 2002. Simulation of the population balances for liquid–liquid systems in a nonideal stirred tank. Part 2—parameter fitting and the use of the multiblock model for dense dispersions. Chem. Eng. Sci. 57 (10), 1815–1825. https://doi.org/10.1016/S0009-2509(02)00067-2. https://linkinghub.elsevier.com/retrieve/pii/S0009250902000672.

Andersson, R., Andersson, B., 2006. On the breakup of fluid particles in turbulent flows. AIChE J. 52 (6), 2020–2030. https://doi.org/10.1002/aic.10831. URL http://doi.wiley.com/10.1002/aic.10831.

Andersson, R., Helmi, A., 2014. Computational fluid dynamics simulation of fluid particle fragmentation in turbulent flows. Appl. Math. Model. 38 (17–18), 4186–4196. https://doi.org/10.1016/j.apm.2014.01.005.

Ashar, M., Arlov, D., Carlsson, F., Innings, F., Andersson, R., 2018. Single droplet breakup in a rotor-stator mixer. Chem. Eng. Sci. 181, 186–198. https://doi.org/10.1016/j.ces.2018.02.021. URL https://linkinghub.elsevier.com/retrieve/pii/S0009250918300836.

Batchelor, G.K., 1951. Pressure fluctuations in isotropic turbulence. Math. Proc. Cambridge Philos. Soc. 47 (2), 359–374. https://doi.org/10.1017/S0305004100026712. URL https://www.cambridge.org/core/product/identifier/S0305004100026712/type/journal_article.

Calabrese, R.V., Chang, T.P.K., Dang, P.T., 1986. Drop breakup in turbulent stirred-tank contactors. Part I: Effect of dispersed-phase viscosity. AIChE J. 32 (4), 657–666. https://doi.org/10.1002/aic.690320416. URL http://doi.wiley.com/10.1002/aic.690320416.

Chen, Z., Prüss, J., Warnecke, H.-J., 1998. A population balance model for disperse systems. Chem. Eng. Sci. 53 (5), 1059–1066. https://doi.org/10.1016/S0009-2509(97)00328-X. URL https://linkinghub.elsevier.com/retrieve/pii/S000925099700328X.

Coulaloglou, C.A., Tavlarides, L.L., 1977. Description of interaction processes in agitated liquid-liquid dispersions. Chem. Eng. Sci. 32 (11), 1289–1297. https://doi.org/10.1016/0009-2509(77)85023-9.

Davidson, P.A., 2004. Turbulence: An Introduction for Scientists and Engineers. Oxford University Press, New York.

Diemer, R., Olson, J., 2002. A moment methodology for coagulation and breakage problems: Part 3—generalized daughter distribution functions. Chem. Eng. Sci. 57 (19), 4187–4198. https://doi.org/10.1016/S0009-2509(02)00366-4. URL https://www.sciencedirect.com/science/article/pii/S0009250902003664.

Foroushan, H.K., Jakobsen, H.A., 2020. On the dynamics of fluid particle breakage induced by hydrodynamic instabilities: A review of modelling approaches. Chem. Eng. Sci. 219, 115575. https://doi.org/10.1016/j.ces.2020.115575. URL https://linkinghub.elsevier.com/retrieve/pii/S000925092030107X.

Galinat, S., Masbernat, O., Guiraud, P., Dalmazzone, C., Noïk, C., 2005. Drop break-up in turbulent pipe flow downstream of a restriction. Chem. Eng. Sci. 60 (23), 6511–6528. https://doi.org/10.1016/j.ces.2005.05.012.

Galinat, S., Torres, L.G., Masbernat, O., Guiraud, P., Risso, F., Dalmazzone, C., Noik, C., 2007. Breakup of a drop in a liquid-liquid pipe flow through an orifice. AIChE J. 53 (1), 56–68. https://doi.org/10.1002/aic.11055. arXiv:arXiv:1402.6991v1, URL http://doi.wiley.com/10.1002/aic.11055.

Håkansson, A., 2020. On the validity of different methods to estimate breakup frequency from single drop experiments. Chem. Eng. Sci. 227, 115908. https://doi.org/10.1016/j.ces.2020.115908. URL https://linkinghub.elsevier.com/retrieve/pii/S0009250920304401.

Håkansson, A., Trägårdh, C., Bergenståhl, B., 2009. Dynamic simulation of emulsion formation in a high pressure homogenizer. Chem. Eng. Sci. 64 (12), 2915–2925. https://doi.org/10.1016/j.ces.2009.03.034. URL https://linkinghub.elsevier.com/retrieve/pii/S0009250909002164.

Han, L., Luo, H., Liu, Y., 2011. A theoretical model for droplet breakup in turbulent dispersions. Chem. Eng. Sci. 66 (4), 766–776. https://doi.org/10.1016/J.CES.2010.11.041. URL https://www.sciencedirect.com/science/article/pii/S0009250910007037.

Han, L., Gong, S., Li, Y., Ai, Q., Luo, H., Liu, Z., Liu, Y., 2013. A novel theoretical model of breakage rate and daughter size distribution for droplet in turbulent flows.

Chem. Eng. Sci. 102, 186–199. https://doi.org/10.1016/J.CES.2013.06.046. URL https://www.sciencedirect.com/science/article/pii/S0009250913004697.
Han, L., Gong, S., Ding, Y., Fu, J., Gao, N., Luo, H., 2015. Consideration of low viscous droplet breakage in the framework of the wide energy spectrum and the multiple fragments. AIChE J. 61 (7), 2147–2168. https://doi.org/10.1002/aic.14830. URL http://doi.wiley.com/10.1002/aic.14830.
Herø, E.H., Forgia, N.L., Solsvik, J., Jakobsen, H.A., 2019. Determination of Breakage Parameters in Turbulent Fluid-Fluid Breakage. Chem. Eng. Technol. 42 (4), 903–909. https://doi.org/10.1002/ceat.201800610.
Herø, E.H., La, N., Forgia, J., Solsvik, H.A. Jakobsen, 2020. Single Drop Breakage in Turbulent Flow: Statistical Data Analysis. Chem. Eng. Sci. X, 100082. https://doi.org/10.1016/j.cesx.2020.100082. URL https://linkinghub.elsevier.com/retrieve/pii/S2590140020300289.
Hinze, J.O., 1955. Fundamentals of the Hydrodynamic Mechanism of Splitting in Dispersion Processes. AIChE J. 1 (3), 289–295. URL https://onlinelibrary.wiley.com/doi/pdf/10.1002/aic.690010303#accessDenialLayout.
Hsia, M., Tavlarides, L.L., 1983. Simulation analysis of drop breakage, coalescence and micromixing in liquid-liquid stirred tanks. Chem. Eng. J. 26 (3), 189–199. https://doi.org/10.1016/0300-9467(83)80014-8. URL https://linkinghub.elsevier.com/retrieve/pii/0300946783800148.
Jakobsen, H.A., 2014. Chemical reactor modeling: Multiphase reactive flow. Springer, Berlin.
Karimi, M., Andersson, R., 2019. Dual mechanism model for fluid particle breakup in the entire turbulent spectrum. AIChE J., e16600 https://doi.org/10.1002/aic.16600. URL https://onlinelibrary.wiley.com/doi/abs/10.1002/aic.16600.
La Forgia, N., Herø, E.H., Solsvik, J., Jakobsen, H.A., 2018. Dissipation rate estimation in a rectangular shaped test section with periodic structure at the walls. Chem. Eng. Sci. 195, 159–178. https://doi.org/10.1016/j.ces.2018.11.039.
Lasheras, J., Eastwood, C.D., Martínez-Bazán, C., Montañés, J., 2002. A review of statistical models for the break-up of an immiscible fluid immersed into a fully developed turbulent flow. Int. J. Multiph. Flow 28 (2), 247–278. https://doi.org/10.1016/S0301-9322(01)00046-5. URL https://www.sciencedirect.com/science/article/pii/S0301932201000465.
Lehr, F., Millies, M., Mewes, D., 2002. Bubble-Size distributions and flow fields in bubble columns. AIChE J. 48 (11), 2426–2443. https://doi.org/10.1002/aic.690481103. URL http://doi.wiley.com/10.1002/aic.690481103.
Liao, Y., Lucas, D., 2009. A literature review of theoretical models for drop and bubble breakup in turbulent dispersions. Chem. Eng. Sci. 64 (15), 3389–3406. https://doi.org/10.1016/j.ces.2009.04.026.
Luo, H., Svendsen, H.F., 1996. Theoretical Model for Drop and Bubble Breakup in Turbulent Dispersions. AIChE J. 42 (5), 1225–1233. https://doi.org/10.1002/aic.690420505. URL http://www.ncbi.nlm.nih.gov/pubmed/19947509 http://doi.wiley.com/10.1002/aic.690420505.
Maaß, S., Kraume, M., 2012. Determination of breakage rates using single drop experiments. Chem. Eng. Sci. 70, 146–164. https://doi.org/10.1016/j.ces.2011.08.027.
Maaß, S., Gäbler, A., Zaccone, A., Paschedag, A.R., Kraume, M., 2007. Experimental investigations and modelling of breakage phenomena in stirred liquid/liquid systems. Chem. Eng. Res. Des. 85 (5 A), 703–709. https://doi.org/10.1205/cherd06187.
Maaß, S., Buscher, S., Hermann, S., Kraume, M., 2011. Analysis of particle strain in stirred bioreactors by drop breakage investigations. Biotechnol. J. 6 (8), 979–992. https://doi.org/10.1002/biot.201100161.
Martínez-Bazán, C., Montañés, J.L., Lasheras, J.C., 1999a. On the breakup of an air bubble injected into a fully developed turbulent flow. Part 1. Breakup frequency. J. Fluid Mech. 401. https://doi.org/10.1017/S0022112099006680. S0022112099006680. URL http://www.journals.cambridge.org/abstract_S0022112099006680.
Martínez-Bazán, C., Montañés, J.L., Lasheras, J.C., 1999b. On the breakup of an air bubble injected into a fully developed turbulent flow. Part 2. Size PDF of the resulting daughter bubbles. J. Fluid Mech. 401. https://doi.org/10.1017/S0022112099006692. S0022112099006692. URL http://www.journals.cambridge.org/abstract_S0022112099006692 http://www.journals.cambridge.org/abstract_S0022112099006680.
Martínez-Bazán, C., Rodríguez-Rodríguez, J., Deane, G.B., Montaes, J.L., Lasheras, J.C., 2010. Considerations on bubble fragmentation models. J. Fluid Mech. 661, 159–177. https://doi.org/10.1017/S0022112010003186.
Nachtigall, S., Zedel, D., Kraume, M., 2016. Analysis of drop deformation dynamics in turbulent flow. Chin. J. Chem. Eng. 24 (2), 264–277. https://doi.org/10.1016/j.cjche.2015.06.003.
Narsimhan, G., Gupta, J., Ramkrishna, D., 1979. A model for transitional breakage probability of droplets in agitated lean liquid-liquid dispersions. Chem. Eng. Sci. 34 (2), 257–265. https://doi.org/10.1016/0009-2509(79)87013-X. URL https://linkinghub.elsevier.com/retrieve/pii/000925097987013X.
Pope, S., 2000. Turbulent Flows. Cambridge University Press, Cambridge.
Ramkrishna, D., 2000. Population balances: Theory and applications to particulate systems in engineering. Academic Press, San Diego.
Shinnar, R., 1961. On the behaviour of liquid dispersions in mixing vessels. J. Fluid Mech. 10 (02), 259. https://doi.org/10.1017/S0022112061000214. URL http://www.journals.cambridge.org/abstract_S0022112061000214.
Solsvik, J., 2017. Turbulence modeling in the wide energy spectrum: Explicit formulas for Reynolds number dependent energy spectrum parameters. Eur. J. Mech. B. Fluids 61, 170–176. https://doi.org/10.1016/j.euromechflu.2016.10.011. URL https://linkinghub.elsevier.com/retrieve/pii/S0997754616303211.
Solsvik, J., Jakobsen, H.A., 2015. Single drop breakup experiments in stirred liquid-liquid tank. Chem. Eng. Sci. 131, 219–234. https://doi.org/10.1016/j.ces.2015.03.059.
Solsvik, J., Jakobsen, H.A., 2016a. A review of the statistical turbulence theory required extending the population balance closure models to the entire spectrum of turbulence. AIChE J. 62 (5), 1795–1820. https://doi.org/10.1002/aic.15128. URL http://doi.wiley.com/10.1002/aic.15128.
Solsvik, J., Jakobsen, H.A., 2016b. Development of Fluid Particle Breakup and Coalescence Closure Models for the Complete Energy Spectrum of Isotropic Turbulence. Ind. Eng. Chem. Res. 55 (5), 1449–1460. https://doi.org/10.1021/acs.iecr.5b04077. URL http://pubs.acs.org/doi/10.1021/acs.iecr.5b04077.
Solsvik, J., Tangen, S., Jakobsen, H.A., 2013. On the constitutive equations for fluid particle breakage. Rev. Chem. Eng. 29 (5), 241–356. https://doi.org/10.1515/revce-2013-0009.
Solsvik, J., Skjervold, V.T., Han, L., Luo, H., Jakobsen, H.A., 2016a. A theoretical study on drop breakup modeling in turbulent flows: The inertial subrange versus the entire spectrum of isotropic turbulence. Chem. Eng. Sci. 149, 249–265. https://doi.org/10.1016/J.CES.2016.04.037. URL https://www.sciencedirect.com/science/article/pii/S000925091630196 8#bib11.
Solsvik, J., Maaß, S., Jakobsen, H.A., 2016b. Definition of the Single Drop Breakup Event. Ind. Eng. Chem. Res. 55 (10), 2872–2882. https://doi.org/10.1021/acs.iecr.6b00591.
Tomiyama, A., Celata, G., Hosokawa, S., Yoshida, S., 2002. Terminal velocity of single bubbles in surface tension force dominant regime. Int. J. Multiph. Flow 28 (9), 1497–1519. https://doi.org/10.1016/S0301-9322(02)00032-0. URL https://linkinghub.elsevier.com/retrieve/pii/S0301932202000320.
Vankova, N., Tcholakova, S., Denkov, N.D., Vulchev, V.D., Danner, T., 2007. Emulsification in turbulent flow: 2. Breakage rate constants. J. Colloid Interface Sci. 313 (2), 612–629. https://doi.org/10.1016/j.jcis.2007.04.064. URL https://linkinghub.elsevier.com/retrieve/pii/S0021979707005413.
Vejražka, J., Zedníková, M., Stanovský, P., 2018. Experiments on breakup of bubbles in a turbulent flow. AIChE J. 64 (2), 740–757. https://doi.org/10.1002/aic.15935. URL https://onlinelibrary.wiley.com/doi/10.1002/aic.15935.
Walstra, P., Smulders, P.E., 1998. Emulsion formation. In: Binks, B.P., (Ed.), Modern Aspects of Emulsion Science. Royal Society of Chemistry, Cambridge, pp. 56–99 (Chapter 2). doi: 10.1039/9781847551474-00056. http://ebook.rsc.org/?DOI=10.1039/9781847551474-00056.
Zaccone, A., Gäbler, A., Maaß, S., Marchisio, D., Kraume, M., 2007. Drop breakage in liquid–liquid stirred dispersions: Modelling of single drop breakage. Chem. Eng. Sci. 62 (22), 6297–6307. https://doi.org/10.1016/J.CES.2007.07.026. URL https://www.sciencedirect.com/science/article/pii/S000925090700526X#bib6.

Chapter 10

Concluding Remarks

This work focuses on experimental investigation of drop breakage with the aim to elucidate the breakage phenomena and obtain data for model validation. The research goals were identified in Section 1.2 as:

- Design and construct an experimental facility for the investigation of single particle breakage in turbulent flow.
- Characterize the turbulence level of the continuous flow in the experimental facility.
- Determine and outline a procedure for extracting information on the kernel functions from the observed breakage events.
- Perform experiments under different flow conditions, system conditions and dispersed phase properties.
- Investigate the experimental data to elucidate the breakage phenomena.

In this section, the achieved results are summarized by the research goals. The discussion is structured in a top-down approach, starting by considering the experimental results and its impact on the understanding of the breakage phenomena. Then, the experimental procedure is discussed before the design of the experimental facility is considered.

10.1 Characterize the Turbulence Level of the Continuous Liquid Flow in the Experimental Facility

LDV-measurements were performed to obtain the turbulent characteristics of the continuous liquid flow. The procedure and results are described in Paper 1, Chapter 6. By using LDV, one obtains the instantaneous velocities over a period of time of a very small stationary volume, which may be considered a single point. The instantaneous velocity values found in each point is time averaged to characterize the turbulence of the continuous phase channel flow. The values utilized in the drop breakage investigations is thus spatially well differentiated, but temporally course due to the averaging procedure.

Hence, the effect of the instantaneous turbulence characteristics during the breakage events are unknown.

10.2 Investigate the Experimental Data to Elucidate the Breakage Phenomena

In Papers 3 and 4, Chapters 8 and 9, data on the breakage kernels are presented. From these empirical data, conclusions on the breakage phenomena and the modeling of kernel functions are reached.

10.2.1 Trends in the Kernel Functions

As an overall conclusion it can be said that the empirical data is in adequate agreement with previous experimental investigations, as well as known model concepts. Hence, it is concluded that the constructed experimental setup can be used to investigate fluid particle breakage.

Direct comparisons of the kernel function values between this work and previous works reported in the literature are challenging, due to differences in experimental setup and procedure between the studies. On the other hand, the trends are interesting to compare. The trends represented by the kernel functions are the general change in the experimentally determined values when varying the mother drop size, ϵ or k. In this work, the trends in breakage probability and breakage time are in reasonable agreement with previous experimental investigations.

Some previous studies have reported the breakage probability and average number of daughters by Weber number, and the current results show similar trends. However, the use of Weber number may be generally criticized for obscuring the dependence on the physical parameters and properties, which complicates comparisons.

10.2.2 Impact on Modeling

For the breakage time and breakage probability, known model concepts may be fitted to achieve adequate predictions locally. In other words, the narrow variations of the independent variables in this study allows for adequate model predictions. Nevertheless, the determined model parameters are different from those found in previous experimental investigations, although these parameters provided adequate model predictions in their respective studies.

For the cascade breakage event definition the experimentally determined average number of daughters vary for different flow characteristics and system properties. This result is in contrast with the existing model frameworks. The available model frameworks does not predict the average number of daughters, as discussed in Chapter 2. Moreover, the experimentally determined average number of daughters are non-integer values, which is currently only possible in the model framework of Diemer and Olson [56]. Conversely, the experimentally determined daughter size distribution function retains a

general shape for changing flow characteristics and system properties, which is closer to the assumptions employed in available model frameworks. The shape of the daughter size distribution is exponential, where the smallest daughter sizes are always significantly more common than other outcomes of breakage and the probability of obtaining a daughter size is decreased as the daughter size increases.

For the initial breakage event definition the binary breakage assumption is in agreement with the experimental results. However, the experimentally determined shapes of the daughter size distributions changes for different flow characteristics and system properties. No existing model framework predicts this behavior.

10.3 Determine and Outline a Procedure for Extracting Information on the Kernel Functions From the Observed Breakage Events

The methodology for extracting breakage data from individual videos is defined and described in Paper 2, Chapter 7. The methodology includes details on extracting data from a single frame or image, such as obtaining the size of the drop, as well as extracting data from several frames, such as obtaining the breakage time.

Contrary to previous investigations, both of the two breakage event definitions found in the literature [57] are employed in this work. The advantage of the initial breakage event definition is its simple formulation. The event is considered ended at the time instance when the drop separates into two (still deformed) drops. In empirical work, the size of these daughters is challenging to determined if the deformed daughter drops undergo further breakage. Hence, the determined daughter size distributions may be inaccurate. Moreover, while the initial breakage event definition is commonly employed, it is unclear how the breakup of short-lived daughter drops can be considered independent from the initial breakage event. Especially when a daughter drop breaks without obtaining a spherical and stable shape, but instead undergoes continuous deformation.

On the other hand, interpretations through the cascade breakage event definition do consider whether sequential breakups are dependent on the initial breakage. In this definition the deformed daughter drops are observed until stabilizing in a spherical shape. Due to the increased regularity of the shapes of the observed daughter drops, the determination of their sizes is significantly more accurate than for the initial breakage definition. That is not to say that the cascade breakage event definition is without weaknesses. The intermediary daughters are observed for a longer time. It is possible that some of the intermediary daughters interact with turbulent structures before the breakage event is concluded. This potential daughter-turbulence interaction affects the breakage process, but is impossible to account for in the current procedure. In addition, as the intermediary daughters should be observed until a spherical shape is obtained, daughters breaking at the wall presents a challenge. Currently, the breakage event is considered finished for these particular daughters, but that is a necessary simplification which may not be correct.

In Paper 3, Chapter 8, the methodology for determining the kernel functions is described. This procedure covers how to combine and utilize data obtained from single

experiments performed under similar conditions. The procedure is transparent and well described. However, the procedure is applied to a large volume. The size of the volume may impact the results as noted in Paper 4, Chapter 9; *While the models are formulated in a Eulerian framework, the experimental data is essentially determined in an Langrangian framework, taken from a larger volume. This is a practically necessary simplification, the impact of which was discussed in Herø et al. [65, P.19]. It is noted that the breakage frequency is determined from the breakage time and the breakage probability. The breakage time is determined from local values associated with each breakage event while the breakage probability is determined as an average value of the whole test section. The limiting accuracy of the breakage probability function might require improvements, thus other approaches for determining this kernel function have been suggested in the literature (Vejrazka et al. [80], Håkansson [81]).* Hence, a refinement of the procedure or a refinement on how the procedure is applied may improve the accuracy of the results obtained.

Paper 3 includes a description of the statistical analysis employed. The number of experimental repetitions required was unknown when designing the facility and deciding on the experimental procedure. The statistical analysis showed that a relatively low number ($\sim$30) of experiments where needed for statistically relevant results [65], which has an impact on the subsequent experimental design as discussed in the following section.

10.4 Design and Construct an Experimental Facility for the Investigation of Single Particle Breakage in Turbulent Flow

Review of previous experimental studies on fluid particle breakage and homogeneous turbulence were given in Chapters 3 and 4. Based on these reviews, the critical functionalities of an experimental facility were determined, Chapter 5, and the experimental facility, Chapters 5, 6, 7, 8 and 9, was designed and constructed. As concluded in Section 10.2.1, the experimental data confirms the facility can be used to investigate single droplet breakage. Nevertheless, there are two important comments on the final design of the experimental facility.

First, the number of experimental repetitions required were lower than the amount accounted for during the experimental design phase. It follows that the requirement of "Repeatable and reproducible experiments", as discussed in Chapter 5, is less strict than originally considered during the design process of the experimental facility. In particular, the required automation for the repetition of experiments in the experimental facility is lower than expected and less automated facilities may be practically viable.

Second, the continuous phase flow characteristics may impact the experimental results. The facility does not exhibit isotropic turbulence and the breakage events takes place before the channel flow is fully developed. Hence, there are gradients in the turbulent characteristics in the region of interest and along the drop trajectory during breakage. Moreover, as the drops break in different positions, there are different initial conditions for each individual breakage event.

Chapter 11

Suggested Further Work

11.1 Modeling

As discussed in Section 10.2.2, there are discrepancies between the available model frameworks and the experimentally determined average number of daughters and daughter size distributions. Considering the results obtained with the initial breakage event definition the binary breakage assumption is correct. On the other hand, the daughter size distribution function must change shape with changing flow characteristics or changing fluid or system properties. The dependencies of the shape of the daughter size distribution function represents an unresolved challenge.

The experimental results obtained with the cascade breakage definition represents a different challenge in modeling of the breakage phenomenon. The average number of daughters can vary and can be non-integers. In simulations, the average number of daughters must be predicted from the flow characteristics, fluid properties and system properties. In turn, as the daughter size distribution function is not independent from the average number of daughters, the daughter size distribution function must be predicted such that volume and number conservation are achieved.

Two approaches for obtaining the required model framework is suggested here. The first alternative is to formulate a framework where the average number of daughters is predicted and a general form of the daughter size distribution function exists as a function of the average number of daughters as well as fluid flow characteristics, fluid properties and system properties. The drawback of this approach is that obtaining an expression for the daughter size distribution which remains number and volume conserving is not trivial.

The alternative approach is to combine daughter size distribution functions which are valid for integer values of daughter numbers. As a simplified example, take a predicted average number of daughters to be 2.5 and assume that half the breakage events results in 2 daughters and the other half results in 3 daughters. Then, weighted use of two different daughter size distribution functions, valid for 2 and 3 daughters respectively, in the breakage birth source term could yield both number and volume conservation. In this approach, the two daughter size distribution functions may be represent two different

mechanisms of breakage. To the authors knowledge, the use of weighted kernel functions is not previously reported in the literature. Theoretically, it is possible to combine two different binary breakage kernel functions in a way that maintains number and volume conservation. The drawback of this approach, where different kernel functions are combined by weights to obtain a specific average number of daughters, is that several distinct daughter numbers are possible results of a single breakage event. As seen in Paper 3, Chapter 8, the number of daughters from a single breakage event ranges from 2 to ∼20. A larger number of daughters are expected for increased turbulent forces or larger mother drop sizes. To weight different kernel functions every distinct daughter number requires a corresponding daughter size distribution function. Each of these daughter size distribution functions requires validation, which may not be experimentally feasible due to the large number of distinct daughter size distribution functions and the amount of manual labor required for experimental investigations of single droplet breakage.

11.2 Experimental Facility

This section covers potential improvements to the experimental facility and procedure. However, it is easier to define the issue that could be improved, than it is to formulate a practical solution to the issue. Experimental work within fluid particle breakage is challenging.

11.2.1 Independent Variables and System Properties

For improved understanding of the breakage phenomena, it is of interest to investigate a wider range of independent variables and system properties. As seen in Chapter 3, the experimental studies found in the literature consider ϵ in the range $[0.1, 10^4]$ m^2/s^3. In each individual study the value of ϵ is only varied to a very small degree. Ideally, the entire range should be considered in the same experimental setup and procedure.

Expanding the range of ϵ in the experimental facility of the current work is a significant challenge. The capability of the continuous phase pump represents a limit to the available continuous phase velocity. In addition, additional issues will likely arise should a larger continuous phase velocity be achieved. The residence time of the drops in the volume observed by the cameras will be shorter. In turn, there may not be enough time for the entire breakage event to be observed. Alternatively, the breakage time may be decreased to such a degree that higher framerates of the cameras are required for sufficient temporal resolution. The framerate of the cameras utilized in the experimental facility of the current work can not be increased further.

A higher continuous phase velocity may also affect the generation of the mother drop sizes. In the experimental facility of the current work, the injected mother drop sizes are significantly dependent on the continuous phase velocity. A different injection system may generate droplets of consistent sizes independent of the continuous phase velocity, representing an improvement on the current facility. As was the case for ϵ, it would be

of interest to investigate a wider range of mother drop sizes in the same experimental setup and procedure. Based on the studies presented in Chapter 3 the range of mother drop sizes would be $D_m \in [10^{-5}, 10^{-2}]$ m.

Different fluid properties of the continuous and dispersed phases and system properties should be considered, e.g. μ, ρ and γ. There may be some practical limitations to the use of different oils in the experimental facility of the current work. The use of octanol as the dispersed phase gives a relatively low interfacial tension for the system. Changing to an oil that increases the surface tension is expected to lower the probability of breakage for otherwise equal conditions. Hence, obtaining the required samples of breakage might be challenging for systems of higher surface tension. Breakage may also be inhibited by higher viscosity in the dispersed phase, further complicating obtaining sufficient samples of breakage. Finally, it is noted that toxic chemicals complicates HSE measures and may create challenges associated with the preparation of experiments, performing the experiments or the clean-up and disposing of used chemicals.

11.2.2 Continuous Phase Flow

As noted in Chapter 5, the droplet breakages should take place in homogeneous, or near homogeneous, turbulence. However, as discussed in Chapter 4 and Chapter 5, there are practical limitations to performing droplet breakage experiments in such setups. Nevertheless, the continuous phase flow in the experimental facility utilized in this work could be improved.

One area of improvement originates from the drops breaking in different positions. Equal continuous phase conditions for the breaking drops would be advantageous. To obtain such conditions, the gradients in the turbulence level should be minimized. Moreover, the impact of mean flow viscous shear should be avoided by avoiding breakage in regions of mean flow gradients such as the boundary layer.

11.2.3 Image Analysis

As discussed in the Papers 2, 3 and 4 (Chapters 7, 8 and 9), interpreting the videos obtained during the experiments requires substantial manual labor. A fully automated image analysis program would significantly improve the amount of experimental results obtained in a given time by eliminating the manual labor. However, creating an automated image analysis program is not trivial.

The current image analysis program can automatically extract information from individual frames to a reasonable degree. That is, the number of drops, their size, etc. are adequately extracted. The issue is to automatically associate this extracted data with the real droplets. That is, to automatically identify whether it is the same drop in two consecutive frames or whether a breakage has taken place is difficult. Although not quantified in this work, it appears that the automatic image analysis is more accurate with larger than smaller drops. Hence, a possible improvement may be achieved with a finer spatial and temporal resolution of the video. The resulting video would have less

differences between consecutive frames and the drops would occupy a larger number of pixels.

Machine learning could potentially be applied to obtain an automatic image analysis. However, machine learning requires sufficient data for training and validation, which requires many videos to be manually interpreted before the machine learning algorithm can be applied. Due to this prerequisite, the gain of employing machine learning may be limited. Especially as the machine learning algorithm must be retrained to account for new experimental operating conditions, such as liquid flow rate.

11.2.4 Experimental Procedure

Improving the experimental procedure may be a way to provide more accurate experimental results. By considering a smaller observed volume the difference between the Langrarian experimental results and Eulerian model formulation would be smaller. In particular, a smaller volume would improve the determination of the breakage probability, which in turn improves the breakage frequency. A smaller volume also results in similar continuous phase flow conditions associated with each breakage.

The major challenge of employing smaller volumes is that neither the droplet trajectories nor the position of breakage can be controlled. Moreover, it is currently impossible to know where the breakage events begin before performing the manual interpretation of the breakage events. In turn, many breakage events must be interpreted to obtain a statistically sufficient number of breakages for each volume considered. Several of these interpretations may be unnecessary as the volume of breakage may either have sufficient data beforehand or not enough data at the end of processing. The resulting procedure would be significantly more manual labor intensive.

Another possibility to improve the experimental procedure may be to interpret the breakage frequency by use of a different approach. According to the recent review by Håkanson [81] the breakage frequency can not be separated into breakage time and breakage probability. Instead, it should be calculated directly with the procedures suggested by Martinez-Bazan et al. [38] or Vejrazka et al. [80]. Martinez-Bazan et al. [38] suggested that the breakage frequency of a given volume could be determined from

$$b = -\frac{1}{N(D)} \frac{\partial (UN(D))}{\partial x} \tag{11.1}$$

where $N(D)$ is the number of fluid particles of size D in a given volume, U is the velocity of the fluid particle and x is the spatial coordinate in the velocity direction. Vejrazka et al. [80] calculated the breakage frequency of a given volume by

$$b = \frac{\text{number of breakages of fluid particles with size } D \text{ in the volume}}{\text{total time spent by fluid particles of size } D \text{ in the volume}} \tag{11.2}$$

The two approaches requires a change to the experimental procedure, where the number of drops must be measured at different positions. In addition, either the velocity of the drop or the residence time of the drops must be measured depending on which of the two

approaches is selected. Hence, these approaches require smaller volumes to be considered, with the drawbacks as described above. The advantage of these two approaches is that they avoid the issue previously described; *the breakage time is determined from local values associated with each breakage event while the breakage probability is determined as an average value of the whole test section* [65].

11.2.5 Three-Dimensional Analysis

In this work the droplets are measured in 2D, which does not provide information on the drop in the third dimension. The breakage phenomena are a 3D phenomena which ideally should be observed in all three dimensions. However, 3D imaging is associated with significantly larger complexity. The experimental facility must accommodate the field of view from another direction, where the illumination and focus depth required must be accounted for. The complexity of the experimental procedure increases as it must handle data originating from the different field of views. Nevertheless, observing the breaking droplets in 3D constitutes an improvement in the data obtained.

Bibliography

[1] NOROG, 2018 Environmental Report - Environmental Work by the Oil and Gas Industry, Facts and Development Trends, Tech. rep., NOROG (2018).

[2] C. A. Capela Moraes, F. S. Da Silva, L. P. M. Marins, A. S. Monteiro, D. A. De Oliveira, R. M. Pereira, R. D. S. Pereira, A. Alves, G. M. Raposo, L. Figueiredo, R. Orlowski, H. Folhadela, R. Mikkelsen, J. Kolbu, L. McKenzie, Z. M. F. Elamin, O. T. McClimans, Marlim 3 Phase Subsea Separation System: Subsea Process Design And Technology Qualification Program, in: Offshore Technology Conference 2012, Offshore Technology Conference, 2012.

[3] G. G. Stokes, On the effect of the internal friction of fluids on the motion of pendulums. Section II: solution of the equations in the case of a sphere oscillating in a mass of fluid either unlimited, or confined by a spherical envelope concentric with the sphere in i, Trans Cambridge Phil Soc 9 (pt II) (1851) 8–106.

[4] R. Clift, J. R. Grace, M. E. Weber, Bubbles, Drops, and Particles, Academic Press, New York, 1978.

[5] H. A. Jakobsen, Chemical reactor modeling: Multiphase reactive flow, Springer, Berlin, 2014.

[6] N. Kharoua, L. Khezzar, H. Saadawi, CFD Modelling of a Horizontal Three-Phase Separator: A Population Balance Approach, American Journal of Fluid Dynamics 3 (4) (2013) 101–118.

[7] H. S. Skjefstad, Development and assessment of a multi-pipe oil-water bulk separator concept for subsea applications, Ph.D. thesis, NTNU (2019).

[8] D. Ramkrishna, Population balances: Theory and applications to particulate systems in engineering, Academic Press, San Diego, 2000.

[9] J. Lasheras, C. D. Eastwood, C. Martínez-Bazán, J. Montañés, A review of statistical models for the break-up of an immiscible fluid immersed into a fully developed turbulent flow, International Journal of Multiphase Flow 28 (2) (2002) 247–278. doi:10.1016/S0301-9322(01)00046-5.

[10] Y. Liao, D. Lucas, A literature review of theoretical models for drop and bubble breakup in turbulent dispersions, Chemical Engineering Science 64 (15) (2009) 3389–3406. doi:10.1016/j.ces.2009.04.026.

[11] J. Solsvik, S. Tangen, H. A. Jakobsen, On the constitutive equations for fluid particle breakage, Reviews in Chemical Engineering 29 (5) (2013) 241–356. doi:10.1515/revce-2013-0009.

[12] R. Andersson, B. Andersson, On the breakup of fluid particles in turbulent flows, AIChE Journal 52 (6) (2006) 2020–2030. doi:10.1002/aic.10831.

[13] J. Solsvik, H. A. Jakobsen, Single drop breakup experiments in stirred liquid-liquid tank, Chemical Engineering Science 131 (2015) 219–234. doi:10.1016/j.ces.2015.03.059.

[14] C. A. Coulaloglou, L. L. Tavlarides, Description of interaction processes in agitated liquid-liquid dispersions, Chemical Engineering Science 32 (11) (1977) 1289–1297. doi:10.1016/0009-2509(77)85023-9.

[15] M. Konno, M. Aoki, S. Saito, Scale effect on breakup process in liquid-liquid agitated tanks, Journal of Chemical Engineering of Japan 16 (4) (1983) 312–319. doi:10.1252/jcej.16.312.

[16] N. B. Raikar, S. R. Bhatia, M. F. Malone, M. A. Henson, Experimental studies and population balance equation models for breakage prediction of emulsion drop size distributions, Chemical Engineering Science 64 (10) (2009) 2433–2447. doi:10.1016/j.ces.2009.01.062.

[17] P. J. Becker, F. Puel, R. Henry, N. Sheibat-Othman, Investigation of Discrete Population Balance Models and Breakage Kernels for Dilute Emulsification Systems, Industrial & Engineering Chemistry Research 50 (19) (2011) 11358–11374. doi:10.1021/ie2006033.

[18] S. Galinat, O. Masbernat, P. Guiraud, C. Dalmazzone, C. Noïk, Drop break-up in turbulent pipe flow downstream of a restriction, Chemical Engineering Science 60 (23) (2005) 6511–6528. doi:10.1016/j.ces.2005.05.012.

[19] S. Galinat, L. G. Torres, O. Masbernat, P. Guiraud, F. Risso, C. Dalmazzone, C. Noik, Breakup of a drop in a liquid-liquid pipe flow through an orifice, AIChE Journal 53 (1) (2007) 56–68. arXiv:arXiv:1402.6991v1, doi:10.1002/aic.11055.

[20] M. Ashar, D. Arlov, F. Carlsson, F. Innings, R. Andersson, Single droplet breakup in a rotor-stator mixer, Chemical Engineering Science 181 (2018) 186–198. doi:10.1016/j.ces.2018.02.021.

[21] S. Maaß, M. Kraume, Determination of breakage rates using single drop experiments, Chemical Engineering Science 70 (2012) 146–164. doi:10.1016/j.ces.2011.08.027.

[22] H. Luo, H. F. Svendsen, Theoretical Model for Drop and Bubble Breakup in Turbulent Dispersions, AIChE Journal 42 (5) (1996) 1225–1233. doi:10.1002/aic.690420505.

[23] J. O. Hinze, Fundamentals of the Hydrodynamic Mechanism of Splitting in Dispersion Processes, A.1.Ch.E. Journal 1 (3) (1955) 289–295.

[24] A. N. Kolmogorov, On the breakage of drops in a turbulent flow, Dokl. Akad. Navk. SSSR 66 (1949) 825–828.

[25] J. Solsvik, Turbulence modeling in the wide energy spectrum: Explicit formulas for Reynolds number dependent energy spectrum parameters, European Journal of Mechanics - B/Fluids 61 (2017) 170–176. doi:10.1016/j.euromechflu.2016.10.011.

[26] C. A. Mockett, Comprehensive Study of Detached-Eddy Simulation, Ph.D. thesis, Technical University of Berlin, Magdeburg (2009).

[27] J. Solsvik, H. A. Jakobsen, A review of the statistical turbulence theory required extending the population balance closure models to the entire spectrum of turbulence, AIChE Journal 62 (5) (2016) 1795–1820. doi:10.1002/aic.15128.

[28] A. N. Kolmogorov, The Local Structure of Turbulence in Incompressible Viscous Fluid for Very Large Reynolds Numbers Proceedings : Mathematical and Physical Sciences , Vol . 434 , No . 1890 , Turbulence and, Proceedings of the Royal Society A: Mathematical, Physical and Engineering Sciences 30 (1890) (1941) 299–303.

[29] S. Pope, Turbulent Flows, Cambridge University Press, Cambridge, 2000.

[30] K. R. Sreenivasan, On the universality of the Kolmogorov constant, Physics of Fluids 7 (11) (1995) 2778–2784. doi:10.1063/1.868656.

[31] P. A. Davidson, Turbulence: An Introduction for Scientists and Engineers, Oxford University Press, New York, 2004.

[32] G. K. Batchelor, Pressure fluctuations in isotropic turbulence, Mathematical Proceedings of the Cambridge Philosophical Society 47 (2) (1951) 359–374. doi:10.1017/S0305004100026712.

[33] G. I. Taylor, The Spectrum of Turbulence, Proceedings of the Royal Society A: Mathematical, Physical and Engineering Sciences 164 (919) (1938) 476–490. doi:10.1098/rspa.1938.0032.

[34] G. K. Batchelor, Diffusion in a field of homogeneous turbulence, Mathematical Proceedings of the Cambridge Philosophical Society 48 (2) (1952) 345–362. doi:10.1017/S0305004100027687.

[35] J. Solsvik, H. A. Jakobsen, Development of Fluid Particle Breakup and Coalescence Closure Models for the Complete Energy Spectrum of Isotropic Turbulence, Industrial and Engineering Chemistry Research 55 (5) (2016) 1449–1460. doi:10.1021/acs.iecr.5b04077.

[36] Z. Chen, J. Prüss, H.-J. Warnecke, A population balance model for disperse systems, Chemical Engineering Science 53 (5) (1998) 1059–1066. doi:10.1016/S0009-2509(97)00328-X.

[37] N. Vankova, S. Tcholakova, N. D. Denkov, V. D. Vulchev, T. Danner, Emulsification in turbulent flow: 2. Breakage rate constants, Journal of Colloid and Interface Science 313 (2) (2007) 612–629. doi:10.1016/j.jcis.2007.04.064.

[38] C. Martínez-Bazán, J. L. Montañés, J. C. Lasheras, On the breakup of an air bubble injected into a fully developed turbulent flow. Part 1. Breakup frequency, Journal of Fluid Mechanics 401 (1999) S0022112099006680. doi:10.1017/S0022112099006680.

[39] C. Martínez-Bazán, J. L. Montañés, J. C. Lasheras, On the breakup of an air bubble injected into a fully developed turbulent flow. Part 2. Size PDF of the resulting daughter bubbles, Journal of Fluid Mechanics 401 (1999) S0022112099006692. doi:10.1017/S0022112099006692.

[40] C. Martínez-Bazán, J. Rodríguez-Rodríguez, G. B. Deane, J. L. Montaes, J. C. Lasheras, Considerations on bubble fragmentation models, Journal of Fluid Mechanics 661 (2010) 159–177. doi:10.1017/S0022112010003186.

[41] A. Revuelta, J. Rodríguez-Rodríguez, C. Martínez-Bazán, Bubble break-up in a straining flow at finite Reynolds numbers, Journal of Fluid Mechanics 551 (2006) 175–184. doi:10.1017/S0022112005008505.

[42] G. Narsimhan, J. Gupta, D. Ramkrishna, A model for transitional breakage probability of droplets in agitated lean liquid-liquid dispersions, Chemical Engineering Science 34 (2) (1979) 257–265. doi:10.1016/0009-2509(79)87013-X.

[43] V. Alopaeus, J. Koskinen, K. I. Keskinen, J. Majander, Simulation of the population balances for liquid–liquid systems in a nonideal stirred tank. Part 2—parameter fitting and the use of the multiblock model for dense dispersions, Chemical Engineering Science 57 (10) (2002) 1815–1825. doi:10.1016/S0009-2509(02)00067-2.

[44] R. Shinnar, On the behaviour of liquid dispersions in mixing vessels, Journal of Fluid Mechanics 10 (02) (1961) 259. doi:10.1017/S0022112061000214.

[45] A. Håkansson, C. Trägårdh, B. Bergenståhl, Dynamic simulation of emulsion formation in a high pressure homogenizer, Chemical Engineering Science 64 (12) (2009) 2915–2925. doi:10.1016/j.ces.2009.03.034.

[46] M. Karimi, R. Andersson, Dual mechanism model for fluid particle breakup in the entire turbulent spectrum, AIChE Journal (2019) e16600doi:10.1002/aic.16600.

[47] P. Walstra, P. E. Smulders, Chapter 2. Emulsion Formation, in: Binks, B.P., Modern Aspects of Emulsion Science, Royal Society of Chemistry, Cambridge, 1998, pp. 56–99. doi:10.1039/9781847551474-00056.

[48] J. Solsvik, V. T. Skjervold, H. A. Jakobsen, A bubble breakage model for finite Reynolds number flows, Journal of Dispersion Science and Technology 38 (7) (2017) 973–978. doi:10.1080/01932691.2016.1216440.

[49] C. Dorao, H. Jakobsen, hp-adaptive least squares spectral element method for population balance equations, Applied Numerical Mathematics 58 (5) (2008) 563–576. doi:10.1016/j.apnum.2006.12.005.

[50] M. Hsia, L. L. Tavlarides, Simulation analysis of drop breakage, coalescence and micromixing in liquid-liquid stirred tanks, The Chemical Engineering Journal 26 (3) (1983) 189–199. doi:10.1016/0300-9467(83)80014-8.

[51] F. Lehr, M. Millies, D. Mewes, Bubble-Size distributions and flow fields in bubble columns, AIChE Journal 48 (11) (2002) 2426–2443. doi:10.1002/aic.690481103.

[52] L. Han, H. Luo, Y. Liu, A theoretical model for droplet breakup in turbulent dispersions, Chemical Engineering Science 66 (4) (2011) 766–776. doi:10.1016/J.CES.2010.11.041.

[53] L. Han, S. Gong, Y. Li, Q. Ai, H. Luo, Z. Liu, Y. Liu, A novel theoretical model of breakage rate and daughter size distribution for droplet in turbulent flows, Chemical Engineering Science 102 (2013) 186–199. doi:10.1016/J.CES.2013.06.046.

[54] L. Han, S. Gong, Y. Ding, J. Fu, N. Gao, H. Luo, Consideration of low viscous droplet breakage in the framework of the wide energy spectrum and the multiple fragments, AIChE Journal 61 (7) (2015) 2147–2168. doi:10.1002/aic.14830.

[55] J. Solsvik, V. T. Skjervold, L. Han, H. Luo, H. A. Jakobsen, A theoretical study on drop breakup modeling in turbulent flows: The inertial subrange versus the entire spectrum of isotropic turbulence, Chemical Engineering Science 149 (2016) 249–265. doi:10.1016/J.CES.2016.04.037.

[56] R. Diemer, J. Olson, A moment methodology for coagulation and breakage problems: Part 3—generalized daughter distribution functions, Chemical Engineering Science 57 (19) (2002) 4187–4198. doi:10.1016/S0009-2509(02)00366-4.

[57] J. Solsvik, S. Maaß, H. A. Jakobsen, Definition of the Single Drop Breakup Event, Industrial and Engineering Chemistry Research 55 (10) (2016) 2872–2882. doi:10.1021/acs.iecr.6b00591.

[58] E. H. Herø, N. L. Forgia, J. Solsvik, H. A. Jakobsen, Determination of Breakage Parameters in Turbulent Fluid-Fluid Breakage, Chemical Engineering and Technology 42 (4) (2019) 903–909. doi:10.1002/ceat.201800610.

[59] S. Maaß, A. Gäbler, A. Zaccone, A. R. Paschedag, M. Kraume, Experimental investigations and modelling of breakage phenomena in stirred liquid/liquid systems, Chemical Engineering Research and Design 85 (5 A) (2007) 703–709. doi:10.1205/cherd06187.

[60] S. Maaß, S. Buscher, S. Hermann, M. Kraume, Analysis of particle strain in stirred bioreactors by drop breakage investigations, Biotechnology Journal 6 (8) (2011) 979–992. doi:10.1002/biot.201100161.

[61] A. Zaccone, A. Gäbler, S. Maaß, D. Marchisio, M. Kraume, Drop breakage in liquid–liquid stirred dispersions: Modelling of single drop breakage, Chemical Engineering Science 62 (22) (2007) 6297–6307. doi:10.1016/J.CES.2007.07.026.

[62] S. Nachtigall, D. Zedel, M. Kraume, Analysis of drop deformation dynamics in turbulent flow, Chinese Journal of Chemical Engineering 24 (2) (2016) 264–277. doi:10.1016/j.cjche.2015.06.003.

[63] Y. Ji, J. Bellettre, A. Montillet, P. Massoli, Experimental investigation on single drop breakage in two-stream impinging microchannels, Experiments in Fluids 62 (1) (2021) 17. doi:10.1007/s00348-020-03124-0.

[64] R. Andersson, B. Andersson, Modeling the breakup of fluid particles in turbulent flows, AIChE Journal 52 (6) (2006) 2031–2038. arXiv:arXiv:1402.6991v1, doi:10.1002/aic.10832.

[65] E. H. Herø, N. La Forgia, J. Solsvik, H. A. Jakobsen, Single Drop Breakage in Turbulent Flow: Statistical Data Analysis, Chemical Engineering Science: X (2020) 100082doi:10.1016/j.cesx.2020.100082.

[66] R. Andersson, B. Andersson, F. Chopard, T. Norén, Development of a multi-scale simulation method for design of novel multiphase reactors, Chemical Engineering Science 59 (22-23) (2004) 4911–4917. doi:10.1016/j.ces.2004.07.084.

[67] S. Maaß, S. Wollny, R. Sperling, M. Kraume, Numerical and experimental analysis of particle strain and breakage in turbulent dispersions, Chemical Engineering Research and Design 87 (4) (2009) 565–572. doi:10.1016/j.cherd.2009.01.002.

[68] J. M. Lawson, J. R. Dawson, A scanning PIV method for fine-scale turbulence measurements, Experiments in Fluids 55 (12) (2014). doi:10.1007/s00348-014-1857-7.

[69] J. M. Lawson, J. R. Dawson, On velocity gradient dynamics and turbulent structure, Journal of Fluid Mechanics 780 (2015) 60–98. doi:10.1017/jfm.2015.452.

[70] A. Srdic, H. J. Fernando, L. Montenegro, Generation of nearly isotropic turbulence using two oscillating grids, Experiments in Fluids 20 (5) (1996) 395–397. doi:10.1007/BF00191022.

[71] E. L. G. Kit, E. J. Strang, H. J. Fernando, Measurement of turbulence near shear-free density interfaces, Journal of Fluid Mechanics 334 (1997) 293–314. doi:10.1017/S0022112096004442.

[72] S. S. Shy, C. Y. Tang, S. Y. Fann, A Nearly Isotropic Turbulence Generated by a Pair of Vibrating Grids, Experimental Thermal and Fluid Science 14 (3) (1997) 251–262. doi:10.1016/S0894-1777(96)00111-2.

[73] J. Yan, N. S. Cheng, H. W. Tang, S. K. Tan, Oscillating-grid turbulence and its applications: A review, Journal of Hydraulic Research 45 (1) (2007) 26–32. doi:10.1080/00221686.2007.9521740.

[74] R. E. Honey, R. Hershberger, R. J. Donnelly, D. Bolster, Oscillating-grid experiments in water and superfluid helium, Physical Review E - Statistical, Nonlinear, and Soft Matter Physics 89 (5) (2014) 1–11. doi:10.1103/PhysRevE.89.053016.

[75] G. I. Taylor, Statistical theory of turbulence, I-III, Proceedings of the Royal Society A: Mathematical, Physical and Engineering Sciences 151 (874) (1935) 421–464. doi:10.1098/rspa.1935.0159.

[76] K. R. Sreenivasan, On the scaling of the turbulence energy dissipation rate, Physics of Fluids 27 (5) (1984) 1048. doi:10.1063/1.864731.

[77] I. Dahl, Experiments on Single Droplet Breakage in Turbulent Flow, Master Thesis, NTNU, Trondheim (2019).

[78] R. P. Hesketh, T. W. Fraser Russell, A. W. Etchells, Bubble size in horizontal pipelines, AIChE Journal 33 (4) (1987) 663–667. doi:10.1002/aic.690330414.

[79] S. E. Haaland, Simple and Explicit Formulas for the Friction Factor in Turbulent Pipe Flow, Journal of Fluids Engineering 105 (1) (1983) 89–90. doi:10.1115/1.3240948.

[80] J. Vejražka, M. Zedníková, P. Stanovský, Experiments on breakup of bubbles in a turbulent flow, AIChE Journal 64 (2) (2018) 740–757. doi:10.1002/aic.15935.

[81] A. Håkansson, On the validity of different methods to estimate breakup frequency from single drop experiments, Chemical Engineering Science 227 (2020) 115908. doi:10.1016/j.ces.2020.115908.

ISBN 978-82-326-5213-6 (printed ver.)
ISBN 978-82-326-5643-1 (electronic ver.)
ISSN 1503-8181 (printed ver.)
ISSN 2703-8084 (online ver.)

NTNU

Norwegian University of
Science and Technology